A combined *ab initio* and experimental study of Lanthanides and/or transition metal doped oxides

By

Winfred Mueni MULWA

(M.Sc)

A thesis submitted in fulfillment of the requirements for the degree

PHILOSOPHIAE DOCTOR/ DOCTOR OF PHILOSOPHY

in the

Faculty of Natural and Agricultural Sciences

Departments of Physics

at the

University of the Free State

Republic of South Africa

Promoter: Prof. B.F. Dejene

Co-Promoters: Dr. C.N.M. Ouma

Prof. Martin Onani

January 2017

Declaration

This thesis is my original work and has not been presented for the award of a Ph.D degree at the University of the Free State or any other University. I have acknowledged other people's work by referencing adequately.

Winfred Mueni MULWA

Student number: 2014066126

Signed ……on the……day of…….2017

This thesis is submitted with our approval as University supervisors:

Prof. Francis B. Dejene	……..	…….
	Signature	Date
Dr. Cecil N.M. Ouma		February 10, 2017
	Signature	Date
Prof. Martin O. Onani	……	……..
	Signature	Date

Dedication

This thesis is dedicated to my lovely daughters Joyce and Cynthia.

Acknowledgements

- To the **Almighty God;** fear not, for I am with you, He whispered unto me**.** He touched the hearts of my supervisors as they advised me. He watched as I computed, synthesized and characterized, and He gave me the skills and understanding. When I felt like giving up he reminded me that I will be the head but not the tail. Glory be to His holy name.

- I am indebted to Prof. Francis B. Dejene, my supervisor, for having trust in me. You encouraged me when the journey was too tough, you guided me, I feel very fortunate to have the opportunity to work under you. I am deeply honored for your understanding leadership and making sure that this study is completed without any financial constrain. Prof, if only you could listen to my heart for words are not enough!

- Dr. Cecil M. Ouma, my co-supervisor for your unconditional guidance, support, advice and especially your patience during my whole doctoral study. I consider you as the best role model.

- Prof. Martin O. Onani, my co-supervisor, I have no words to describe how grateful I am for your guidance, support and lessons in research. I have learnt a lot from you Prof.

- Prof. J.J. Terblans and Dr. Tshabalala for accepting me as a student in the department of physics.

- The administrative staff: Karen Cronje and Meiki Lebeko for their support and kindness during my research.

- My fellow research group members, Dr. O. K. Echendu Dr. I. Ahemen, Dr. F. G. Hone, Dr. L. F. Koao, Mr. S. J. Motloung, P. P Mokoena, Simon Ogugua, M. A. Lephoto, Sharon Kiprotich, Debelo and Leta; You were wonderful people to work with.

- Dr. Nicholas Makau and Prof. George Amolo for introducing me to computational physics in the year 2009.

- The organizers of the African School on Electronic Structure Methods and Applications (ASESMA) for giving me the opportunity to interact with the experts in the field of computational physics.

- I would like to convey my sincere gratitude to Prof. Shobhana Narasimhan (Theoretical Science Unit JNCASR, Bangalore) for her encouragement to me as a woman scientist.

- Finally, I would like to express my sincere indebtedness to my family and parents for their constant prayers and blessings. I want to thank my husband, Wainaina, for his patience, love and support. 'Behind every good woman, there is a better man'.

Abstract

Ab initio modelling techniques have produced a notable contribution in analysing semiconductor metal oxides properties by use of first principles. These techniques have transformed to a high level of accuracy, owing to the development in algorithms and improved computational ability. In the study of structural, electronic and optical properties of metal oxides, *ab initio* techniques have been used with a lot of success to illustrate these properties. *Ab initio* studies therefore can complement experimental findings or even provide reliable results on properties which have not yet been experimentally investigated. Properties which can be calculated with the use of density functional theory (DFT) include spectroscopic, energetic, electronic and geometric properties.

In this combined experimental and *ab initio* work on metal oxides doped with transition metals, the used of local density approximation with the Hubbard U correlation to compute the structural, electronic and optical properties of $ZnAl_2O_4$ and Cu^{2+}:$ZnAl_2O_4$ was used. The powders of doped and undoped $ZnAl_2O_4$ were effectively synthesized by use of the sol-gel technique. The X-ray diffraction (XRD) pattern for $ZnAl_2O_4$ displayed crystalline peaks corresponding to cubic structure and phase dissociation was not observed. It also showed negligible lattice distortion and a slight shift to higher angles with increase of Cu^{2+} percentage doping. Energy dispersive X-rays spectroscopy (EDS) confirmed pure samples of $ZnAl_2O_4$ components. Scanning electron microscopy (SEM) micrographs showed a uniform, well distributed and spherical morphology. The high resolution transmission electron microscopy (HRTEM) showed the influence of varying Cu^{2+} concentration on the particle agglomeration as well as on the crystallite sizes. The average crystallite sizes of $ZnAl_2O_4$ powders almost remained constant with the increase of Cu^{2+} doping concentration. The lattice spacing approximated from selected area electron diffraction (SAED) was 0.242 nm corresponding to (311) lattice of $ZnAl_2O_4$. Setting excitation at 283 nm, the photoluminescence (PL) emission peaks were at 388 nm, 425 nm and 480 nm in undoped $ZnAl_2O_4$ which was due to oxygen vacancies while the peak at 586 nm was due to Cu^{2+} ions. Computationally, introduction of Cu^{2+} ions did not lead to significant lattice distortion and the PL emission peak was at 435 nm with a transition from Cu_3d to Cu_4p. The substitutional energies in Cu^{2+}:$ZnAl_2O_4$ predicted negative

formation energies for oxygen vacancies suggesting that these vacancies are easily formed in $ZnAl_2O_4$. The two point defects (oxygen vacancy and Cu^{2+} dopant) existed singly as the binding energies were found to be negative.

Both experimental and computational work were carried out on lanthanide-doped metal oxide (γ -Al_2O_3 in this case). The powders of doped and undoped γ -Al_2O_3 were successfully prepared using the sol-gel technique. The Al_2O_3 as well as Ce^{3+}:Al_2O_3 were modelled where the Kohn-Sham equations were solved by the use of local density approximation with the Hubbard U correction. In Al_2O_3:Ce^{3+}, introduction of the dopant caused lattice strain as well as reduction in band gap. The formation energies in all the charge states were negative, suggesting that the γ -Al_2O_3 lattice could easily accommodate Ce^{3+}. The PL emission peak was reported to be at 502 nm with a transition from O_2p to Ce_4f. The X-ray diffraction (XRD) pattern exhibited crystalline peaks corresponding to cubic structure. Due to difference in ionic radius between Al^{3+} andCe^{3+}, lattice distortion was realized. As the doping concentration increased, there was a slight shift to lower angles. Only aluminium and oxygen elements were detected in the EDS analysis. SEM analysis revealed agglomeration on doping. From the HRTEM findings, the crystallite size of 16.0 nm was realized. The lattice spacing approximated from SAED was 0.138 nm corresponding to (440) lattice plane of γ -Al_2O_3. With excitation at 240 nm, the PL emission peaks at 440 nm and 462 nm were due to oxygen vacancies while the peak at 560 nm was due to Ce^{3+} doping. This result shows that Ce^{3+} doping of γ -Al_2O_3 improves its luminescence property therefore making it a possible candidate for blue light emitting diodes application.

DFT work on both transition metal and lanthanide-doped metal oxides was investigated in undoped TiO_2, lanthanides-doped TiO_2 as well as transition metal (Cr^{3+}) doped TiO_2 by the use of local density approximation with the Hubbard U correlation to compute the substitutional energies, thermodynamic transition levels, optical properties and magnetic properties of Cr^{3+}:TiO_2 and lanthanide-doped TiO_2. Unlike $ZnAl_2O_4$ and γ -Al_2O_3, TiO_2 was not experimentally synthesized but was modelled theoretically. Lanthanide doping was found to cause red shift of the band gap from the ultraviolet region to the visible region of the optical absorption spectra in TiO_2. The value of the computed substitutional energy implied that lanthanide ions are easily incorporated in TiO_2 crystal lattice. The most favorable doping

percentage was anticipated to be approximately 3%. On doping TiO_2 with chromium, a transition was observed from paramagnetism to ferromagnetism at 6% doping. The magnetic moment per chromium atom was 2.59 μB for rutile phase of TiO_2 and 2.49 μB for anatase phase. This result makes Cr^{3+} doped TiO_2 a possible candidate for application in memory devices.

Table of Contents

List of Figures

List of Tables

Keywords

$ZnAlO4:Cu^{2+}$, $Al_2O3:Ce^{3+}$, TiO_2:Ln TiO_2:Tm Photoluminescence, Scanning electron microscopy, High resolution transmission electron microscopy, Density functional theory, Dopant levels, Absorption, Wavelength.

Acronyms

- BSE Back-scattered electrons.
- BZ Brillouin zone.
- CB Conduction band.
- CCP Cubic close packed.
- CBM Conduction band maximum
- CPU Central processing unit
- DMS Dilute magnetic semiconductors
- DLTS Deep level transient spectroscopy.
- DFT Density functional theory.
- DOS Density of states.
- EDS Energy dispersive x-ray spectroscopy.
- EL Electroluminescence.
- EOS Equation of state.

- FWHM Full width at half maximum
- FPLMTO Full-potential linear muffin-tin-orbital.
- GGA Generalized gradient approximation.
- GW Green's function.
- GEA Gradient expansion approximation.
- HRTEM High-resolution transmission electron microscopy.
- HF Hartree-Fock.
- HSE06 Heyd-Scuseria-Ernzerhof06.
- IC Integrated circuit
- ICDD International centre for diffraction data.
- JCPDS Joint committee on powder diffraction standards.
- K-M Kubelka-Munk.
- LAPW Linearized augmented planewave
- LDA Local density approximation.
- Ln Lanthanides.
- MBJ Becke-Johnson
- MD Molecular dynamics
- NIR Near infrared.
- PAW Projector augmented planewave.
- PDOS Projected density of states.

- PMT Photomultiplier.
- PL Photoluminescence
- QMC Quantum Monte Carlo
- RE Rare earth
- SAED Selected area electron diffraction
- SE Secondary electrons.
- SEM Scanning electron microscopy.
- TB Tight binding
- TCO Transparent conducting oxides
- TEM Transmission electron microscopy.
- TM Transition metal
- TPSS Tao-Perdew-Staroverov-Scuseria.
- VBM Valence band maximum.
- VESTA Visualization for Electronic and Structural Analysis.
- XC Exchange correlation.
- XRD X-ray diffraction

Chapter 1

Introduction

1.1 Overview

Metal oxide semiconductors are extensively used for energy production and storage, lithium ion cells [1,2], fuel cells [3,4] and solar cells [5,6] and for energy saving light emitting diodes (LEDs) [7,8]. They also find use in medical sciences for example in drug delivery and fluorescent imaging [9,10]. These devices are inadequate in their performances due to the properties of the materials they are made of. The common short comings in semiconductors for solar cells applications are defective carrier transport properties and a small range of absorption wavelength thus restraining the energy-conversion efficiency [11]. The use of semiconductor metal oxides in the dye sensitized solar cells production leads to many advantages due to the probability of attaining high solar conversion efficiency. Nevertheless, the achievement of adequately high efficiency values is still restrained by constant losses during charge division and charge transfer through the electrodes. Use of the doped semiconductor metal oxides could help in improving the device performance. Transition metals oxides have powerful ferromagnetism characteristics and high Curie temperature, hence are used in data storage devices [12]. Doped transition metal oxides for example TiO_2 and Al_2O_3 referred to as diluted magnetic semiconductors are used in the production of electronic devices based on spin [13]. Devices like supercapacitors and batteries present inadequate energy densities because of the material properties that depends on production techniques [14]. Due to their various applications, metal oxide semiconductors are of significant interest [15]. A lot of research has been carried out on metals oxide semiconductors in order to improve their distinct optical and electronic properties. [16] These oxides are under scrutiny in nanotechnology since they are the most abundant minerals on the earth's crust due to their important physical and chemical properties [17]. Intrinsic defects in metal oxide semiconductors may occur during the synthesising process [18], while extrinsic defects (dopants) can be introduced in the semiconductor nanocrystal in order to

introduce defect states within the host band gap. The presence of these two types of defects determines the properties of the semiconductors to a great extent. It is therefore important to examine both computationally and experimentally the extent to which these defects affect the properties of the metal oxide semiconductors.

A lot of research on fundamental studies as well as applications of transition metal (TM) and rare-earth (RE) doped metal oxide semiconductors has been carried out [19-23]. In the case of RE, the unoccupied 4f orbitals facilitate their unique properties in luminescence and electronics. Doping metal oxide semiconductors with optically active luminescent dopants creates radiative recombination centres within the band gap of the semiconductors which brings about luminescence. Strong emissions and luminescence efficiency over a wide range of wavelengths are realized on doping with these luminescent dopants. These strong emissions also depend on the dopant percentage concentration and dopant characteristics.

The introduction of TM ions for example Cu^{2+} and Mn^{2+} into the metal oxide semiconductors has been found to produce metal oxides with different properties because each transition metal has different impact on the host [23,24]. Liang-shi *et al* [25] explained the role played by the crystal structure and shape of the metal oxide semiconductors in improving the effectiveness of TM-doping of these materials. This thesis, concentrates on the synthesis and characterization of $ZnAl_2O_4$ and γ -Al_2O_3 semiconductor metal oxides as well as computational studies of these oxides in addition to TiO_2 because they are intensively used as catalyst supports [26,27]. In addition, the effect of doping with lanthanides and transition metals on the properties of these oxides was also studied.

1.2 Conceptual foundation for computational studies.

A calculation is termed as an *ab initio* calculation (or from first principles) if it depends on fundamental and established laws of nature in the absence of extra assumptions or special models. In the computational materials Science field, only the atomic numbers and quantum mechanics laws are utilized, making the calculations '*ab initio*'. If one uses parameter

originating from experimental values, then the calculation is empirical (at least semi-empirical). If only theoretical values were used, then the calculation is called *ab initio*. Therefore, *ab initio* techniques can also be defined as wave function methods based mainly on quantum mechanics without the use of empirical constants or experimental data. Quantum mechanics provides a conceptual foundation for computational studies. Quantum mechanics is well known as the fundamental physical theory in elucidation of the behaviour of electrons, atomic nuclei and electromagnetic radiation. Quantum mechanics concepts applied to large numbers of particles acts as the origin of the complex occurrences found in biology, chemistry and low energy physics [28]. Materials modelling field is a large and varied one, in terms of the systems that are studied as well as the physical theories that are employed. Different types of computational methods have been devised for materials simulation, incorporating aspects of physics, chemistry, materials science and engineering. Examples of these different computational methods are, Quantum Monte Carlo (QMC), density-functional theory (DFT), empirical tight-binding (TB) and classical molecular dynamics (MD). This work presents findings from computational work using density functional theory [29-31]. Improvements in computer performance and algorithms makes it possible for these techniques to be used in many physical and chemical phenomena. In the experimental approach, some synthesising techniques (such as Molecular beam epitaxy) are very complex, expensive and time-consuming, while some characterization equipment are very expensive, complex, voluminous [32-34]. In this thesis, we combine experimental and computational work in order to see if computation can be used to guide as well as predict experimental results.

1.3 Statement of the Research Problem

Experimental synthesizing and characterising are complex techniques. The chemicals as well as equipments are also very expensive, these are some of the challenges faced during experimental work. DFT has successfully been used to understand and predict an intensive variety of properties of different classes of materials [35]. Due to the availability of powerful computing resources and continuous advances in theoretical methods, the number of atoms that can be

simulated within DFT has largely increased [36]. As the codes used in these simulations became more stable, accurate and computationally inexpensive, the *ab initio* techniques can be used frequently not only to guide experimental findings but also to predict the properties of not yet investigated metal oxide semiconductors therefore allowing the invention of new devices. One key advantage of computations is the level of control they offer compared to experiments. In addition, characterizing a material's fundamental properties is often quicker with computations compared to experiment while still retaining excellent or acceptable accuracy.

Besides qualitative results, *ab initio* computations often rely on their ability to effectively give a good idea on the materials properties. For instance, even though a calculated adsorption energy on a catalyst might not be the same as experimental value, what often matters for experimental guidance is to know the top candidates within a set of potential materials.

In combining computation and experimental work, we take the already experimentally studied material, compute its properties and see the relationship between the experimental findings and computational findings. From there we use the same procedure to compute the properties of materials which have not yet been studied then we use the results to predict the experimental results.

In developing the efficiency of metal oxide semiconductors, improving their luminescence properties is significant although many challenges are faced in the process of manufacturing these oxides. A lot of research has to be done on how to overcome these challenges and improve the luminescence properties of the oxides. The ability to synthesize and characterize oxides with luminescence characteristics for example intensity and colour is determined by many factors such as annealing temperature, excitation wavelength, concentration of impurities, and the form of the synthesized product.

Although there are extensive investigations on the Cu^{2+} doped semiconductor ($ZnAl_2O_4$), the effect that Cu^{2+} has on the optical properties of spinel semiconductors has not yet been investigated computationally using the DFT+U approach. This work therefore aims at comparing the results of computational and experimental investigations of the effect of Cu^{2+} doping on the optical properties of $ZnAl_2O_4$.

The available information in literature on the luminescence effect of Ce^{3+} in γ-Al_2O_3 concentrates on the use of a single doping concentration of Ce^{3+} in which case the luminescence peak produced is usually low and sometimes unnoticeable. Motivated by this, the present research explores the possibility of varying the Ce^{3+} doping concentration over a wide range in order to study the effect on the luminescence peak. Both computational and experimental approaches are used.

Lanthanides are known to produce very important spectroscopic propeties when used as dopants in semiconductors. These properties depend on the electronic configuration and ionic radius of the lanthanides. The effect of the variation in ionic radius along the lanthanide series on the spectroscopic properties of TiO_2 has not yet been exhaustively investigated. This research aims at investigating this effect across the entire lanthanide series computationally.

1.3.1 Research objectives

- To use *ab initio* and experimental techniques to investigate structural, electronic and optical properties of transition metal doped metal oxide semiconductors ($ZnAl_2O_4$:Cu^{2+}).
- To use *ab initio* and experimental techniques to investigate structural, electronic and optical properties of lanthanide doped metal oxide semiconductors (γ-Al_2O_3:Ce^{3+}).
- To use only *ab initio* techniques to investigate energetic, structural, electronic, optical and magnetic properties of transition metal and lanthanide-doped metal oxide semiconductors (TiO_2:Cr^{3+} and TiO_2:Ln).

1.4 Lay Out of the Thesis

Chapter 1 Contains introduction, the research problem and the objectives of this study. The key words that is, doping, metal oxides, transition metals and lanthanides are discussed here. The reason as to why there was choice of combined computational and experimental work is discussed.

Chapter 2 Gives a theoretical background knowledge on luminescence processes for example photoluminescence. Short background knowledge on lanthanides as well as transition metals is emphasized. The structural analysis of $ZnAl_2O_4$, γ -Al_2O_3 and TiO_2 matrices is presented.

Chapter 3 Description of the experimental techniques used in this study are discussed. The experimental procedures followed during the preparation of undoped and doped metal oxide semiconductors as well as the characterization techniques used are discussed in detail in this chapter.

Chapter 4 Effect of Cu^{2+} doping on the structural, electronic and optical properties of $ZnAl_2O_4$: A combined experimental and DFT+*U* study. Experimental and computational findings on doping $ZnAl_2O_4$ with a transition metal were compared.

Chapter 5 Structural, electronic and optical properties of Ce^{3+} doped gamma-alumina. Computational and experimental properties on doping γ -Al_2O_3 with a lanthanide were discussed. The comparison between the two techniques was analysed.

Chapter 6 Reports the energetic, electronic and optical properties of lanthanide doped TiO_2 using DFT+U. This chapter reports purely the use of ab initio technique on lanthanide doping in TiO_2.

Chapter 7 Electronic and Magnetic Structure of Cr^{3+} doped Rutile and Anatase TiO_2; an *ab-initio* DFT+U study. Doping was done using transition metals only as dopants.

Chapter 8 Tuning the electronic and optical properties of TiO_2:an *ab initio* LDA+U study. Doping the metal oxide semiconductors was done using transition metals as well as lanthanides as dopants. Anatase phase of TiO_2 was discussed.

Chapter 9 Conclusion.

A summary of the whole research is presented. Recommendations for future are also provided.

References

[1] P. Poizot, S. Laruelle, S. Grugeon, L. Dupont, J. M. Tarascon, *Nature.* **407** (2000) 496.

[2] H. Huang, E. M. Kelder, J. Schoonman, *J. Power Sources*. **114** (2001) 97.

[3] M. Asamoto, S. Miyake, K. Sugihara, H. Yahiro, *Electrochem. Comm*. **11** (2009) 1508.

[4] M. Mamak, N. Coombs, G. Ozin, *J. Am. Chem. Soc.* **122** (2000) 8932.

[5] H. J. Snaith, L. S. Mende, *Adv. Mater.* **19** (2007) 3187.

[6] M. Gratzel, *Nature*. **414** (2001) 338.

[7] B. J. Kim, Y. R. Ryu, T. S. Lee, H. W. White, *Appl. Phys. Lett*. **94** (2009) 103506.

[8] I.P. Won, G.C. Yi, *Adv. Mater.* **1** (2004) 687.

[9] S. Bae, S. W. Lee, Y. Takemura, *Appl. Phys. Lett.* **89** (2006) 252503.

[10] S.I. Stoeva, J.S. Lee, J.E. Smith, C.A. Mirkin, *J. Am. Chem. Soc.* **128** (2006) 8378.

[11] S. Calnan, *Coatings.* **4(1)** (2014) 162.

[12] Z. Yang, Z. H. Lin, C. Y. Tang, H. T. Chang, *Nanotech.* **18** (2007) 155606.

[13] K. C. Barick, M. Aslam, V. P. Dravid, D. Bahadur, *J. Phys. Chem. C* **112** (2008) 15163.

[14] Z.Rao and S.Wang, *Renew. Sustain, Energy Rev*. **15** (2011) 4554.

[15] E. Comini, C.Baratto, G. Faglia, M.Ferroni, A.Vomiero, G. Sberveglieri, *Prog. Mater Sci.* **54** (2009) 1.

[16] D. Beydoun, R. Amal, G. Low and S. McEvoy, *J. Nanopart. Res.* **1** (1999) 439.

[17] T. Zhai, X.Fang, M.Liao, *Sensors.* **9** (2009) 6504.

[18] Yu. D. Ivakin, M.N.Danchevskaya, O.G. Ovchinnikova, G.P. Muravieva, *J. Mater. Sci.* **41** (2006) 1377.

[19] A. L. Rogach, A. Eychmuller, S. G. Hickey, S. V. Kershaw, *Small*. **3** (2007) 536.

[20] S. A. McDonald, G. Konstantatos, S. G. Zhang, P. W. Cyr, E. J. D. Klem, L. Levina, E. H. Sargent, *Nat. Mater*. **4** (2005) 138.

[21] B. R. Hyun, H. Chen, D. A. Rey, F. W. Wise, C. A. Batt, *J. Phys. Chem B*. **111** (2007) 5726.

[22] X. S. Zhao, I. Gorelikov, S. Musikhin, S. Cauchi, V. Sukhovatkin, E. H. Sargent, E. Kumacheva, *Langmuir*. **21** (2005) 1086.

[23] B. Bodo, P. K. Kalita, *SAIP. Conf. Proc*. **1276** (2010) 31.

[24] R. N. Bhargava, D. Gallagher, *Phys. Rev. Lett*. **72** (1994) 416.

[25] Liang-shi Li, Jiangtao Hu, Weidong Yang and A.Paul Alivisatos, *Nano lett*. **1** (2001) 349.

[26] O.Akdim, U.B. Demirci, P. Miele, *Adv. Sci. Technol.* **65** (2010) 209.

[27] A.D. Ballarini, S.A. Bocanegra, A.A. Castro, *Catal Lett*. **129** (2009) 293.

[28] M. Karelson and V. S. Lobanov, *Chem. Rev.* **96** (1996) 1027.

[29] P. Hohenberg and W. Kohn, *Phys. Rev*.**136** (1964) 864.

[30] W. Kohn and L. J. Sham, *Phys. Rev*.**140** (1965) 1133.

[31] M. C. Payneet al., *Rev. Mod. Phys.* **64** (1992) 1045.

[32] F. L. Meng, H. H. Li, L. T. Kong, J. Y. Liu, Z. Jin, W. Li, Y. Jia, J. H. Liu and X. J. Huang, *Anal. Chim. Acta.* **736** (2012) 100.

[33] M. Ongwandee, R. Moonrinta, S. Panyametheekul, C. Tangbanluekal and G. Morrison, *Build. Environ.* **46** (2011) 1512.

[34] D. M. Bon, I. M. Ulbrich, J. A. de Gouw, C. Warneke,W. C. Kuster, M. L. Alexander, A. Baker, A. J. Beyersdorf,D. Blake, R. Fall, J. L. Jimenez, S. C. Herndon, L. G. Huey,W. B. Knighton, J. Ortega, S. Springston and O. Vargas, *Atmos. Chem. Phys.***11** (2011) 2399.

[35] J. Hafner, C. Wolverton and G. Ceder, *MRS Bull.* **31(9)** (2006) 659.

[36] K. T. Butler, J. M. Frost, J. M. Skelton, K. L. Svane and A. Walsh, *Chem. Soc. Rev.* **45** (2016) 6138.

Chapter 2

Theoretical Background

2.1 Metal oxides

Among the large group of functional materials, metal oxides play an important role in many scientific and technological fields. For many years, these materials have been extensively researched on due to their physiochemical properties and important applications in solid state physics and chemistry. Metal oxides, exhibit a very wide variety of complex structures and interesting properties. These metal elements are able to form a large variety of oxide compounds, giving the motivation for designing new materials. These oxides display fascinating electronic and magnetic properties depending on the adjustments in electronic structure and bonding. Additionally, metal oxides having multivalent oxidation states have attracted much attention among specialists in nuclear waste because they often exhibit superior catalytic reaction performance [1]. Metal oxides are essential class of materials which are widely used in several fields, such as in catalysis, biomedicine transistors, sensors and solar energy storage and conversion [2-5]. Nanostructured metal oxides have attracted tremendous interest in recent years because of their unique electrical, mechanical and optical properties when their structural feature size is down to nanoscale [6]. There are a variety of metal oxide nanostructures, ranging from nanoparticles, nanowires, nanotubes and nanoporous structures. Metal oxides are very cheap, very stable and can be produced in large volumes [7].

2.2 Structure, Properties and Applications of TiO_2

In 1972, Fujishima and Honda discovered the occurrence of photocatalytic splitting of water on a TiO_2 electrode in combination with a platinum counter electrode dipped in an aqueous solution

(electrolyte) placed under ultraviolet (UV) light [8]. TiO_2 is the most promising photo catalyst due to its appropriate electronic band structure, photo stability, chemical inertness, and commercial availability [9]. A variety of morphologies of semiconductor metal oxide TiO_2 such as nanotubes, nanorods, nanostructured films nanoparticles, nanoporous structures and nanowires, have already been researched on [10-12]. A lot of TiO_2 based composites have been prepared [13]. Nevertheless, the high efficiency of TiO_2 metal oxides as a semiconductor photocatalyst is sometimes restrained by to its wide band gap. The band gap of bulk TiO_2 is found in the UV region (3.0 eV for the rutile phase, 3.2 eV for the anatase phase and 3.4 for the brookite phase), representing a small fraction of the solar energy (<10%). This means that one of the goals in improving the performance of TiO_2 metal oxides is to increase their optical activity by adjusting the onset of the response from UV to visible region. The adjusting includes incorporation of transition metals into TiO_2 by doping [14]. Successful utilization of clean, safe, and abundant solar energy by the TiO_2 photocatalyst helps to overcome the energy crisis and environmental challenges [15]. Enormous efforts have been devoted to the investigation of TiO_2 metal oxides, which has led to numerous applications in the field of photovoltaics, photocatalysis and sensors [16-18]. Titanium dioxide (TiO_2) is extensively used as a pigment, in sunscreens [19], etc. Naturally, TiO_2 occurs in three different polymorphs, that is, rutile, anatase, and brookite. In catalytic application anatase is the most suitable phase. The differences in lattice structures among the three phases of TiO_2 cause different electronic band structures. Anatase is found to be stable at low temperatures and used as photocatalyst in waste water treatment [20]. Rutile is stable at high temperatures and used in industrial products such as paint [21]. Brookite is found in minerals and belong to orthorhombic crystal system which is complicated and rare, although Kominami et al. [22] found out that brookite TiO_2 has the potential to be used as a photocatalyst. Anatase and rutile TiO_2 are more frequently used as they are easy to synthesize [23]. Anatase TiO_2 is most active photocatalytic component because of its charge carrier dynamics and chemical properties [24]. Rutile phase is thermodynamically more stable than anatase TiO_2. However, anatase formation is kinetically favoured at lower temperature. The crystallization from amorphous to anatase and anatase to rutile usually occurs in the temperature ranges of 450-550 ^{0}C and 600-700 ^{0}C respectively [21]. The thermodynamic stability of the TiO_2 depends on the particle size. The particle size of less than 11 nm corresponds to stability of the

brookite phase, for particles 11nm to 35 nm the stable phase is anatase and rutile is the most stable phase at the size greater than 35 nm [25].

2.3 Structure, Properties and Applications of $ZnAl_2O_4$

Metal oxides have significant roles to play in physics, chemistry and material science. These elements can form a large diversity of oxide compounds. They can also adopt an extensive number of structural geometries with an electronic structure that can display metallic, semiconductor or insulator characteristics [26]. Some of these metal oxides have general formula AB_2O_4, and crystallizes into the cubic close packed (CCP) structure of oxygen. They have crystal structure corresponding to that of the mineral $MgAl_2O_4$, which is the original compound of this class known as spinel [27]. Various categories of spinel compounds display interesting mechanical, magnetic, electrical and catalytic properties [28]. These unique properties have led to the technological importance of spinel oxide materials. In technological applications spinel oxides have increasingly become important in transformer and load coils of telecommunication equipment, they are also used as natural industrial refractory materials, catalysts or catalyst support compounds [29]. Therefore, the spinel oxides are of considerable interest from the technical point of view. The basis for these several technological applications of spinel oxides is due to their structural flexibility, given that various properties of these oxides can be manipulated by altering the chemical composition of the compound through cation redistribution or by substitution using an appropriate dopant [30-34].

Zinc aluminate ($ZnAl_2O_4$) spinel, is a mixture of aluminium and zinc oxides. It is usually known as gahnite and it is a naturally available mineral with a crystal structure belonging to spinel group. This mineral was originally known as automolite in 1807 in Sweden. Later on it was named after J.G. Gahn a Swedish chemist in the years (1745-1818). A normal metal oxide of this nature has a cubic structure. Experimentally, the band gaps of $ZnAl_2O_4$ and $ZnGa_2O_4$ are approximately 3.8−3.9 and 4.1−4.3 eV respectively [35]. The gahnite unit cell comprises of 32 oxygen ions, 16 octahedral site cations, and 8 tetraheral site cations, resulting to a very high

degree of complexity. In a spinel structure of the chemical formula AB_2O_4, A stands for a divalent metal ion such as zinc and iron, while B stands for trivalent metal ions such as aluminium and chromium. The divalent A cations are found in the 8 tetrahedral interstices and the trivalent B cations are in the 16 octahedral interstices. The above distribution of cations is thermodynamically not favourable to be most stable, given that the configurational degree of disorder prevents the site preferential energy. Therefore, spinel inversion takes place, that is A and B cations exchange interstices through diffusion and finally all the A cations are in octahedral interstices. $ZnAl_2O_4$ is to a large extent used as a catalyst in chemical reactions, such as synthesis of methanol [36,37]. The optical properties of $ZnAl_2O_4$ have been researched on and the report states that polycrystalline $ZnAl_2O_4$ has an optical band gap approximately 3.87 eV and is very reflective at wavelengths below 300 nm [38,39].

2.4 Structure, Properties and Applications of γ -Al_2O_3

Al_2O_3 forms a wide variety of phases. The alumina phases are arrived at by dehydration of various aluminum hydroxides. The two most important ones are gibbsite which is an aluminium trihydroxide $Al(OH)_3$, and boehmite which is an aluminium-oxidehydroxide: AlO(OH). The dehydration process is conducted by heating the aluminum hydroxide in air. The α -phase is the most stable among the other alumina phases. It is characterized by slightly distorted hexagonal close-packed oxygen sub-lattice, where the aluminium ions are in the octahedral vacancies and is the final product from thermal or dehydroxylation treatments of all the hydroxides. Aluminum oxide has advantages such as its thermal, chemical, and physical properties when compared with several ceramics materials, due to its high performance as a coating material and is widely used for firebricks, abrasives and integrated circuit packages. Alumina (Al_2O_3), a traditional ceramic material forms an active research field in materials science because of its interesting properties for example transparency over a wide range of wavelengths [40-41], electrical insulation with a wide band gap of 6 eV or more, and chemical inertness. Al_2O_3 occurs in different polymorphs, that is, α, γ, θ, δ and κ-phases [42-46] γ and δ-Al_2O_3 polymorphs display low surface energy

hence used in catalyst applications where by a large surface area is of significance [47] κ-Al_2O_3 phase shows the largest hardness compared to α-Al_2O_3 [48]. To understand the formation of these different phases and further control thereof is of great interest for the researchers.

2.5 Lanthanides

Lanthanides are elements in the periodic table starting from Lanthanum (^{57}La) to Lutetium (^{71}Lu). Due to similar chemical characteristics with the lanthanides, Yttrium (^{39}Y) and Scandium (^{21}Sc) are part of lanthanides. The electronic structure of lanthanide atoms can be described in the configuration, $4f^n5d^{0-1}6s^2$ and in terms of a core with occupied shells equivalent to the (Xe) atom. Therefore the configuration becomes, $[Xe]^{54}4f^n5s^25p^65d^{0-1}6s^2$ (n = 1,2,.,14). This shows, after $5s^25p^65d^{0-1}6s^2$ are fully occupied, the 4f shell will slowly be filled from n= 0 to 14electrons. The 4f electrons of the lanthanides are shielded by the filled $5s^25p^6$ subshells. They are localized; therefore they are found close to the nucleus and are of low energy. Lanthanides are characterized by reduction in atomic radius as we move from lanthanum (La) to lutetium (Lu). Apart from Ce, Eu and Yb which are characterized by cubic structures, the other lanthanide elements crystallize in a hexagonal close packed structure. Given that conduction bands in solid state are made of the $5d^16s^2$ valence electrons, then the lanthanide ions are normally trivalent both in their atomic state and in the solid state. This is with an exception of Ce which can exist as trivalent Ce^{3+} as well as tetravalent Ce^{4+}. Tb also exists as trivalent Tb^{3+} as well as tetravalent Tb^{4+}. Trivalent states of Ce and Tb are optically active while the tetravalent states of Ce and Tb are optically inactive. Lanthanide doped luminescent materials are expansively used in the lighting industry [49-51]. Lanthanide ions with luminescent properties are easily accommodated in host crystal lattice as the f-electrons making up the photoactive centre are well shielded [52-54].

2.6 Transition metals

Transition metal oxides show a wide variety of electronic properties, extending from insulating to metallic and even up to superconducting properties. These metal oxides can often be tuned from one electronic phase to another by varying the temperature, pressure, or by doping. Because of this, for a long time the transition metal oxides (TMO) have been the subject of intense experimental and theoretical research. In particular the d-band transition metal oxides are of great interest owing to their catalytic properties. The transition metal oxides form a wide, important and still not yet well understood category of compounds, for example, metal-containing compounds in medicine. These materials have important electronic and magnetic properties. The properties of transition metal oxides strongly depend on oxide's defects for example vacancies. This is because they alter the geometric and electronic structure as well as chemical properties of these oxides. The source of many important properties of transition metal oxides is not always clear, which is a crucial problem to address in solid state physics.

2.7 Intrinsic and extrinsic doping in semiconductor metal oxides.

There are two types of semiconductors determined by their chemical properties. Intrinsic semiconductors are pure semiconductor where there is equal number of electrons and holes. There are no external dopants in them. In this type of semiconductors, the Fermi level is positioned exactly at the middle of the energy band gap. They are usually identified by their high electrical resistivity and low carrier concentration.

Extrinsic semiconductors are also known as impure semiconductors because they contain some external impurities. The properties of these semiconductors depend strongly on the type of dopant and also the percentage doping. The Fermi level is not exactly at the centre of the band gap. There are two types of extrinsic semiconductors. These are n-type and the p-type

semiconductors. In n-type semiconductors, electrons are the majority charge carriers in the material, with the Fermi level closer to the bottom of the conduction band. In p-type semiconductors holes are the majority charge carriers and the Fermi level is closer to the top of the valence band. N-type semiconductors are produced with donor impurities (dopants) while p-type semiconductors are produced with acceptor impurities. Donor impurities generate states near the conduction band while acceptors generate states near the valence band. Doping is an extensively used technique to modify the electronic, optical, and magnetic properties of semiconductors metal oxides, which are very important for their practical applications. Using transition metals and lanthanides as dopants manipulates the electronic structure of the semiconductors, morphology and gives intense emissions in a wide range of wavelengths which is determined by the impurity type, concentration and crystal dimensions.

2.8 Luminescent Materials

In 1603, Casciarolo from Italy discovered a material in its solid state which could glow in darkness after being subjected to some source of light. This is an example of a luminescent material. We can therefore define luminescent materials as materials which are capable of converting incident light energy into an emission, where the emission peaks are found the infrared, visible or ultraviolet regimes of the electromagnetic spectrum.

2.8.1 Types of Luminescence

When the atoms of a material are excited by an incident source of light, the sudden emission illustrates luminescence. This extra energy is liberated from the atoms as infrared, visible or ultraviolet radiations. Different types of luminescence are named as per the type of excitation. For example, photoluminescence (PL) is the type of luminescence whose excitation is by photons. When the excitation is by high energy electrons, then we talk of cathodoluminescence

(CL), and by electric current, it is known as electroluminescence (EL). In this study, we focused on the PL.

2.8.2 Photoluminescence

Photoluminescence in semiconductors is classified into two, that is, intrinsic and extrinsic, which is according to the characteristics of electronic transitions causing it. Regarding intrinsic photoluminescence, there is no introduction of dopant atoms therefore luminescence is caused by the fundamental defects found in the crystal structure. As per extrinsic photoluminescence dopant atoms are purposely introduced in the crystal structure. Fig. 2.1 shows photoluminescence schematic diagram, where high energy photons are absorbed followed by emission of low energy photons.

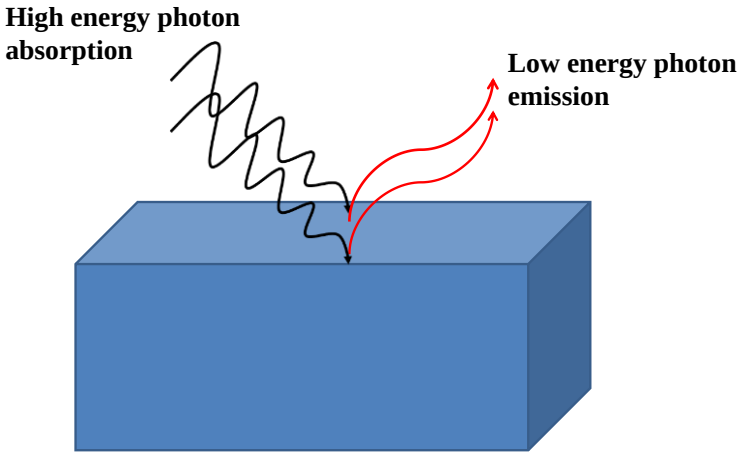

Figure 2.1 Photoluminescence schematic diagram [55]

2.8.3 Fluorescence and Phosphorescence

The mean duration taken by an excited electron to remain in its excited state prior to transition to its ground state is known as its decay lifetime. Based on this decay lifetime, there are two types of PL namely, phosphorescence and fluorescence. Phosphorescence refers to the persistent glow of a material after it has been subjected to an excitation while fluorescence is the light emission of a material only when the exciting radiation is on, but no emission when exciting radiation is off. Phosphorescence decay lifetime is approximately 99.99 ns while that of fluorescence is approximately 9.99 ns. This means that fluorescence is the sudden emission upon radiation energy absorption while phosphorescence is the gradual emission even after excitation radiation is off.

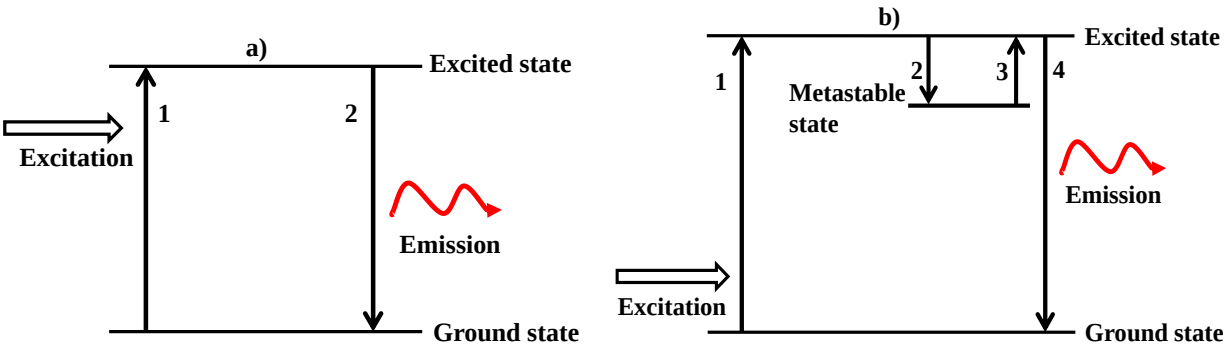

Figure 2.2 Schematic diagram of a) Fluorescence b) Phosphorescence taken from ref. [57]

Reuven Chen and Stephen W S McKeever [56] found out that phosphorescence is due to considerable shallow captured charge carriers meaning that phosphorescence will rely on temperature while fluorescence will not. As shown in Figure 2.2, due to the excitation radiation, electrons are excited to excited state from the ground state during transition number 1. Through transition number 2, fluorescence occurs as the electrons lose energy from excited state back to ground state. Due to the presence of defects, excited electrons can lose energy not to the ground state but to the metastable state as shown in transition number 2 in Fig. 2.2 b). If this electron gains more radiation energy, it goes back to excited state through transition 3. Transition 4

represents phosphorescence which is a prolonged emission taking place upon relaxing of electrons from excited states to ground state.

2.8.4 Excitation Mechanism

The excitation or absorbed energy is the energy required for luminescence. The energy is either absorbed by the host or by intentionally introduced impurity. Often times, the emission is produced by the impurity atom. When this impurity atom generates the desired emission, then it is known as activator atom. When the absorption by the activator ions is very weak such that reasonable emission cannot be produced, a second impurity (sensitizer) is introduced. The sensitizer absorbs the energy and subsequently transfers it to the activators, thereby inducing luminescence [81-82].

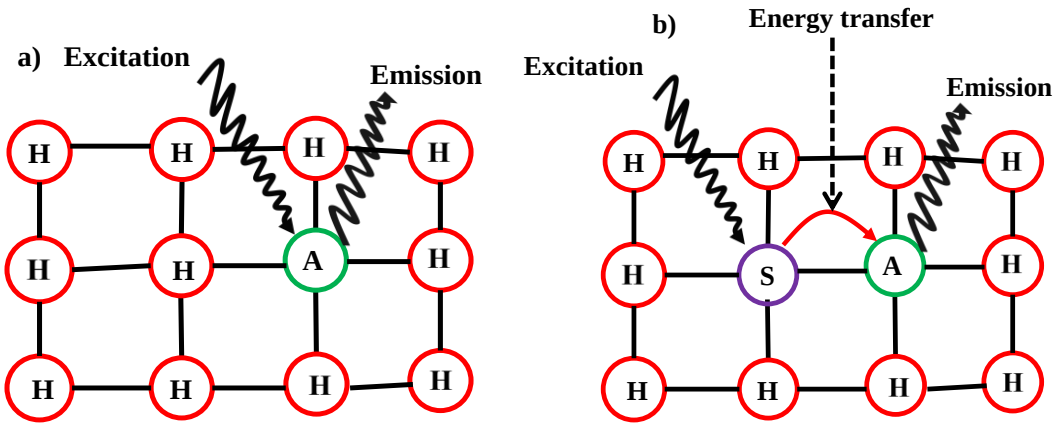

Figure 2.3 Schematic diagram of a) activator (A) in host (H) nanocrystal lattice. b) Energy transfer from sensitizer (S) to activator (A) [59]

References

[1] Z. Liu, W. Xu, S.Yao, A.C. Peck, F. Zhao, J.A Michorczyk, *J. Catal.* **321** (2015) 90.

[2] P. Judeinstein, C. Sanchez, *J. Mater. Chem.* **6** (1996) 511.

[3] M. B. Gawande, R. K .Pandey, R. V. Jayaram, *Catal. Sci. & Tech*. **2** (2012) 1113.

[4] L. E. Kreno, K. Leong, O. K. Farha, M. Allendorf, R. P. Van Duyne, J. T. Hupp, *Chem. Rev*. **112** (2011) 1105.

[5] G. F. Fine, L. M. Cavanagh, A. Afonja, R. Binions, *Sensors*, **10** (2010) 5469.

[6] Z. L. Wang, *J. Phy. Condens. Matter,* **16** (2004) R829.

[7] E.Comini, G. Sberveglieri, *Mater. Today*, **13** (2010) 36.

[8] A. Fujishima, K. Honda, *Nature*, **238** (1972) 37.

[9] A. O. Ibhadon, P. Fitzpatrick, *J. Catal.* **3** (2013) 189.

[10] A. Mazzarolo, K. Lee, A. Vicenzo, P. Schmuki, *Electrochem. Commun.* **22** (2012) 162.

[11] J. Liu, Z. Liu,C. Zhu, M. Zhang, M. Wan, *Mater. Lett.* **159** (2015) 61.

[12] O. Li, B. Cheng, X. Yang, R. Li, B. Liu, J. Liu, *J. Phys. Chem.* C, **117** (2013) 8516.

[13] W. J. Ong, L. L. Tan, S. P. Chai, S. T. Yong, A. R. Mohamed, *Nanoscale,* **6** (2014) 1946.

[14] H. Yu, H. Irie, Y. Shimodaira, Y. Hosogi, M. Miyauchi, K. Hashimoto, *J. Phys. Chem. C.* **114** (2010) 16481.

[15] X. Hu, G. Li, J. C. Yu, *Langmuir*. **26** (2009) 3031.

[16] Y. Bai, I. M. Sero, F. Angelis, J. Bisquert, P. Wang, *Chem. Rev.* **114** (2014) 10095.

[17] S. K. Deb, *Sol. Energy Mater. Sol. Cells*. **92(2)** (2008) 245.

[18] J. Bai, B. Zhou, *Chem. Rev.* **114** (2014) 10131.

[19] S. Sherbiny, F. Morsy, M. Samir, *Appl. Nanosci.* **4** (2014) 305.

[20] M. A. Lazar, S. Vargheses, S. S. Nair, *J. Catal.* **2** (2012) 572.

[21] D.A. Hanaor, C. C. Sorrell, *J. Mater. Sci.* **46** (2011) 855.

[22] H. Kominami, Y. Ishii, M. Kohno, H. Konishi, Y. Kera, B. Ohtani, *Catal. Lett.* **91** (2003) 1.

[23] K. Woan, G. Pyrgiotakis, W. Sigmund, *Adv. Mater.* **21** (2009) 2233.

[24] H. Park, H. I. Kim, G. H. Moon, W. Choi, *Energy Environ. Sci.* **9** (2016) 411.

[25] H. Zhang, J. F. Banfield, *J. Phys. Chem. B.* **104** (2000) 3481.

[26] J. C. Love, L. A. Estroff, J. K. Kriebel, R. G. Nuzzo, G. M. Whitesides, *Chem. Rev.* **10** (2005) 1103.

[27] Y. H. Fawzy, S. A. El All, R. M. Radwan, *J. Phys. D: Appl. Phys.* **40** (2007) 5707.

[28] R. K. Selvan, V. Krishnan C. O. Augustin, H. Bertagnolli, C. S. Kim, A. Gedanken, *Chem. Mater*. **20** (2008) 429.

[29] N. W. Grimes, *Phys. Technol.* **6** (1975) 22.

[30] N. Fujiwara, H. Yasuoka, Y. Ueda, *Phys. Rev. B.* **57** (1981) 3539.

[31] J. L. Dormann, M. Nogues, *J. Phys. Condens. Mater.* **2** (1990) 1223.

[32] G. Srinivasan, E.T. Rasmussen, R. Hayes, *Phys. Rev. B* **67** (2003) 014418.

[33] B. Antic, G. F. Goya, H. R. Rechenberg, V. Kusigerski, M. Mitric, *J. Phys. Condens. Mater*. **16** (2004) 651.

[34] S. Kumar, R. A. Kumar, A. Dogra, V. R. Reddy, A. Banerjee, *J. Appl. Phys*. **99** (2006) 910.

[35] S.K. Sampath, T.F. Cordaro, *J. Am. Ceram.Soc*. **81** (1998) 649.

[36] N. J. van der Laag, M. D. Snela, P. C. M. M. Magusin, G. de With, *J. Eur. Ceram. Soc.* **24** (2004) 2417.

[37] X. Wei, D. Chen, *Mater. Lett.* **60** (2006) 823.

[38] R. Pandey, J. D. Gale, S. K. Sampath, J. M. Recio, *J. Am.Ceram. Soc.* **82** (1999) 3337.

[39] V. Ciupina, I. Carazeanua, G. Prodan, *J. Optoelectron. Adv.Mater.* **6** (2004) 1317.

[40] M. Aguilar-Frutis, M. Garcia, and C. Falcony, *Appl. Phys. Lett.* **72** (1998) 1700.

[41] B. Holm, R. Ahuja, Y. Yourdshahyan, B. Johansson, and B. I. Lundqvist, *Phys. Rev. B* **59**, (1999) 12777.

[42] J. M. Andersson, E. Wallin, and U. Helmersson, *Thin Solid Films.* **513** (2006) 57.

[43] M. Sridharan, M. Sillassen, J. Bottiger, J. Chevallier, and H. Birkedal, *Surf. Coat. Technol.* **202** (2007) 920.

[44] S. K. Pradhan, P. J. Reucroft, and Y. K. Ko, *Surf. Coat. Technol.* **176** (2004) 382.

[45] M. Delmas, D. Poquillon, Y. Kihn, C. Vahlas, *Surf. Coat. Technol.* **200** (2005) 1413.

[46] A. Khanna and D. G. Bhat, *Surf. Coat. Technol.* **201** (2006) 168.

[47] N. K. Nag, *Catal. Lett.* **24** (1994) 37.

[48] M. Kathrein, W. Schintlmeister, W. Wallgram, U. Schleinkofer, *Surf. Coat. Technol.* **163** (2003)181.

[49] C.R. Ronda, *J. Alloys Comp.* **225** (1995) 524.

[50] C.R. Ronda, *J. Lumin.* **100** (2002) 301.

[51] T. Justel, H. Nikol, C. Ronda, *Chem. Int. Ed.* **37** (1998) 3084.

[52] V. C. Costa, M. J. Lochhead, K. L. Bray, *Chem Mater*. **8** (1996)783.

[53] M.J. Weber, *Non-Cryst Solid.* **123** (1990) 208.

[54] W. R. Glomm, S. Volden, J. Sjöblom, M. Lindgren, *Chem Mater*. **17** (2005) 5512.

[55] W. C. Walker, *J. Phys. Chem.Solids.* **24** (1963) 1667.

[56] J. Liqiang, Q. Yichun, W. Baiqi, L. Shudan, J. Baojiang, Y. Libin, F. Wei, F. Honggang, S. Jiazhong, *Sol. Energy Mater. Sol. Cells.* **90** (2006) 1773.

[57] C. Feldmann, T. Jüstel, C. R. Ronda, P. J. Schmidt, *Adv. Funct. Mater.***13** (2003) 511.

[58] J. A. Deluca, *J. Chem. Educ*. **57** (1980) 541.

[59] Z. Xia, J. Zhuang, H. Liu, L. Liao, *J. Phys. D Appl. Phys.* **45** (2011) 015302.

Chapter 3

Research Techniques/Equipments

3.1 Introduction

The *ab initio* calculations were performed within the DFT formalism as implemented in the Quantum ESPRESSO code. The *ad hoc* Hubbard correction was utilized in all the calculations while the Xcrysden program was used to obtain and analyse the crystal structures of $ZnAl_2O_4$, γ -Al_2O_3 and TiO_2. Synthesis and characterization techniques used to experimentally investigate the properties of the metal oxides used in this study are presented. The structure of the $ZnAl_2O_4$ and γ -Al_2O_3 powders was analysed experimentally using the X-ray diffraction (XRD). The crystal size was analysed by use of XRD and the high resolution transmission electron microscopy (HRTEM). Morphology was analysed using the scanning electron microscope (SEM) and HRTEM. The absorption properties of the metal oxides were investigated using UV-VIS-NIR spectrophotometer. The photoluminescence (PL) properties were determined using F-7000 Fluorescence while energy dispersive X-ray spectroscopy (EDS) gave the composition of the powders. All the above mentioned techniques are discussed in the following sections.

3.2 X-Ray Diffraction

Powder X- ray diffraction (XRD) is an analytical technique, mainly used for phase determination of a crystalline material. The crystal structure of the unit cell is described by this technique. XRD patterns of the materials reported in this thesis were obtained using a Bruker AXS Discover Model diffractometer with CuKα (1.5418Å) radiation. X-ray diffractometer basically has three components namely; X-ray detector, a sample holder and an X-ray tube as shown below.

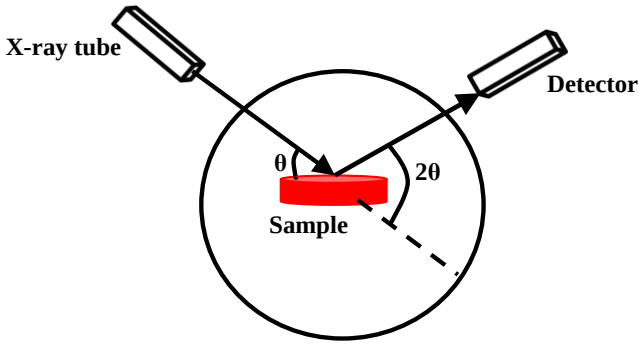

Figure 3.1 A schematic diagram of an X-ray diffractometer.

The X-ray diffractometer operates in such a way that the samples rotate in the line of parallel X-ray beam incident at an angle θ with the sample. A detector, rotated at an angle 2θ is used to detect the diffracted X-rays. The negative terminal of a cathode ray tube is heated to generate electrons. These electrons are accelerated towards the target by a high voltage. X-ray spectra are generated with the popular components being K_α and K_β. In the case of a single-crystal diffraction, Copper is the most common material used as a target. The x-ray diffractometer used in this work to investigate the XRD measurements was PANalytical X'Pert PRO using CuK_α radiation of $\lambda = 1.5405$ nm. To achieve monochromatic X-rays required for diffraction, filtering is done by use of crystal monochromator.

3.2.1 Applications

In order to characterize crystallinity of the synthesized powders, the X-ray diffraction (XRD) technique is used. Constructive interference whose source is the monochromatic beam of X-rays is used in the production of XRD peaks.

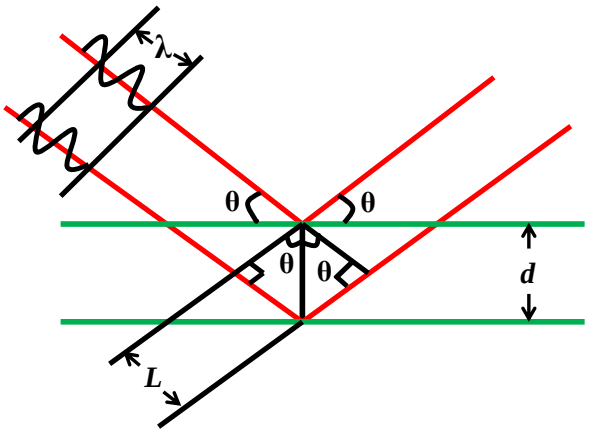

Figure 3.2 Schematic diagram of X-rays reflected from two adjacent crystal planes

Taking the distance separating the two adjacent planes to be *d*, then the two planes have a path length difference of 2*d*sinθ. If the integral number of wave lengths is equal to *d*, then we expect constructive interference of the X-rays. X-rays are diffracted when their state obey Bragg's law [1], that is,

$$n\lambda = 2d \sin \theta \qquad (3.2.1)$$

where *n* is a whole number, λ is the X-ray's wavelength and *d* is the interplanar spacing producing the diffraction, and θ is the angle of diffraction.

Bragg's law was generated between 1912 and 1913 [2].

Basically XRD characterization is carried out to detect the crystalline phase of the powders, type of structure and presence of any impurity in the powders [3]. The XRD peaks and their intensities from the powders are compared with the standard data from the International Centre for Diffraction Data (ICDD), this helps us to know the powder's crystalline phase. The average crystallite size is determined by the Scherrer equation;

$$D_{hkl} = \frac{0.9\lambda}{\beta_{\frac{1}{2}} \cos\theta} \quad (3.2.2)$$

where D_{hkl} = mean particle size of the crystal, λ = wavelength of incident X-ray, θ = corresponding Bragg angle, $\beta_{\frac{1}{2}}$ = full width at the half maximum height (FWHM) of the peak. A 50% error is expected on the calculated value of crystallite size [4].

3.3 Photoluminescence Spectroscopy (PL)

There are two types of photoluminescence, i.e fluorescence and phosphorescence. A category of electromagnetic spectroscopy useful in investigating the fluorescence or phosphorescence of the synthesized powders is known as Fluorescence spectroscopy. In the current work, the excitation source is ultraviolet light which excites electrons in the powders and consequently causing an emission of light. fluorescence spectrophotometer is useful in the investigation of fluorescence intensity, i.e taking the readings of different intensities of emitted fluorescence. A fluorescence spectrophotometer comprises of four main parts i.e a photomultiplier, sample holder, radiation source (150 W−Xenon lamp), and a monochromator in both excitation and emission sides. Excitation radiation is provided by a monochromatized xenon flash lamp with a varying wavelength [5]. The photomultiplier tube (PMT) is used in detecting the emissions. High resolution and the spectral purity is mainly provided the monochromator on using the narrow slits. The electronic energy levels can be analysed by the transition energies from the PL spectrum. By the use on a constant excitation wavelength, luminescence emission spectrum at different wavelengths is provided by the detector.

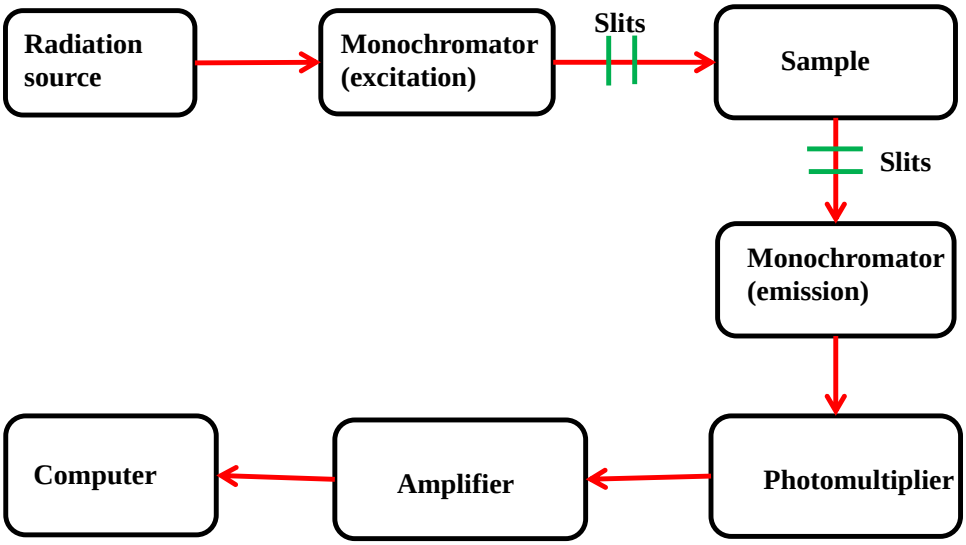

Figure 3.3 A schematic diagram of Photoluminescence system

3.4 UV-VIS-NIR Spectroscopy/ Diffuse Reflectance spectroscopy

Absoption techniques are associated with investigation of the reduction of the intensity of a monochromatic light beam as it goes through the sample. In the current work, the Varian Cary 100 Conc. UV-Vis spectrophotometer was the absorption technique used. The UV-VIS-NIR spectrophotometer technique determines the intensity of radiation traversing through the powders and relates it with the intensity of radiation prior to reaction with the powders. The key purpose for the use of this technique is to establish the band gap of the powders by use of the Tauc's relation [6]. Both UV-VIS-NIR Spectroscopy and diffuse reflectance spectroscopy utilize the visible light energy to move valence electrons to unoccupied orbitals. Diffuse reflection is the portion of the beam which comes back to the surface after being scattered within the powder.

Diffuse Reflectance spectroscopy is derived from a linear correlation linking analyte concentration and reflectance. This correlation is called Kubelka-Munk function [7].

$$f(R) = K = \frac{(1-R)^2}{2R} = \frac{K}{S} \qquad (3.4.1)$$

where: R stands for absolute reflectance of powder sample, K represents molar absorption coefficient and S stands for scattering coefficient. Diffuse reflectance depends on two factors namely: sample uniformity and particle size. As per the uniformity, Kubelka- Munk function is obtained from uniform samples of infinite depth. To investigate carefully the peak intensity variations, it is important to circulate the analyte as uniformly as possible. In the case of particle size, reduction in particle size causes reduction in bandwidths and modification of relative intensities.

3.5 Energy Dispersive X-ray Spectrometry (EDS)

By bombarding powder sample with a beam of electrons, localized chemical evaluation is achieved. At the same time, the powder sample emits X-ray spectrum, which is utilized in Energy Dispersive X-ray Spectrometry (EDS). The beam of electrons generates secondary electrons as it moves through the sample. Due to this, holes will be found in the electron shells previously occupied by the secondary electrons. For stability reasons, electrons from outer electron shells will fill the create holes in the inner shells. The filling of holes in the inner shells by electrons from outer shells calls for loss of energy, given that the outer electron shell are at high energy states compared to the inner ones. The lost energy is in X-ray form. These X-rays have their characteristics depending on which shells produced second electrons and which shells substituted them [8]. For example, by substituting electrons from the innermost shell (K shell) with M shell electrons, a K_β is emitted from the powder. Whereas, when K shell electrons are replaced with L shell electrons, a K_α X-ray is produced from the powder. The depth from which the K_β and K_α radiations are produced is same as the depth from which the secondary electrons were produced.

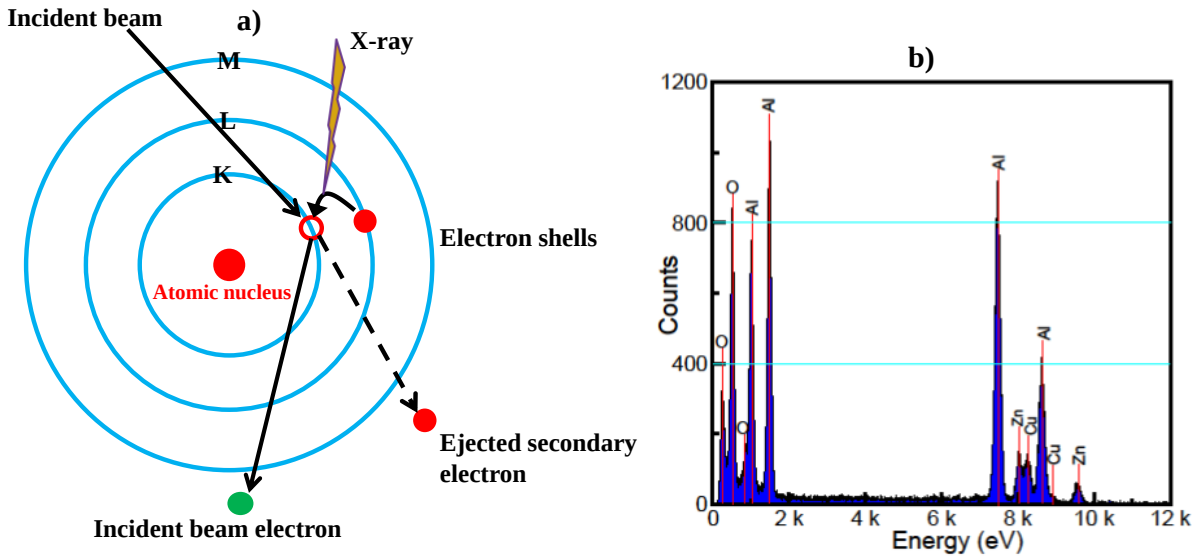

Figure 3.4 a) schematic of X-ray emission from an atom b) EDS spectrum of $ZnAl_2O_4:Cu^{2+}$

3.6 High resolution Transmission electron microscopy (HRTEM)

Compared to the traditional transmission electron microscope (TEM), High resolution transmission electron microscopy (HRTEM) imaging technique enables imaging of the interior microstructure of fine specimens. The electron gun is made of thermionic tungsten which has a high resistivity. In order to accord the electrons adequate energy which is more than its work function, the thermionic tungsten is subjected to high temperatures of 2800K in a vacuum. HRTEM anode potential is generally 100-400 kV. It is successfully used in ascertaining the electron diffraction arrangements of different systems such as crystalline and amorphous. As per the crystalline systems, the electrons are dispersed by the regular alignment of atoms through precise angles provided by Bragg's law. In the current work, the powder samples HRTEM micrographs were acquired using the FEI Tecnai F 20 G2 model. The system had the following settings, electron probe magnitude at less than 0.3 nm, image resolution at less than 0.23 nm and accelerating voltage at approximately 200kV. It was also fitted with CCD camera and EDS detector.

3.7 Scanning Electron Microscope (SEM)

SEM uses the mechanism of scanning of samples with a beam of electrons inorder to generate high resolution micrographs of the sample surface. SEM was invented in 1937 by Manfred Von Ardenne as a microscope with powerful magnification. The beam of electrons reacts with atoms of the sample generating different noticeable signals. These signals comprise of details on the sample's surface shape and anatomy [9]. From the reactions of the beam of electrons and the sample atoms, signals such as characteristic X-rays, secondary electrons (SE), back-scattered electrons (BSE) and photons of different energies are generated [10]. From SEM, signals whose source is SE or BSE are used for imaging, while the characteristic X-rays (see section 3.4.2) are important in fundamental composition investigation. These signals are discussed in depth in [11]. SEM images have a distinctive three-dimensional occurrence owing to the narrow electron beam producing them. At different surface shapes, the SE and BSE signals fluctuate making these two types of signals of great importance. The percentage of predominant electrons that take off as BSE escalates with increase in atomic number. This means that BSE micrographs are different depending on the chemical composition of the sample, i.e. the higher the atomic number, the radiant the micrograph. SEM micrographs represent predominantly the surface shape of the sample [11].

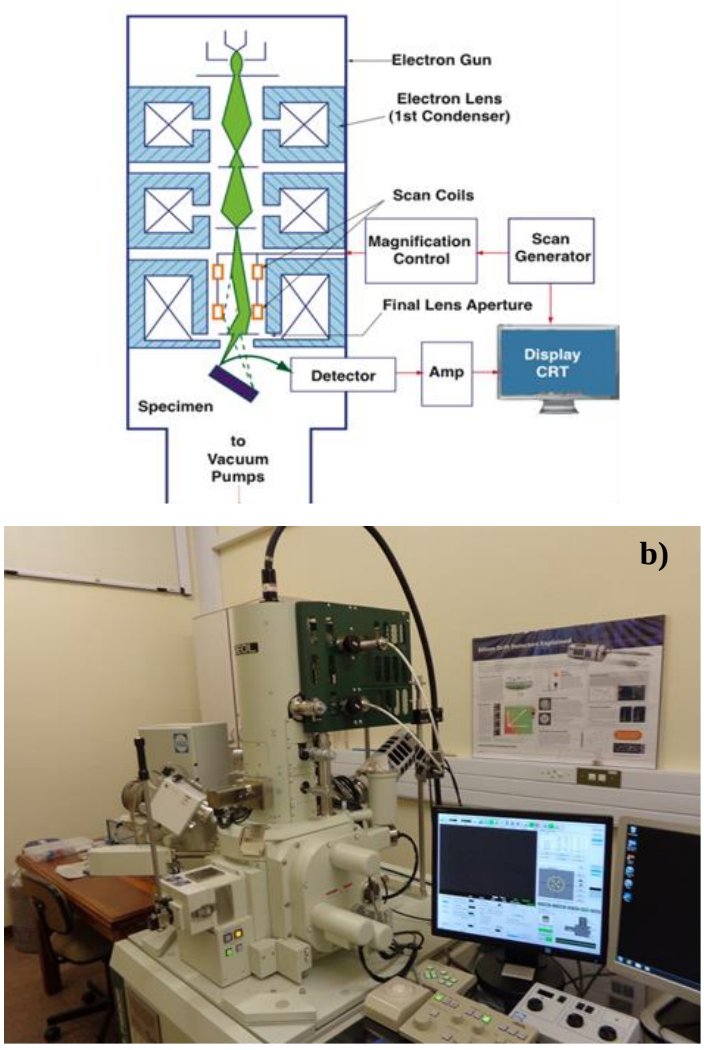

Figure 3.5 a) Schematic diagram of SEM. b) JEOL JSM-7800F scanning electron microscopes (SEM) at the Microscopy Center, University of Free State.

3.8 *Ab initio* techniques

3.8.1 Introduction

The gradual development of *ab initio* calculations owes to the increase in computational resources and improvement in algorithms. These first principle calculations not only confirm experimental findings but also guide and predict materials and their promising properties. Using quantum theory, one can easily differentiate between metals and insulators, or even characterise materials based on their optical, magnetic and elastic properties.

3.8.2 The many-body system

In order to describe quantum mechanical behaviour of atoms one should consider in details the interactions between electrons and nuclei [12].

Let $\hat{H}$ denote the Hamiltonian of a many electron system. The states of well-defined energy are the eigenstates of $\hat{H}$:

$$\hat{H}\,\psi_K(r_1\sigma_1 \ldots\ldots r_N\sigma_N) = E_K\,\psi_K(r_1\sigma_1 \ldots\ldots r_N\sigma_N) \tag{3.8.1}$$

where K , is the entire set of many-electron quantum numbers, ψ represents the electron wave function and E represents the total energy of the system. Particles having half interger spins, such as electrons, are described by an antisymmetric wave functions as;

$$\psi(r_1\sigma_1 \ldots, r_i\sigma_i \ldots r_j\sigma_j \ldots r_N\sigma_N) = -\psi(r_1\sigma_1 \ldots r_j\sigma_j \ldots r_i\sigma_i \ldots\ldots r_N\sigma_N) \tag{3.8.2}$$

and they are found to obey the Pauli exclusion principle. These particles are known as fermions. Pauli Exclusion Principle states that no two electrons can have the same set of quantum numbers,

and electrons with the same spin cannot occupy the same state simultaneously. Bosons are particles described by symmetric wave functions under particle interchange and have integral or zero intrinsic spin. Given that there are $N!$ distinct permutations of the labels 1,2,…., N , going by equation (3.8.2) all have the same $|\psi|^2$. Therefore, the probability of getting any electron with spin σ_1 in volume element $d^3 r_1$, is;

$$N!\left|\psi_K(r_1\sigma_1 ..... r_N\sigma_N)\right|^2 d^3 r_1 ..... d^3 rN \tag{3.8.3}$$

Considering all the interactions between electrons and nuclei, an actual Hamiltonian operator $\hat{H}$ is expressed as,

$$\hat{H} = -\frac{\hbar^2}{2m_e}\sum_i \nabla_i^2 + \sum_{iI}\frac{Z_I e^2}{\left|r_i - R_I\right|} + \frac{1}{2}\sum_{i\geq j}\frac{e^2}{\left|r_i - r_j\right|} - \sum_I \frac{\hbar^2}{2M_I}\nabla_I^2 + \frac{1}{2}\sum_{I\geq J}\frac{Z_I Z_J e^2}{\left|R_I - R_J\right|} \tag{3.8.4}$$

where electron mass m_e and charge e are denoted by lower case subscripts, at the same time, the nuclei with mass M_1 and core charge Z_1 are represented by upper case subscripts [13]. The terms represented in the equation (3.8.4) above are the electronic kinetic energy operator $\hat{T}_e = -\frac{\hbar^2}{2m_e}\sum_i \nabla_i^2$, the nuclei potential acting on the electrons $\hat{V}_{en} = \sum_{i,I}\frac{Z_I e^2}{\left|r_i - R_I\right|}$, the repulsion from the electron-electron interactions $\hat{V}_{ee} = \frac{1}{2}\sum_{i\geq j}\frac{e^2}{\left|r_i - r_j\right|}$, the nucleic kinetic operator $\hat{T}_n = -\sum_I \frac{\hbar^2}{2M_I}\nabla_I^2$ and the repulsion due to nuclei-nuclei interactions operator $V_{nn} = \frac{1}{2}\sum_{I\geq J}\frac{Z_I Z_J e^2}{\left|R_I - R_J\right|}$. The terms in the equation (3.8.4) may be written in the simplest form as

$$\hat{H} = \hat{T}_e + \hat{V}_{en} + \hat{V}_{ee} + \hat{T}_n + \hat{V}_{nn} \tag{3.8.5}$$

3.8.3 Born-Oppenheimer approximation

Born-Oppenheimer approximation [14] also called the adiabatic approximation, is the first approximation which aims at solving the many-body Schrödinger equation. The calculations in this approximation are based on the fact that for a system of interacting particles, the electrons and nuclei motions can be disassociated given that the mass of the nuclei is much greater compared to the mass of the electrons. Using this approximation, equation (3.8.5) is now expressed as;

$$[T_e + V_{ee} + V_{en}]\psi\left(\left\{r_i, \sigma_j\right\}\right) = E\,\psi\left(\left\{r_i, \sigma_j\right\}\right) \tag{3.8.6}$$

Equation (3.8.6) can be solved by the use of wavefunctions that explicitly contain interatomic distances, and this is applicable for only small systems.

3.8.4 Hartree approximation

From the previous explanation, it is clear that the Born-Oppenheimer approximation makes the many-body Schrödinger equation a bit clear, but still the electron-electron interaction term is complicated therefore further approximations are crucial. It is because of this need that the use of the molecular orbital technique to approximate the wavefunctions was brought in by Hartree [15]. In this approach, the total wavefunction for the system are approximated as a product of orthonormal molecular orbitals. This is known as the Hartree approximation. Hartree assumed that, each electron movement is independent of the other electrons in the system but will experience an average field resulting from the other electrons.

The Hartree equation is expressed as;

$$\left[-\frac{1}{2}\nabla^2 + V_{ext}(r) + V_H\right]\psi_i = \varepsilon_i \psi_i(r) \tag{3.8.7}$$

where $V_{ext}(r)$ and V_H are the ion-electron and Hartree potentials. ψ_i are the spin orbitals and ε_i are Lagrange multipliers.

3.8.5 Hartree-Fock theory

The many-body Schrödinger equation was simplified further by Hartree approximation but now this approximation did not satisfy the Pauli exclusion principle which demands the wavefunction to be antisymmetric with respect to electron interchange. This is when Fock came in and proved that Hartree artifact can be antisymmetric by appropriately adding and subtracting all possible permutations of the Hartree artifact. This is the origin of Hartree-Fock (HF) wavefunction. The final wavefunction is the determinant of a matrix, known as the Slater determinant [16-17]. Slater expressed the wavefunction using a single Slater determinant which consists of spin orbitals. The expression is as shown below;

$$\Psi = \frac{1}{\sqrt{N!}}\begin{vmatrix} \Psi_1(X_1) & \Psi_2(X_1) & \cdots & \Psi_N(X_1) \\ \Psi_1(X_2) & \Psi_2(X_2) & \cdots & \Psi_N(X_2) \\ \vdots & \vdots & & \vdots \\ \Psi_1(X_N) & \Psi_2(X_N) & \cdots & \Psi_N(X_N) \end{vmatrix} \tag{3.8.8}$$

where ψ_1 are the spin orbitals and X_1 comprises of both the space and spin coordinates. If there is no non-singular linear transformation to change the determinant, then the spin orbital ψ_i can be taken as an orthonormal set. To normalize ψ_i, a Lagrange multiplier, ε_i should be introduced and the Hamiltonian is minimized as a function of ψ_i, that is;

$$\frac{\delta}{\delta\psi}\left[\langle \hat{H} \rangle - \sum_j \varepsilon_j \int \left|\psi_i\right|^2 dr\right] = 0 \tag{3.8.9}$$

The Hamiltonian is then decreased to a set of one-electron equations of the form

$$\left[-\frac{1}{2}\nabla^2 + V_{ext}(r) + V_x + V_H\right]\psi_i = \varepsilon_i \psi_i(r) \tag{3.8.10}$$

where V_x represents the exact exchange that incorporates the effects of Pauli exclusion principle and V_H represents the Hartree potential. The Hartree-Fock equation is then expressed as;

$$\varepsilon_i \psi_i = \left(-\frac{1}{2}\nabla^2 + V_{ion}(r)\right)\psi_i(r) + \sum_j \int dr' \frac{\left|\psi_j(r')\right|^2}{\left|r - r'\right|}\psi_i(r) - \sum_j \delta_{\sigma_i \sigma_j} \int dr' \frac{\psi_j^*(r')\psi_i(r')}{\left|r - r'\right|}\psi_j(r) \tag{3.8.11}$$

Hartree-Fock approximation is found to be qualitatively accurate, although, the single-determinant form of the wave function does not take the effect of correlations between electrons into account. This results into inaccurate description of the electronic structure.

3.8.6 Density functional theory (DFT)

Kohn, Sham and Hohenberg developed the idea of density functional theory (DFT) in early 1960's [18-19]. DFT is the standard tool used by condensed matter physicists as well as quantum chemists in predicting ground state electronic properties of materials [20]. In quantum mechanics, DFT has been used to investigate different electronic structure properties of many-body systems. Within this formalism, different fundamental properties of a many electron systems can be calculated using functionals known to be spatially dependent on the electron density [21]. Although DFT is formally exact, in practice, approximations are required to implement this formalism. These approximations lead to inaccurate results when predicting

properties of the system being modelled. DFT is different from other quantum mechanical approximations because it is a non-interacting theory which does not result to a correlated N -body wavefunction [22]. Being same as Hartree-Fock theory in many ways, DFT is a one-electron theory within the Kohn-Sham formalism [21].

3.8.7 The Hohenberg-Kohn Theorem.

This theorem clearly proves that the ground state electron density $n(r)$ influences the external potential $V_{ext}(r)$ in a given electron interacting setup [23]. The theory explains that if a setup comprising of N interacting electrons is controlled by an external potential V_{ext} , then a distinctive ground state electron density $n_0(r)$ decreases the corresponding energy functional.

$$E[n] = F[n] + \int n(r) V_{ext}(r) dr \tag{3.8.12}$$

where F is a universal functional of n . Therefore the entire ground-state electronic energy E_0, is the least of the functional E . Regarding the Hohenberg-Kohn theorem, Levy [24] came up with a conventional N -electron functional F given by,

$$F[n(r)] = \min_{\psi \to n(r)} \left\langle \psi \left| \hat{F} \right| \psi \right\rangle \tag{3.8.13}$$

where the expected value is evaluated by thoroughly scrutinizing over all N -electron wave functions ψ which reduces to a certain density $n(r)$. We now chose the wave function ψ which successfully reduces the expected value of $\hat{F}$. It is important to know that $\hat{F}$ is given by,

$$\hat{F} = \sum_i -\frac{1}{2}\nabla_i^2 + \frac{1}{2}\sum_{i \neq j} \frac{1}{\left| r_i - r_j \right|} \tag{3.8.14}$$

We now examine a N -electron ground state wave function, ψ_0 which generates a density, n_0. This gives us the ground state energy as,

$$E_0 = \left\langle \psi_0 \left| \hat{F} + \hat{V}_{ext} \right| \psi_0 \right\rangle \tag{3.8.15}$$

Basing our argument on equation (3.7.2) we find that,

$$F[n_0] = \min_{\psi \to n_0} \left\langle \psi \left| \hat{F} \right| \psi \right\rangle = \left\langle \psi^0_{\min} \left| \hat{F} \right| \psi^0_{\min} \right\rangle \tag{3.8.16}$$

As per the minimum principle,

$$F[n_0] + \int \hat{V}_{ext}\, n_0(r)\, d^3r = \left\langle \psi^0_{\min} \left| \hat{F} + V_{ext} \right| \psi^0_{\min} \right\rangle \geq E_0 \tag{3.8.17}$$

Given that,

$$F[n_0] = \left\langle \psi^0_{\min} \left| \hat{F} \right| \psi^0_{\min} \right\rangle \leq \left\langle \psi_0 \left| \hat{F} \right| \psi_0 \right\rangle \tag{3.8.18}$$

and

$$F[n_0] + \int \hat{V}_{ext}\, n_0(r)\, d^3r = \left\langle \psi^0_{\min} \left| \hat{F} + V_{ext} \right| \psi^0_{\min} \right\rangle \leq E_0 \tag{3.8.19}$$

Given that $\psi^0_{\min}$ and ψ_0 generate equal density n_0, referring to equations (3.7.6) and (3.7.8) we get,

$$E[n_0] = F[n_0] + \int \hat{V}_{ext}\, n_0(r)\, d^3r = E_0 \tag{3.8.20}$$

Hence proved.

3.8.8 The Kohn-Sham Equations.

Referring to the Hohenberg-Kohn theorems [18], the accurate structure of the general functional F is not clear. For it to be an effective potential system, Kohn and Sham [19], pressumed that the ground-state density $n_0(r)$ is the density of non-interacting electrons system. The functional $F[n(r)]$ is divided into four components and E gets to be,

$$E[n(r)] = T_S[n(r)] + \frac{1}{2}\int\int \frac{n(r)n(r')}{|r - r'|} dr dr' + E_{XC}[n(r)] + \int n(r)V_{ext}(r)dr \tag{3.8.21}$$

where $T_S[n(r)]$ is taken to be kinetic energy of the non-interacting electron gas of density $n(r)$,that is,

$$T_S[n(r)] = -\frac{1}{2}\sum_i^N \int \psi_i^*(r)\nabla^2\psi_i(r)dr \tag{3.8.22}$$

A typical exchange-correlation functional $E_{XC}[n(r)]$ is explained in equation (3.8.21). When a normalization constraint is introduced on the density of the electron, i.e. $\int n(r)dr = N$, the variational principle in equation (3.8.23) is arrived at.

$$\frac{\delta}{\delta n(r)}\left[E[n(r)] - \mu\int n(r)dr\right] = 0$$

$$\Rightarrow \frac{\delta E[n(r)]}{\delta n(r)} = \mu \tag{3.8.23}$$

where μ is taken as the chemical potential.

We now improve equation (3.8.23) relative to effective potential, $V_{eff}(r)$, i.e,

$$\frac{\delta T_S[n(r)]}{\delta n(r)} + V_{eff}(r) = \mu \tag{3.8.24}$$

Given that,

$$V_{eff}(r) = V_{ext}(r) + \int \frac{n(r)}{|r - r|} dr' + V_{XC}(r) \tag{3.8.25}$$

and

$$V_{XC}(r) = \frac{\delta E_{XC}[n(r)]}{\delta n(r)} \tag{3.8.26}$$

It is worth noting that ground state energy $n_0(r)$ illustrates non-interacting electrons in motion inside an external potential $V_{eff}(r)$, that is,

$$n_0(r) = \sum_{i=1}^{N} |\psi_i(r)|^2, \tag{3.8.27}$$

Fluctuation of the $E[n(r)]$ as a function of $\psi_i^*(k)$ generates a one electron Schrödinger equation,

$$\left(\frac{1}{2}\nabla_i^2 + V_{eff}(r) - E_i\right)\psi_i(r) = 0 \tag{3.8.28}$$

which can be self-consistently worked out as

$$V_{eff}(r) = V_{eff}(n_0(r)) \tag{3.8.29}$$

As long as the E_{XC} is known, and we are examining a non-interacting electron setup, therefore equation (3.8.24) and (3.8.25) will give us an accurate procedure for calculating ground state energy E_0 of an interacting system, provided that the exchange correlation functional E_{XC} is known. Search for the exact form of E_{XC} is still on progress. A lot of proposals have been put

across, tested on several materials but sometimes there is success and other times failure. Some of the investigated E_{XC} functionals are discussed below.

3.8.9 The Local Density Approximation (LDA)

This functional (LDA) [25] is one of the most significant functionals that was proposed by Hohenberg and Kohn in early 1960s. It is the first approximation to be used in condensed matter pseudo potential calculations and is the foundation of any development in the context of the exchange-correlation functionals. The expectations when interpreting LDA is that; First, the exchange-correlation energy per electron $E_{XC}[n(r)]$ is locally approximated at point, r. Secondly, the exchange-correlation energy per electron should equal to the energy of a homogeneous electron gas $E_{XC}^{\hom}[n(r)]$. Thirdly, both the electron gas energy and the exchange-correlation energy per electron must have the same local density $n(r)$. Considering fluctuating densities in LDA, the exchange-correlation energy functional $E_{XC}[n(r)]$ is indicated as,

$$E_{XC}^{LDA}[n(r)] = \int n(r) E_{XC}[n(r)] d^3 r \tag{3.8.30}$$

Given that

$$E_{XC}[n(r)] = E_{XC}^{\hom}[n(r)] \tag{3.8.31}$$

In the case of homogeneous systems [25]. Equation (3.8.1) can only hold for non-magnetic set-ups. The exchange-correlation energy per electron can be splitted into two parts, that is, exchange and correlation as,

$$E_{XC}[n(r)] = E_X[n(r)] + E_C[n(r)] \tag{3.8.32}$$

Dirac in 1930 [29] derived the formula for exchange energy per electron $E_X[n(r)]$ as,

$$E_X[n(r)] = -\frac{3}{4}\left(\frac{3n(r)}{\pi}\right)^{\frac{1}{3}} \tag{3.8.33}$$

This exchange energy per electron can be analysed completely [13]. The correlation energy per electron $E_C[n(r)]$ cannot be analysed completely, therefore need for an approximation [26]. In 1980, with the use of quantum Monte-Carlo code [27], Ceperley and Alder carried out the first approximation of $E_C[n(r)]$ for an homogeneous electron gas. Analytical parameterization of $E_C[n(r)]$ was reported by several researchers such as Hedin et al [28]. Parameterization reported by Perdew and Zunger [42] is popularly used.

LDA causes underestimation of bond lengths owing to over binding. LDA's success is ascribed to the fact that, first, LDA normally underestimates $E_C[n(r)]$ at the same time over estimating $E_X[n(r)]$ causing unexpected deletion of errors arising from putting together exchange and correlation energies. Secondly, LDA fulfils the law that exchange-correlation hole combines to precisely one removed electron [29]. LDA also has its own shortcomings in that, it allows partial deletion of electronic self-interaction [25] in set-ups where the density $n(r)$ has fluctuations throughout the perfect set-up. Thirdly, LDA underestimates the band gap in semiconductors owing to LDA's derived discontinuity in the exchange-correlation potential [30].

3.8.10 Generalized gradient approximation (GGA)

GGA exchange correlation functionals were introduced because Hohenberg and Kohn observed that LDA failed in real systems. First, they suggested a scheme known as gradient expansion approximation (GEA). The findings of Hohenberg and Kohn were improved further by Perdew and others [31-33], proposing general functionals of the type;

$$E_{XC}^{GGA}[n] = \int d^3 r f(n, \nabla n) \tag{3.8.34}$$

where $E_{XC}^{GGA}[n]$ define the exchange correlation energy. The GGA method gives better results for predicting molecular geometries and ground-state energies, but it is computationally more expensive than LDA [34]. GGA is also reliable for predicting magnetic properties of 3d transition metals [35]. In spite of all the successes, GGA has its shortcomings. It does not predict accurately the lattice parameters of graphite and does not perfectly treat hydrogens bond [36]. More developed and may be more accurate than the GGA functionals are the new meta-GGA functionals for example the ones parametrized by Tao-Perdew-Staroverov-Scuseria (TPSS) [37].

3.8.11 Hybrid functionals and GW approximation

Under normal circumstances, LDA as well as GGA, underestimates semiconductor band gaps, whereas the Hatree-Fock technique overestimates the semiconductor band gap. Appropriate functionals that predict accurately band gaps should be constructed by appropriate combination of the local or semi local DFT exchange energy functionals and the non-local Hartree-Fock exchange energies. Hybrid functionals like HSE06 have been suggested to elucidate the band gap problem [38-39]. These techniques are frequently dependable in predicting band gaps, the only limitation being they are computationally expensive. GW approximation [40] is also very expensive computationally although it gives exact prediction of the band gaps. All these techniques are restricted to smaller systems, particularly when computational resources are inadequate. The revised Becke-Johnson (MBJ) potentials [41-42] have of lately attracted a lot of attention as an uncomplicated technique for calculating accurate band gaps. This technique needs minimum computational resources and its accuracy is nearly same as that of HSE06 and GW.

3.8.12 Plane waves

Clear definition of the unit cell is very important in computational modelling of solids. The unit cell is defined by the use of unit vectors $\vec{a}_1, \vec{a}_2,$ and $\vec{a}_3$. In crystalline solids, atoms are normally displayed in a systematic repeating pattern. If the nuclei are displayed in a periodically repeating pattern, then also their lattice potential U(r) acting on the electrons must be periodic. Therefore the single electron Schrodinger equation under periodic potential U(r) is expressed as [29].

$$\left(-\frac{1}{2}\nabla^2 + U(r)\right)\psi = \varepsilon\psi \tag{3.8.35}$$

The Bloch theorem states that the one-electron wavefunctions obey the equation

$$\psi_K(r) = \exp^{ik.r}\ \mu_K(r) \tag{3.8.36}$$

where $\mu_\kappa(r)$ has the periodicity of the lattice. This allows the plane wave expansion of the electron wavefunctions,

$$\psi_{i,K}(r) = \sum_G C_{i,K+G}\, e^{i(K+G).r} \tag{3.8.37}$$

where the *G* represents the reciprocal lattice vectors. The Kohn-Sham equations in K space then decreases to the matrix eigenvalue equation;

$$\sum_{G'}\left\{\frac{1}{2}\left|K+G\right|^2\delta GG' + V_{ext}\left(G-G'\right) + V_H\left(G-G'\right) + V_{xc}\left(G-G'\right)\right\}C_{i,K+G} = \in_i C_{i,K+G} \tag{3.8.38}$$

where V_{ext} represents the static total electron-ion potential, V_H represents the Hartree potential of the electrons, i and $\in$ are the Kohn-Sham eigenvalue, V_{xc} is the exchange-correlation

potential and $C_{i,K+G}$ represents the coefficient of plane-wave basis state. Under normal circumstances, not all wave vectors are important, therefore a cut-off energy defined as,

$E_{cut} = \frac{1}{2}\left|K + G_{\max}\right|^2$, is used. E_{cut} is the kinetic energy cut-off.

3.8.12.1 Energy cut off

In DFT calculations, cut off energy for plane wave basis is an important parameter. The Cut off energy convergence as a function of the total energy is evaluated at a fixed K -point mesh and experimental lattice parameter (or lattice parameter acquired from an existing crystallographic database). High cut off energies are unnecessary because they increase the computational cost while not necessarily improving the accuracy of the results.

3.8.12.2 K -points

The first Brillouin zone is defined as the Wigner-Seitz cell of the reciprocal lattice described by the planes that are perpendicular bisectors between the lattice points and the origin of the reciprocal lattice [13]. The frequently used method in sampling of the first Brillouin zone is the consistently spaced Monkhorst-Pack K -point grid [43]. Chadi and Cohen [44] introduced a different sampling scheme which is not very popular compared to the Monkhorst-Pack K -point grid. The Monkhorst-Pack grids are represented as $n1 \times n2 \times n3$ grids, resulting to a total number of K -points presented as $n1.n2.n3$. This means that the computational cost strongly depends on the total number of K -points. For example a dense grid of $3 \times 3 \times 3$ grid will require more central processing unit (CPU) time than a less dense grid of $2 \times 2 \times 2$. Although, a dense grid predicts more accurate results for ground state properties, but one must consider to balance between the accuracy of the results and the computational costs. The size of the unit cell strongly determines

how dense the K -point grid should be. The total number of K -points is inversely proportional to the size of the unit cell, because the size of the Brillouin zone is the same as the size of the reciprocal lattice unit cell.

3.8.13 Brillouin zone sampling

In ascertaining, exactly the properties of materials, a continuous system of K-points across the reciprocal space is used to represent the Brillouin zone (BZ). In order to get the electronic properties using ab initio calculations, the functions should be integrated over the BZ as;

$$F(r) = \frac{\Omega}{(2\pi)^3} \int f(k) d^3 k \tag{3.8.39}$$

where $f(k)$ stands for Fourier transformations of the function $F(r)$ while Ω stands for volume of the unit cell. These functions are perfectly symmetric and periodic within *k*-space. In this work, in order to avoid dopant to dopant communication, a big supercell was created. Relating the BZ volume and the supercell volume, we get;

$$\Omega_{BZ} = \frac{(2\pi)^3}{\Omega_{CELL}} \tag{3.8.40}$$

This means that the bigger the supercell the smaller the BZ therefore few *k*-points will be required to represent the BZ. In the current work, the Monkhorst-Pack scheme was used [43]. This scheme is an unbiased procedure for finding the set of *k*-point to be used in sampling of the BZ. This sampling is in fractional co-ordinate form and it is presented in a rectangular grid of points (k_x, k_y, k_z) derived from;

$$kn_1 n_2 n_3 = \sum_{i=1}^{3} \frac{2n_i - N_i - 1}{2N_i} G_i \tag{3.8.41}$$

If the Fourier components for a single $f_i(k)$ is expanded to $N_i R_i$ in every direction, then equation (3.8.39) is integrated over equivalent points. Based on the above explanation, the total energy of a system can be calculated with the use of few *k*-points. The errors coming up during the calculations are minimized by using an extensive set of Monkhorst and pack *k*-points.

3.8.14 Pseudopotentials

Bonding determines the variation of wave functions in a system. In the area close to the nucleus, the wave functions oscillate speedily while far away from the nucleus (valence region), the wave functions are of regular surface. The electronic structure type of bonding strongly depends on these different type of wave functions. In *ab initio* calculations, the applications of pseudopotentials approximation in electronic structure calculations utilizes only the valence electrons given that the core electrons are taken to be fixed. Given that the potential of the core electrons is far down from the surface, making the core orbitals more extensive will demand numerous plane waves. Involving numerous plane waves means too much space in the cluster will be occupied and many processors required if we have to save on time.

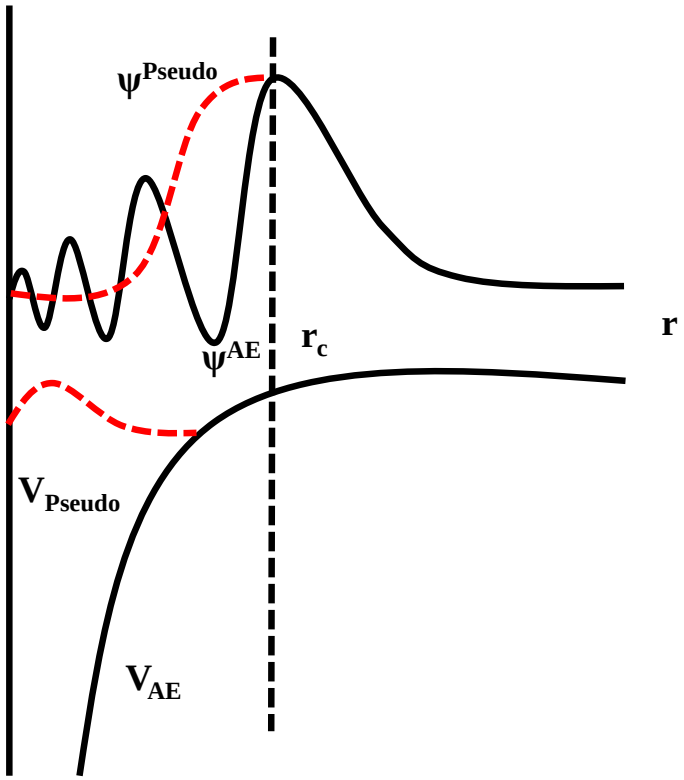

Figure 3.6 Schematic diagram of pseudo electrons (red lines) and all-electron (black lines) potentials and their equivalent wave functions.

In pseudopotential approximation, a less strong ionic pseudopotential (V_{pseudo}) found in the core region of radius (r_c) is used to substitute the electrostatic potential $\left(-\frac{z}{r}\right)$ The pseudopotentials utilize the spurious pseudo wave functions instead of the true all-electron (AE) wave functions. These spurious pseudo wave functions oscillate smoothly in the core region unlike the instantaneous oscillating AE wave functions as seen in Fig. 3.6. In the figure, pseudo electrons and all-electron potentials as well as their equivalent wave functions coincide at a radius r_c. The instantaneous oscillation is attributed to the deep seated ionic potential in the area around the nucleus. For Pauli exclusion principle to be obeyed, the valence and core wave functions have to be perpendicular to each other. This shows that smooth oscillations are necessary in the core region. From the above explanation, it is clear that the pseudo potentials are established so as to replicate the effect of fixed core electrons. Before the pseudo potentials are used, they are usually

tested to make sure that all the essential characteristics of the valence electrons in a system are correctly illustrated [45].

3.8.15 Density function theory and the Hubbard term U

The Mott insulators represents one of the most known and reported failures of DFT [46]. The strong Coulomb repulsion between electrons determines the insulating character at ground state in these systems in that, this strong Coulomb repulsion prevailing in the electron's kinetic energy (minimized by delocalization), forces them to localize on atomic-like orbitals (Mott localization) [47]. This behaviour is described by full account of the multi-determinant nature of the N-electron wave function and of the many-body terms of the electronic interactions. For example, in molecular dissociation processes, the localization of electrons on the resulting fragments are described if the ionic terms of the ground state wave function are allowed to decrease their weight and at the same time the distance between the fragments increases. This can only take place if the N-electron wavefunction is arrived at as a linear combination of multiple Slater determinants. This means that, when electrons are strongly localized, their motion becomes "correlated" and their wave function acquires a marked many-body character. The insulating properties of these materials cannot be determined by band theory. Based on the above-mentioned reasons, they are generally classified as "strongly-correlated" materials. Describing the properties of these systems within DFT is not easy (although the unknown exact exchange-correlation energy functional would be able to predict their ground state properties due to the expression of the electron-electron interaction as a functional of the electronic charge density, and to the utilization of an effective single particle (Kohn-Sham) representation of this quantity. It is well known that most of the frequently used approximate exchange-correlation (xc) functionals for example, the Local Density Approximation (LDA) [48] or the Generalized Gradient Approximation (GGA), seriously fail in predicting the insulating properties of these materials, while the other physical properties are poorly predicted, including their equilibrium crystal structure, , their vibrational spectrum, their magnetic moments etc. These challenges can be addressed by the most approximate xc functionals to over-delocalize valence electrons and to

over-stabilize metallic ground states. Other failures of approximate xc functionals for example, the incorrect account of the exchange interaction and the resulting incomplete cancellation of the electronic self-interaction contained in classical (density-density) Coulomb integrals may occasionally concur to the over-delocalization of electronic states. One of the simplest models that have been formulated to rationalize the physics of correlated materials, is the Hubbard model [49] whose real-space second quantization formalism is ideally suited to describe systems with electrons localized on atomic orbitals. The Hubbard Hamiltonian can be written as

$$H_{Hub} = \sum_{\langle i,j\rangle,\sigma} \left(C_{i,\sigma} C_{j,\sigma} + h.c. \right) + U \sum_{i} n_{i,\uparrow} n_{i,\downarrow} \qquad (3.8.42)$$

where $\langle i, j\rangle$ denotes nearest neighbour atomic sites, sites, $C_{i,\sigma}, C_{j,\sigma}$ and n_i are electronic creation, annihilation and number operators for electrons of spin σ on site i .

The LDA+U (here I mean the Hubbard U correction applied to a generic approximate DFT functionals, but not necessarily LDA) is among the simplest corrective approaches that were formulated to improve the accuracy of DFT functionals in describing the ground state of correlated systems [50-54]. Here the Hubbard Hamiltonian is used to describe "strongly correlated" electronic states (basically the localized d or f orbitals), while the remaining valence electrons are treated at the "standard" level of approximation. Within LDA+U the total energy of a system can be written as

$$E_{LDA+U}[\rho(r)] = E_{LDA}[\rho(r)] + E_{Hub}\left[\left\{n^{I\sigma}_{mm}\right\}\right] - E_{dc}\left[\left\{n^{I\sigma}\right\}\right] \qquad (3.8.42)$$

where in equation (3.8.42) the term E_{Hub} contains electron-electron interactions as modelled in the Hubbard Hamiltonian.

3.8.16 Formation energies within DFT

The formation energy of an impurity in a semiconductor is the difference between the energy of the semiconductor when it has an impurity and the energy of the semiconductor when it has no impurity. When a semiconductor has an impurity in its crystal lattice, it experiences some stress. The energy originating from this stress is what is known as the formation energy. The formation energy of an impurity *X* in a charge state *q* can be defined as;

$$E^{f}\left[X^{q}\right] = E_{tot}\left[X^{q}\right] - E_{tot}\left[bulk\right] - \sum_{i} n_{i}\mu_{i} + q\left[E_{F} + E_{v} + \Delta V\right] \qquad (3.8.43)$$

where $E_{tot}[X]$ indicates, total energy derived from a supercell calculation with one impurity X in the cell. $E_{tot}[bulk]$ represents the total energy for the equivalent supercell consisting of bulk semiconductor only. n_i indicates the number of atoms of type i that have been added to (n_i>0) or removed from (n_i<0) the supercell when the impurity is introduced. μ_i are the corresponding chemical potentials of these materials. From equation (3.8.43) above, it is clear that formation energy strongly depends on concentration of the impurities. In thermodynamic equilibrium, the concentration C of an impurity is given by the expression;

$$C = N_{sites}\ N_{config}\ \exp\left(-E^{f}/KT\right) \qquad (3.8.44)$$

where E^{f} is the formation energy, N_{sites} being the number of sites in the crystal lattice where the impurity can be incorporated. N_{config} is the number of equivalent configurations in which the impurity can be incorporated, K is Boltzmann's constant, while T is temperature. Within DFT, the use of LDA is preferred to GGA. The two have different lattice constant, thus causing a difference in band gap and in the calculated formation enthalpies between GGA and LDA [55].

3.8.17 Optical properties from DFT

Impurities introduce impurity levels in the band gap or near the valence or conduction band edges of a semiconductor. The experimental detection of these impurity levels often forms the basis for the analysis of the impurity. Investigation on these levels is therefore an important priority. The levels that are of experimental relevance always involve transitions between different charge states therefore, the Kohn–Sham levels originating from band structure calculations cannot directly be identified with any levels that are relevant for experiment. The thermodynamic transition level $\varepsilon^{therm}\left(q_1/q_2\right)$ is defined as the Fermi-level position where charge states q_1 and q_2 have same value of energy. This level is observed in deep level transient spectroscopy (DLTS) experiments where after transition, the final charge state is able to completely relax to its equilibrium configuration. The optical transition level $\varepsilon^{opt}\left(q_1/q_2\right)$ corresponding to a transition between charge states q_1 and q_2 is defined in the same way as the thermodynamic transition level, only that, the energy of the final state q_2 is calculated with the use of the atomic configuration of the initial state q_1 [56]. The optical level is observed experimentally where after transition, the final charge state cannot relax to its equilibrium configuration. This is what is observed in photoluminescence (PL) experiments. When an electron recombines with a hole, a photon of energy E_{PL} is emitted. $E_{PL} = E_g - \varepsilon^{therm}\left(q_1/q_2\right) - E_{rel}$ where, E_{rel} is the Frank-Condon shift. From the Figure 3.8.1, the difference between the band gap and the PL length is the optical ionization energy, that is,

$$\varepsilon_A^{therm}\left(q_1/q_2\right) = E_g - E_{PL} = \varepsilon^{therm}\left(q_1/q_2\right) - E_{rel} \quad . \tag{3.8.45}$$

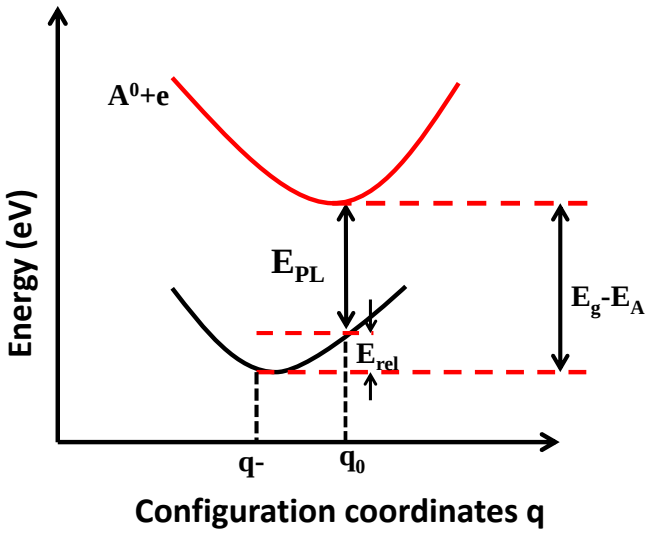

Figure 3.7 Schematic configuration coordinate diagram illustrating the difference between thermal and optical ionization energies for an acceptor A.

3.8.17.1 Dielectric constants

Frequency dependent dielectric tensor is used to explain the linear response of a system to an external time-varying electric field $\varepsilon(\omega) = \varepsilon_1(\omega) + i\varepsilon_2(\omega)$. A dielectric tensor $\varepsilon(\omega)$ is regarded as a second rank tensor with the elements, ε_{xx}, ε_{yy}, ε_{zz}, ε_{xz} and ε_{yz}. *x*, *y* and *z* represents the three dimensional x, y and z axis.

$$\varepsilon(\omega) = \begin{bmatrix} \varepsilon_{xx} & \varepsilon_{xy} & \varepsilon_{xz} \\ \varepsilon_{yx} & \varepsilon_{yy} & \varepsilon_{yz} \\ \varepsilon_{zx} & \varepsilon_{zy} & \varepsilon_{zz} \end{bmatrix} \qquad (3.8.46)$$

The dielectric tensor is symmetrical, therefore for the elements which are no on the diagonal running from the upper left to the lower right, $\varepsilon_{xy} = \varepsilon_{yx}$, $\varepsilon_{xz} = \varepsilon_{zx}$ and $\varepsilon_{yz} = \varepsilon_{zy}$.

The experimental complex refractive index is connected to calculated dielectric constant by the equation,

$$\hat{n} = n + ik = \sqrt{\varepsilon} \tag{3.8.47}$$

3.8.17.2 Tauc determination of band gap.

The optical properties of semiconductors are characterized by the optical band gap, which is significant in solar cell applications given that it is the fundamental quantity that describes light absorption in the semiconductors. The optical band gap can be determined with the use of a Tauc plot [57] where the linear part of the function $[\alpha(E)\times E]^{\frac{1}{2}}$ against the photon energy E is extrapolated. In the function, $\alpha(E)$ represents the absorption coefficient calculated using;

$$\alpha = \frac{4\pi K}{\lambda} \tag{3.8.48}$$

Where λ represents the free space wavelength of light and K represents the extinction coefficient. K is represented as;

$$K = \frac{\sqrt{\sqrt{\varepsilon_1^{\,2} + \varepsilon_2^{\,2}} - \varepsilon_1}}{\sqrt{2}} \tag{3.8.49}$$

ε_1 and ε_2 are the variables in equation (3.8.49) representing real and imaginary parts of the dielectric function respectively.

References

[1] J. Wark, *Contem. Phys.* **37** (1996) 205.

[2] D. W. Jones, *Contemp. Phys.* **54** (2013) 287.

[3] I. A. Belio-Reyes, L. Bucio, E. Cruz-Chavez, *J Endod.* **35** (2009) 875.

[4] A. V. Radha, O. B. Miguel, S. V. Ushakov, A. Navrotsky, *J. Am. Ceram. Soc*. **92** (2009) 133.

[5] C. Gomes Silva, R. Juarez, T. Marino, R. Molinari, H. Garcia, *J. Am. Ceram. Soc*. **133** (2010) 595.

[6] J. Tauc, R. Grigorovici and A. Vancu, *Phys. Status Solidi.* **15** (1966) 627.

[7] Z. Lopez-Cabana, C. M. Torres, G. Gonzalez, *Nanoscale Res. Lett.* **6** (2011) 523.

[8] S. B. Yu, A. D. Watson, *Chem. Rev*. **99** (1999) 2353.

[9] N. A. Stelmashenko, J. P. Craven, A. M. Donald, E. M. Terentjev, B. L. Thiel, *J. Microsc*. **204** (2001) 172.

[10] N. A.Yamamoto, M. Nakano, T. Suzuki, *Surf. Interface Anal*. **38** (2006) 1725.

[11] R. F. Egerton, *Physical principles of electron microscopy.* Springer US. (2005) 125.

[12] R. G. Woolley, *Adv. Phys.* **25** (1976) 27.

[13] R. M. Martin, *Electronic structure: basic theory and practical methods*,Cambridge University Press,UK. (2004).

[14] P. R. Bunker, *J. Mol. Spectrosc.* **28** (1968) 422.

[15] B. Delley, *J. Chem. Phys.* **92** (1990) 508.

[16] J.C. Slater, *Phys. Rev.* **34** (1929) 1293.

[17] J.C. Slater, *Phys. Rev.* **81** (1951) 385.

[18] P. Hohenberg, W. Kohn, *Phys. Rev.* **136** (1964) B864.

[19] W. Kohn, L. J. Sham, *Phys. Rev.* **140** (1965) A1133.

[20] P. Giannozzi, S. Baroni, N. Bonini, M. Calandra, R. Car, C. Cavazzoni, D. Ceresoli, G. L. Chiarotti, M. Cococcioni, I. Dabo, A. Dal Corso, *J. Phys. Condens. Matter*. **21** (2009) 395502.

[21] W. Kohn, A. D. Becke, R. G. Parr, *J. Phys. Chem.* **100** (1996) 12974.

[22] J. Neugebauer, *Phys. Rep.* **489** (2010) 1.

[23] P. Hohenberg, W. Kohn, *Phys. Rev. B* **136** (1964) 864.

[24] M. Levy, *P. Natl. Acad. Sci.* **76** (1979) 6062.

[25] J. P. Perdew, A. Zunger, *Phys. Rev.* **B 23** (1981) 5048.

[26] P.A.M. Dirac, *Proc. Cambridge Phil. Roy. Soc*. **26** (1930) 376.

[27] D.M. Ceperley and B.J. Alder, *Phys. Rev. Lett.* **45** (1980) 566.

[28] L. Hedin and B.Lundqvist, *J. Phys. C.* **4** (1971) 2064.

[29] M.C. Payne, M.P. Teter, D.C Allan, T.A. Arias, J.D. Joannopoulos, *Rev. Mod. Phys.* **64** (1992) 1045.

[30] R.O. Jones and O. Gunnarson, *Rev. Mod. Phys.* **61** (1989) 689.

[31] J. P. Perdew, J. Chevary, S. Vosko, K. Jackson, M. Pederson, D. Singh, C. Fiolhais, *Phys. Rev. B* **46** (1992) 6671.

[32] J. P. Perdew, K. Burke, M. Ernzerhof, *Phys. Rev. Lett.* **77** (1996) 3865.

[33] J. P. Perdew, K. Burke, M. Ernzerhof, *Phys. Rev. Lett.* **80** (1998) 891.

[34] F. Neese. *J. Biol. Inorg. Chem.* **11** (2006) 702.

[35] H. C. Kandpal, G. H. Fecher, C. Felser, *J. Phys. D: Appl. Phys.* **40** (2007) 1507.

[36] X. Sha, B. Jackson, *Surf. Sci.* **496** (2002) 318.

[37] J. Tao, J. P. Perdew, V. N. Staroverov, G. E. Scuseria, *Phys. Rev. B.* **91** (2003) 146401.

[38] J. Heyd, J. E. Peralta, G. E. Scuseria, R. L. Martin, *J. Chem. Phys.* **123** (2005) 174101.

[39] J. Paier, M. Marsman, K. Hummer, G. Kresse, I. C. Gerber, J. G. Angyan, *J. chem. Phys*. **124** (2006) 154709.

[40] L. Hedin, *Phys. Rev*. **139** (1965) A796.

[41] F. Tran, P. Blaha, *Phys. Rev. lett.* **102** (2009) 226401.

[42] A. D. Becke, E. R. Johnson, *J. Chem. Phys.* **124** (2006) 221101.

[43] H. Monkhorst, J. Pack, *Phys. Rev. B* **13** (1976) 5188.

[44] D. Chadi, M. L. Cohen, *Phys. Rev. B* **8** (1973) 5747.

[45] N.A.W. Holzwarth, G.E. Matthews, R.B. Dunning, A.R. Tackett and Y. Zeng, *Phys. Rev. B.* **55** (1997) 2005.

[46] P. Hohenberg and W. Kohn, *Phys. Rev.* **136** (1964) B864.

[47] I.G. Austin and N.F. Mott, *Science.* **168** (1970) 71 .

[48] J.P. Perdew and A. Zunger, *Phys. Rev.* **5048** (1981) B23.

[49] B. Himmetoglu, A. Floris, S. Gironcoli, M. Cococcioni, *Int. J. Quantum Chem.* **114** (2014) 14.

[50] V.I. Anisimov, O. Gunnarsson, *Phys. Rev. B* **43** (1991) 7570.

[51] V.I. Anisimov, J. Zaanen, and O.K. Andersen, *Phys. Rev. B* **44** (1991) 943.

[52] V.I. Anisimov, I.V. Solovyev, M.A. Korotin, M.T. Czy˙zyk, and G.A. Sawatzky, *Phys. Rev. B* **48** (1993) 16929.

[53] I.V. Solovyev, P.H. Dederichs, and V.I. Anisimov, *Phys. Rev. B* **50** (1994) 16861.

[54] V.I. Anisimov, F. Aryasetiawan, A.I. Lichtenstein, *J. Phys.: Condens. Matter* **9** (1997) 767.

[55] C. Stampfl, C. G. Van de Walle, *Phys. Rev. B* **65** (2002) 155212.

[56] C. G. Van de Walle, *J. Appl. Phys.* **95** (2004) 3851.

[57] J. Tauc, *Mater, Res. Bull.* **3** (1968) 37.

Chapter 4

Effects of Cu^{2+} doping on Structural, electronic and optical properties of $ZnAl_2O_4$: A combined experimental and DFT+U study

4.1 Introduction

$ZnAl_2O_4$ belongs to the spinel class of semiconductors with a wide band gap ~3.8 eV [1]. Depending on the synthesis method, the material's crystal structure is either inverse or normal cubic spinel [2]. Spinel semiconductors are associated with a group of metal oxides whose common chemical compound is AB_2O_4 where A and B are cations with A atoms having a valence of 2 and B atoms having a valence of 3. These A and B cations occupy 12.5% of the 64 tetrahedral interstitials and 50% of the 32 octahedral interstitials respectively [3]. Spinel structures, have many advantages such as low annealing temperatures and high quantum yields [4], high mechanical resistance [5], high photoluminescence efficiency, high chemical and thermal stability, high photocatalytic activity, low surface acidity and hydrophobic behavior [6]. All these advantages make spinel semiconductors suitable for many applications such as, catalysts, electroluminescence displays, stress imaging devices, highly efficient phosphors, photo-electronic devices and optical coating [7]. Due to these vast applications lots of research has been directed towards understanding the fundamental properties of theses spinel semiconductors as well as how these properties can be enhanced. In addition, based on the above mentioned applications, several morphologies of spinel $ZnAl_2O_4$ have been investigated namely; nanotubes, nanorods and porous structures among others [8].

This material has been studied both theoretically [9,10] and experimentally [11–12]. Theoretically, using first principles calculations, the high-pressure phase transformation of $ZnAl_2O_4$ and $ZnGa_2O_4$ has also been investigated where it was observed that there is a first-order phase transition in $ZnGa_2O_4$ and $ZnAl_2O_4$ [9]. Density functional theory (DFT) combined with inelastic neutron-scattering experiments have also been used to investigate the phonon spectrum

of this material in the spinel structure[10]. Experimentally, there was no phase transition on pressure increase up to 43 GPa. [11].

Despite $ZnAl_2O_4$ attracting both theoretical and experimental investigations, the effect of doping on the optical properties of $ZnAl_2O_4$ is still an open book. Optical properties of spinel materials are known to strongly dependent mainly on the synthesis methods [13] and their anatomy [14]. Particle size is also known to have significant influence on the optical characteristics of spinel semiconductors [15]. Studies have shown that, as the size of particles approach the nano regime, differences in morphology and size distribution results in differences in the chemical and physical properties [16]. This in turn implies that the size of particle has direct influences on the surface characteristics and is also likely to affect the defect levels as well as photoluminescence characteristics of the material [15].

Doping of semiconductors with transition metal elements has been shown both experimentally [17] and theoretically [18] to have an effect on the host's mechanical, electronic and physical properties. The introduction of a dopant within the host lattice usually results in defect/dopant levels being observed within the host's band gap as well as either an improvement or a decline in optical emissions of the host [19]. The effect of a dopant on the optical properties of the host is largely dependent on the type and nature of the dopant, the dopant concentration and the presence of other defects interacting with the dopant within the host's lattice [20].

Cu^{2+} forms deep trap energy levels between valence band and conduction band (t_2 energy level of Cu^{2+}). When used as a dopant, these energy levels acts as recombination centers (luminescence centers) for the excited electron-hole pairs, resulting in strong luminescence [21]. This has been observed experimentally in the case of ZnO [22–25] as well as ZnS [21]. In the case of ZnS, Cu^{2+} was found to lead to blue and green emissions at 420 and 520 nm respectively [26]. This observed green emission peaks have been attributed to the recombination between the shallow donor level (sulphur vacancy) and the t_2 level of Cu^{2+} [21]. Although there are extensive investigations on the Cu^{2+}-doped semiconductors, the effect that Cu^{2+} has on the optical properties of spinel semiconductors still warrants an investigation.

In this study we endeavor to investigate both experimentally and theoretically within the DFT formalism with Hubbard correction, the effect of doping on the structural, electronic and optical properties of $ZnAl_2O_4$ as function of doping concentration.

4.2 Methodology

4.2.1 Experimental details

Zinc aluminate was synthesized by sol-gel technique [27] with the use of citric acid as a chelating agent as realized from earlier findings [28]. This method is advantageous in that it can speedily produce fine and homogeneous samples after the pyrolysis of the gel [29]. Stoichiometric quantities of the metal nitrates (Zn:Al=1:2) were dissolved in deionized water to achieve metal nitrate compound. The citric acid solution was acquired independently by introduction of citric acid into deionized water, such that the molar quotient of citric acid to the metal ions is 2:1. The citric acid solution was then added to the nitrate solution accompanied by constant mixing to guarantee homogeneous solution. After absolute mixing, the solution was then heated up at 70 ^oC and constantly stirred using a magnetic stirrer to evaporate the water for 3hrs. A yellowish gel was obtained. The gel was then placed in an oven at 110^oC in order to dry. The $ZnAl_2O_4$ citrate was realized in a fluffy powder form. This was grinded and calcined at 600 ^oC for 2hrs to obtain the $ZnAl_2O_4$ powder samples. The synthesis of $ZnAl_2O_4$ nanostructures with Cu^{2+} cations as dopants was performed by adding different amounts of $Cu(NO_3)_2.4H_2O$ to the $Zn(NO_3)_2.6H_2O$ and $Al(NO_3)_3.9H_2O$, to obtain concentrations of 0.31, 0.62, 0.93, 1.24 mol% Cu^{2+}.

4.2.2 Characterization techniques

The crystal structures of the powders were investigated using the Bruker AXS Discover diffractometer with Cu-Kα (1.5418 Å) radiation. High-resolution transmission electron microscope (HR-TEM) was done using the Shimadzu Superscan SSX-550 system. Scanning electron microscopy (SEM) and selected area electron diffraction (SAED) were used to determine the morphology of synthesised nanoparticles. The optical properties were obtained via the use of the Agilent HP1100 diode-array UV-visible spectrophotometer while photoluminescence (PL) spectroscopy was done using the Hitachi F-7000 fluorescence spectrometer.

4.2.3 Computational details

Ab initio calculations were done within the DFT formalism with the ad hoc Hubbard correction *U* (DFT+*U*) as implemented in the DFT code quantum ESPRESSO code [30]. Self-consistent calculations were used to solve the Kohn-Sham equations employing local density approximation (LDA) with the Hubbard *U* correction (LDA+*U*) [31] for the exchange-correlation (XC) potential. By converging the value of *U* with respect to the experimental band gap of ZnO and CuO, the values of *U* for Zn and Cu were found to be 5.0 eV and 4.0 eV respectively. Within this approach, the Hubbard U introduced is evaluated just as an empirical parameter needed to rectify the band gap [32–35]. Equilibrium properties were then obtained using; A 60 Rydberg (Ry) cut-off energy for the plane waves and a $2\times 2\times 2$ Monkhorst-Pack [36] mesh was used for the Brillouin-zone integration. The self-consistent calculations were converged to 10^{-6} Ry. The calculated equilibrium lattice constant and band gap of $ZnAl_2O_4$ were 7.09 Å and 4.0 eV compared to experimental values of 8.04 Å and 4.38 eV and theoretical values of 7.99 Å [10] for lattice constant and band gap of 3.8 eV [9].

Supercells of 112 atoms were then constructed from the optimized unit cell coordinates. Doping was done via the substitution of Zn atoms with copper, until the desired concentration was reached, and the supercell was relaxed by allowing only the ions to move keeping the volume fixed. From this, substitutional energies, thermodynamic transition levels as well as optical transitions were obtained using the methodology of [32]. Using the methodology of [37-38], we included the finite size and image charge corrections in calculating the substitutional energies at different charge states. A uniformly distributed 38 k-points dense mesh was then used to obtain the optical properties according to the formalism presented in [39-40]. Thermodynamic charge transition level can also be obtained from the plot of substitutional energies at different charge states as a function of the Fermi level position where the Fermi level is allowed to shift from the top of the valence band to the bottom of the conduction band. The transition level in this case is the point at which any two lines intersect (a schematic of this is shown in results section). In order to avoid severe dopant-dopant interactions within the crystal lattice on dopant concentration increase, we have only the next-nearest Zn^{2+} location with respect to the initial substitution in this work. Fig. 4.1 (a) and (b) show the undoped $ZnAl_2O_4$ and $ZnAl_2O_4$: Cu^{2+} supercells.

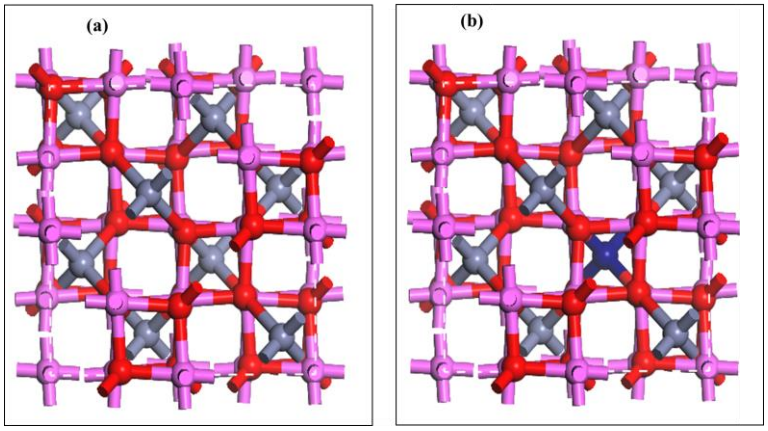

Figure 4.1 (a) Undoped $ZnAl_2O_4$ and (b) $ZnAl_2O^4$:Cu^{2+} Grey balls represent Zn atoms, red balls represent O atoms, magenta balls represent Al atoms and blue ball represent Cu^{2+} atom.

4.3 Results and discussion

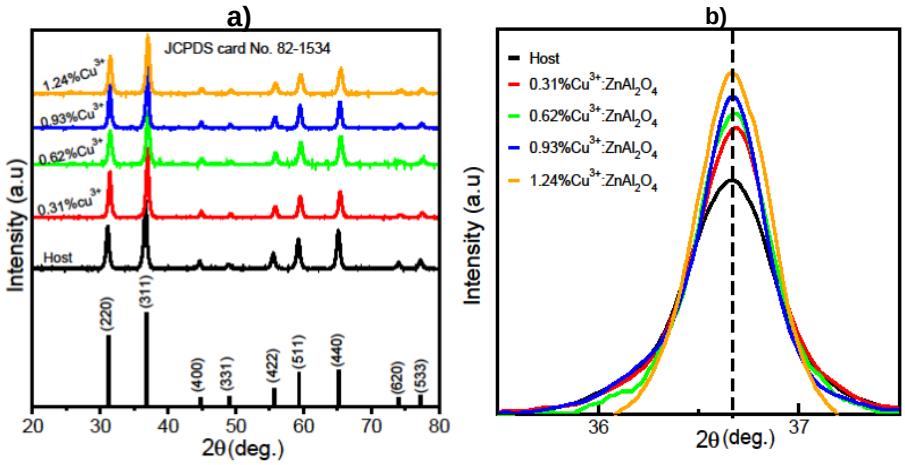

Figure 4.2 (a) XRD patterns of the Cu^{2+} $(0-1.24\ \%)$:$ZnAl_2O_4$ and (b) Gaussian fits of (311) diffraction peak.

To investigate the structure, crystal orientation, particle size and phase determination, XRD analysis was conducted on $ZnAl_2O_4$ and $ZnAl_2O_4$:Cu^{2+} samples. The observed diffraction peaks recorded in the obtained XRD patterns agrees well with those of the standard patterns of cubic $ZnAl_2O_4$ spinel, JCPDS card No.82-1534. $ZnAl_2O_4$ has a normal spinel crystal structure with the space group Fd3m. The diffraction peaks can be classified as (220), (311), (400), (331), (422), (511), (440), (620) and (533) diffraction lines. Energy dispersive X-rays (EDS) investigation revealed the occurance of Zn and Al in the 1:2 mole ratio ascertaining the formation of single-phase $ZnAl_2O_4$ nanoparticles. The ratio of the peak intensity of prepared samples to the standard peak intensity is constant. There was no peak pattern due to aluminum or zinc oxides or other phases observed in the XRD report indicating that Cu^{2+} ions were incorporated in $ZnAl_2O_4$ lattice. The XRD peaks pattern realized agreed well with the spinel structure findings of [41]. From Figure 4.2 (b), the Gaussian fits of the diffraction peak with highest intensity (311) positions shifted slightly towards the higher angles on Cu^{2+} percentage concentration increase.

This slight shift was attributed to the small lattice strain caused when Cu^{2+} is substitutes in Zn^{2+} at a lattice site, given that there is no significant difference between the ionic radii of Cu^{2+} (0.73 Å) and Zn^{2+} (0.74 Å). From the ionic radii, it is clear that substituting Zn^{2+} with Cu^{2+} will not cause significant lattice distortion. This was consistent with the calculated *ab initio* results shown in Table 4.1.

Table 4.1: Calculated averaged Mulliken bond lengths of the $ZnAl_2O_4$:x% Cu^{2+} $(0 \leq x \leq 1.24\ \%)$

	0%	0.31%	**0.**62%	0.93**%**	1.24**%**
Zn-O	1.95	1.95	1.95	1.95	1.95
Al-O	1.91	1.91	1.91	1.91	1.91
Cu^{2+}-O	-	1.94	1.94	1.94	1.94

The mean crystallite size of the compound is evaluated based on the line broadening of the (311) peak using Debye-Scherer equation:

$$D_{(hkl)} = \frac{0.9\lambda}{\beta_{\frac{1}{2}} \cos\theta} \qquad (4.2.1)$$

where $D_{(hkl)}$ = mean particle size of the crystal, λ = wavelength of incident X-ray, θ = corresponding Bragg angle, $\beta_{\frac{1}{2}}$ = full width at the half maximum height (FWHM) of the peak.

Table 4.2 presents calculations obtained from XRD pattern. The lattice constant was calculated using the equation;

$$a = d_{hkl}\sqrt{h^2 + k^2 + l^2} \qquad (4.2.2)$$

where a = lattice constant, d_{hkl} = inter-planar distance and *h*, *k* and *l* are the miller indices of the planes. From the SAED pattern, we realized that $ZnAl_2O_4$ nanoparticles have inter-planar spacing of 2.823 Å, 2.416 Å, 2.020 Å, 1.632 Å, 1.553 Å and 1.420 Å corresponding to the planes

(220), (311), (400), (422), (511) and (440), respectively. Further analysis on the highest intensity peak (311) revealed that the inter-planar spacing was 2.424 Å, 2.422 Å, 2.420 Å, 2.418 Å and 2.416 Å for the 0%Cu^{2+}, 0.31%Cu^{2+}, 0.62%Cu^{2+}, 0.93%Cu^{2+} and 1.24%Cu^{2+} respectively. This caused a reduction in lattice constant as the defect percentage is increased as shown in Table 4.2.

Table 4.2: Analyzed XRD pattern corresponding to 2θ at 36.834

Concentration	Lattice constant a_o (Å)	2θ	FWHM(β)	Size (nm)
Host	8.039	36.834	0.6271	14.0
0.31%Cu^{2+}	8.033	36.835	0.6272	13.9
0.62%Cu^{2+}	8.026	36.837	0.6272	13.9
0.93%Cu^{2+}	8.019	36.839	0.6272	13.9
1.24%Cu^{2+}	8.013	36.841	0.6271	14.0

From Table 4.2, it can be seen that from the (311) diffraction peaks, there is no significant broadening of the peaks, meaning that the crystallite sizes almost remained constant.

4.3.1 Morphological studies

Figure 4.3 shows the SEM micrographs of the $ZnAl_2O_4$ and $ZnAl_2O_4$: Cu^{2+} phosphor calcined at 600 ^oC for 2 hrs. From Figure 4.3, it is clear that phosphor synthesized by the sol-gel technique reveals uniform, distributive and spherical morphology. Phosphor nanoparticles with uniform size are therefore important in production of highly efficient and uniform luminescence [42]. This is because as mentioned earlier, size and size rationing has a direct influence on the luminescent characteristics of a phosphor. Smaller nanoparticles have a tendency to possess extra surface luminous states occurring from their magnified surface/bulk volume quotient. This shows that finer nanoparticles have better luminescent characteristics compared to the sizable particles [43,44].

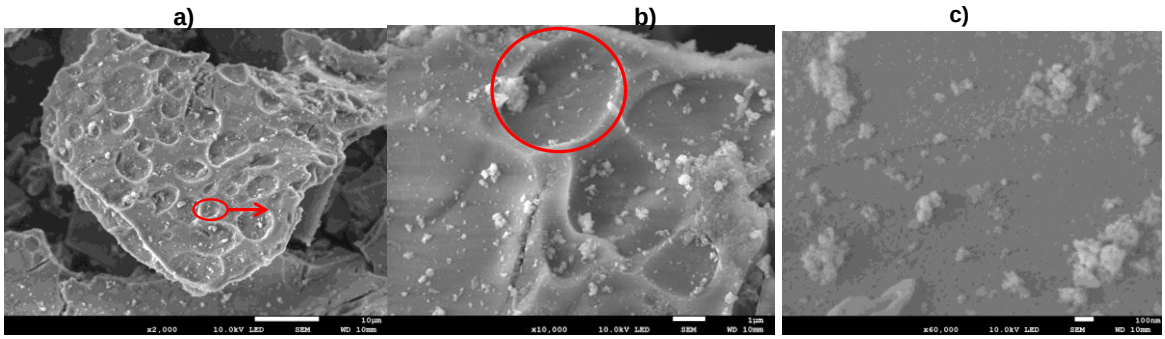

Figure 4.3 SEM micrographs of $ZnAl_2O_4:Cu^{2+}$ (a) × 2000 (b) × 10000 (c) × 60000 magnifications.

Figure 4.3 (c) shows existence of angular particles composed of very small crystals. The average particle size is about 40.00 nm. Apart from angular crystals, the powders show porous structures. The identified portion in Figure 4.3 (a) is magnified to obtain the identified part in Figure 4.3 (b). This shows that the samples are highly porous.

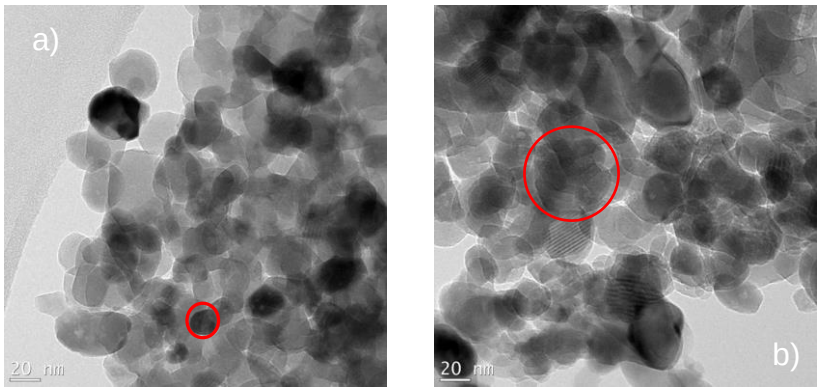

Figure 4.4 TEM micrographs of (a) $ZnAl_2O_4$ and (b) $ZnAl_2O_4$:1.24%Cu^{2+}.

Figure 4.4, exhibits the HR-TEM micrograph of the sol-gel synthesized samples. The Figure indicates that these particles of nano size are comparably spherical. HR-TEM (Figure 4.4) showed that the crystallite sizes (in nm-scale) and particle agglomeration is influenced by the Cu^{2+} concentration percentage. The average estimated crystallite size from Figure 4.4 in both host and doped HR-TEM images is around 14.05 nm. This is consistent to what was observed in

the XRD line broadening calculations. The host particles are slightly dispersed from each other while in the doped system, sticking of particles to one another is witnessed in Figure 4.4(b) which is due to the slight distortion on substituting Cu^{2+} (ionic radius 0.73 Å) in Zn^{2+} (ionic radius 0.74 Å) site. As can be seen in Figure 4.4, the particle distribution of undoped $ZnAl_2O_4$ is non agglomerated while that of $ZnAl_2O_4$: Cu^{2+} is agglomerated.

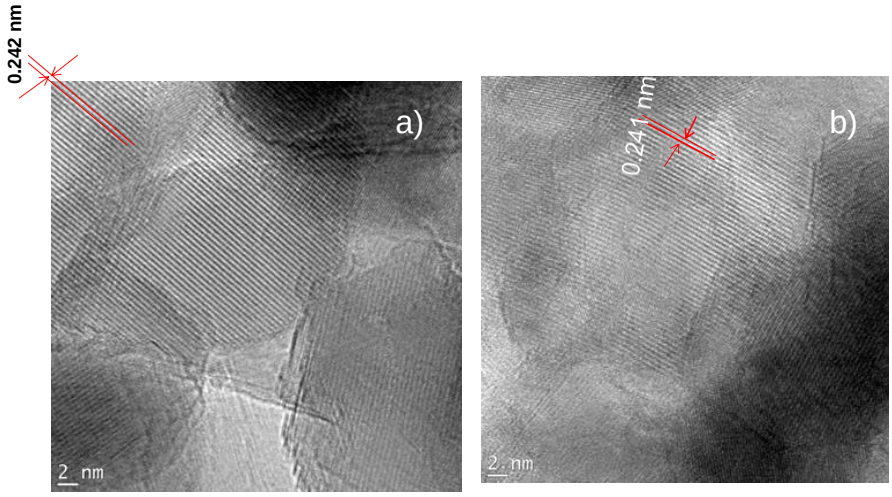

Figure 4.5 The lattice fringes of (a) $ZnAl_2O_4$ (b) $ZnAl_2O_4$:1.24%Cu^{2+}

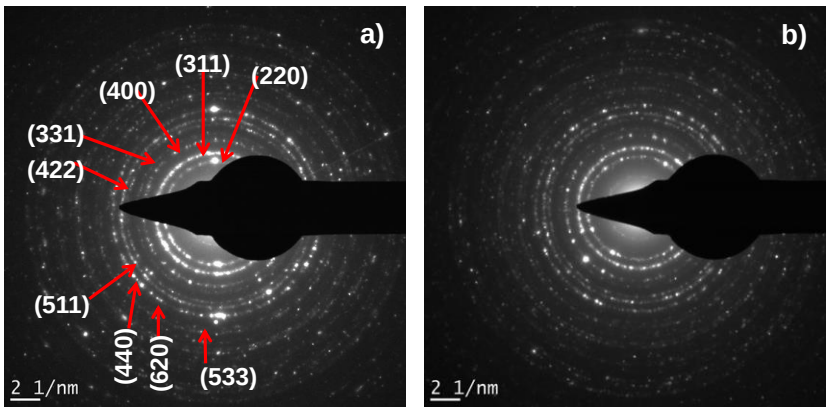

Figure 4.6 Selected area electron diffraction of (a) $ZnAl_2O_4$ (b) $ZnAl_2O4$:1.24%Cu^{2+}

Figure 4.5 (a) shows the interplanar distance of pristine $ZnAl_2O_4$ to be 2.42 Å while Figure 4.5 (b) shows the reduction of the interplanar distance to 2.41 Å of introduction of Cu^{2+} in the $ZnAl_2O_4$ crystal lattice. This reduction in interplanar distance means a reduction in the lattice constant as presented in Table 4.2. Figure 4.6 (a) shows the (hkl) miller indices of $ZnAl_2O_4$. The diameter of the diffraction rings which was arrived at by use of imageJ program was found to be directly proportional to $\sqrt{h^2 + k^2 + l^2}$. It is from this relationship that we were able to label the diffraction rings as shown in Figure 4.6 (a). Figure 4.6 (b) shows diffuse diffraction spots compared to Figure 4.6 (a). These diffraction spots mean that there was lattice strain on introduction of a dopant. They also show that there was reduction in the interplanar distance as explained before (Figure 4.5 (b)).

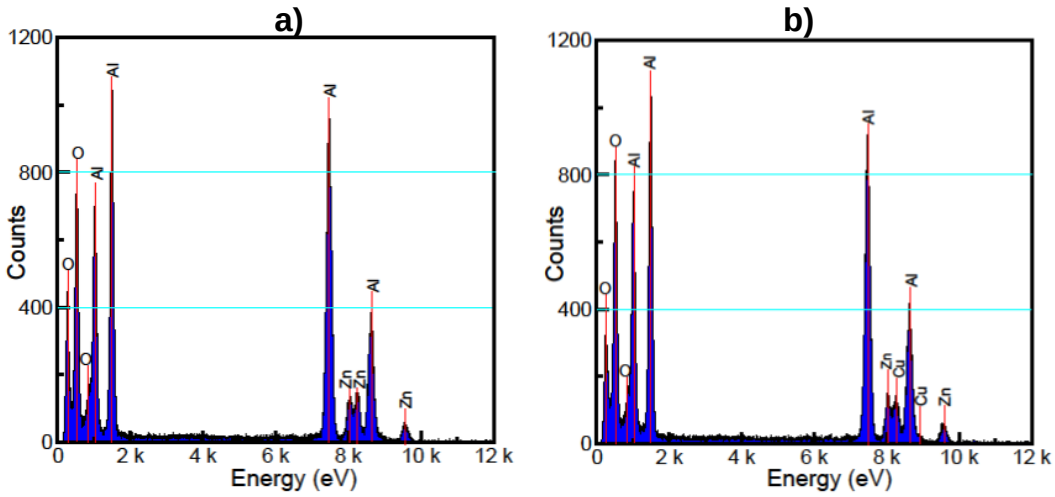

Figure 4.7 EDS spectra of (a) $ZnAl_2O_4$ (b) $ZnAl_2O_4$:Cu^{2+}

Figure 4.7: shows the EDS spectra of $ZnAl_2O_4$ and $ZnAl_2O_4$:Cu^{2+} with the peaks corresponding to Zn, Al, O in pristine $ZnAl_2O_4$ and peaks corresponding to Zn, Al, O and Cu in $ZnAl_2O_4$:Cu^{2+} The estimated percentage of Cu, Zn, Al and O corresponds well with the quantities of Cu, Zn, Al and O used in respective precursors. The results show that the sol-gel technique is very successful as no depletion of elements arose during the synthesis. An O characteristic peak appeared at 0.25, 0.5 and 0.75 KeV while that of Zn appeared at 8.3, 8.5 and 9.5 KeV, and Al at 1.0, 1.5, 7.5 and 8.7 KeV. The Cu^{2+} peak was observed at 8.3 and 8.9 KeV for the doped system.

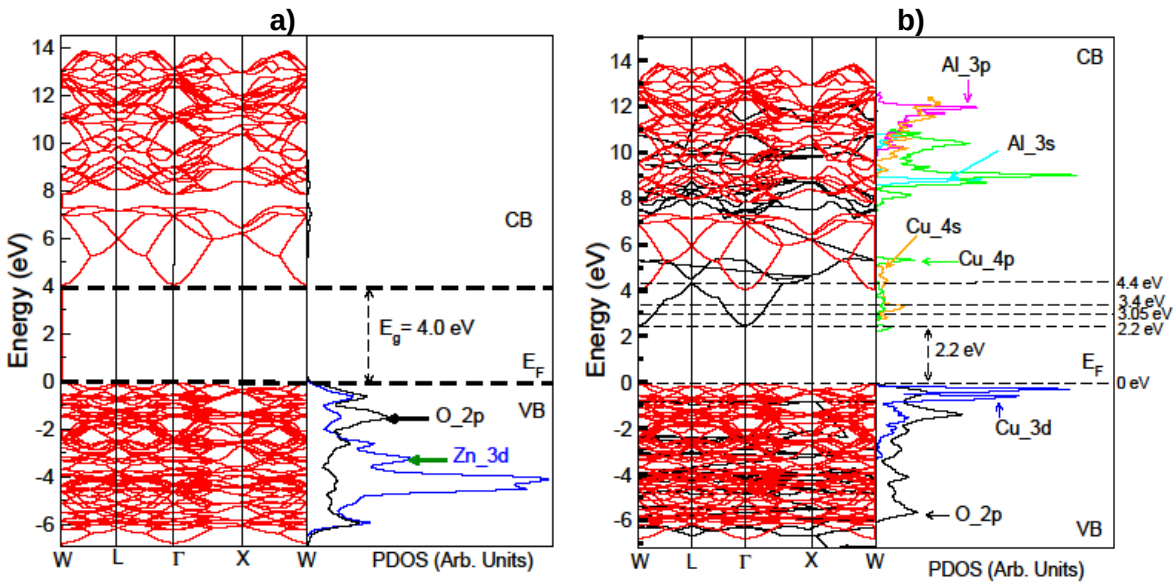

Figure 4.8 Band structure and PDOS of (a) pristine $ZnAl_2O_4$, (b) 1.24% $ZnAl_2O_4$: Cu^{2+}

Theoretically, upon optimizing the unit cell of $ZnAl_2O_4$ and using the Murnaghan's equation of state (EOS) [45], the equilibrium lattice constant was found to be 7.09 Å which corresponds to the experimental lattice constant of 8.039 Å reported in Table 4.2 [46]. Suppose a semiconductor with a direct band gap, at the band edge, the absorption coefficient is obtained by use of equation (4.3.1);

$$\alpha = \frac{A}{h\nu}\left(h\nu - E_g\right)^{\frac{1}{2}} \qquad (4.3.1)$$

Where α = absorption coefficient, $h\nu$ = photon energy, E_g = energy gap and A = a constant determined by the type of transition. For any photon energy, equation (4.3.1) can be rearranged to;

$$(\alpha h\nu)^2 = A^2(h\nu - E_g) \qquad (4.3.2)$$

From equation (4.3.2), the band gap can be obtained by plotting $(\alpha h\nu)^2$ as a function of $h\nu$ and determining the intercept on the $h\nu$ axis by extrapolating the linear part of the plot to $(\alpha h\nu)^2 = 0$

as shown in figure 4.12 (c). Figure 4.12 (c) agrees well with the transition in Figure 4.8 which is a direct band gap model at Γ giving an effective band gap of 2.2 eV. According to the electronic configurations, of the elements involved, Cu_4p as well as Cu_4s orbitals are found in the conduction band while Cu_3d orbital makes a filled valence band. The expected transition is therefore from Cu_3d to Cu_4p or from Cu_3d to Cu_4s.

4.3.2 Substitutional energies and thermodynamic charge transitions

In order to determine how easy it is to incorporate the dopant into the host lattice, we calculated *ab initio*, the defect substitutional energies at different charge states. The computed substitutional energies at different defect states are shown in Table 3. From the calculated substitutional energies it can be seen that it is possible to easily dope $ZnAl_2O_4$ with Cu^{2+} as there substitutional/formation energies are sufficiently low especially for one (1) and two (2) atom substitutions.

Table 4.3: Calculated substitutional energies (eV) of doped $ZnAl_2O_4$ at different defect states in different charge states. ε^{therm} is the thermodynamic transition level, E_{PL} is the calculated PL energy, λ_{PL} is the emission wavelength and E_{rel} is the Frank-Condon shift.

	Charge state					ε^{therm}	E_{PL} (eV)	λ_{PL} (nm)	E_{rel}
	-2	-1	0	+1	+2	(-2/-1)	(-2/-1)	(-2/-1)	
O_{vac}	-7.01	-7.07	-7.14	-7.19	-7.24	0.91	2.96	418.92	0.13
Cu_{zn}	1.09	1.03	0.98	0.92	0.86	0.95	2.94	421.77	0.11
$Cu_{zn}+O_{vac}$	-4.11	-4.18	-4.23	-4.29	-4.33	1.02	2.85	435.09	0.13
Binding energy	-1.81	-1.86	-1.93	-1.98	-2.05				

From Table 4.3 it can be seen that both oxygen vacancy O_{vac} as well as Cu_{Zn}+O_{vac} defect complex (pair) spontaneously forms in $ZnAl_2O_4$ because they had negative formation energies. Only Cu_{Zn} had positive formation energy although this was also very low. We then calculated the binding energy of the defect complex. The binding energy can be obtained as $E_B = E^f_{O_{vac}} + E^f_{Cu_{Zn}} - E^f_{Cu_{Zn}-O_{vac}}$ where, E_B is the binding energy, $E^f_{O_{vac}}$, $E^f_{Cu_{Zn}}$ and $E^f_{Cu_{Zn}-O_{vac}}$ are the calculated substitutional/formation energies of defects. The calculated binding energies were negative indicating that the Cu_{Zn}+O_{vac} defect complex cannot form with $ZnAl_2O_4$ and that these two point defects exist individually within the lattice. This implies that it is possible to experimentally observe distinctive emission peaks associated with O_{vac} and Cu_{Zn} alone with no peaks associated with Cu_{Zn}+O_{vac}. This is confirmed from the emission spectra in Figure 4.11a) and b) where some peaks were deduced as occurring as a result of either O_{vac} or Cu_{Zn}. On plotting the substitutional energy as function of the Fermi level position (i.e. Fermi level position shifts from the VBM to CBM), it is evident, from Figure 4.9, that the -1/-2 transition level was the one that was found to be the closest to conduction band. The values of this level for all the defects are also presented in Table 4.3. These thermodynamic transition levels can be compared to experimentally observed defect levels obtained via the use of Deep level transient spectroscopy [47,48]. Each of thermodynamic transition levels usually has an associated optical transition. We then calculated the associated optical transition using

$$E_{PL} = E_g - \varepsilon^{therm}(-2/-1) - E_{rel} \quad (4.3.3)$$

where, E_{PL} is the optical transition, E_g is the band gap energy, $\varepsilon^{therm}(-2/-1)$ is thermodynamic transition level (-1 and -2 charge sates have just been used to illustrate how the calculation is done). E_{rel} is the lattice relaxation energy (the Frank-Condon shift). The obtained PL energies and wavelengths are presented in Table 4.3. From the calculated PL energies and wavelengths, we found that Cu^{2+} doping led to blue luminescence in $ZnAl_2O_4$ implying that Cu^{2+} doped $ZnAl_2O_4$ can be used as a blue pigment ceramic. A schematic

representation of the optical transition is presented in Figure 4.10. The Cu^{2+} doped $ZnAl_2O_4$ production of blue emission at 435 nm (see Figure 10) agrees well with the findings of [49]. The blue emission is ascribed to the spin-orbit splitting of the Cu^{2+} d^9 state into $^2D_{5/2}$ and $^2D_{3/2}$ states and oxygen vacancies.

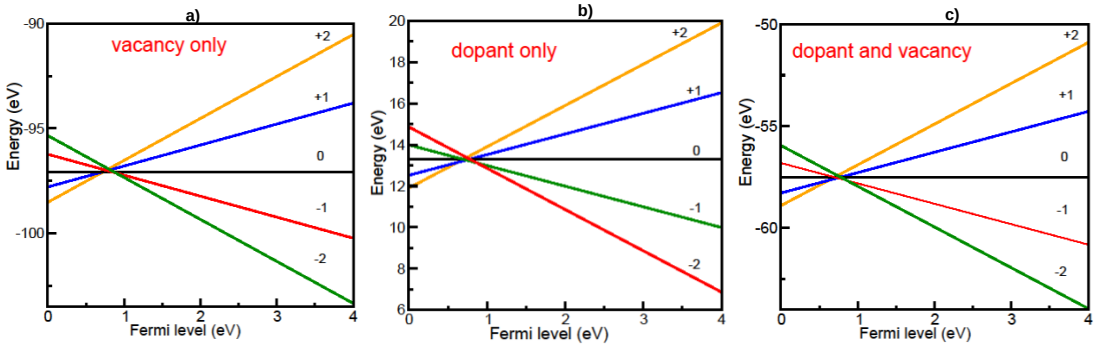

Figure 4.9 Calculated thermodynamic transition levels for ZnAl2O4: Cu2+at different dopant concentrations.

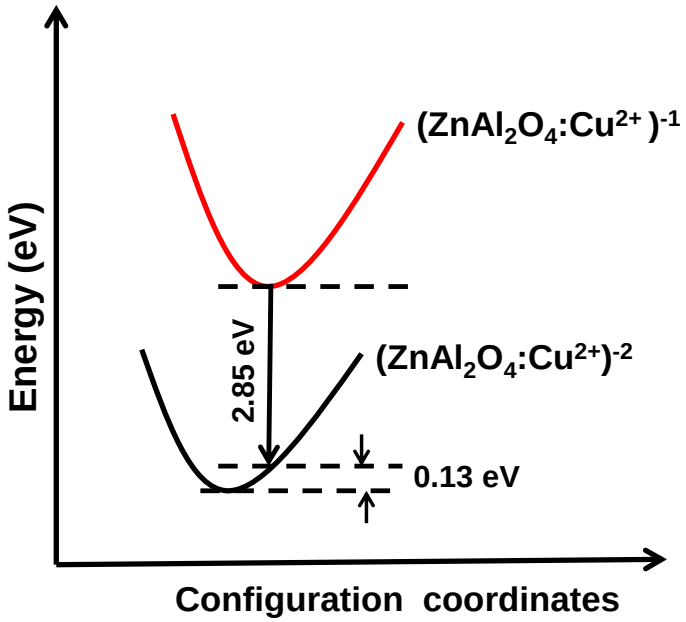

Figure 4.10 Calculated configuration coordinate diagram for Cu2+ doped ZnAl2O4 showing the PL emission energy for exchanging an electron in the conduction band for one atom substitution.

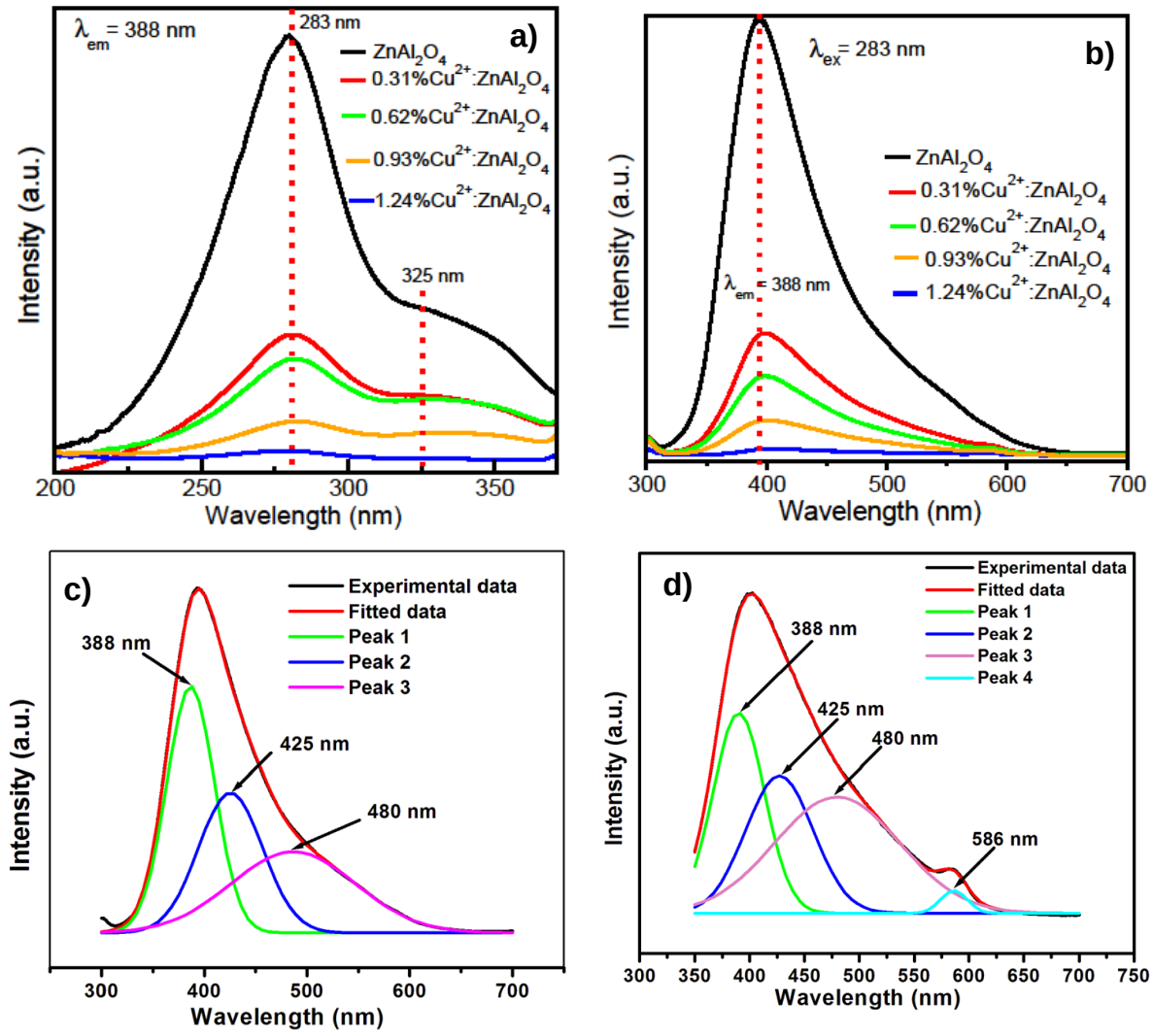

Figure 4.11 PL (a) optical absorption spectra of the undoped and different % of ZnAl2O4:Cu2+ (b) emission spectra for ZnAl2O4 and ZnAl2O4:Cu2+$^{(0-1.24\ \%)}$ phosphor (c) Deconvoluted experimental curve (pristine) (d) Deconvoluted 1.24%Cu2+:ZnAl2O4 spectrum.

Photoluminescence spectroscopy is a useful tool for the investigation of the excited electron-hole pairs recombination phenomena in semiconductors. It is used in determining transitions related to defects in a semiconductor [50]. Defects densities depend on formation procedures, morphology and size of the crystallites. From Figure 4.12 (b), the $ZnAl_2O_4$ band gap (absorption

energy) was determined along with the relative energetic positions of inter-band gap defect states. This absorption energy, that is 4.38 eV (283 nm) was used to get the emission spectra in Figure 4.11 (b). Monitoring the excitation spectra at 388 nm emission, it was observed that there was a highest intensity peak at 283 nm as shown in Figure 4.11 (a). This peak can be attributed to the elementary band-to-band electron transition within filled O_2p orbitals and empty Al_3s orbitals, with possibility of few Al_3p wave functions incorporated as has been previously proposed for pure $ZnAl_2O_4$ [2]. This phenomenon has also been confirmed computationally in Figure 4.8, where the valence band was completely occupied O_2p orbitals while the conduction band had empty orbitals. In Figure 4.11 (a), a shoulder at 325 nm is also observed in the excitation spectra. The shoulder is related to electronic excitation between occupied O_2p and unoccupied Zn_4s orbitals and is known to depend heavily on the spinel's intrinsic characteristics (mostly spinel defects). For transition metal doped oxides, the optical response is usually explained by the charge transfer shift or transition within multiplet stages of 3d electrons [51]. The reduction in intensities with increase in dopant concentration (Figure 4.11 (a) and (b)) is due to non-radiative recombination. This non-radiative recombination process takes place when some defects acts as traps that is, the excess free electrons produced on doping, generates a non-radiative channel and in this channel the energy released on recombination is absorbed by a number of electrons. The reduction in luminescence intensity can also be as a result of particle agglomeration witnessed when we compared doped and undoped systems in Figure 4.4. In principle, a reverse mechanism can take place (de-excitation transition), where an electron is transferred from a metal ion to a ligand [52-53]. The emission spectra of undoped $ZnAl_2O_4$ as well as $ZnAl_2O_4$:Cu^{2+} samples are wide and were thus deconvoluted (see Figure 4.11 (c) and (d)). In Figure 4.11 c), there are Gaussian peaks at 388 nm (3.19 eV), 425 nm (2.91 eV) and 480 nm (2.58 eV) in the case of undoped $ZnAl_2O_4$. Since the band gap of $ZnAl_2O_4$ is 4.38 eV, these peaks can be ascribed to intra-band gap defects for example oxygen vacancies which give donor levels near the oxide's conduction band edge [54]. In the undoped system, electron transition took place from valence band maximum (VBM) into the oxygen vacancy energy level (intra-band gap defects) before transiting from this level to the conduction band (CB). Due to vibrational relaxation, this electron loses energy and drops back to the intra-band gap defects and consequently dropping back to the VBM. It then goes through radiative recombination with a

hole in the VBM at the same time emitting blue light. Figure 4.11 d) shows the deconvoluted spectra of $ZnAl_2O_4:Cu^{2+}$ where peaks at 388 nm, 425 nm and 480 nm and 586 nm were observed. The additional peak at 586 nm is associated with Cu^{2+} as a luminescent centre. This type of emission from Cu^{2+} was also realized by Tongtong Xuan *et al* [55] where doping CdS with Cu^{2+} caused a red shift from 563 nm to 586 nm (undoped and doped CdS respectively). The peak at 586 nm (2.1 eV) corresponds to the Cu_4p states at 2.2 eV in the band gap of $ZnAl_2O_4$ as seen in Figure 4.8 (b).

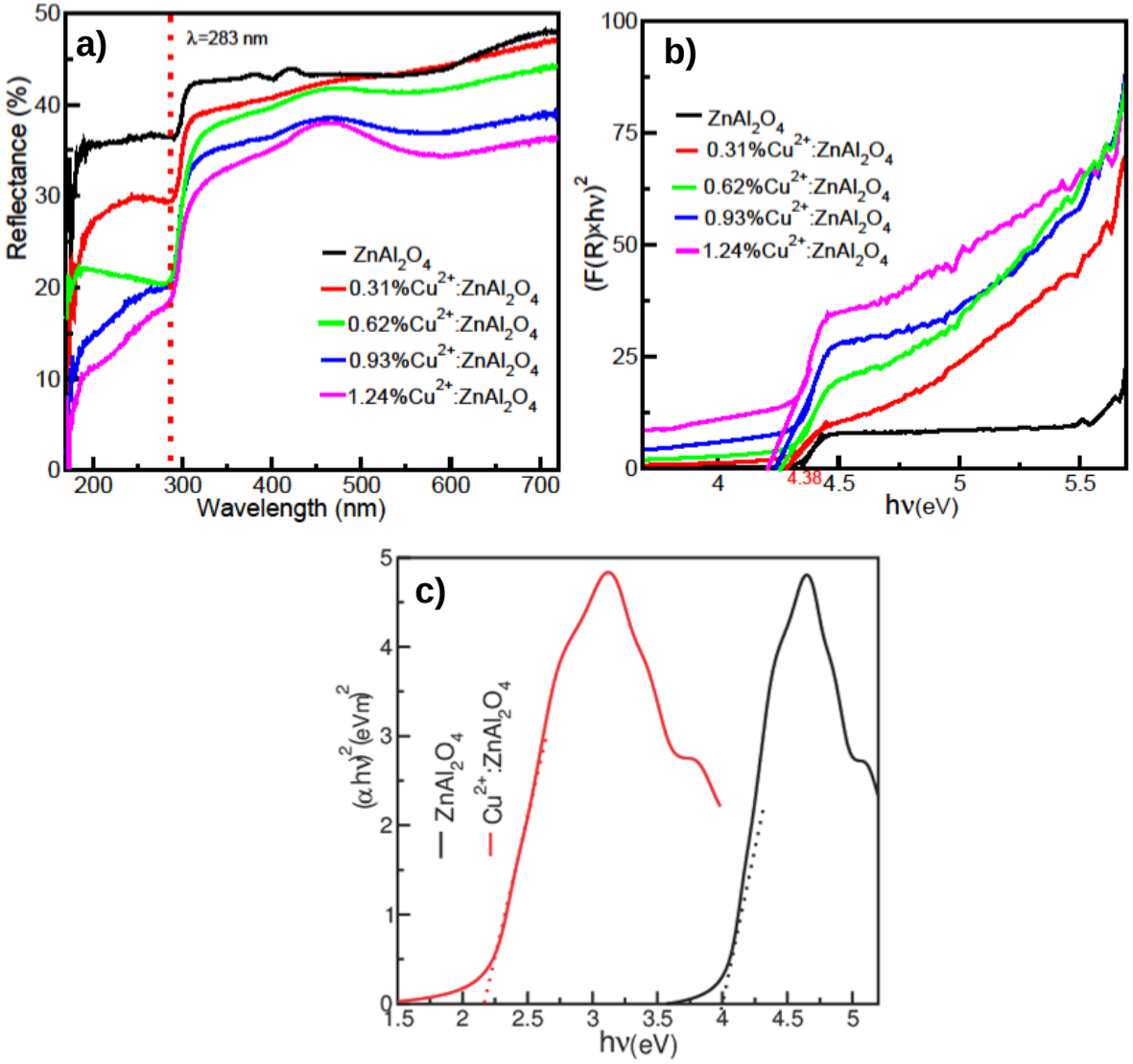

Figure 4.12 (a) Reflectance spectrum of host ZnAl2O4: (b)Kubelka-Munk plot and band gap energy estimation for host ZnAl2O4. (c) DFT Tauc determination of band gap.

Figure 4.12 (a) shows the UV-vis diffuse reflectance spectra of $ZnAl_2O_4$ samples at 283 nm. The information which can be extracted from the UV-visible spectra is the band gap energy, which is arrived at by extrapolating the linear portion of Figure 4.12 b), and the point of intersection with the x-axis gives us the value of the band gap. Upon doping, the electrons were not excited directly to the conduction band minimum since oxygen vacancies as well as empty Cu^{2+} s and p states capture the electrons. This shows that oxygen defects as well as sub-band states of Cu^{2+} are accountable for the slight decrease of effective band gap of $ZnAl_2O_4$ as confirmed in Figure 4.8. The red shift realized in $ZnAl_2O_4$ band gap upon Cu^{2+} introduction and shifting of absorption edge are commanded by the nanoparticle's surface, lattice strain and oxygen vacancies [56]. Given that $ZnAl_2O_4$ is regarded as a semiconductor with a direct band gap, the band gap size of the powders were approximated from plots of $(\alpha hv)^2$ as a function of hv , that is the kubelka-Munk relation [57]. This was presented in Figure 4.12 (b) where h = planks constant, α = Kubelka-Munk (K-M) absorption coefficient, and v = frequency. The straight potions realized from the plots are extrapolated up to the hv axis in order to acquire the size of band gap at different doping concentrations, giving the host band gap at 4.38 eV (283 nm). It was noted that, there was very small changed in the band gap, owing to the fact that the crystallite size of the samples did not change much as was shown in Table 2. This is in agreement with [58] where a band gap of 4.11 eV was obtained. It is worth noting that the excitation peak observed at 283 (UV region) was as a result of the elementary band-to-band electron excitations and it corresponds to the band gap of the analyzed powders.

4.4 Conclusions

Experimental characterization and theoretical calculations were used to study the properties of $ZnAl_2O_4$ and $ZnAl_2O_4$:Cu^{2+}. Structural characterization shows a cubic spinel structure without phase segregation. Both experiment and ab *initio* calculation show small lattice distortion for the doped structure which is attributed to the similarity of ionic radii of Cu^{2+} and Zn^{2+} ions. The introduction of Cu^{2+} in the host did not affect its structure. Theoretical calculation show that the

doped spinel emits blue light (435 nm), while experimental result indicate that it emits in the blue region (at 425 and 480 nm). DFT+*U* results were consistent with the experimental findings on both the structural and optical properties of $ZnAl_2O_4$:Cu^{2+} with the Tauc's transition energy relating very well with that in the electronic structure calculations. HR-TEM and XRD confirmed the cubic structure of $ZnAl_2O_4$ and the crystallite size of the samples. Non-radiative relaxations which were due to the new defect sites in the host gave rise to concentration quenching in PL results.

References

[1] R.F. Martins, O.A. Serra, J. Braz, *Chem. Soc*. **21** (2010) 1395.

[2] S.K. Sampath, J.F. Cordaro, *J. Am. Ceram. Soc*. **81** (1998) 649.

[3] J. Popović, B. Gržeta, B. Rakvin, E. Tkalčec, M. Vrankić, S. Kurajica, *J. Alloys Compd.* **509** (2011) 8487.

[4] Y. Yang, X.W. Sun, B.K. Tay, J.X. Wang, Z.L. Dong, H.M. Fan, *Adv. Mater.* **19** (2007) 1839.

[5] S. Mathur, M. Veith, M. Haas, H. Shen, N. Lecerf, V. Huch, S. Hüfner, R. Haberkorn, H.P. Beck, M. Jilavi, *J. Am. Ceram. Soc*. **84** (2001) 1921.

[6] J. Wrzyszcz, M. Zawadzki, J. Trawczyński, H. Grabowska, W. Miśta, *Appl. Catal. A Gen.* **210** (2001) 263.

[7] K. Kumar, K. Ramamoorthy, P.M. Koinkar, R. Chandramohan, K. Sankaranarayanan, *J. Nanoparticle Res.* **9** (2007) 331.

[8] X. Li, Z. Zhu, Q. Zhao, L. Wang, *J. Hazard. Mater.* **186** (2011) 2089.

[9] S. López, A.H. Romero, P. Rodriguez-Hernandez, A. Munoz, *Phys. Rev. B Condens. Matter Mater. Phys.* **79** (2009) 214103.

[10] C.M. Fang, C.-K. Loong, G.A. de Wijs, others, *Phys. Rev. B* **66** (2002) 144301.

[11] D. Levy, A. Pavese, A. Sani, V. Pischedda, *Phys. Chem. Miner.* **28** (2001) 612.

[12] H.J. Reichmann, S.D. Jacobsen, *Am. Mineral.* **91** (2006) 1049.

[13] J.L. Wilson, P. Poddar, N.A. Frey, H. Srikanth, K. Mohomed, J.P. Harmon, S. Kotha, J. Wachsmuth, *J. Appl. Phys.* **95** (2004) 1439.

[14] M. Fernandez-Garcia, A. Martinez-Arias, J. C. Hanson, J. A. Rodriguez, *Chem. Rev.*

104(9) (2004) 4063.

[15] Z.Q. Yu, C. Li, N. Zhang, *J. Lumin.* **99** (2002) 29.

[16] L. Wischmeier, T. Voss, I. Rückmann, J. Gutowski, A.C. Mofor, A. Bakin, A. Waag, *Phys. Rev. B* **74** (2006) 195333.

[17] L.D. DeLoach, R.H. Page, G.D. Wilke, S.A. Payne, W.F. Krupke, IEEE, *J. Quantum Electron.* **32** (1996) 885.

[18] M. D Segall, P. J. Lindan, M. A. Probert, C. J. Pickard, P. J. Hasnip, S. J. Clark, M. C. Payne, *J. Phys. Condens. Matter* **14** (2002) 2717.

[19] H.M. Yadav, S. V. Otari, V.B. Koli, S.S. Mali, C.K. Hong, S.H. Pawar, S.D. Delekar, *J. Photochem. Photobiol. A Chem.* **280** (2014) 32.

[20] W. Chen, J.Z. Zhang, A.G. Joly, *J. Nanosci. Nanotechnol.* **4** (2004) 919.

[21] A.A. Khosravi, M. Kundu, L. Jatwa, S.K. Deshpande, U.A. Bhagwat, M. Sastry, S.K. Kulkarni, *Appl. Phys. Lett.* **67** (1995) 2702.

[22] R. Elilarassi, G. Chandrasekaran, *J. Mater. Sci. Mater. Electron.* **21** (2010) 1168.

[23] L. Ma, S. Ma, H. Chen, X. Ai, X. Huang, *Appl. Surf. Sci.* **257** (2011) 10036.

[24] Y. Chen, X.L. Xu, G.H. Zhang, H. Xue, S.Y. Ma, *Phys. B Condens. Matter* **404** (2009) 3645.

[25] M. Caglar, F. Yakuphanoglu, *Appl. Surf. Sci*. **258** (2012) 3039.

[26] S. Lee, D. Song, D. Kim, J. Lee, S. Kim, I.Y. Park, Y.D. Choi, *Mater. Lett.* **58(3)** (2004) 342.

[27] N. Bayal, P. Jeevanandam, *J. Alloys Compd.* **516** (2012) 27.

[28] H. Liu, Z. Zhang, Z. Gong, Y. Yang, *Solid State Ionics* **166** (2004) 317.

[29] X.L. Duan, D.R. Yuan, L.H. Wang, F.P. Yu, X.F. Cheng, Z.Q. Liu, S.S. Yan, *J. Cryst. Growth* **296** (2006) 234.

[30] P. Giannozzi, S. Baroni, N. Bonini, M. Calandra, R. Car, C. Cavazzoni, D. Ceresoli, G.L. Chiarotti, M. Cococcioni, I. Dabo, others, *J. Phys. Condens. Matter* **21** (2009) 395502.

[31] A.G. Petukhov, I.I. Mazin, L. Chioncel, A.I. Lichtenstein, *Phys. Rev. B* **67** (2003) 153106.

[32] W.M. Mulwa, C.N.M. Ouma, M.O. Onani, F.B. Dejene, *J. Solid State Chem.* **237** (2016) 129.

[33] A. Janotti, D. Segev, C. Van de Walle, *Phys. Rev. B* **74** (2006) 045202.

[34] A. Calzolari, A. Ruini, A. Catellani, *J. Am. Chem. Soc.* **133** (2011) 5893.

[35] A. Calzolari, M.B. Nardelli, *Sci. Rep.* **3** (2013).

[36] H.J. Monkhorst, J.D. Pack, *Phys. Rev. B* **13** (1976) 5188.

[37] C. Freysoldt, J. Neugebauer, C.G. Van de Walle, *Phys. Status Solidi* **248** (2011) 1067.

[38] C. Freysoldt, J. Neugebauer, C. Van de Walle, *Phys. Rev. Lett.* **102** (2009) 016402.

[39] J. Sun, H.-T. Wang, J. He, Y. Tian, *Phys. Rev. B* **71** (2005) 125132.

[40] P. Nath, S. Chowdhury, D. Sanyal, D. Jana, *Carbon.* **73** (2014) 275.

[41] M. Zawadzki, W. Staszak, F.E. López-Suárez, M.J. Illán-Gómez, A. Bueno-López, *Appl. Catal. A Gen.* **371** (2009) 92.

[42] J. G. Li, X. Li, X. Sun, T. Ishigaki, *J. Phys. Chem. C* **112** (2008) 11707.

[43] I. Yu, *Mater. Res. Bull.* **41** (2006) 1403.

[44] S. H. Shin, J. H. Kang, D. Y. Jeon, D. S. Zang, *J. Solid State Chem.* **178** (2005) 2205.

[45] F. D. Murnaghan, *Proc. Natl. Acad. Sci. U. S. A.* **30** (1944) 244.

[46] M. Zawadzki, *Solid State Sci.* **8** (2006) 14.

[47] C.G. Van de Walle, *J. Appl. Phys*. **95** (2004) 3851.

[48] D. V. Lang, *J. Appl. Phys.* **45** (1974) 3023.

[49] R. Viswanatha, S. Chakraborty, S. Basu, D.D. Sarma, *J. Phys. Chem. B* **110** (2006) 22310.

[50] T. Schmidt, K. Lischka, W. Zulehner, *Phys. Rev. B* **45** (1992) 8989.

[51] K. Izumi, S. Miyazaki, S. Yoshida, T. Mizokawa, E. Hanamura, *Phys. Rev. B* **76** (2007) 75111.

[52] L. Prodi, F. Bolletta, M. Montalti, N. Zaccheroni, *Coord. Chem. Rev.* **205** (2000) 59.

[53] S. Clement, S. Mohammed Aly, D. Fortin, L. Guyard, M. Knorr, A.S. Abd-El-Aziz, P.D. Harvey, *Inorg. Chem.* **47** (2008) 10816.

[54] C. Ragupathi, L.J. Kennedy, J.J. Vijaya, *Adv. Powder Technol.* **25** (2014) 267.

[55] T. Xuan, S. Wang, X. Wang, J. Liu, J. Chen, H. Li, L. Pan, Z. Sun, *Chem. Commun.* **49** (2013) 9045.

[56] S. Mathur, M. Veith, M. Haas, H. Shen, N. Lecerf, V. Huch, S. Hüfner, R. Haberkorn, H. P. Beck, M. Jilavi, *J. Am. Ceram. Soc.* **84** (2001) 1921.

[57] C. Ragupathi, J.J. Vijaya, A. Manikandan, L.J. Kennedy, *J. Nanosci. Nanotechnol.* **13** (2013) 8298.

[58] G. Buvaneswari, V. Aswathy, R. Rajakumari, *Dye. Pigment.* **123** (2015) 413.

Chapter 5

Structural, electronic and optical properties of Ce^{3+} doped γ --alumina.

5.1 Introduction

γ -Al_2O_3 has been the most frequently used catalyst support in industrial scale owing to its high surface area and it is relatively inexpensive [1]. γ -Al_2O_3 preferred morphological properties for example, pore size distribution, pore volume and base/acid properties mainly owe to its phase composition, local microstructure and surface chemical composition [2]. The γ -Al_2O_3 nanopowder is extensively utilized in electronics [1] metallurgy [2], fine ceramics [3] and composite materials [4] owing to its superfine morphology. Conventionally, γ -Al_2O_3 was evaluated as a cubic defect spinel type where oxygen atoms are in a cubic close-packed fashion [5] with a space group symmetry Fd-3m. Microstructural [6], hydrothermally steady material [7] impressively depends on the procedures used during synthesis as well as the synthesis conditions. However, the morphological similarities of transition alumina [8] is a challenge. The explicit location of Al atoms (and vacancies) is disputable and appears to be influenced by the synthesizing conditions of the γ -Al_2O_3 [9].

Different approaches and processes have been developed aimed at preparing nanoscale ceramics powders such as heterogeneous azeotropic distillation, Laser induced chemical vapour deposition and sol-gel process [10-13]. Varma *et al*. prepared a spherical powder with the average diameter of $2\,\mu m$ by sol-spray drying technique using ($Al(NO_3)_3$ as raw material [14]. However, the most catalytically active phase (γ -Al_2O_3) does not have perfect crystallinity at high temperatures as a result of phase transformations [15]. The conversion from γ -Al_2O_3 to α - Al_2O_3, results to a substantial scale down of the surface area, inducing decay of the catalytic occurrence [16]. Thermal equilibrium can be inflated by restraining or decelerating phase transformation. It has been proved that rare earth element incorporation, for example cerium, will not only put into an

equilibrium the pore structure of the alumina but in addition delay the phase transformation from γ-Al_2O_3 to α-Al_2O_3, [17,18].

The technologically important features of a catalyst strongly depends on the hydrothermal equilibrium and texture of the support [19]. As a result, the precise area of surface, size of the pore, shape and any chemical or physical transformations will result in a more steady system of great significance. Moreover, nanostructured systems display fascinating features due to their shape and quantum size consequences [20]. Regarding catalyst supports in particular, the large surface area is with respect to one-dimensional nanostructures will always intensify adsorption and catalytic properties [19-21]. Based on this argument, several surveys have reported the synthesis of amorphous or crystalline γ-Al_2O_3 nanoparticles, which most consistently take into account hydrothermal critique [22-23] or extensive engraving of porous alumina templates [24-25].

γ-Al_2O_3 is transparent over a broad range of wavelength, from in the ultraviolet region to the near infrared region. It also has perfect mechanical characteristics and good chemical stability which makes it a good candidate as a host material for luminescent rare earth ions. Rare earth doped alumina (γ-Al_2O_3) is currently a popular candidate phosphors with potential of long lasting luminescence [26–28].

Ce^{3+}-doped γ-Al_2O_3 has been investigated experimentally. Kumar *et al*.,[18] reported that cerium doping effectively retards the transformation of γ-Al_2O_3 to α–Al_2O_3 and that cerium inclusion in nanostructured alumina exhibited pore structure of a higher stability in comparison to stability of pure alumina [18]. On the other hand, Xiaodong *et al*.,[29] attributed the decelerating effect on γ-Al_2O_3 phase transformation to the introduction of Ce-Zr oxides into its lattice. Motivated by the dearth of available information on the effect of Ce^{3+} on the optical properties of γ-Al_2O_3 and the confirmation that Ce^{3+} has the lowest substitutional energy when used to dope anatase-TiO_2 among other lanthanides [23], we therefore chose Ce^{3+} as the dopant in this study.

5.2.1 Materials and synthesis

Cerium nitrate ($Ce(NO_3)_3.6H_2O$), aluminium nitrate ($Al(NO_3)_3.9H_2O$) and citric acid ($C_6H_8O_7.H_2O$) all readily purchased from supplier, were used to synthesize γ-Al_2O_3 powders and introduction of cerium into the γ-Al_2O_3 crystal lattice using the sol-gel technique [30]. The initial solution was prepared by dissolving aluminum nitrate and citric acid into deionized water. The concentration of aluminum nitrate was 0.5M. The molar ratio of citric acid to aluminum nitrate was 0.5. The solution was placed on a hot plate (50 ^oC) and constantly stirred for three hours (3 hrs) using a magnetic stirrer until it changed to yellowish solution. The temperature was then increased to 80 ^oC with continuous stirring for two hours. After which the solution changed to a transparent sticky gel. The gel was transferred to an oven maintained at 110 ^oC. All the liquid evaporated and large amount of gas evolution was observed when the gel was in the oven. After one hour, the gel swelled into a fluffy, citrate precursor. This precursor was grounded into fine powders with the help of a mortar and a pestle. The fine powder was calcined at 950 ^oC for three hours (3 hrs) in a muffle furnace to improve their crystallinity and optical properties. Al_2O_3 powder phosphors with different concentrations of Ce^{3+} were also synthesized and characterized. The amounts of aluminium nitrate and citric acid used were 2.785 g and 2.328 g respectively. To avoid concentration quenching effects, the dopants (Ce^{3+}) concentration was kept as low as reasonably achievable and the experiments were designed in such a way that the doping concentration raged from 0.31 to 1.24 mol%. The amounts of the different dopant concentration were 0.016g, 0.025g, 0.032g and 0.04g corresponding to 0.31, 0.62, 0.93 and 1.24 mol % doping concentration.

5.2.2 Characterization techniques

In order to characterize the phase and crystal structure of the γ-Al_2O_3 nanoparticles an X-ray diffraction (XRD) system with a Siemens Diffractometer D5000 and a Cu K_α radiation source at

40 kV, 30 mA and λ = 1.5418 Å, XRD was used. The morphology of the nanostructure was investigated using the Shimadzu Superscan SSX-550 system scanning electron microscope (SEM) operated at 20 kV and equipped with energy dispersive X-ray spectroscopy (EDS) detector. Transmission electron microscope (TEM) and selected area electron diffraction (SAED) micrographs used for morphology, particle size and structure determination were recorded using a Philips EM420 transmission electron microscope. Optical absorption experiments were performed using an Agilent HP1100 diode-array UV-visible spectrophotometer. Room temperature photoluminescence (PL) of the samples was measured using a Hitachi F-7000 fluorescence spectrometer at room temperature.

5.3 Computational details

Density functional theory (DFT) as implemented within the plane-wave self-consistent code quantum ESPRESSO [31] was used for all the calculations in this research. The exchange-correlation approximation within the DFT formalism was carried out using the local density approximation (LDA) as parameterized by Perdew-Wang [32]. The nuclei core's effect on the system was analyzed using norm conserving pseudopotentials [33]. Using the following converged calculation parameters, kinetic energy cut-off of 60 Ry, Gaussian smearing of 0.02 eV, 8×8×8 Monkhorst-Pack [34] k-point mesh and electronic energy convergence criterion of 10^{-6} Ry gave a lattice constant of 7.79 Å and a band gap of 3.5 eV were obtained compared to experimental values of 7.91 Å [35]. Another theoretical study obtained the lattice constant to be 7.89 Å [36]. The underestimation of the lattice constant with LDA is known trend [37]. Band gap underestimation within LDA is also known and has been documented in several studies [38,39]. On the hand, hybrid functionals have been documented as being successful in describing the band gap of many semiconductors compared to LDA [38,39]. However, it's also worth noting that, despite hybrid functionals being successful in overcoming the band gap under estimation issue[39], they are also known to fail in some cases such as in the prediction of the defect properties [40–42].

Using the optimized unit cell, a supercell of 80 atoms was obtained by multiplying the unit cell using a 2×2×2. The undoped γ -Al_2O_3 supercell was then optimized by relaxing only the atomic positions keeping the volume fixed using a 2×2×2 Monkhorst-Pack [34] *k*-point mesh. The kinetic energy cut-off and electronic energy convergence were similar to that of the unit cell. The supercell was then doped by substituting an Al atom with a Ce atom (0.31-1.24% doping percentage). Although anion substitution is also possible, cation substitution results in lower substitution energies compared to the anion substitution in the case of rare earth doped semiconductors [43–45]. Al atoms occupy both the tetrahedral and octahedral sites within the lattice thus Ce doping was done on each of these sites. Since Ce is a strongly correlated element, we added the Hubbard correction term U to its 4f electrons within the DFT+U formalism so as to properly account for its properties which could not have been accounted for in the case of using DFT alone. DFT+U is robust in accounting for the properties of transition metals as well as rare earth and lanthanide elements [46,47]. The choice of U is however highly dependent on the material property being converged with respect to experimental findings. Common material properties that have been used to obtain the value of U include; charge localization, Lattice parameter and band gap energy [48–50]. In this study we have adopted the reported methodology of [51] where the calculated band gap energy was converged with respect to experimental gap. A value of U=4 eV for Ce was chosen. Ce dopant substitution energy was obtained as stated by the Zhang–Northrup formalism where the substitution energy was obtained as,

$$E_{\mathrm{Ce}}^{q} = E_{\mathrm{X}} - E_{\mathrm{P}} + n\left(\mu_{\mathrm{Al}} - \mu_{\mathrm{Ce}}\right) + q\left(E_{\mathrm{VBM}} + E_{\mathrm{Fermi}}\right) + E_{\mathrm{corr}} \qquad (5.3.1)$$

where E_{X} is the total energy of Ce doped Al_2O_3, E_{P} is the total energy of the pristine Al_2O_3, E_{corr} is the charged defect correction for charged defect in a supercell of finite size [52,53], E_{Fermi} is the fermi energy, E_{VBM} is energy of valence band maximum, q is the given charge state, μ_{Al} and μ_{Ce} are the chemical potentials of Al and Ce respectively, n is the number of atoms substituted.

A thermodynamic charge transition level is the Fermi level position at which the dopant substitution energy is same in two different charge states. This can be obtained in two ways; the first one is by using the expression

$$\varepsilon^{q/q'} = \frac{\left(E_{Ce}^{q'} - E_{Ce}^{q} \right)}{\left(q - q' \right)} \tag{5.3.2}$$

where E_{Ce}^{q} and $E_{Ce}^{q'}$ are the dopant substitutional energies for q and q' obtained using equation (5.3.1). The second is by making plots of E_{Ce}^{q} as function of the E_{Fermi} for all the investigated charge states. The intersection point of any two lines is the thermodynamic transition level. After obtaining the thermodynamic transition levels, optical transition levels were then obtained using the relation,

$$E_{PL} = E_g - \varepsilon^{therm}(q/q') - E_{rel} \tag{5.3.3}$$

where E_{PL} is the optical transition level, E_g is the band gap, $\varepsilon^{therm}(q/q')$ is the associated thermodynamic transition level and E_{rel} is the Franck-Condon shift.

5.4 Results and Discussion

This section discusses the results of the experimental characterization of γ -Al_2O_3 based on x-ray diffraction, optical absorption, scanning electron microscopy, high resolution transmission electron microscope, energy dispersive X-ray spectroscopy, selected area electron diffraction and

photoluminescence. Results of DFT+U computation on structural, energetic, electronic and optical properties of the material are also presented and discussed.

5.4.1 XRD analysis

The XRD patterns of the pristine and Ce^{3+} doped γ -Al_2O_3 at different concentrations are presented in Figure 5.1. From the observed diffraction patterns it is evident that all the samples exhibited the spinel structure with space group Fd-3m as indexed by JCPDS card no.80-0955. All the observed peaks were in agreement with the international center for diffraction data (ICDD) database and also the powder XRD studies of [54]. The presence of peaks show the crystalline nature of the powders. It can also be seen from Figure 5.1 that, doping γ -Al_2O_3 with Ce^{3+} leads to narrowing of the peaks.

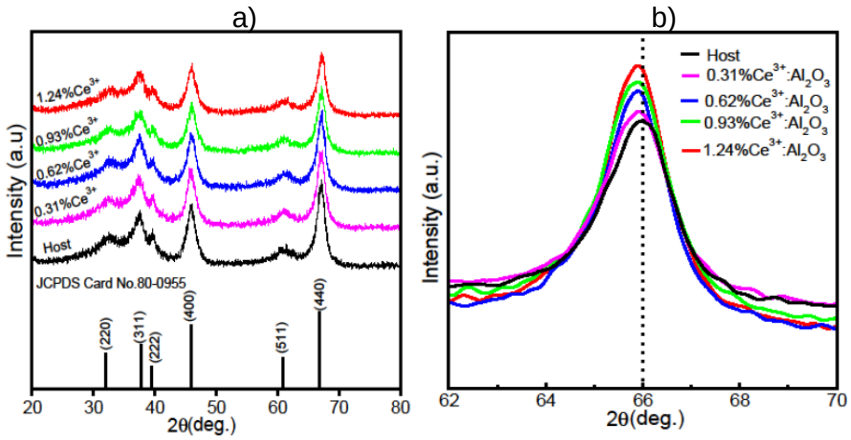

Figure 5.1 (a) XRD pattern of γ -alumina calcined at 950 ^{o}C (b) Gaussian fits of main diffraction peak (440).

The powder diffraction peak narrowing is as a consequence of the crystallite sizes. This means that in microscopic crystallites, the available planes are not sufficient to initiate total destructive interference resulting in realization of narrowing of peak. The peak narrowing is ascribed to

lattice strain due to the introduction of Ce^{3+} activator ions. In all the doped samples, Ce^{3+} is located at the Al^{3+} site. Since the ionic radius of Ce^{3+} (1.11Å) is bigger than that of Al^{3+} (0.50Å). The introduction of Ce^{3+} will strain the lattice (See Figure 5.2a) and 5.2b). In Figure 5.2, the presence of the dopant on the Al site leads to bond breaking and re-ordering thus as can be seen in the figure, resulted in a slight distortion around the dopant. It can therefore be deduced that if an element with a bigger ionic radius substitutes an element of smaller ionic radius, lattice distortion around this site will be evident.

Figure 5.1(b) presents an analysis of the highest intensity peak. From the figure it can be seen that, as the dopant concentration increases, the highest intensity peak slightly shifts to lower angles (i.e. to the left) in comparison to the host (undoped) peak. A similar shift was also observed by [55] where on doping ordered mesoporous γ -alumina, the peaks shifted to the lower angles. Another study [56] has also observed the shifting of diffraction peaks to lower angles on increasing the Ce^{3+} concentration when Ce^{3+} was used to dope ZnO nanorods. In our study, the (440) peak was found to decrease in intensity as doping concentration increased. This can be attributed to the distortion of the crystal structure of the host on incorporation of the dopant [57].

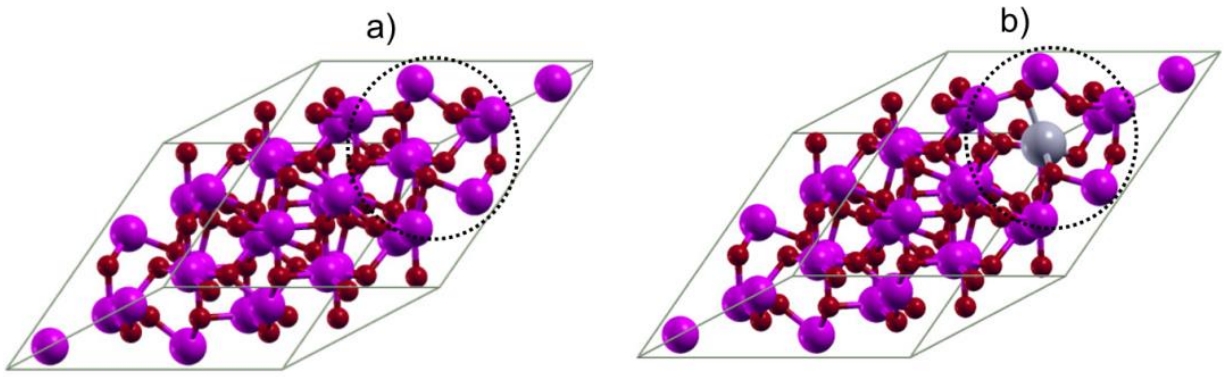

Figure 5.2 DFT relaxed configurations of (a) pristine γ -alumina and (b) doped γ -alumina.

Table 5.1. The averaged γ-Al_2O_3 and $Al_2O:Ce^{3+}$ crystallite size analysis at different doping concentrations for the (440) plane.

	2θ	**FWHM** (β)	**Crystallite Size (nm)**	**Compressive Lattice strain**
Host	66.00	1.85	5.14	0.0124
0.31%Ce^{3+}	65.99	1.66	5.73	0.0111
0.62%Ce^{3+}	65.98	1.13	8.40	0.0075
0.93%Ce^{3+}	65.96	0.93	10.28	0.0062
1.24%Ce^{3+}	65.95	0.75	12.70	0.0050

The width of the XRD peaks allows us to calculate crystallite size on average. The crystallite size is arrived at from the full width at half maximum (FWHM(β)) of the diffraction peaks using the Debye-Scherer method [49] using the following equation:

$$d = \frac{k\lambda}{\beta \cos \theta} \tag{5.4.1}$$

Where d is the average crystalline size, λ being the X-ray wavelength, k is Scherer's constant (0.92), β regarded as the full width at half maximum (FWHM) intensity of a Bragg reflection ignoring instrumental broadening and θ is the Bragg's angle (See Table 5.1). The average crystallite size of $Al_2O_3:Ce^{3+}$ at different doping concentration was then approximated to be 5.1 nm, 5.7 nm, 8.4 nm, 10.3 nm and 12.7 nm for host γ-Al_2O_3, γ-Al_2O_3:0.31%Ce, γ-Al_2O_3:0.62%Ce, γ-Al_2O_3:0.93%Ce and γ-Al_2O_3:1.24%Ce doping respectively. The establishment of γ-alumina is anticipated, since it was found to be the most thermodynamically stable phase, among transition aluminas, when the crystalline size is less than approximately 13 nm.

The lattice constant of cubic Al_2O_3 was calculated based on the XRD patterns using the equation;

$$a = d_{hkl}\sqrt{\left(h^2 + k^2 + l^2\right)} \tag{5.4.2}$$

where a is the lattice constant in Å, d_{hkl} is the inter-planar distance in Å, hkl are the miller indices. The interplanar distance is got from the SAED pattern. The value of the lattice constant obtained using Eq.5.0 is presented in Table 5.2. The DFT calculated value was 7.19 Å. This underestimation of the lattice constant as stated earlier, is an artifact of the DFT formalism however, our results are consistent with other *ab initio* studies [36].

Table 5.2. Comparison between inter-planar spacing (d), miller indices (hkl) and lattice constant (a)

hkl	d_{hkl} (Å)	a (Å)
220	2.80	7.92
311	2.38	7.89
222	2.28	7.90
400	1.97	7.88
511	1.51	7.85
440	1.38	7.81

5.4.2 SEM analysis

Through SEM investigation, powders morphologies and the possible agglomerations were investigated. Images of the samples used in this study obtained using SEM are presented in Figure 5.3 (a) and 5.3 (b) where, Figure 5.3 (a) is the SEM image of pristine γ -Al_2O_3 at ×70,000 magnification. The figure shows almost spherical particles densely populated. Figure 3b) is the SEM image for γ -Al_2O_3:Ce^{3+} at the same magnification as of the pristine. From the micrograph, it is evident that on doping, there was some slight agglomeration of the particles. Both Figures 5.3 (a) and (b) show surfaces with high porosity. For further analysis of the morphological properties, TEM analysis was conducted.

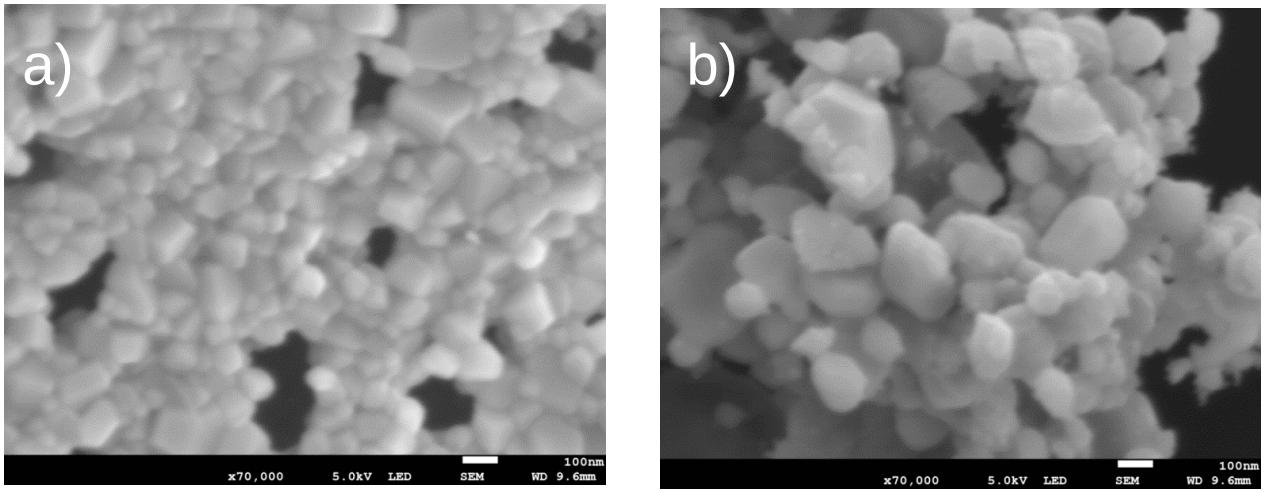

Figure 5.3 SEM micrographs of (a) Pristine Al_2O_3 (b) γ -Al_2O_3:Ce^{3+} annealed at 950 ^oC

5.4.3 HR-TEM analysis.

HR-TEM images of pristine γ -Al_2O_3 and γ -Al_2O_3:Ce^{3+} powders annealed at 950 ^oC are shown in Figures 5.4(a)-(d). Figure 5.4 (a) and (c) represent pristine systems of γ -Al_2O_3 with an average crystallite size of 16 nm $\pm$ 6 nm. This shows that the crystallite sizes from HR-TEM analysis are in agreement with those derived from XRD traces. Figure 5.4(b) and (d) shows the average diameter of γ -Al_2O_3:Ce^{3+} crystal lattice to be in the order of 20 nm. This is consistent with what was obtained by [58] from the phase diagram of γ -Al_2O_3.

The average grain size diameter of pristine γ -Al_2O_3 (Figure 5.4 (a) and (c)) is 31 nm while that of the doped system was 20 nm. This reduction of the grain size from 31 nm to 20 nm on doping is confirmed by the selected area electron diffraction (SAED) patterns. The SAED patterns in Figure 5.4 (c) shows diffraction rings composed of discrete spots while the SAED patterns in Figure 5.4 (d) show continuous ring patterns indicating decrease in grain size (i.e structural differences between undoped and doped systems).

The diameter of the diffraction rings in SAED patterns was obtained by the use of imageJ program and it is consistent with $\sqrt{h^2 + k^2 + l^2}$ given that (hkl) represent the miller indices of planes corresponding to the ring. Using this relationship, the rings obtained from SAED corresponds to (440), (400), (311) as shown in Figure 5.4 (d). These SAED results agree well with XRD results because from XRD, the planes (440), (400) and (311) had high intensities. The other peaks in XRD had low intensities and were represented by diffuse rings in the SAED. Therefore, using the SAED patterns, we were able to confirm the cubic crystalline structure of γ -Al_2O_3 nanoparticles in that, the SAED patterns revealed that γ -Al_2O_3 nanoparticles had inter-planar spacing of 0.138, 0.197 and 0.238 nm corresponding to (440), (400) and (311) planes respectively as shown in Figure 5.4 (c).

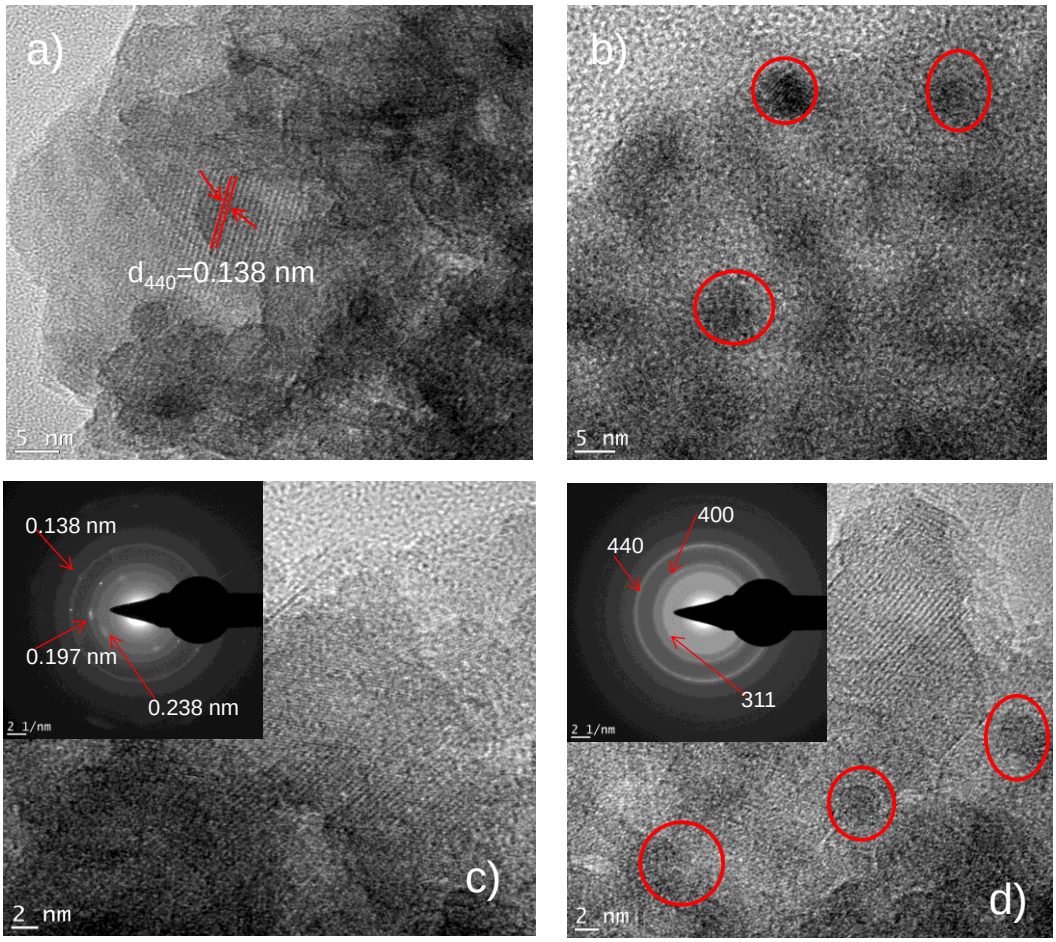

Figure 5.4 HRTEM micrographs showing lattice fringe scaling and corresponding SAED (inset) analysis.

5.4.4 EDS analysis

In order to confirm whether the samples used were contaminated or not, an EDS analysis was done. As can be seen in Figures 5.5 (a) and (b), only aluminum and oxygen were detected in the case of pristine γ -Al_2O_3 (Figure 5.5 (a)) and aluminum, oxygen and cerium were detected in the case of Al_2O_3:Ce^{3+}.

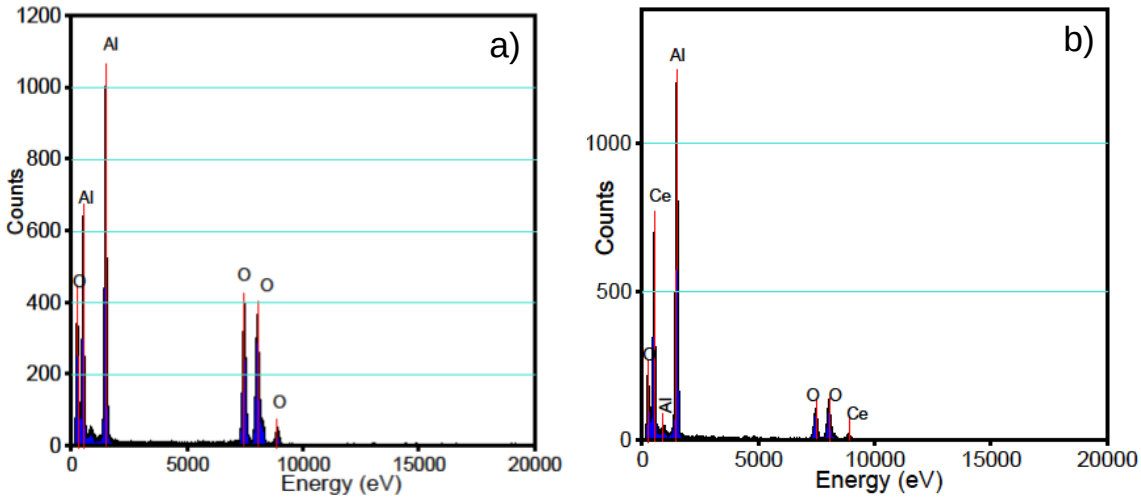

Figure 5.5 EDS spectrum of (a) Pristine γ -Al_2O_3 and (b) Al_2O_3:Ce^{3+}

5.4.5 Electronic properties

The band structures and projected density of states (PDOS) of pristine and doped γ -Al_2O_3 were investigated within the DFT+U formalism with the Hubbard, U, term added to the 4*f* orbital of γ -Al_2O_3:Ce^{3+}. From the calculations gamma alumina was found to have a direct band gap at Γ (gamma) of 3.5 eV while the experimentally obtained band gap was 5.16 eV. This underestimation as earlier stated is a known artifact of the DFT formalism [38,39]. Another DFT study [59] reported a band gap of 3.9 eV using DFT with the full-potential linear muffin-tin-orbital (FPLMTO) method. As can be seen in Figures 5.6 (a) and 5.6 (b), the presence of Ce led to a red shift i.e. the band gap decreased on doping. The presence of dopant led also to the introduction of new states within the band gap of the undoped alumina hence the decrease in the fundamental band gap.

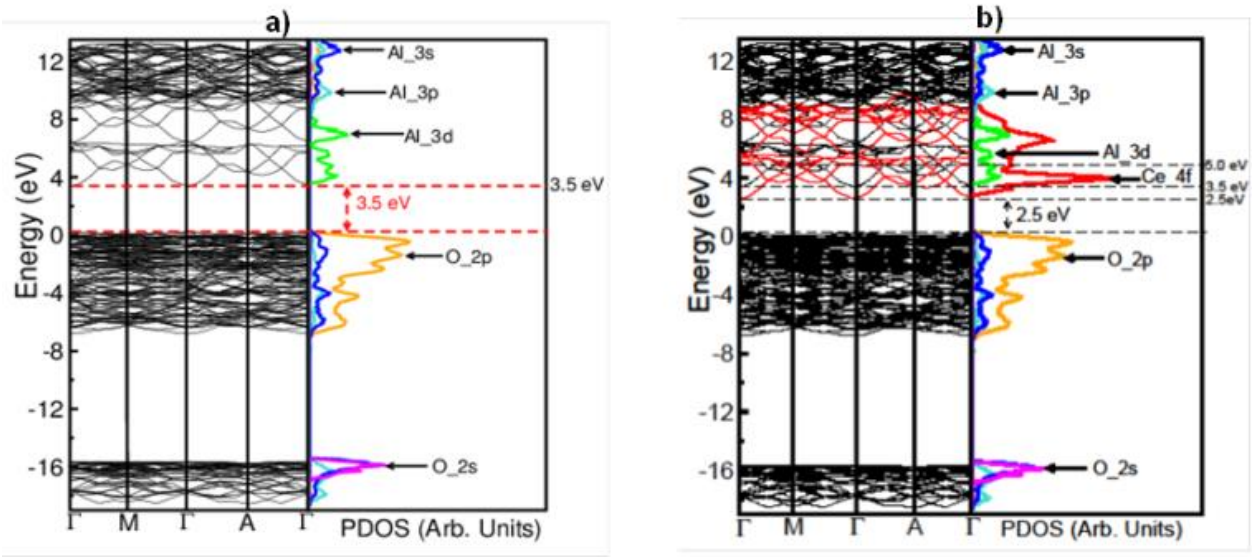

Figure 5.6 DFT band structure and PDOS of (a) pristine γ -Al_2O_3, (b) γ -Al_2O_3:Ce^{3+}

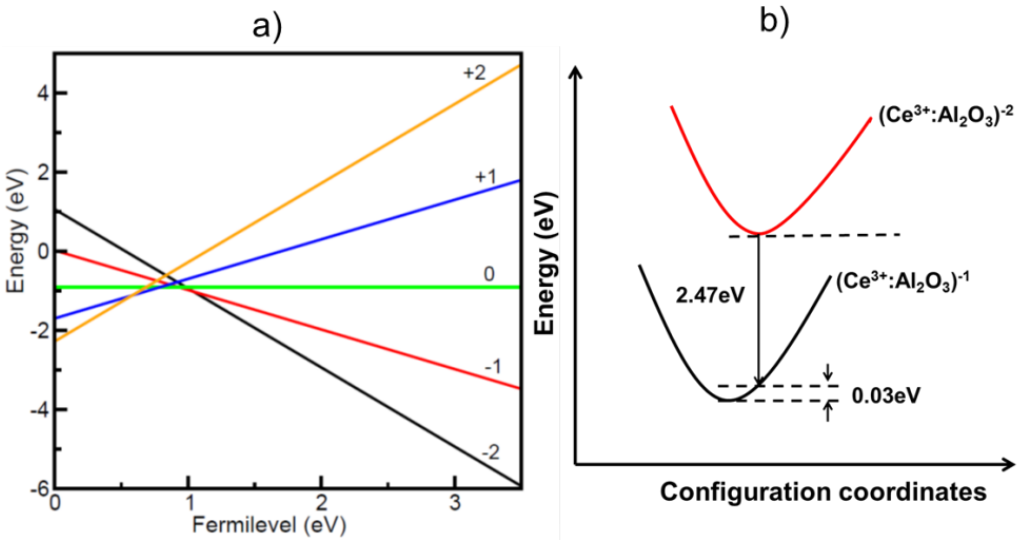

Figure 5.7 DFT Calculated Photoluminescence for undoped γ -Al_2O_3 and doped γ -Al_2O_3:Ce^{3+}

5.4.6 Formation energies and thermodynamic charge transitions.

Substitutional (formation) energy of Ce^{3+} doped γ-Al_2O_3 at different charge states were calculated using equation (5.3.1). Formation energy is an indicator of what energy penalty has to be paid for a defect to be created within a host lattice. The lower the formation energy, the easier it is for the defect to be created. The calculated formation energies at different charge states are presented in Table 5.3. All the calculated substitutional energies are negative. Negative formation energies imply that Ce^{3+} atom can be easily incorporated in γ-Al_2O_3.

Table 5.3. Calculated formation energies at different charge states under Al-rich conditions, thermodynamic transition level ε^{therm} w.r.t VBM, optical transition level E_{PL} w.r.t VBM and lattice relaxation energy E_{rel}

Formation energy (eV)				
Charge state				
-2	-1	0	+1	+2
-0.44	-1.48	-2.41	-3.2	-3.78
Thermodynamic transitions (eV)				
	(+2/-1)	(+1/0)	(0/-1)	(-1/-2)
	0.58	0.79	0.92	1.01
Optical transitions (-1/-2)				
	$E_{PL\,(eV)}$	λ_{PL}	E_{rel}	
	2.47	502 nm	0.03	

On plotting the dopant substitutional energy as a function of Fermi level position along the band gap, we were able to locate the thermodynamic charge transition levels $\varepsilon^{q/q'}$ and compared

them to those obtained using equation (5.3.2) (see Figure 5.7 (a)). In Figure 5.7 (a), the charge state of the system is represented by the slope of each line, and the point of intersection between any two slopes is the thermodynamic charge transition location. Both the calculated and plotted thermodynamic transition levels were found to be the same. From Figure 5.7 (a), the highest defect state, which is represented by the position of the thermodynamic transition level, w.r.t to the valence band maximum (VBM), was found to be (-1/-2) transition. This was the transition that was then used to obtain the optical transition level using equation (5.3.3). (See Figure 6.7(b)) for a schematic representation.

The calculated optical transition levels and wavelengths (see Table 5.3) were 2.47 eV and 502 nm respectively. This implies that Ce^{3+} doping in Al_2O_3 led to a bluish-green emission at 502 nm thus, Ce^{3+} doped Al_2O_3 can be used as a bluish-green pigment. Experimentally, Figure 5.8 b) shows blue emission at 445 nm and 475 nm thus, despite the shortcomings of DFT, we were able to predict to some degree of consistency that Ce^{3+} doping leads to blue emission in γ -Al_2O_3.

5.4.7 Photoluminescence (PL) properties

UV-visible analysis was conducted in order to get the absorption energy. From Figure 5.9 (b), the absorption was at 240 nm (5.16 eV). This is equal to the excitation energy. This excitation energy was then used to get emission spectra in Figure 5.8 (b). The broad band spectra could give all the peaks especially due to the dopant, therefore excitation spectra were necessary to confirm the absorption spectra. In order to confirm the absorption spectra, we plotted the excitation spectra (Figure 5.8(a)) at 445 nm emission. This gave a maximum intensity peak at 240 nm. In the spinel type γ -Al_2O_3 structure, the excitation peak at 240 nm of host γ -Al_2O_3 (black) is due to the vacancies (defects) found in the crystal lattice which participate in the absorption of UV light in the nanostructured γ -alumina powder and also the surface defects. The excitation (absorption) peak at 244 nm is associated with the $4f \rightarrow 5d$ electric dipole in 1.24% γ -Al_2O_3:Ce^{3+} for the allowed absorption transition of Ce^{3+}.

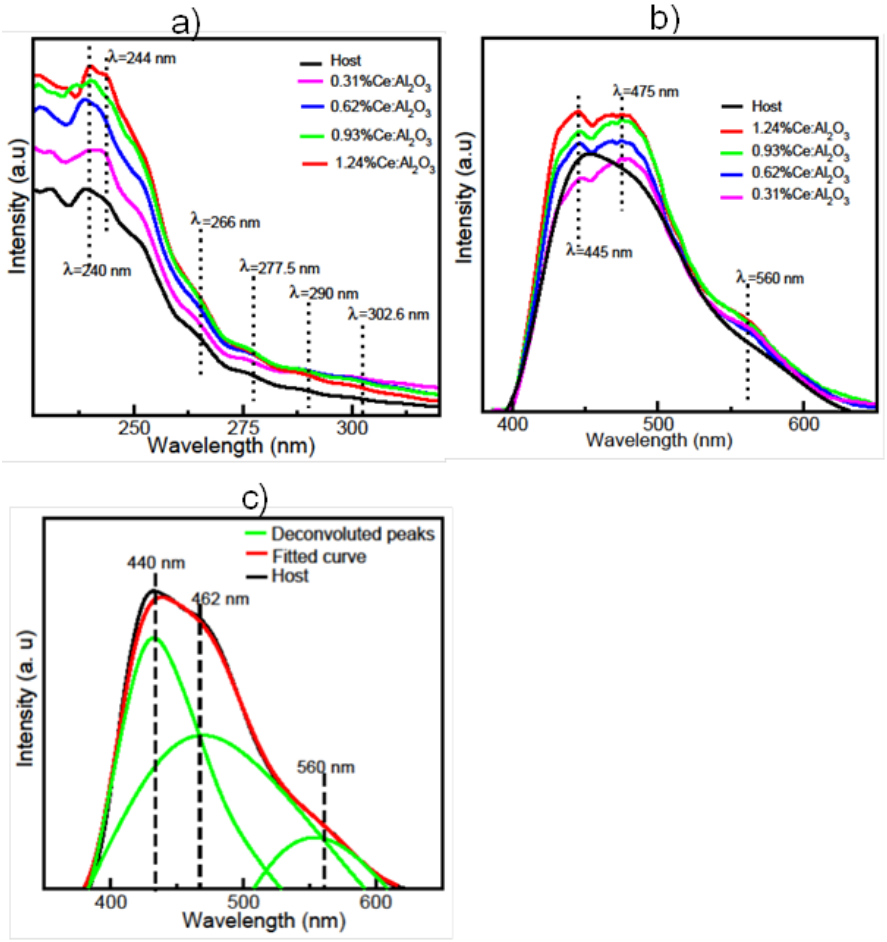

Figure 5.8 (a) Excitation (b) Emission spectra of pristine γ -Al_2O_3 and γ -Al_2O_3:Ce^{3+} (c) Deconvoluted pristine γ -Al_2O_3 emission spectrum

There are other peaks of less intensities associated with the $4f \rightarrow 4f$ forbidden transitions and centered at 266.0 nm, 277.5 nm, 290.0 nm and 302.6 nm. As seen in Figure 5.8 (a), the intensity of the excitation peaks increases with increase in concentration of Cerium. This shows that as more Ce^{3+} is introduced in the γ - Al_2O_3 lattice, more absorption is realized. Li *et al* also observed the same trend with increase of Ce^{3+} concentration [60].

On recording the emission spectrum at a 240.0 nm excitation, the intensity of the emission peaks increased as Ce^{3+} is increased. This shows that, increasing Ce^{3+} concentration causes an increase in the number of emitting ions. Figure 5.8 (b) shows two emission peaks at 445.0 nm and 475.0

nm both in the blue region. These two peaks correspond to 5*d* to 4*f*($^2F_{5/2}$) and 5*d* to 4*f*($^2F_{7/2}$) transitions of Ce^{3+} ion. The energy dissimilarity between the two peaks is ~1500cm^{-1} because of the spin-orbital coupling in crystal field [61]. The emission spectrum consists of an emission peak at 560.0 nm which was the effect of the electron conversion from the least crystal-splitting constituent of 5*d* position to the ground state Ce^{3+}. This green emission from cerium was also realized by [62]. On deconvoluting the host emission peak (Figure 5.8 (c)), peaks were obtained at 440 nm, 462 nm and 560 nm which are in the blue and green regions. These emission peaks of the host are due to oxygen vacancies. It is also suggested that the surface defects generated new energy levels.

Figure 5.9 (a) presents the diffuse reflectance of pristine γ-Al_2O_3 as well as γ-Al_2O_3:Ce^{3+} at different doping levels. From Figure 5.9 (a), pristine Al_2O_3 had the highest reflectance and also least absorption as seen in Figure 5.9 (b). As the concentration of Ce^{3+} is increased, Ce^{3+} absorbs more energy that is, reduction in reflection. There is a red shift to the higher wavelength, which is confirmed by the reduction of the band gap (see Figure 5.6 (a) and 5.6 (b)) as cerium concentration is increased. The size of the band gap was realized by plotting the square of the incorporated light (corresponding in size to the square of the Kubelka-Munk function $F(R)^2$) as a function of radiant energy (See Figure 5.9 (b)).

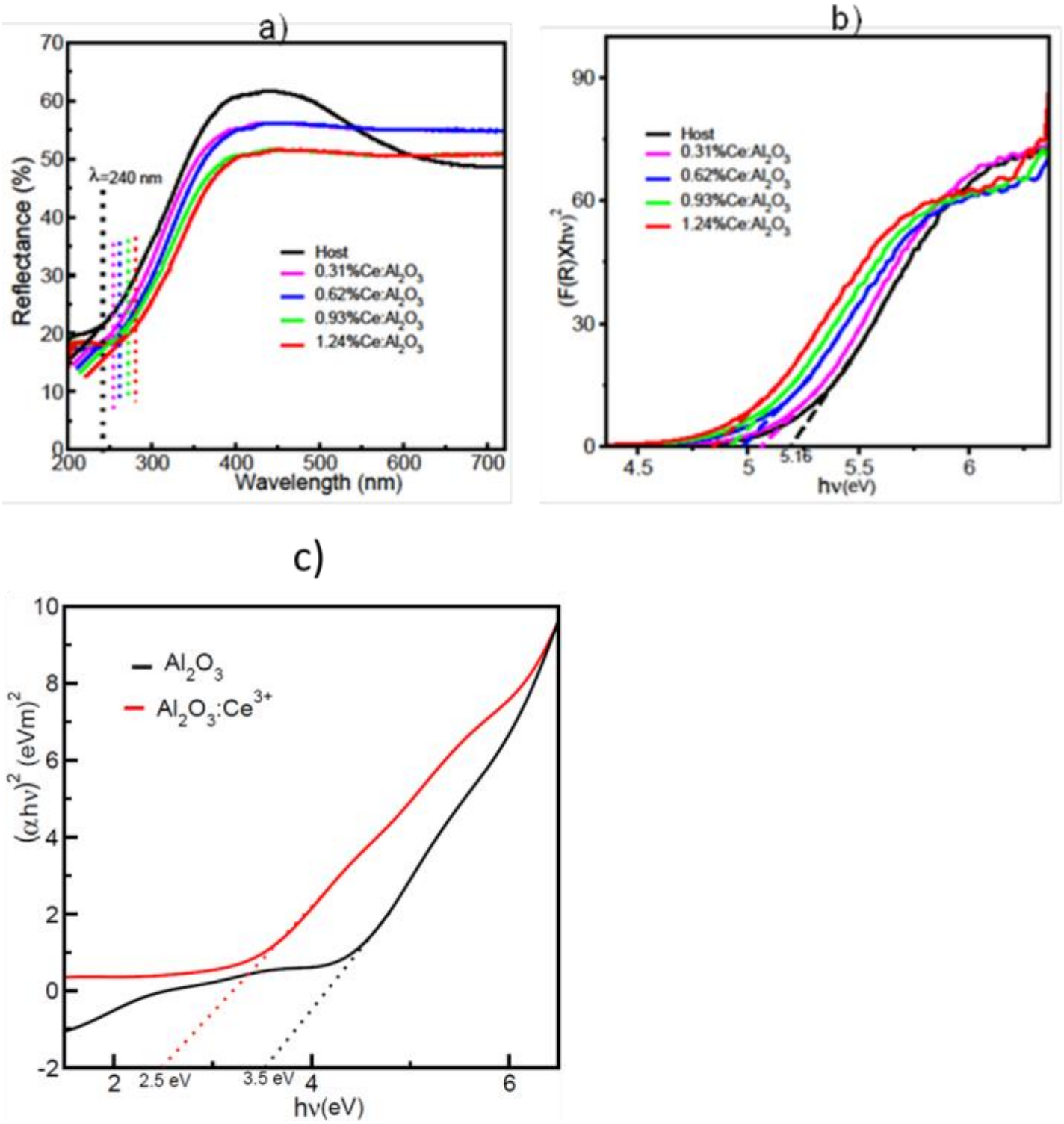

Figure 5.9 (a) Reflectance spectra of γ -Al_20_3 and γ -Al_2O_3:Ce^{3+} (b) Kubelka-Munk plot and band gap energy of γ -Al_2O_3 and γ -Al_2O_3:Ce^{3+} (c) Tauc plot to determine optical band gap before and after doping from DFT.

Extrapolating the linear part of Figure 5.9 (b) to $F(R)^2=0$, gives a host band gap of 5.16 eV (240 nm), which has the same energy as that obtained in Figure 5.8 (a). Figure 5.9 (b) shows a reduction in band gap as the concentration of Ce^{3+} is increased. This observation is also consistent with DFT calculated results. Ce^{3+} has an ionic radius of 1.11 Å and it replaces Al^{3+} at substitutional site. Al^{3+} has an ionic radius of 0.50 Å, this shows that on doping, there will be an increase in crystallite size which causes a reduction of the band gap. These optical absorption characteristics are in agreement with the properties of a direct band gap semiconductor.

From our analysis of the DFT+U calculated absorption data, we compared pristine γ -Al_2O_3 and γ -Al_2O_3:Ce^{3+} Tauc models based on the equation

$$\alpha(h\nu) = A\left(h\nu - E_g\right)^n \qquad (5.4.3)$$

Where A is a constant and n indicates the shift type i.e. n=2 denotes indirect-permitted shift, $n=\frac{1}{2}$ for direct allowed shift, n=3 indicates indirect prohibited shift and $n=\frac{3}{2}$ indicating direct forbidden shift [63, 64]. Al_2O_3 is a direct band gap system, therefore $n=\frac{1}{2}$ Substituting this in equation (5.4.3) one gets,

$$\alpha(h\nu) = A\left(h\nu - E_g\right)^{1/2} \qquad (5.4.4)$$

Tauc plots can therefore be generated by plotting $(\alpha h\nu)^2$ versus photon energy $h\nu$. From these plots, the $h\nu$ intercept was obtained by extrapolating the linear portion of the curve. This gives the transition energy (See Figure 5.9 (c). As can be seen in Figure 5.9 (c), the $h\nu$ intercept for pristine and doped γ -Al_2O_3 was 3.5 eV and 2.5 eV respectively. This is consistent with the DFT calculated band gaps in Figure 5.6. In the case of pristine γ - Al_2O_3, the gap was as results of a *p-d* transition i.e. a transition from *p* states in the valence band maximum to *d* states in the conduction band minimum. On doping γ -Al_2O_3 with Ce^{3+}, there was an introduction of Ce 4*f*

states at 2.5 eV indicating a *p-f* transition. It can also be seen in Figures 5.9b) and 5.9c) that both the Kubelka-Munk and Tauc plots gave consistent results.

5.5 Conclusion

In conclusion, the pristine γ-Al_2O_3 and γ-Al_2O_3:Ce^{3+} powder phosphors were successfully synthesized using the sol-gel technique. Structural characterizations as well as theoretical calculations show a defective cubic spinel structure. As confirmed from XRD data and SAED diffraction patterns, γ-Al_2O_3 and γ-Al_2O_3:Ce^{3+} are highly crystalline. The SEM micrographs showed that the particles are spherical in shape while the HR-TEM micrographs showed a grain size of approximately 5nm. The present work reveals that computational methods based on first principle quantum mechanics expertise are important tools in the anticipation of properties of technologically important complex materials.

References

[1] R. McPherson, *J. Mater. Sci.* **15** (1980) 3141.

[2] B.C. Gates, *Chem. Rev.* **95** (1995) 511.

[3] P.B. Koeneman, I.J. Busch-Vishniac, K.L. Wood, *Microelectromechanical Syst. J.* **6** (1997) 355.

[4] M.K. Aghajanian, N.H. Macmillan, C.R. Kennedy, S.J. Luszcz, R. Roy, *J. Mater. Sci*. **24** (1989) 658.

[5] B.C. Lippens, J.H. De Boer, *Acta Crystallogr*. **17** (1964) 1312.

[6] P. Sarkar, D. De, H. Rho, *J. Mater. Sci.* **39** (2004) 819.

[7] M. Kanezashi, K. Yada, T. Yoshioka, T. Tsuru, *J. Am. Chem. Soc.* **131** (2008) 414.

[8] M. Trueba, S.P. Trasatti, *J. Inorg. Chem.* **2005** (2005) 3393.

[9] K. Sohlberg, S.J. Pennycook, S.T. Pantelides, *Chem. Eng. Commun.* **181** (2000) 107.

[10] T. Miyahara, H. Kanzaki, R. Hamada, S. Kuroiwa, S. Nishiyama, S. Tsuruya, *J. Mol. Catal. A Chem.* **176** (2001) 141.

[11] H. Shan, Z. Zhang, *J. Eur. Ceram. Soc.* **17** (1997) 713.

[12] Y. Adraider, Y.X. Pang, F. Nabhani, S.N. Hodgson, M.C. Sharp, A. Al-Waidh, *Ceram. Int.* **40** (2014) 6151.

[13] J. K. Guo, C. D. Feng, *Mater. Res. Soc. Korea.* **1** (1995) 227.

[14] H.K. Varma, T.V. Mani, A.D. Damodaran, K.G. Warrier, U. Balachandran, *J. Am. Ceram. Soc.* **77** (1994) 1597.

[15] A. Boumaza, L. Favaro, J. Lédion, G. Sattonnay, J.B. Brubach, P. Berthet, *J. Solid State Chem.* **182** (2009) 1171.

[16] K. N. Kumar, J. Tranto, J. Kumar, J. E. Engell, *J. Mater. Sci. Lett.* **15** (1996) 266.

[17] Q. Wei, Z. X. Chen, Z. H. Wang, Y. L. Hao, J. X. Zou, Z. R. Nie, *J. Alloys Compd.* **387** (2005) 292.

[18] K.-N.P. Kumar, J. Tranto, B.N. Nair, J. Kumar, J.W. Høj, J.E. Engell, *Mater. Res. Bull.* **29** (1994) 551.

[19] S. Gravani, K. Polychronopoulou, V. Stolojan, Q. Cui, P.N. Gibson, S.J. Hinder, *Nanotechnology*. **21** (2010) 465606.

[20] M. C. Daniel, D. Astruc, *Chem. Rev.* **104** (2004) 293.

[21] J. Hulteen, *J. Mater. Chem.* **7** (1997) 1075.

[22] D. Kuang, Y. Fang, H. Liu, C. Frommen, D. Fenske, *J. Mater. Chem.* ***13*** (2003) 660.

[23] C.L. Lu, J.G. Lv, L. Xu, X.F. Guo, W.H. Hou, Y. Hu, *Nanotechnology*. **20** (2009) 215604.

[24] X. X. Sun, J. Liang, J. F. Zhao, Q. Ma, B. S. Xu, *Appl. Phys. A.* **98** (2010) 263.

[25] Z. L. Xiao, C.Y. Han, U. Welp, H. H. Wang, W. K. Kwok, G.A. Willing, *Nano Lett.* **2** (2002) 1293.

[26] R. J. Xie, N. Hirosaki, K. Sakuma, Y. Yamamoto, M. Mitomo, *Appl. Phys. Lett.* **84** (2004) 5404.

[27] C.-J. Jia, L.-D. Sun, F. Luo, X.-C. Jiang, L.-H. Wei, C.-H. Yan, *Appl. Phys. Lett.* **84** (2004) 5305.

[28] D. Matsuura, *Appl. Phys. Lett.* **81** (2002) 4526.

[29] X. Wu, B. Yang, D. Weng, *J. Alloys Compd*. **376** (2004) 241.

[30] S.F. Wang, C.F. Zhuang, Y.G. Yuan, X. Xiang, G.Z. Sun, Q.P. Ding, *Trans. Indian Ceram. Soc.* **73** (2014) 37.

[31] P. Giannozzi, S. Baroni, N. Bonini, M. Calandra, R. Car, C. Cavazzoni, et al., QUANTUM ESPRESSO: A Modular and Open-Source Software Project for Quantum Simulations of Materials, *J. Phys. Condens. Matter*. **21** (2009) 395502.

[32] J.P. Perdew, Y. Wang, *Phys. Rev. B* **45** (1992) 13244.

[33] N. Troullier, J.L. Martins, *Phys. Rev. B* **43** (1993) 2006.

[34] H. J. Monkhorst, J. D. Pack, *Phys. Rev. B* **13** (1976) 5188.

[35] R. S. Zhou, R. L. Snyder, *Struct. Sci.* **47** (1991) 617.

[36] G. Gutiérrez, A. Taga, B. Johansson, *Phys. Rev. B* **65** (2001) 12101.

[37] C.N.M. Ouma, M.Z. Mapelu, N.W. Makau, G.O. Amolo, R. Maezono, *Phys. Rev. B* **86** (2012) 104115.

[38] J. Paier, M. Marsman, K. Hummer, G. Kresse, I.C. Gerber, J.G. Angyán, *J. Chem. Phys.* **124** (2006) 154709.

[39] J. Heyd, J.E. Peralta, G.E. Scuseria, R.L. Martin, *J. Chem. Phys.* **123** (2005) 174101.

[40] T. Maeta, K. Sueoka, *J. Appl. Phys.* **116** (2014) 73505.

[41] A. Chroneos, B.P. Uberuaga, R.W. Grimes, *J. Appl. Phys.* **102** (2007) 83707.

[42] A. Chroneos, H. Bracht, R.W. Grimes, B.P. Uberuaga, *Appl. Phys. Lett.* **92** (2008) 172103.

[43] S. Sanna, B. Hourahine, T. Frauenheim, U. Gerstmann, *Phys. Status Solidi.* **5** (2008) 2358.

[44] S. Sanna, W. Schmidt, T. Frauenheim, U. Gerstmann, *Phys. Rev. B.* **80** (2009) 104120.

[45] C.N.M. Ouma, W.E. Meyer, *Phys. B Condens. Matter*. **439** (2014) 141.

[46] B. Himmetoglu, A. Floris, S. de Gironcoli, M. Cococcioni, *J. Quantum Chem.* **114** (2014) 14.

[47] M. Cococcioni, S. De Gironcoli. *Phys. Rev. B* **71** (2005) 35105.

[48] M. Nolan, S. Grigoleit, D.C. Sayle, S.C. Parker, G.W. Watson, *Surf. Sci.* **576** (2005) 217.

[49] C.W.M. Castleton, J. Kullgren, K. Hermansson, *J. Chem. Phys.* **127** (2007) 244704.

[50] L.J. Bennett, G. Jones, *Phys. Chem. Chem. Phys.* **16** (2014) 21032.

[51] W.M. Mulwa, C.N.M. Ouma, M.O. Onani, F.B. Dejene, *J. Solid State Chem.* **237** (2016) 129.

[52] C. Freysoldt, J. Neugebauer, C.G. Van de Walle, *Phys. Status Solidi.* **248** (2011) 1067.

[53] C. Freysoldt, J. Neugebauer, C. Van de Walle, *Phys. Rev. Lett.* **102** (2009) 016402.

[54] J.D. Kamminga, L.J. Seijbel, *J. Res. Inst. Stand. Technol.* **109** (2004) 65.

[55] Q. Sun, Y. Zheng, Z. Li, Y. Zheng, Y. Xiao, G. Cai, *Phys. Chem. Chem. Phys.* **15** (2013) 5670.

[56] J. Yang, M. Gao, L. Yang, Y. Zhang, J. Lang, D. Wang, *Appl. Surf. Sci.* **255** (2008) 2646.

[57] G. Bhagavannarayana, S. Parthiban, S. Meenakshisundaram, *Cryst. Growth Des.* **8** (2007) 446.

[58] P. S. Santos, H. S. Santos, S. P. Toledo, *Mater. Res. Bull.* **3** (2000) 104.

[59] R. Ahuja, J.M. Osorio-Guillen, J.S. de Almeida, B. Holm, W.Y. Ching, B. Johansson, *J. Phys. Condens. Matter* **16** (2004) 2891.

[60] G. Li, Y. Lai, T. Cui, H. Yu, D. Liu, S. Gan, *Mater. Chem. Phys.* **124** (2010) 1094.

[61] G. Blasse, A. Bril, *J. Chem. Phys.* **47** (1967) 5139.

[62] H. L. Li, X. J. Liu, L. P. Huang, *J. Am. Ceram. Soc.* **88** (2005) 3226.

[63] J. I. Pankove, *J. Appl. Phys*. **47** (1976) 5387.

[64] A. Rahmati, M. Ghoohestani, H. Badehian, M. Baizaee, *Mater. Res.* **17** (2014) 303.

Chapter 6

Energetic, Electronic and Optical Properties of Lanthanides Doped TiO_2: An ab initio LDA+U Study

6.1 Introduction

Titanium dioxide (TiO_2) has vast applications in electronics, energy and photonics among other applications [1]. Some of the key applications include photocatalysis where solar energy is converted into hydrogen energy via the splitting of water, decomposing toxic organic and inorganic pollutants to purify water and air, and providing super-hydrophilicity to solid surfaces [2]. TiO_2, a wide band gap compound semiconductor, is known to be active only in the ultraviolet (UV) region of the solar spectrum. However, in order for TiO_2 to fully utilize the major part of the solar spectrum, besides UV which is just 5% of the solar spectrum, several studies aimed at improving the properties of TiO_2 via doping and co-doping TiO_2 with various elements have been carried out with varied measures of success [3]. TiO_2 has rutile, anatase and brookite polymorphs. Rutile and brookite are direct band gap semiconductors. The higher photocatalytic activity of the anatase TiO_2 over the rutile and brookite polymorphs can be attributed to the indirect band gap of the anatase which leads to a slow decay lifetime of photoexcited charge carriers.[1]

Good photo-catalysts are known to have conduction band edges that are more negative than the reduction (redox) potential of water. However, visible-light photo-catalysts have been found to be either unstable under light illumination (CdSe) [4] or have low activity (Fe_2O_3) [5]. Attempts have been made in trying to use transition metal (TM) oxides such as Cr_2O_3 as photo-catalysts since they have good visible light absorption [6]. Experimentally, Cr_2O_3 has a band gap of 3.4 eV [7] which is larger than the experimental band gap of rutile. This explains why Cr_2O_3 conduction band edges were found to be more negative compared to the redox potential of water

[8]. Therefore, incorporating a dopant into TiO_2, in such a way that the conduction band levels are made more negative than the redox potential of water can facilitate the visible light absorption of the host oxide under visible irradiation.

The most widely used semiconductor photo-catalyst is titanium dioxide (TiO_2), because it is relatively easy and inexpensive to synthesize, it is highly stable under irradiation conditions, non-toxic, and can completely degrade several classes of pollutants in aqueous and gas phases [2,3]. However, its success as a semiconductor photo-catalyst is limited by its wide band-gap (3.2 eV) and the recombination of the photogenerated electron-hole pairs [4]. A 3.2 eV (387 nm) band gap necessitates the use of UV light in the photo-production of electrons and holes.

Conflicting reports exist in the literature regarding the photocatalytic activities on semiconductors doped with transition metal ions [5]. The disparities are due to a number of reasons including; variability in the synthetic procedures employed for the preparation of catalysts which lead to the formation of photo-catalysts with varying physio-chemical characteristics, varying experimental conditions used in the photocatalytic reactions and the different quantitative methods used for analysis of reactant or product concentrations[6]. In recent times, Herrmann *et al*.,[7] made a compelling argument that both *n*- and *p*-doping by transition metal ions leads to an increase in the recombination rate of the photogenerated electron-hole pairs. In recent years, anion doping has gained popularity and the prime motivation in this direction has been in extending the visible light response of large band-gap semiconductors[8,9].

It has been reported that TiO_2 co-doped with La^{3+} and Eu^{3+} exhibits better photocatalytic properties compared to that of pristine TiO_2[10]. The improved photocatalytic properties resulted from transitions of 4*f* electrons in the dopants. A similar observation was made when TiO_2 was doped with lanthanides[11,12]. Doping TiO_2 with lanthanides has been the subject of intense investigation both experimentally [11–14] and theoretically [15–17]. This is because lanthanide doping could remarkably improve the photocatalytic activity of TiO_2 as it registers visible light response as well as strong redox potential at the same time. Lanthanides are among the rare-earth elements with great luminescent properties. They are characterized by the 4*f* orbitals which in some cases are shielded by filled $5p^6 6s^2$ sub orbitals leading to very important spectroscopic

properties[18] however, lanthanides ions are not excited efficiently without a host [19]. Their properties are known to greatly depend on their electronic configuration and ionic radius, which decreases steadily along the lanthanide series with respect to the fillings of the 4*f* orbitals[20].

Density functional theory (DFT) has been the basis for most of the electronic structure calculations, however it has limitations when it comes to describing properties such as band gaps (see ref [21–24]). Another key shortcoming of standard DFT is that it cannot accurately describe systems with strong correlation effects. This is because within DFT, the electron–electron interaction is expressed as the sum of the Hartree and exchange-correlation (XC) terms however, the XC term is usually approximated. Due to this approximation, the XC term cannot accurately account for electronic interactions in strongly correlated systems, hence the need for DFT+*U* technique where a Hubbard correction *U* is added to the standard DFT formalism [25,26].

In this study we investigate lanthanide doped anatase TiO_2 using density functional theory with Hubbard *U* correction (DFT+*U*) because lanthanides are known to have 4*f* orbitals which cannot be accurately described using standard DFT. The electronic and optical properties of anatase doped TiO_2 with each of tsphe eleven (11) different lanthanides namely: La, Ce, Pr, Nd, Pm, Sm, Eu, Gd, Tm, Yb and Lu have been investigated. In addition we have also calculated the dopant substitutional energies, thermodynamic charge transitions energies as well as their optical absorption spectra.

6.2 Calculation models and methods

Projector augmented plane wave (PAW) method [27] as implemented in the Quantum ESPRESSO code[28], has been used to study the properties of interest within the DFT+*U* formalism. PAW potentials were used for Ti, O and all the lanthanides investigated in this study. PAW is an improvement to the pseudopotential approximation as it combines the pseudopotential approximation with linearized augmented-plane-wave (LAPW) method[29,30], making PAW more accurate compared to the pseudopotential approximation. The Brillouin zone of the unit cell of anatase TiO_2 was sampled using a converged Monkhorst-Pack [31] k-point

mesh of 6x6x3 and kinetic energy cut-off of 80 Ry. Standard DFT is known to severely underestimate the band gap in semiconductors. In the case of TiO_2, the band gap of anatase TiO_2 obtained using spin polarized local density approximation (LDA) was found to be 1.89 eV compared to the experimental value of 3.2 eV [32]. This underestimation stems from the wrong energy position of the 3*d* orbitals of Ti within the pseudopotential description which intern courses (spurious) interaction with the O *sp* bands. To correct for the band gap underestimation in standard LDA, we have adopted the methodology of [33–35] where an *ad hoc* Hubbard *U* potential is included in the DFT+*U* scheme. Within this formalism, the Hubbard *U* values used should not be considered as empirical parameters introduced to correct the gap and not the physical on-site electron-electron screened potentials, in the sense of the many-body Hubbard Hamiltonian. The unphysical Ti_{3d}-O_{2sp} is overcome by including a Hubbard potential U = 10 eV on 3*d* orbital of Ti and 5 eV on the 2*p* orbital of O was found to produce the experimental value of gap of TiO_2. A similar approach was used to obtain *U* values for the lanthanide ions whereby we used lanthanide sesquioxides varied the Hubbard term until a band gap close to experimental value is arrived at. The experimental data used was obtained from [36–38]. The obtained values of *U* for the case of lanthanides were found to be consistent with other studies [36].

The calculated equilibrium parameters were; a = 3.792Å c/a = 2.502, which were in good agreement with experimental values, a = 3.785Å and c/a = 2.513[39], as well as another theoretical LDA+*U* results, a = 3.819Å and c/a = 2.502 [40]. After obtaining the equilibrium structure, 72 atom supercells were constructed from the equilibrium structure. The choice of the 72 atom supercell was made by calculating the dopant substitutional energy as function of supercell size up to 288 atoms, the substitutional energy difference between the 72 atom unit cell and the 288 atom unit cell was found to be ~1 eV thus due to computational efficiency, the 72 atom unit was preferred. Doping was then done by substituting Ti atoms with lanthanide atoms. In order to avoid significant dopant-dopant interaction within the lattice, lanthanide atoms were introduced at the next-nearest Ti atom sites from the site of the first substitution until the desired dopant concentration was achieved. The atomic positions of the supercells containing the dopants were then relaxed keeping the volume constant. Figure 6.1 shows a supercell containing a dopant within its lattice.

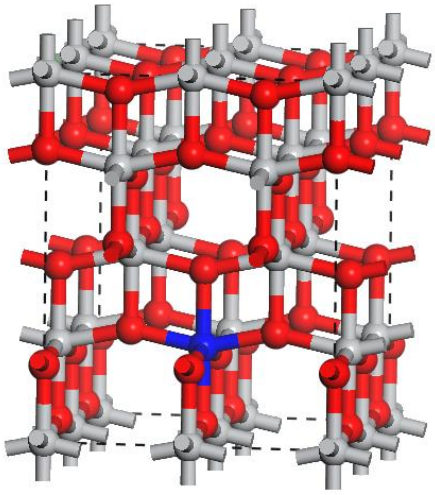

Figure 6.1 A supercell of doped anatase TiO_2 (Red, Grey and Blue balls represents O, Ti and dopant atoms respectively).

6.3 Optical properties

The response function for the optical properties of a solid, describing the absorption or emission of electrons or photons is the dielectric function. From the imaginary part of the dielectric function, it is possible to obtain some of the optical properties of a solid. In this study, the optical properties have been obtained through the frequency-dependent dielectric function, $\varepsilon(\omega) = \varepsilon_1(\omega) + i\varepsilon_2(\omega)$, using the formalism of Ehrenreich and Cohen [41]. Within this formalism, the imaginary part of the dielectric function is given as:

$$\varepsilon_2(\omega) = \frac{4\pi^2 e^2 \hbar}{m^2 \omega^2} \sum_{vc} \frac{2}{(2\pi)^2} \int_{BZ} \delta\left[\omega_{cv}(k) - \omega\right] \left| M_{cv}(k) \right|^2 d^3k \qquad (6.2.1)$$

where the integral is over the first Brillouin zone, $M_{cv}(k) = \langle u_{ck} \left| \hat{e}.\nabla \right| u_{c}k \rangle$ are the dipole matrix elements for the direct transitions between valence and conduction bands states. $\hbar\omega_{cv}(k) = E_{ck} - E_{vk}$ is the excited energy, $\hat{e}$ is the polarization vector of the electric field, and $u_{ck}(r)$ is the periodic part of the Bloch wave function for a conduction band state with

wave vector *k*. Although DFT is known to underestimate the band gap of semiconductors, our results show that optical properties obtained using DFT outputs are surprisingly in good agreement with experiment. This is attributed to the ability of the local density approximation to yield accurate matrix elements between occupied and empty states.

In this study our first goal was to determine the doping percentage that would yield visible light absorption in TiO_2 since high concentrations may lead to low photocatalytic activity. Large impurity states in the band gap that act as recombination centres for photoexcited electron-hole pairs. To achieve this, some of the optically active lanthanide elements namely; Gd, Eu and Sm were used to determine this optimal doping percentage. This was done by plotting the optical absorption of spectrum of TiO_2 doped with each of the chosen lanthanide ions individually at different concentrations as seen in Figure 6.2. From the figure, it can be seen that the doping percentage that led to absorption on the visible regime is 2.7778% (~3.0%) which is within the experimental doping percentage range [35].

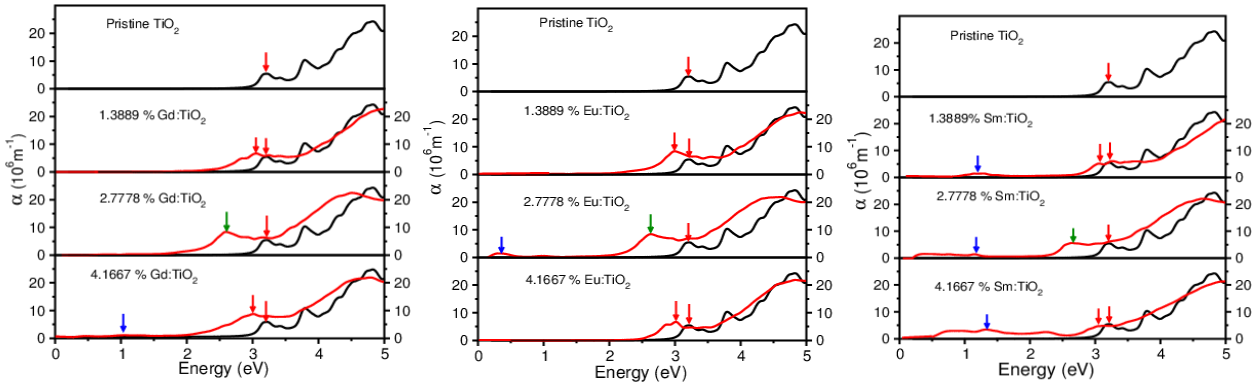

Figure 6.2 Calculated absorption spectra of TiO_2 doped with different lanthanide elements at different percentage concentrations. (Red, Green and Blue arrows represent UV, visible and IR absorption peaks respectively).

Table 6.1: Extracted absorption coefficient of doped anatase TiO_2.

Ln:TiO_2	dopant	*U* (eV)	Absorption peaks (ev)		Absorption peaks (nm)		
0%			3.2		387.5		UV
1.3889%	Gd	2	3.1		400		UV
	Eu	3	3.1		400		UV
	Sm	2	1.1 3.1	1127	400	IR	UV
2.7778%	Gd	2	2.6		476		Visible
	Eu	3	0.4 2.6	3100	476	IR	Visible
	Sm	2	1.1 2.6	1127	476	IR	Visible
4.1667%	Gd	2	1.1 3.1	1127	400	IR	UV
	Eu	3	3.1		400		UV
	Sm	2	1.3 3.1	953	400	IR	UV

After obtaining the doping percentage that leads to absorption in the visible regime, substitutional energies, electronic properties and optical properties for all the dopants were obtained at this dopant percentage (~3.0%).

6.3.1 Dopant Substitutional energies

According to the Zhang–Northrup[42] formalism, the dopant substitutional energy at any given charge state q can be obtained as

$$E^{q}_{\text{dopant}} = E_{\text{undoped}} - E_{\text{doped}} + n\mu_{\text{Ti}} - n\mu_{\text{dopant}} + q\left(E_{\text{VBM}} + E_{\text{Fermi}}\right) + E^{q}_{\text{corr}} \quad (6.2.1)$$

where E_{undoped} is the total energy of pristine TiO_2, E_{doped} is the total energy of the lanthanide doped TiO_2, μ_{Ti} and μ_{dopant} are the chemical potentials of Ti and dopant respectively, n is the number of atoms substituted or added to the supercell, E_{VBM} and E_{Fermi} are the energy of the valence band maximum and fermi energy respectively and E^{q}_{corr} is the correction made to calculated substitutional energies due to finite size errors and image charge corrections obtained using the charge model of Freysoldt *et al*.[43,44].,

$E_{corr} = E_{\text{iso}} - E_{\text{per}} - q\Delta V_{q/b}$, E_{iso} is the self-energy of the isolated charge distribution, E_{per} the electrostatic energy of the system subject to periodic boundary conditions and $q\Delta V_{q/b}$ is the potential alignment term. The calculated substitutional energies at different charge sates are presented in Table 6.2.

6.3.2 Thermodynamic transition levels

Using the calculated substitutional energies, it is possible to obtain the thermodynamic charge transition level $\varepsilon^{q/q'}$ which is defined as the Fermi energy position where a dopant in two different charge states has the same dopant substitutional (formation) energy [45]. This can be obtained for say 0 and +1 charge states as follows.

$$\varepsilon^{0/+1} = \frac{\left(E^{+1}_{\text{dopant}} - E^{0}_{\text{dopant}}\right)}{((0)-(+1))} \qquad (6.2.2)$$

where E^{+1}_{dopant} and E^{0}_{dopant} are the dopant substitutional energies for +1 and 0 charge states obtained using equation (6.2.1). Additionally, the same thermodynamic charge transition levels can be obtained by making plots of dopant substitutional energies as functions of the Fermi level position as presented in Figure 6.3. In the figure, the gradient of each line is the defect charge state, and the intersection of two lines is the thermodynamic charge transition level of the defect. The thermodynamic charge transition levels can be associated with defect levels observed from deep level transient spectroscopy (DLTS) or temperature dependent Hall measurements[45].

6.3.3 Substitutional energies

Dopant substitutional energies were calculated using equation (6.2.1). In order to bench mark our calculation with previous studies [46,47]. We have calculated the dopant substitutional energies at ~1.4% doping (one (1) atom lanthanide substitution) in the neutral charge state so as to compare our methodology to previous studies (see Table 6.2). From the table it can be seen that our results are consistent previous studies when it comes to the order of which atom easily dopes anatse TiO_2 i.e. Ce < Gd < Pr < Eu. There is difference in the substitutional energies compared to previous studies, this can be attributed to [47] not using the Hubbard term in the study and [46] using different values of U on the lanthanides compared to the ones used in this study. The different values of U resultes from using different experimental results used to bench mark/ callibrate the Hubbard term.

Table 6.2 Substitutional energies and averaged bond lengths of ~1.4% Ln-doped TiO_2.

			Substitutional energy (eV)		Bond lengths	
At. No.	Atom	*U* (eV)	This work	Other works	Ti-O (Å)	Ln-O (Å)
58	Ce	3	-1.73	-2.2[46], 1.58[47]	1.912	1.981
59	Pr	2	0.62	1.4[46], 2.83[47]	1.916	1.991
63	Eu	3	3.08	10.5[46], 5.52[47]	1.911	1.971
64	Gd	2	-1.44	0.2[46], 1.76[47]	1.922	1.982
	TiO_2				1.901	

We then proceeded using equation 6.2.2, to calculate the dopant substitutional energies at ~3.0 dopant concentration percentage (two (2) atom lanthanide substitution) (see Table 6.3. From the table it can be seen that the substitutional energies varies depending on the charge state. It can also be seen from the table that it is easy to dope TiO_2 with a majority of the lanthanide elements since the dopant substitutional energies are relatively low (≤ 3 eV) hence the reason why lanthanide doped TiO_2 have attracted lots of experimental scrutiny. Ce and Gd had the lowest substitutional energies compared to the rest of the lanthanides. Their formation energies were also negative indicating the ease of doping anatase TiO_2 with Ce and Gd. This is consistent with [46,47] as well as an experimental study that reported Ce as having the highest photo-catalytic

activity in TiO_2 [48]. The order of the dopant substitutional energies in ascending order are as follows; Ce < Gd < Pr < Pm < Nd < Lu < La < Yb < Tm < Eu. This order is also consistent with ab initio results of [47]. We then calculated the dopant substitutional energies as a function of the Fermi level also using equation (6.2.2) and the results are presented in Figure 6.3. As earlier mentioned, the intersection of any two lines in each of the figures, that is, the Fermi level position at which the dopant substitutional energies of the dopant in two different charge states are equal. This was also confirmed using equation (6.2.2). From Figure 6.3 it is evident that thermodynamic transitions resulting from the doped systems occur very close to the valence band maximum (VBM), about 1.5 eV above the VBM, Equation (6.2.2) was then used to identify the possible transitions associated with the doped systems (see Table 6.3) than may be observed experimentally through DLTS measurements.

Table 6.3 Substitutional energies (in eV) of ~3.0% Ln-doped TiO_2 at different charge states under Ti-rich conditions.

Atm. No	Dopant	*U* (eV)	-3	-2	-1	0	1	2	3
57	La	2	3.35	3.05	2.75	2.48	2.14	1.80	1.53
58	Ce	3	0.15	-0.17	-0.95	-1.31	-1.63	-2.22	-2.69
59	Pr	2	1.59	1.36	1.11	0.86	0.59	0.32	0.02
60	Nd	3	2.26	2.06	1.86	1.66	1.46	1.26	1.06
61	Pm	1.5	1.96	1.73	1.48	1.21	0.94	0.67	0.54
62	Sm	2	3.53	3.30	3.05	2.91	2.64	2.39	2.12
63	Eu	3	4.00	3.76	3.51	3.26	3.01	2.67	2.54
64	Gd	2	-0.40	-0.63	-0.88	-1.13	-1.30	-1.54	-1.74
69	Tm	2	5.82	5.28	4.78	2.84	2.39	2.35	2.31
70	Yb	2	3.32	3.09	2.94	2.81	2.54	2.31	2.04
71	Lu	3.5	2.52	2.29	1.99	1.72	1.59	1.25	0.98

Table 6.4 Calculated thermodynamic charge transition levels in eV of ~3.0% Ln-doped TiO2 referenced to the valence band maximum (VBM).

At. No.		(+3/+2)	(+1/0)	(0/-1)	(-2/-3)	(0/-2)	(-1/-3)
57	La	--	--	--	0.30	0.28	--
58	Ce	0.47	--	--	--	--	--
59	Pr	--	--	--	--	--	--
60	Nd	--	--	0.20	--	--	0.20
61	Pm	--	--	--	--	0.26	0.24
62	Sm	--	--	--	--	--	--
63	Eu	0.13	0.25	--	0.23	0.25	--
64	Gd	--	--	--	--	--	--
69	Tm	--	--	0.45	--	--	--
70	Yb	--	--	--	--	--	--
71	Lu	--	--	--	0.23	0.29	--

As can be seen from the Table, Pr, Sm, Gd, Yb had no possible thermodynamic charge transition levels. A survey of present available literature indicate that no DLTS measurements have been done of the lanthanide doped TiO_2. However, the absence of thermodynamic charge transition levels can in part be attributed to the inadequacies of standard DFT/DFT+U when it comes to defect studies [49] hence the need for techniques beyond the one used in this present study. Ce, Nd, Sm, Gd and Tm had levels that exhibited negative U characteristic. A defect has negative-U properties if it can trap two electrons (or holes) with the second being bound more strongly than the first [50]. How these negative U defects affect the photocatalytic properties of doped TiO_2 is still an open question.

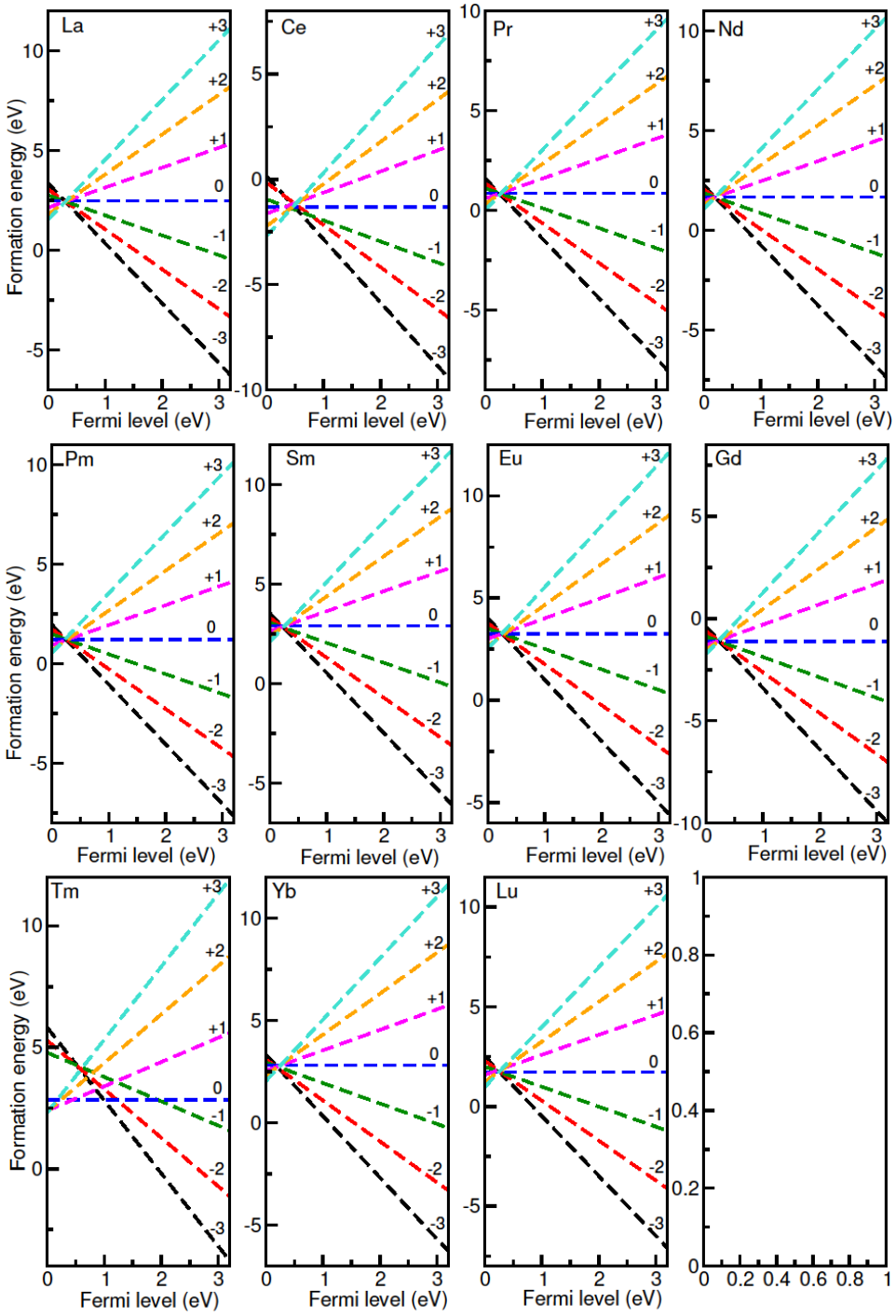

Figure 6.3 Calculated substitutional energies of doped TiO_2 as a function of the Fermi level.

6.4 Electronic properties

In order to understand the electronic properties of doped TiO_2, we calculated and obtained the projected density of states using LDA+*U*. As can be seen in Figure 6.4, the band gap of pristine TiO_2 is 3.2 eV and it is characterized by Ti 3*d* and O 2*p* orbitals in valence and conduction band respectively. On doping TiO_2, there is hybridization of Ti 3*d* and O 2*p* with the dopant states, there was no hybridization between the O 2*p* states or Ti 3*d* states with 4*f* states when TiO_2 is doped with La (see Figure 6.4 a)). Figure 6.4 also shows four sets of results as a consequence of the location of the impurity levels within the host band gap.

It can be seen from Figure 6.4 that, as the atomic number increases from La to Lu, the energy level of the impurity states shifts from conduction band (La,Ce,Pr,Nd,Pm) through the middle of the band gap (Sm,Eu,Gd) to the valence band (Tm,Yb,Lu). It can also be seen in the case of Sm, Eu and Gd (see Figure 6.3 (b)) that the dopant impurity levels are inside the band gap of TiO_2. It therefore implies in these three cases that, if photon energy is absorbed, the electrons in the valence band will first be excited to the new states (impurity states) and finally excited to the conduction band. From the PDOS of La, Pr and Nd it can be seen in Figure 6.3 (a) and (b) that they don't introduce any impurity states within the band gap TiO_2. Although Pr and Nd have dopant states deep in the conduction band, La was found not to be having the 4*f* states an observation also made by [51]. Lu, Yb and Tm introduced acceptor states while Ce and Pm introduced donor states within the band gap of TiO_2 as seen in Figures 6.3 (a), 6.3 (b) and 6.3 (c) which are likely the source of absorption peaks that lead to visible light absorption in doped TiO_2. Similar to previous studies [47], it was observed in this study that doping anatse TiO_2 with lanthanide ions resulted in delocalized 4*f* states and that it is these delocalized 4*f* states that produce impurity energy levels within the band gap. The 4*f* states were found not to hybridize with either the O 2*p* states or Ti 3*d* states unlike the case of transition metal doped TiO_2 [17]. The impurity energy levels due to the delocalized 4*f* states are broader than peaks of transition metal-doped TiO_2. This is consistent with what was observed by [47] and the reason for this broadening was explained as resulting from 4*f* states possessing seven orbits for electrons to occupy. Another consistency with [47] was observed in the comparison of doped and undoped

anatase TiO_2 where PDOS of doped TiO_2 were broader in comparison to the undoped. This was attributed to the reduction of crystal symmetry which results in electronic nonlocality [52].

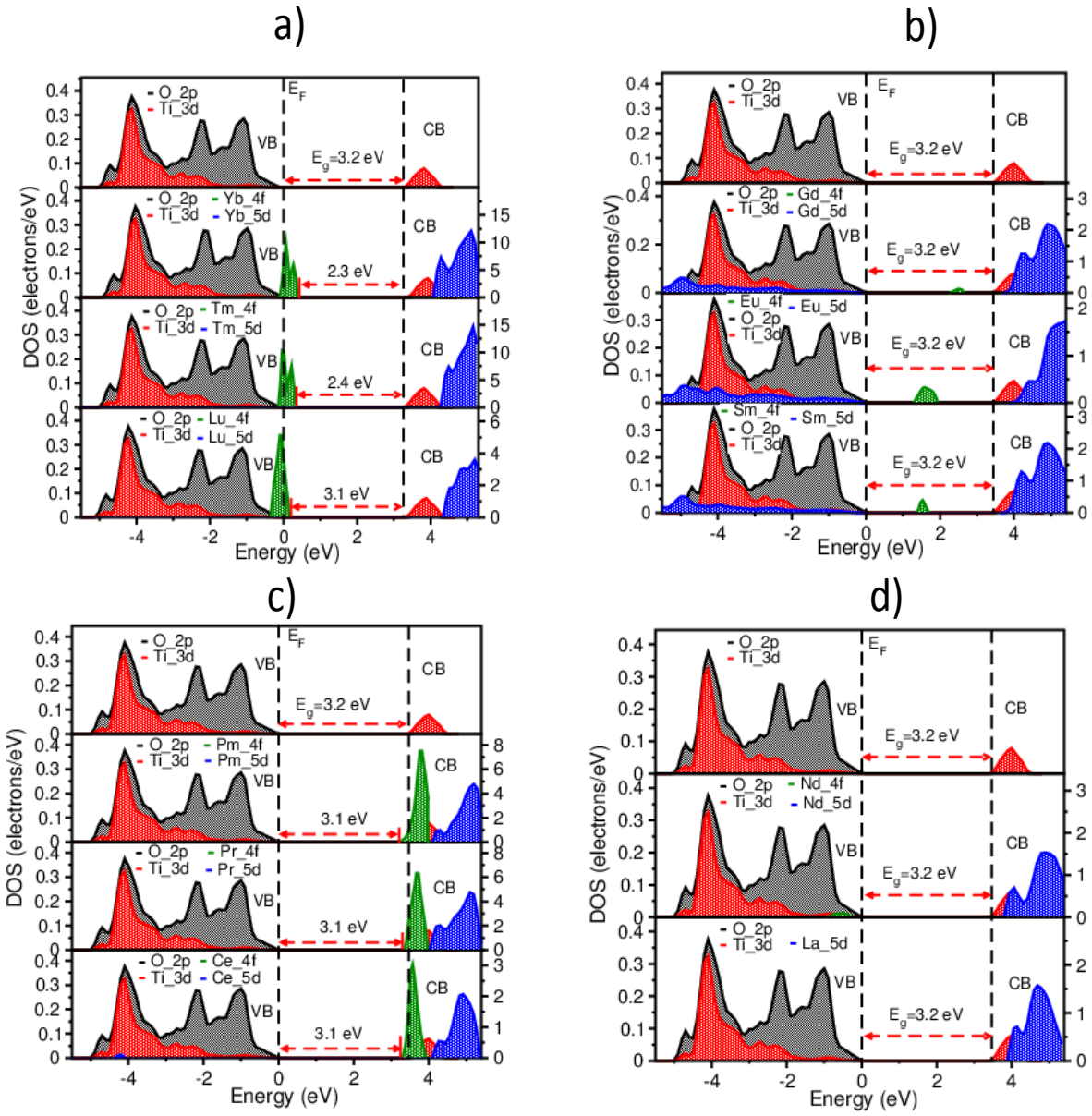

Figure 6.4 Calculated projected density of states of doped TiO_2.

6.4.1 Relationship between electronic and optical properties

The optical properties of a semiconductor are mainly determined by its electronic structure, because of this, we investigated the relationship between electronic structure and optical properties of lanthanide-doped TiO_2 systems.

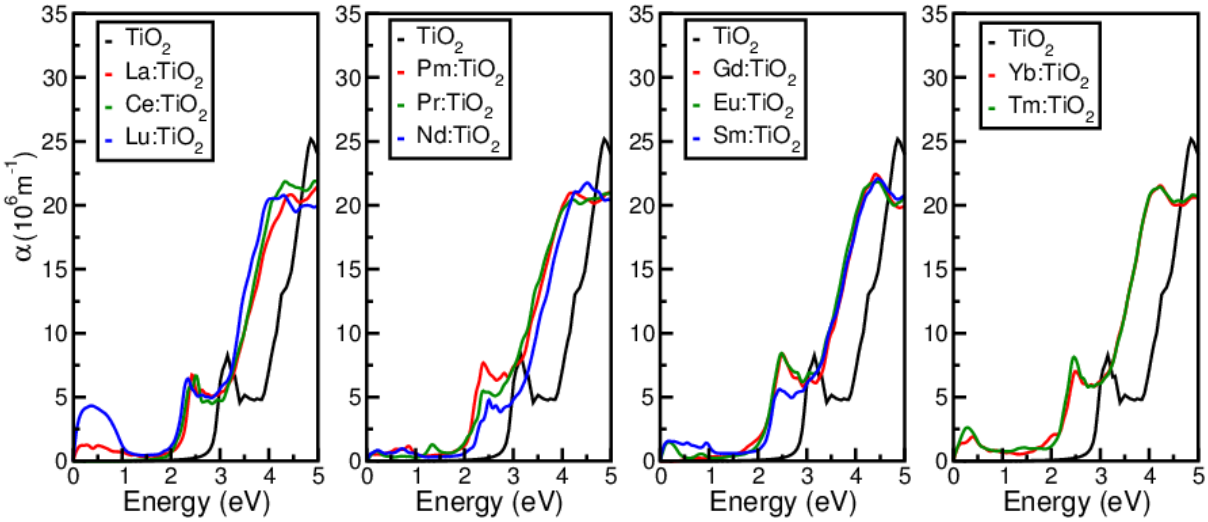

Figure 6.5 Optical absorption spectra of Ln:TiO_2

Table 6.5: Extracted absorption coefficients of Ln: TiO_2.

Ln:TiO_2	U (eV)	Absorption peaks (eV)		Absorption peaks (nm)			
0%			3.2		387.5	UV	
La	2	0.6	2.5	2066.7	496	IR	Visible
Ce	3		2.5		496		Visible
Pr	2	1.4	2.4	885.7	516.7	IR	Visible
Nd	3	0.7	2.4	1771.4	516.7	IR	Visible
Pm	1.5	0.8	2.4	1550	516.7	IR	Visible
Sm	2	1.0	2.6	1240	476.9	IR	Visible
Eu	3	1.0	2.6	1240	476.9	IR	Visible
Gd	2		2.6		476.9		Visible
Tm	2	0.4	2.5	3100	496	IR	Visible
Yb	2	0.4	2.5	3100	496	IR	Visible
Lu	3.5	0.4	2.4	3100	516.7	IR	Visible

As seen in Figure 6.4 from the PDOS of Pristine TiO_2, the band gap of anatase TiO_2 was found to be 3.2 eV, which is consistent with the optical absorption coefficient presented in Figure 6.5 and Table 6.5. Pristine TiO_2 had an optical absorption peak at 3.2 eV (388 nm) which is in the

UV region in conformity with experimental results [53]. This peak at 388 nm was used as benchmark to locate the other peaks resulting from lanthanide-doped TiO_2. For an orderly discussion on absorption coefficients, of lanthanide doped TiO_2, using the impurity state position we have come up with four categories.

Category I: Impurity states located at or around the valence band maximum (VBM) (Yb, Tm and Lu). The 4*f* impurity states of the lanthanides are at the top of the VB and new absorption peaks were observed to occur at 2.5 eV (496 nm) for Yb and Tm and 2.4 eV (516.7 nm) for Lu owing to the narrowing of the band gap as shown in Figure 6.5. This was consistent with experimental results [54,55] where absorption peaks of Yb, Tm and Lu were observed at 2.6 eV (476 nm), 2.75 eV (450 nm) and 2.8 eV (442 nm) respectively where all dopants led to peaks in the visible regime. The difference in energies might be attributes to the exchange-correlation functional which is an approximated term within the DFT formalism.

Category II: Impurity states withinin the band gap region of the host (Gd, Eu and Sm). When the lanthanides are in the octahedral discrete point charges field, the crystal field theory necessitates the intraband transition of lanthanide 4*f* electronic states [56]. Due to the position of the impurity states around the mid gap region of the host band gap, and the intraband transitions, the absorption coefficient peaks of Sm, Eu and Gd were found to shift absorption peak of the host from 3.2 eV (388 nm) which is in UV region to the visible light region at 2.6 eV (476.9 nm) as also shown in Figure 6.5 in agreement with [57–59] where the absorption peaks of Gd, Eu and Sm were observed at 2.0 eV (620 nm).

Category III: Impurity states at/around conduction band minimum (CBM) (Pm, Pr and Ce). The impurity states of Pm Pr and Ce were found to adequately cover the CBM resulting in the narrowing the bandgap to 3.1 eV which facilitates the shifting of absorption peaks from 3.2 eV (388 nm) in the pristine TiO_2 to 2.4 eV (516.7 nm) after both Pm and Pr doping and to 2.5 eV (496 nm) on Ce doping as seen in Figure 6.5. These results are in good agreement with experimental results [60,61] in which the absorption peaks on Pm, Pr and Ce absorption were observed at 2.8 eV (442 nm) for Pm and Pr while for Ce the peak was at 2.9 eV (422 nm).

Category IV: Clean band gap (Nd and La). The 4*f* states of Nd are found right inside the VB resulting in reduction in electronic occupation O 2*p*. The crystal field effect thus facilitates the shifting of absorption coefficient of the undoped host into the visible region at around 2.4 eV (516.7 nm). This was also in agreement with experimental results [62] where the absorption peak resulting from Nd doping was observed at 2.57 eV (482 nm). In the case of La doping, no impurity states from the 4*f* states were observed either within the band gap or at/around VBM or CBM. However on ploting the absorption spectrum of the La-doped system, an optical absorption peak in the visible region at 2.5 eV (496 nm) was observed. There is no explanation in literature on why La behaves in this manner. It has only been reported that it has an "exceptional phenomena [51]".

6.5 Conclusions

We have investigated the electronic and optical properties of pristine anatase TiO_2 as well as lanthanides-doped TiO_2. In addition substitutional energies of one atom and two atom substitution were investigated using DFT calculations applying LDA+*U* method. Ce and Gd had the least substitution energy in all charge states. The calculated thermodynamic transition levels exhibited negative U behaviour in the case of Ce, Nd, Sm, Gd and Tm. An optimal doping concentration was realized at 2.78% (~3.00%) which was within the experimental doping range. Doping TiO_2 with lanthanide ions was fund to results in shifting the absorption peaks of the pristine for the UV into the visible regime. Lanthanide doping in TiO_2 was also found to lead to narrowing of the band gap(i.e. red shift). From our study there was consistency in calculated electronic and optical properties of both the pristine and lanthanide doped TiO_2 with both the observed experimental results as well as other theoretical investigations.

References

[1] J. Zhang, P. Zhou, J. Liu, J. Yu, *Phys. Chem. Chem. Phys*. **16** (2014) 20382.

[2] I.K. Konstantinou, T.A. Albanis, *Appl. Catal. B Environ.* **42** (2003) 319.

[3] Y. Zhang, Z.-R. Tang, X. Fu, Y.-J. Xu, *ACS Nano.* **4** (2010) 7303.

[4] M. Ni, M.K.H. Leung, D.Y.C. Leung, K. Sumathy, *Renew. Sustain. Energy Rev.* **11** (2007) 401.

[5] M.D. Hernández-Alonso, F. Fresno, S. Suárez, J.M. Coronado, *Energy Environ. Sci.* **2** (2009) 1231.

[6] M. Yan, F. Chen, J. Zhang, M. Anpo, *J. Phys. Chem. B.* **109** (2005) 8673.

[7] J. M. Herrmann, *J. Photochem. Photobiol. A Chem.* **216** (2010) 85.

[8] Z. Zhang, X. Wang, J. Long, Q. Gu, Z. Ding, X. Fu, *J. Catal.* **276** (2010) 201.

[9] R. Long, N.J. English, *Phys. Rev. B* **83** (2011) 155209.

[10] A.B. Yusov, V.P. Shilov, *Russ. Chem. Bull.* **49** (2000) 1925.

[11] D.M. Tobaldi, A.S. Škapin, R.C. Pullar, M.P. Seabra, J.A. Labrincha, *Ceram. Int.* **39** (2013) 2619.

[12] S.H.I. Huixian, T. Zhang, W. Hongliang, *J. Rare Earths* **29** (2011) 746.

[13] K.T. Ranjit, I. Willner, S.H. Bossmann, A.M. Brau. *J. Catal.* **204** (2001) 305.

[14] K.T. Ranjit, I. Willner, S.H. Bossmann, A.M. Braun, *Environ. Sci. Technol.* **35** (2001) 1544.

[15] S. Matsuo, N. Sakaguchi, K. Yamada, T. Matsuo, H. Wakita, *Appl. Surf. Sci.* **228** (2004) 233.

[16] D. Li, N. Ohashi, S. Hishita, T. Kolodiazhnyi, H. Haneda, *J. Solid State Chem.* **178** (2005) 3293.

[17] T. Umebayashi, T. Yamaki, H. Itoh, K. Asai, *J. Phys. Chem. Solids.* **63** (2002) 1909.

[18] J. C.G. Bünzli, C. Piguet, *Chem. Soc. Rev.* **34** (2005) 1048.

[19] B. M. Tissue, *Chem. Mater*. **10** (1998) 2837.

[20] W. Liu, W. Küchle, M. Dolg, *Phys. Rev. A.* **58** (1998) 1103.

[21] J. Paier, M. Marsman, K. Hummer, G. Kresse, I.C. Gerber, J.G. Angyán, *J. Chem. Phys.* **124** (2006) 154709.

[22] J. Heyd, G. E. Scuseria, M. Ernzerhof, *J. Chem. Phys.* **118** (2003) 8207.

[23] V. Blum, R. Gehrke, F. Hanke, P. Havu, V. Havu, X. Ren, K. Reuter, M. Scheffler, *Comput. Phys. Commun.* **180** (2009) 2175.

[24] C.N.M. Ouma, M.Z. Mapelu, N.W. Makau, G.O. Amolo, R. Maezono, *Phys. Rev. B* **86** (2012) 104115.

[25] B. Himmetoglu, A. Floris, S. de Gironcoli, M. Cococcioni, *J. Quantum Chem.* **114** (2014) 14.

[26] M. Cococcioni, S. De Gironcoli, *Phys. Rev. B* **71** (2005) 35105.

[27] G. Kresse, D. Joubert, *Phys. Rev. B* **59** (1999) 1758.

[28] P. Giannozzi, S. Baroni, N. Bonini, M. Calandra, R. Car, C. Cavazzoni, *J. Phys. Condens. Matter*. **21** (2002) 395502.

[29] O. K. Andersen, *Phys. Rev. B* **12** (1975) 3060.

[30] D. D. Koelling, G. O. Arbman, *J. Phys. F Met. Phys.* **5** (1975) 2041.

[31] H. J. Monkhorst, J. D. Pack, *Phys. Rev. B* **13** (1976) 5188.

[32] H. Tang, H. Berger, P.E. Schmid, F. Levy, G. Burri, *Solid State Commun.* **87** (1993) 847.

[33] A. Janotti, D. Segev, C. Van de Walle, *Phys. Rev. B* **74** (2006) 045202.

[34] A. Calzolari, M.B. Nardelli, *Sci. Rep.* (2013) 3.

[35] A. Calzolari, A. Ruini, A. Catellani, J. *Am. Chem. Soc.* **133** (2011) 5893.

[36] R. Gillen, S.J. Clark, J. Robertson, *Phys. Rev. B* **87** (2013) 125116.

[37] A. V Prokofiev, A.I. Shelykh, B.T. Melekh, *J. Alloys Compd.* **242** (1996) 41.

[38] S. Kimura, F. Arai, M. Ikezawa, *J. Phys. Soc. Japan.* **69** (2000) 3451.

[39] T. Arlt, M. Bermejo, M. A. Blanco, L. Gerward, J. Z. Jiang, J. S. Olsen, *Phys. Rev. B* **61** (2000) 14414.

[40] M. E. Arroyo-de Dompablo, A. Morales-García, M. Taravillo, *J. Chem. Phys.* **135** (2011) 54503.

[41] H. Ehrenreich, M. H. Cohen, *Phys. Rev.* **115** (1959) 786.

[42] S. Zhang, J. Northrup, *Phys. Rev. Lett.* **67** (1991) 2339.

[43] C. Freysoldt, J. Neugebauer, C. G. Van de Walle, *Phys. Status Solidi.* **248** (2011) 1067.

[44] C. Freysoldt, J. Neugebauer, C. Van de Wall, *Phys. Rev. Lett.* **102** (2009) 016402.

[45] C. G. Van de Walle, *J. Appl. Phys.* **95** (2004) 3851.

[46] W. Chen, P. Yuan, S. Zhang, Q. Sun, E. Liang, Y. Jia, *Phys. B Condens. Matter* **407** (2012) 1038.

[47] Z. Zhao, Q. Liu, *J. Phys. D. Appl. Phys.* **41** (2008) 85417.

[48] Y. Du, M. Du, Y. Qiao, J. Dai, J. Xu, P. Yang, *Colloid J.* **69** (2007) 695.

[49] A. Janotti, C.G. Van de Walle, *Phys. Status Solidi.* **248** (2011) 799.

[50] G.D. Watkins, *Adv. Solid State Phys.* Springer, (1984) 163.

[51] W. Guan, F. Ji, Z. Xie, R. Li, N. Mei, *J. Nanomater.* **2015** (2015) 4.

[52] G. Shao, *J. Phys. Chem. C*. **112** (2008) 18677.

[53] G. K. Boschloo, A. Goossens, J. Schoonman, *J. Electrochem. Soc*. **144** (1997) 1311.

[54] M. Pal, U. Pal, R. Silva Gonzalez, E. Sanchez Mora, P. Santiago, *J. Nano Res.* **5** (2009) 193.

[55] K. Binnemans, *Chem. Rev.* **109** (2009) 4283.

[56] B. Henderson, G. F. Imbusch, *Optical spectroscopy of inorganic solids.* Oxford University Press, Oxford. (2006).

[57] M.A. Farrukh, M. Shahid, I. Muneer, S. Javaid, M. Khaleeq-ur-Rahman, *J. Mater. Sci. Mater. Electron.* **27** (2016) 2994.

[58] A. Podhorodecki, G. Zatryb, P. Sitarek, J. Misiewicz, D. Kaczmarek, J. Domaradzki. *Thin Solid Films.* **517** (2009) 6331.

[59] Q. Xiao, Z. Si, Z. Yu, G. Qiu, *Mater. Sci. Eng. B* **137** (2007) 189.

[60] J. Reszczynska, D.A. Esteban, M. Gazda, A. Zaleska, *Physicochem. Probl. Miner. Process.* **50** (2014) 515.

[61] A. Malik, S. Hameed, M.J. Siddiqui, M.M. Haque, M. Muneer, *J. Photoenergy*. **2013** (2013).

[62] D. Nassoko, Y. F. Li, J. L. Li, X. Li, Y. Yu, *Int. J. Photoenergy*. **2012** (2012).

Chapter 7

Electronic and magnetic properties of transition metal (Cr^{3+})-doped rutile and anatase TiO_2: an *ab initio* DFT+U study.

7.1 Introduction

TiO_2 plays an important role in the fields of dilute magnetic semiconductors (DMS) and photocatalysis. For both applications TiO_2 requires tailored electronic properties, which can be manipulated by selectively diluting the system by insertion of dopants. DMS have been investigated in the past in order to gain new insights in the functional principles and the manipulation of the magnetic and semiconducting properties. The search for magnetic semiconductors or for half-metals used for spin-injection led to the discovery of the new material class of d-electron magnets. The prospect of controlling the charge and the electron spin as information carriers would make it possible to combine information processing and storage at the same time [1-3]. The second major application is in the field of photocatalysis, where the favourable electronic gap range of 1.0 to 2.8 eV can be also achieved by doping. Impurity doping is an important technique for improving the response of TiO_2-based photoelectrolysis cells [2]. Chromium ions substituted for Ti^{4+} in the TiO_2, lattice have so far yielded optimal results. Substitutional Cr^{3+} in TiO_2 has a strong preference for ferromagnetic ordering. Stabilization of ferromagnetism is achieved through p-type doping. However, the description of the transition from paramagnetism to ferromagnetism varies within different levels of dopant concentration. We examine the effects of varying Cr^{3+} concentration in the TiO_2 matrix.

In our study, we computationally investigate TiO_2 anatase and rutile doped with chromium atoms, where the Cr^{3+} is sited at the Ti^{4+} site at various doping levels. Magnetic order is most common in metallic materials with narrow bands of d electrons therefore in this case, the carriers of the magnetic moments in doped semiconductors (TiO_2) is the chromium atoms. The magnetic moment is produced by the d–electrons, this is called d-electron magnetism and has been widely

studied in the recent past [4]. Regarding TiO_2 anatase from a photocatalytic aspect, we are mainly interested in the manipulation of the band gap by incorporation of impurities. TiO_2 anatase and rutile phases have band gaps of 3.2 eV [5] and 3.0 eV [6], respectively which corresponds to the ultraviolet region of the absorption spectrum [7]. The creation of electron-hole pairs comes up due to photon absorption. Photocatalytic and photoelectrochemical applications like the photoinduced decomposition of water on TiO_2 electrodes requires photon absorption as demonstrated by Fujishima and Honda [8]. In the photocatalytic utilization, creation of the electron-hole pair makes valence band (VB) become the oxidative band and the conduction band becomes reductive band. Surrounding molecules can therefore be oxidized or reduced for example radicals which are harmful to organic compounds like bacteria and fungi. Therefore, TiO_2 can be used as a purifier removing gaseous or aqueous contaminants [9,10]. In addition to water and air purification, TiO_2 has other photocatalytic applications, like antifogging and self-cleaning surfaces [11]. Since UV light only makes up 5% of the sunlight spectrum we aim to shift the absorption spectrum of TiO_2 into the visible region so as to improve the absorption rate and therefore the photocatalytic efficiency. In this case we modify the band gap using chromium impurities.

7.2 Calculation details

Within DFT, the electron–electron interaction is expressed as the sum of the Hartree and exchange-correlation (XC) terms although, the XC term is usually approximated. Due to this approximation, the XC term cannot accurately account for electronic interactions in strongly correlated systems, hence the need for DFT+U technique where a Hubbard correction U is added to the standard DFT formalism 12]. Plane wave method-based spin-polarized DFT+U calculations were performed as implemented in the Quantum ESPRESSO code [13]. The Perdew-Wang of the local density approximation with the Hubbard U correction (LDA+U) parameterization was utilized for the exchange correlation potentials. The norm-conserving pseudopotentials [14] were used for electron-ion interaction. Doping was performed by substituting one, two, three, four, five, six and seven Ti lattice atoms by Cr atoms corresponding

to the Cr doping concentration of 1%, 3%, 4%, 5%, 6%, 8% and 10%, respectively. This was done in order to investigate the effect of doping concentration on the magnetic properties of TiO_2:Cr^{3+}. A 72 atom supercell was modelled by $2\times 2\times 1$ repetition of the anatase unit cell. Plane waves with an energy up to 60 eV were included in the basis set, in order to avoid Pulay stress and other related problems. The Brillouin-Zone integration was performed using a $2\times 2\times 2$ Γ centered k-mesh with Gaussian smearing set to 0.05 eV. The total energy was converged at 1.0 $x10^{-6}$ eV. To compare and evaluate the structural changes induced by the impurities, calculations on pure TiO_2 were done initially to obtain structural and electronic data that can be used as a reference. To investigate the stability of the doped system we calculated the defect formation energies according to the following formula [15].

$$E^{f}[X] = E_{tot}[X] - E_{tot}[bulk] + n(\mu_0 - \mu_x) \qquad (7.2.1)$$

where E_{tot} is the total energy of the doped supercell with one Ti atom replaced by the impurity X(X=Cr), E_{tot}[bulk] is the total energy for the pristine system. n indicates the number of Ti atoms that have be replaced in the supercell by the dopant atoms, μ_0 and μ_x are the corresponding chemical potentials. The chemical potentials were calculated with respect to the free atom.

In order to get more stable atomic configuration and lattice parameters, the geometry optimization was performed for pure and doped systems using Broyden-Fletcher-Goldfarb-Shanno (BFGS) quasi-newton minimization scheme [16]. Supercells of optimised pure anatase TiO_2 and 6% Cr^{3+} doped TiO_2 are shown in figure 7.1.

7.3 Results and discussions

7.3.1 Geometrically optimized structure properties

It is only rutile and anatase phases which play a key role in the applications of TiO_2 in industry because of their simple tetragonal structure compared to complicated orthorhombic brookite structure. Many of the technological applications utilize the anatase phase (figure 7.1) rather than the rutile one, as this appears to be more catalytically active and exhibits a higher electron mobility. Rutile and anatase are both tetragonal, containing 6 and 12 atoms per unit cell, respectively. In both structures each Ti atom is coordinated to six O atoms and each O atom is coordinated to three Ti atoms. In each case, the TiO_6 octahedron is slightly distorted, with two Ti-O bonds slightly greater than the other four, and with some of the O-Ti-O bond angles deviating from 90^o. The distortion is greater in anatase than in rutile. The structure of rutile and anatase crystals has been described frequently in terms of chains of TiO_6 octahedra having common edges [17-18]. Two and four edges are shared in rutile and anatase, respectively. The calculated lattice parameters after geometry optimization are a = 4.5936Å, c = 2.9587Å and a = 3.784Å, c = 9.515Å for rutile and anatase, respectively from LDA+U calculations. The obtained lattice parameters are in good agreement with other theoretical calculations [19] which implies that our calculation methods are reasonable and the obtained results are trustworthy. The averaged bond lengths of the pure anatase TiO_2 and geometric optimized (0-10%) TiO_2:Cr^{3+} are provided in table 7.1. From table 7.2 the LDA+U obtained lattice parameters confirm what was realized experimentally [21]. These results also agree very well with Deskins *et al.* findings. [20].

Table 7.1: Average Mulliken bond lengths of pure TiO_2 and TiO_2:Cr^{3+} models after geometry optimization

System	Ti-O (Å)	O-O (Å)	Cr-O (Å)
Pure TiO_2	1.9759	2.719	_
1%Cr:TiO_2	1.9445	2.68	1.9353
3%Cr:TiO_2	1.9483	2.678	1.9345
4%Cr:TiO_2	1.9485	2.7001	1.9342
6%Cr:TiO_2	1.9399	2.7101	1.9341
7%Cr:TiO_2	1.9392	2.7111	1.9340
8%Cr:TiO_2	1.9390	2.7111	1.9339
10%Cr:TiO_2	1.9391	2.7112	1.9339

Table 7.2: A comparison between calculated structural properties of rutile and anatase phases with experimental data.

	a (Å)	c (Å)
Rutile		
Experiment	4.587[21]	2.954[21]
This work	4.5936	2.9587
Anatase		
Experiment	3.782[21]	9.502[21]
This work	3.784	9.515

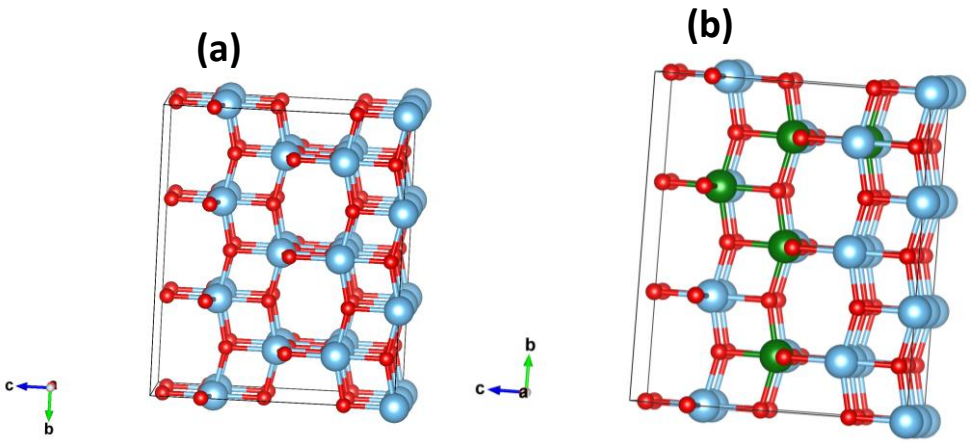

Figure 7.1 A supercell of (a) Pristine TiO_2 (b) Cr doped TiO_2 (Red, Blue and Green balls represents O,Ti and dopant atoms respectively).

The geometric optimized structures of pure anatase TiO_2 and 6% Cr-doped anatase were realized by the application of VESTA (Visualization for Electronic and Structural Analysis) [22] visualizing tool as shown in figure 7.1. In figure 7.1(a), the blue atoms represent titanium, while the red atoms represent oxygen. In figure 7.1 (b), the blue atoms are titanium, red atoms are oxygen and green balls are chromium atoms seated at Ti site. Formation energy was calculated at various substitution sites and sites with the lowest formation energy were utilized.

7.3.2 Magnetic properties

From the projected density of states output file, at the Lowdin charges part, we were able to get the magnetic moment per Cr atom. A large magnetic moment of 2.59 μB in rutile and 2.49 μB in anatase per Cr atom is found for 6% Cr-doped rutile and anatase. After 6% doping of TiO_2 with chromium, both phases reached magnetic saturation as shown in figure 7.2 (a).

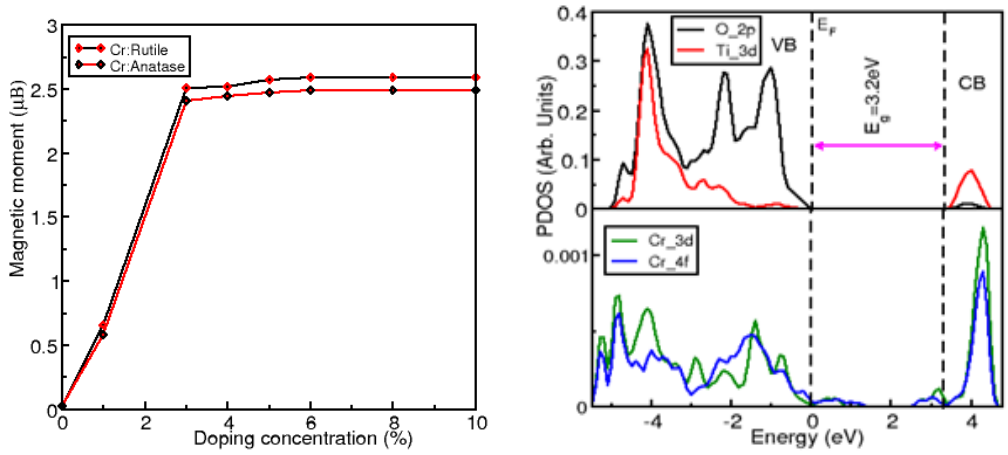

Figure 7.2 (a) Magnetic saturation in rutile and anatase. (b) PDOS of Cr doped TiO_2

The higher magnetic moment of 2.59 μB in rutile and 2.49 μB in anatase per Cr atom observed in our two phases are higher than expected. Chromium is magnetic, therefore there is a possibility that all the contribution to the magnetic moment is due to Cr atoms but there are high chances that Ti magnetic moments contributed a certain amount of magnetic moment. When we look at the hybridization of Ti_3d and Cr_3d in figure 7.2 (b), both Cr and Ti may have contributed to the observed high magnetic moments. From literature, the magnetic moment of Ti atom is 2.0 μB [23] and that of Cr is 3.0 μB [24]. Given that Cr was introduced at Ti substitutional site, then we calculated the difference in their magnetic moment as 1.0 μB. This clearly shows that both the magnetic moment of Ti and Cr are not parallel and the magnitude of the resultant magnetic moment depends on the angle between the two. The difference in magnetic moments between rutile and anatase is therefore attributed to the distortion in the crystal structure (which affects the angle between Ti magnetic moments and Cr magnetic moments) in which case the structure of the anatase phase is more distorted relative to the rutile phase as mentioned earlier. The symmetries of the rutile and anatase structure in magnetic phase are, D_{4h}^{14} for rutile, and D_{4h}^{19} for anatase.

The participation of Ti_3d electrons makes the understanding of magnetic properties in rutile and anatase more interesting.

7.3.3 Electronic properties

The top panel of figure 7.2 (b) shows pure anatase with a band gap of 3.2 eV which is exactly same as experimental value. This confirms the accuracy of our results. Impurity states are realized just below the conduction band minimum (CBM) as well as above the valence band maximum (VBM), after 4% doping of anatase with chromium. Figure 7.3 (a) and (b) confirm what is realized in figure 7.2 (b) from density of states point of view. Figures 7.2 (b) and 7.3 show an effective photocatalyst, that is, a band gap with no additional states inside. Additional states inside a band gap become electron-hole traps and recombination centers causing a reduction in the lifetime of the photoinduced charged carries, leading to a decrease of photocatalytic efficiency. Figure 7.3 (a) and (b) shows that after 6% doping (part f), the crystal structure undergoes deformation (part g and h). As seen in figure 7.3 (a) and (b), when the doping percentage is increased, more impurity states appear within the bad gap and the shape of the conduction band and valence band remains the same. After 6% doping (part f), any more increase of Cr^{3+} in TiO_2 causes a change in the shape of the valence and conduction bands. This is attributed to the crystal structure undergoing deformation (part g and h). As seen in figure 7.3, doping TiO_2 with Cr^{3+} introduces acceptor states at 4% doping in both rutile and anatase making TiO_2 a possible luminescent material. These acceptor states can act as recombination centres, thus having a negative impact on the photocatalytic property of TiO_2.

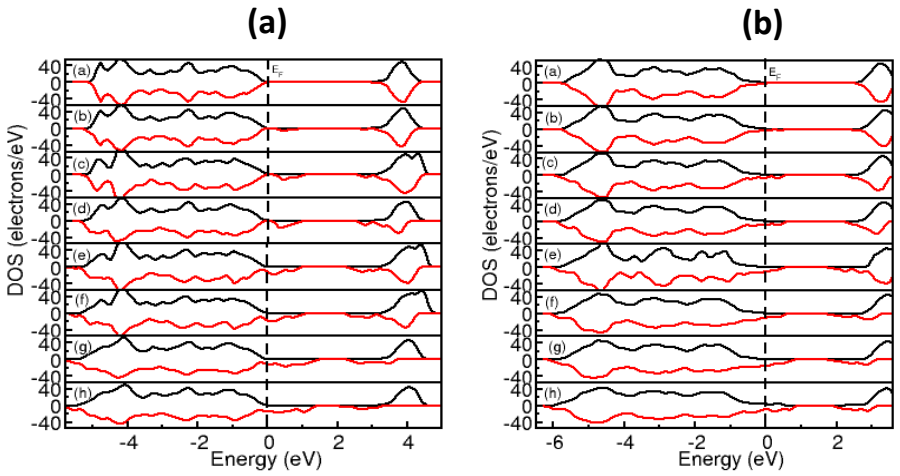

Figure 7.3 Calculated DOS of pristine and 1-10%Cr^{3+}:TiO_2 as a function of energy (a) rutile (b) anatase.

7.3.4 Photocatalytic performance.

The effect of Cr^{3+} doping on the photocatalytic effect (clean bandgap) is also shown in figure 7.3 (a) and (b). As the concentration of Cr^{3+} is increased, more dopant states are seen to be encroaching into the bandgap both from valence band maximum and conduction band minimum. This represents a shift in the absorption band edge towards longer wavelength with the increasing Cr^{3+} concentration (red shift). The red shift is maximum at 4% doping of TiO_2 with Cr^{3+} which is consistent with the experimental findings [25]. After this doping concentration, the size of the band gap remains constant. Even after attaining optimal doping concentration at 4%, with further increase in doping, crystal deformation is achieved at 6% doping, which is also the magnetic saturation point as shown in figure 7.2.

7.4 Conclusion

Cr^{3+} doped rutile and anatase are magnetic semiconductors. They acquire magnetic moment saturation at 6% doping in each case with 2.59 μB in rutile and 2.49 μB in anatase. The transition point from paramagnetism to ferromagnetism is at 6% Cr^{3+} doping in both phases. The large magnetic moments originates from two sources, that is, involvement of the 3d electrons of the Cr^{3+} ions and the formation of acceptor bound magnetic polarons, in which the spins of the holes and chromium are aligned through exchange interaction. After 6% magnetic saturation is achieved and addition of more Cr^{3+} atoms does not improve magnetic properties but distorts the crystal lattice. This study clearly shows the importance of doping TiO_2 with Cr^{3+} to enhance its magnetic and photocatalytic properties.

References

[1] D.V. Talapin, J. S. Lee, M. V. Kovalenko, E. V. Shevchenko, *Chem. Rev.* **110** (2010) 389.

[2] F. Matsukura, H. Ohno, A. Shen, Y. Sugawara, *Phys. Rev. B* **57** (1998) 2037.

[3] J. D. Rinehart, A. M. Schimpf, A. L. Weaver, A. W. Cohn, D. R. Gamelin, *J. Amer. Chem. Soc.* **135** (2013) 18782.

[4] D. N. Woodruff, R. E. Winpenny, R. A. Layfield, *Chem. Rev.* **113** (2013) 5110.

[5] M. Landmann, E. Rauls, W. G. Schmidt, *J. Phys.: Condens. Matter.* **24** (2012) 195503.

[6] K. Woan, G. Pyrgiotakis, W. Sigmund, *Adv. Mater.* **21** (2009) 2233.

[7] N. Meng, K. H. Micheal, Y. C. Dennis Leung, K. Sumathy, *Renew. Sustainable Energy Rev.* **11** (2007) 401.

[8] A. Fujishima, K. Honda, *Nature* **238** (1972) 37.

[9] M. Anne, T. Dulay, *Chem. Rev*. **93** (1993) 341.

[10] M. R. Hoffmann, S. T. Martin, W. Choi W, D. W. Bahnemann, *Chem. Rev.* **95** (1995) 69.

[11] Y. Lai, Y. Tang, J. Gong, D. Gong, L. Chi, C. Lin, Z. Chen, *J. Mater. Chem.* **22** (2012) 7420.

[12] M. Cococcioni, S. De Gironcoli, *Phys. Rev. B* **71** (2005) 35105.

[13] P. Giannozzi, S. Baroni, N. Bonini, M. Calandra, R. Car, C. Cavazzoni, D. Ceresoli, G. Chiarotti. L. M. Cococcioni, I. Dabo, A. Dalcorso, S. Fabris, G. Fratesi, S. deGironcoli F. Mauri, R. Mazzarello, S. Paolini, A. Pasquarello, L. Paulatto, C. Sbraccia, S. Scandolo, G. Sclauzero, A. P. Seitsonen, A. Smogunov, P. Umari, R. M. Wentzcovitch, *J. Phys.: Condens. Matter* **21** (2009) 395502.

[14] D. R. Hamann, M. Schluter, C. Chiang, *Phys. Rev.Lett*. **43** (1979) 1494.

[15] C. G. Van de Walle, J. Neugebauer, *J. Appl. Phy*. **95** (2004) 385.

[16] B. G. Pfrommer, M. Cote, S. G. Loulle, M. I. Cohen, *J. Comput. Phys.* **131** (1997) 233.

[17] F. A. Grant, *Rev. Mod. Phys.* **31** (1959) 646.

[18] L. Kavan, M. Grtzel, S. E. Gilbert, C. Klemenz, H. J. Scheel, *J.Am. Chem.Soc.* **118** (1996) 6716.

[19] M. E. Dompablo, M. Morales-Garcia, Taravill, *J. Chem. Phys.* **135** (2011) 54503.

[20] N. Aaron, N. Deskins, D. Michel, *Phys. Rev. B* **75** (2007) 195212.

[21] J. K. Burdett, T. Hughbanks, G. J. Miller, J. W. Richardson, J. V. Smith, *J. Am. Chem. Soc.* **109** (1987) 3639.

[22] K. Momma, F. Izumi, *J. Appl. Crystallogr*. **44** (2011) 1272.

[23] M. Castro, S. Liu, H. Zhai, L. Wang, *J. Chem. Phys.* **118** (2003) 2116.

[24] J. S. Dyck, C. Drasar, P. Lostak, C. Uher, *Phys. Rev. B* **71** (2005) 115214.

[23] P. Yan-Hua P, H. Gui-Feng, H. Wei-Qing. *Adv. Powder Technol*. **23** (2012) 8.

Chapter 8

Tuning the electronic and optical properties of lanthanide (Nd, Tm) and transition metal (Cr, Nb) doped TiO_2: an *ab initio* LDA+U study.

8.1 Introduction

Technological applications of titanium dioxide (TiO_2) are vast, ranging from optics and electronics to optoelectronics among other applications. Its application in photocatalysis, photogeneration of hydrogen and solar energy utilization has generated lots of interest [1-3]. TiO_2 has three polymorphs namely anatase, brookite and rutile. Among the three polymorphs, the anatase phase has been the subject of intense studies both experimentally and theoretically [4]. However, its wide band gap of 3.2 eV is known to lead to low photon utilization efficiency of sunlight because only the ultraviolet light(<400nm) can afford the energy for the electron transition from the valence band (VB) to the conduction band (CB) [5-10]. Furthermore, the quantum yield is low due to rapid recombination between excited electrons and holes [10]. Therefore, in order to enhance the photocatalytic activity of TiO_2, extending its optical absorption range into visible-light region and reducing the recombination of excited electron-hole (e-h+) pairs, several studies have proposed doping TiO_2 as a way of improving its optical properties. This is because the dopant element can effectively lower the e-h+ pairs recombination rate, which promotes the photocatalytic efficiency and extends optical response from ultraviolet to visible region [11-13].

8.2 Doped TiO_2

Doped TiO_2 has been the subject of intense investigations both experimentally and theoretically [14-16]. These studies on doped TiO_2 have shown that the location of dopants within the band structure of the host TiO_2 matrix is known to modify the properties of the host differently [17-

20]. Substitutional dopants introduce electronic states within the band gap either below the conduction band minimum (CBM) or above the valence band maximum (VBM), which consequently narrows the band gap [20]. Besides the location of dopant, the nature of dopant also plays important roles on the properties of TiO_2. Studies have shown that non-metal doping extends the photo-response of TiO_2 from UV to visible light by introducing impurity states within the band gap or narrowing the effective band gap. Among the non-metals, nitrogen (N) doping has been widely studied experimentally [14] and theoretically [21-22]. However, the main problems with N doping is the creation of localized 2p states just above the VBM which acts as a trap for the photo-generated carriers, and decreases the photo-generated current [23]. Besides non-metal doping, transition metal doping in TiO_2 has also been explored [24-26]. Lanthanides, which are sometimes known as the inner transition metals (TM), can be effective in shifting the absorption edge of TiO_2 towards visible light along with enhanced photocatalytic activity. This is the subject of this study where TiO_2 is doped with lanthanides, Nd and Tm and compared to doping with the transition metals Cr and Nb. Transition metals as well as lanthanides are known to exhibits a number of relatively narrow and intense luminescence bands in the visible and near infrared regions of the photoemission spectrum and are normally characterized by very sharp optical emissions ranging from the ultraviolet (UV) to the infrared (IR) [27].

8.3 Calculation details

The computations were performed using the plane-wave self-consistent code quantum ESPRESSO [28] where density functional theory (DFT) has been implemented. The basis set within this code is expanded in terms of plane waves. In this study, the exchange-correlation functional has been approximated using the local density approximation(LDA) with the Hubbard U correction added to correlated orbitals of transition metals (TM) as well as the lanthanide metals. Norm-conserving pseudopotentials were used to account for the interactions between valence and core electrons. One of the known shortcomings of DFT is that it cannot correctly account for effect of strong correlations in strongly correlated systems however, studies have

shown that this can be overcome by adding a Hubbard correction, U, to the DFT formalism [29-30]. The DFT+U approach makes use of an effective on-site columbic interaction U(U = U - J) for the correlated orbitals. The terms U and J represent the energy cost for adding an extra electron at a particular site and the screened exchange energy, respectively [30]. Although the DFT+U approach has been successful in describing the properties of correlated systems, its choice is still ambiguous since so far, there are several different techniques in which researches have arrived at making the choice for the value of U. Some of these techniques include; converging U as function of an experimentally observed property, obtaining U using the linear response method among others [29-30]. Since as mentioned above there are several ways of obtaining the value of U, in this study we have obtained our values of from previous studies. The values of U for Ti, O, Tm, and Nd were U=10 eV, U=5 eV, U=2eV, and U=3eV respectively as obtained in [31] for Nb U=4eV [32] and Cr U=6.0eV [33].

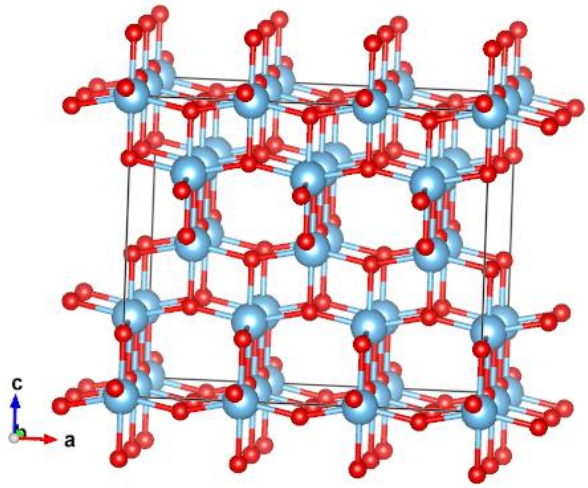

Figure 8.1 Pristine anatase TiO_2 (Light blue and red balls represent Ti and O atoms respectively).

The equilibrium structural properties of anatase TiO_2 unit cell were obtained using the following converged parameters; plane wave kinetic energy cutoff of 80 Ry, $8\times 8\times 6$ k-point mesh and all the total energies were converged to 10^{-6} Ry. The optimized bulk anatase TiO_2 lattice parameters were a = 3.787Å and c= 9.539 Å in agreement with the experimental values of a = 3.785 Å and

c= 9.514 Å [34]. An almost cubic 72 atom anatase supercell (Figure 8.1) originating from duplication of the anatase unit cell was modelled. Experimentally, dopant concentrations ranges from 0 to 4% thus, in our study we have varied the dopant concentration from 0 to ~3% (2.78%). This was by substituting up to 2 atoms of the same species in 72 atom supercell with either Tm, Nd, Cr or Nb. Once the dopant has been added, only the atomic positions were allowed to relax keeping the volume constant. One atom substitution is pretty straight forward since all the atoms are equivalent through symmetry. However, with two atom substitutions, there are several possible configurations that can be obtained. In this study we have used the site-occupancy disorder approach of [35]. Within this approach, a group of symmetry operators on the initial structure is used to generate, via atomic substitutions, a trial list of all the possible configurations. Two configurations are only equivalent if and only if an isometric relation can be used to relate them.

Table 8.1. Generated independent configurations for two (2) atom substitutions and their respective degeneracies for both Ti and O.

Ti		**O**		**O**		**O**	
Config.	**Degeneracy**	**Config.**	**Degeneracy**	**Config.**	**Degeneracy**	**Config.**	**Degeneracy**
1	12	1	12	13	24	25	24
2	24	2	24	14	12	26	24
3	24	3	24	15	12	27	48
4	48	4	48	16	24	28	24
5	24	5	24	17	49	29	24
6	24	6	48	18	96	30	24
7	48	7	96	19	48	31	12
8	24	8	48	20	24	32	12
9	24	9	48	21	24	33	24
10	12	10	24	22	48	34	48
11	12	11	24	23	48		
		12	24	24	12		

Configurational statistics are then performed on the trial list of generated configurations where every configuration is characterized using energy and degeneracy (See Table 8.1 for generated configurations). As seen from the table 8.1, the number configurations increases with the number atoms to be substituted thus, we did not go beyond two (2) atom substitutions as the number of conflagrations were going to be large.

For each of generated configurations we calculated the dopant substitution energies as

$$E_{dopant} = E_{doped} - E_{pristine} - 2(\mu_{dopant} + \mu_{Ti}) \qquad (8.3.1)$$

for Ti substitutions and

$$E_{dopant} = E_{doped} - E_{pristine} - 2(\mu_{dopant} + \mu_{O}) \qquad (8.3.2)$$

for O substitutions where E_{doped} and $E_{pristine}$ are the total energies of the doped and pristine anatase TiO_2 respectively and μ is chemical potential of the respective species.

Table 8.2. Maximum and minimum probability configurations for both Ti and O.

	Max		**Min**	
Temp (K)	Ti	O	Ti	O
0	10	9	3	32
100	10	9	3	32
200	10	9	3	32
300	10	9	3	32

Using the data obtained from equations (8.3.1) and (8.3.2) above, we did configurational averages as well as some thermodynamics calculations as elucidated in [36] so as to obtain the maximum and minimum probability configurations from the set of configurations that had been generated (see Table 8.2). These are the configurations that were then used in the rest of this study.

8.4 Results and discussions

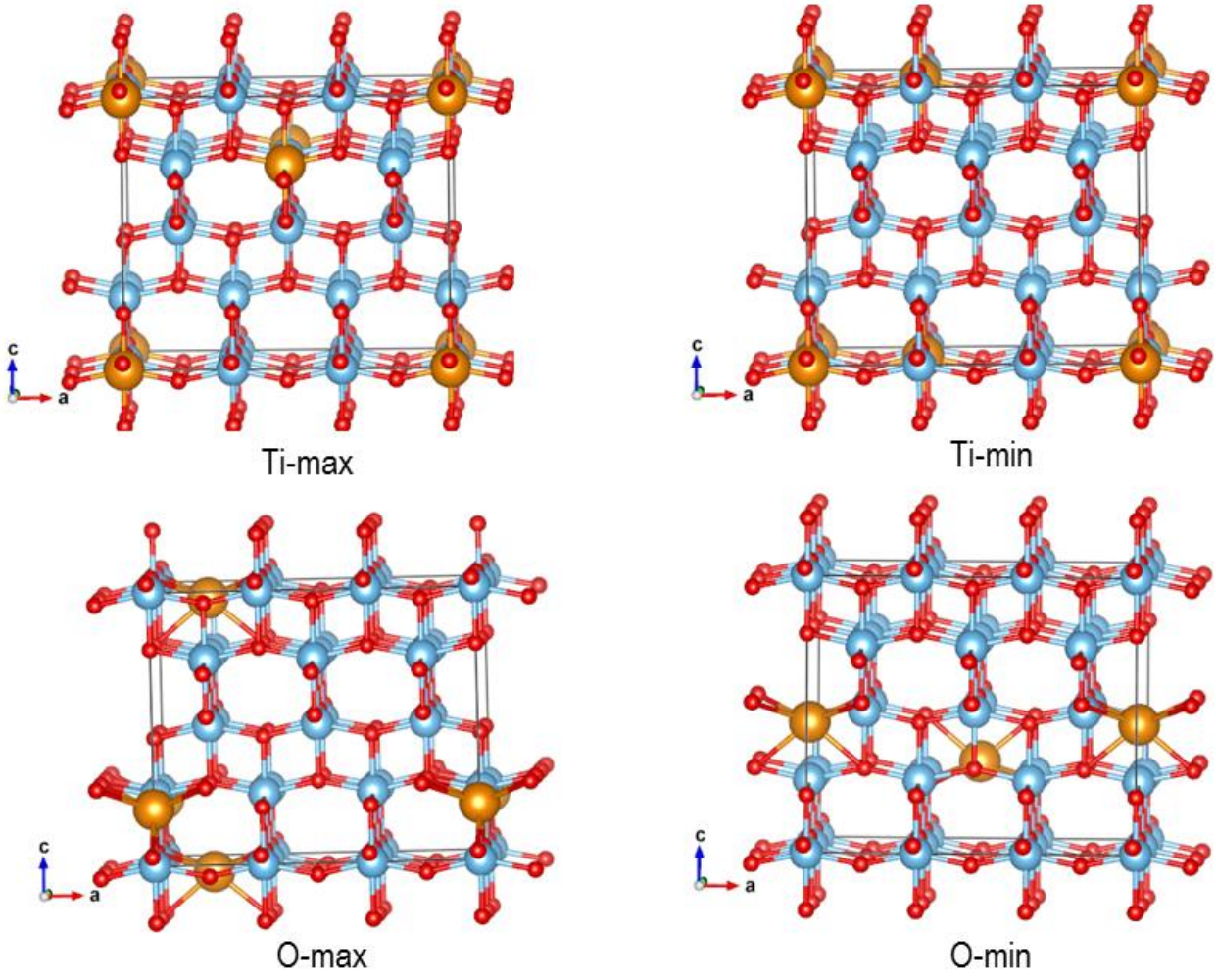

Figure 8.2 Configurations for two (2) doped anatase TiO_2 (Golden, Light blue and red balls represent lanthanide and transition metal, Ti and O atoms respectively).

8.4.1 Geometrically optimized structure properties

The calculated lattice parameters after geometry optimization were a = 3.78Å, c = 9.52Å for anatase TiO_2 from LDA+U calculations which are in good agreement with other theoretical

calculations [37], giving credence to the technique used. The averaged Mulliken bond lengths of the pure anatase TiO_2 and 2.78% doping concentration after geometry optimization are provided in Table 8.3. As seen from the table, it is evident that the presence of the dopant within the host matrix leads to some distortion within the lattice. Cr, Nd and Tm caused greater distortion than Nb. This can be attributed to atomic radius differences, since the atomic radius of Nd (1.82 Å) and Tm (1.77 Å) being greater than that of Ti (1.47 Å). Cr has an atomic radius of 1.30 Å which is relatively less than that of Ti. The atomic radius of Nb (1.46 Å) is very close to that of Ti (1.47 Å) hence very negligible distortion was observed. Cr on the other has an atomic radius which is 0.17 Å less than that of Ti causing an elongation of the bond lengths on doping. From the Table 8.3, it was also found that apart from doping with Cr, the Ti-O bond decreased on doping with other dopants compared to the Ti-O bond in pristine TiO_2.

Table 8.3: Average Mulliken bond lengths of pure and x:TiO_2 (x=Nb,Nd,Tm,Cr) after geometry optimization.

2.78%	**Nb**			**Nd**			**Tm**			**Cr**		
x:TiO_2	Ti-O	Nb-O	O-O	Ti-O	Nd-O	O-O	Ti-O	Tm-O	O-O	Ti-O	Cr-O	O-O
0%dopant	1.975	-	2.64	1.975	-	2.64	1.975	-	2.64	1.975	-	2.64
Ti_conf.10	1.943	1.976	2.62	1.945	1.98	2.63	1.955	1.978	2.61	1.995	1.972	2.65
Ti_conf.3	1.945	1.979	2.62	1.946	1.982	2.62	1.96	1.979	2.62	1.997	1.97	2.66
O_conf.9	1.946	1.978	2.63	1.947	1.984	2.61	1.958	1.98	2.61	1.998	1.971	2.65
O_conf.32	1.945	1.977	2.62	1.946	1.983	2.61	1.959	1.981	2.62	1.998	1.97	2.66

8.4.2 Electronic and optical properties

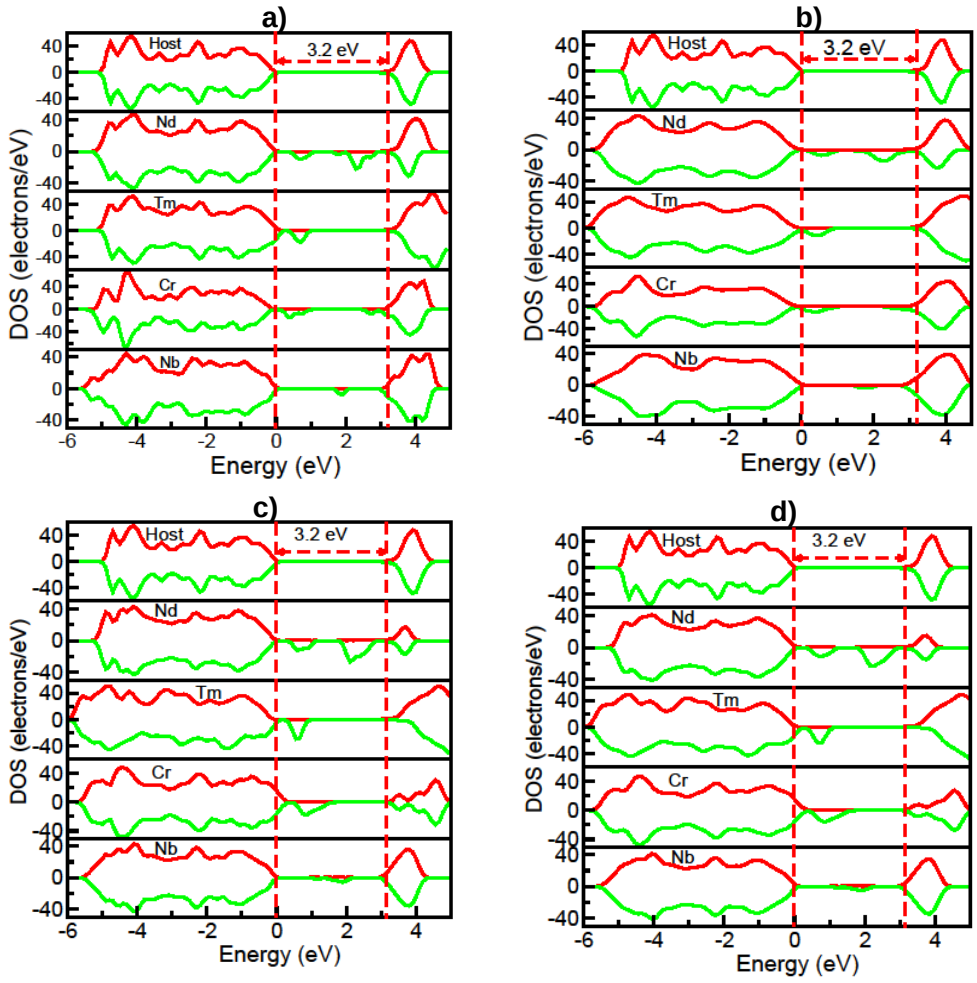

Figure 8.3 Band gap and total density of states of x:TiO_2 (x=Nd, Tm, Cr or Nb)at 2.78% dopant concentration for (a) Ti_10 configuration (b) Ti_3 configuration (c) O_9configuration (d) O_32configuration

Firstly, the effect of the dopant on the band gap of TiO_2 was investigated. This was done by identifying the position of band gap states on doping TiO_2 with different dopants (Figure 8.3). As seen in the Figure 8.3 generally there was location of states within the bandgap. This agrees very well with the Nd states realized in Figure 8.5. In all the doped systems in Figure 8.3, Tm doping,

was found to produce peaks on the valence band. This introduction of impurity states on the valence band on doping TiO_2 with Tm was also realized by Mulwa et al [38]. There was hybridization between Cr_3d states and Ti_3d as well as O_2p given that Cr_3d states appeared on both the conduction and valence band edges.

TiO_2 has promising applications in optoelectronics especially as a transparent conducting oxide (TCO). Its suitability as a TCO anchors on its optical properties such as its optical absorption and reflectivity. These properties were obtained following the methodology of [36]. Nd and Tm are lanthanide elements known to have good optical and luminescence properties as dopants in many semiconductors, while Cr and Nb are optically active transition metals. In this work, we have investigated all the possible inequivalent configurations for Nd, Tm, Cr and Nb to determine whether the position of the dopant has any influence on the host properties.

8.4.3 Effects of position of the dopant

Figure 8.2 shows two different positions of Nd dopant in TiO_2 (configuration 3 and 10), referring to Figure 8.4, Nd has a major peak at 2.6 eV. Figure 8.5 shows Nd major peaks at 2.7 eV. This clearly shows that different positions of dopants in the crystal structure causes different positions of density of states resulting to different absorption peaks.

8.4.4 Effect of doping concentration

As stated earlier, substituting one Ti, atom gave only one equivalent configuration. Figure 8.4 shows the effect on absorption spectra on increasing the concentration of the dopant. From Figure 8.4, the peak is in the UV region (387 nm) at 1.3889% doping but at 2.7778%, there was a red shift in both dopants to 477 nm, confirming that both transition metals and lanthanides doping introduce new states in the bandgap causing the red shift.

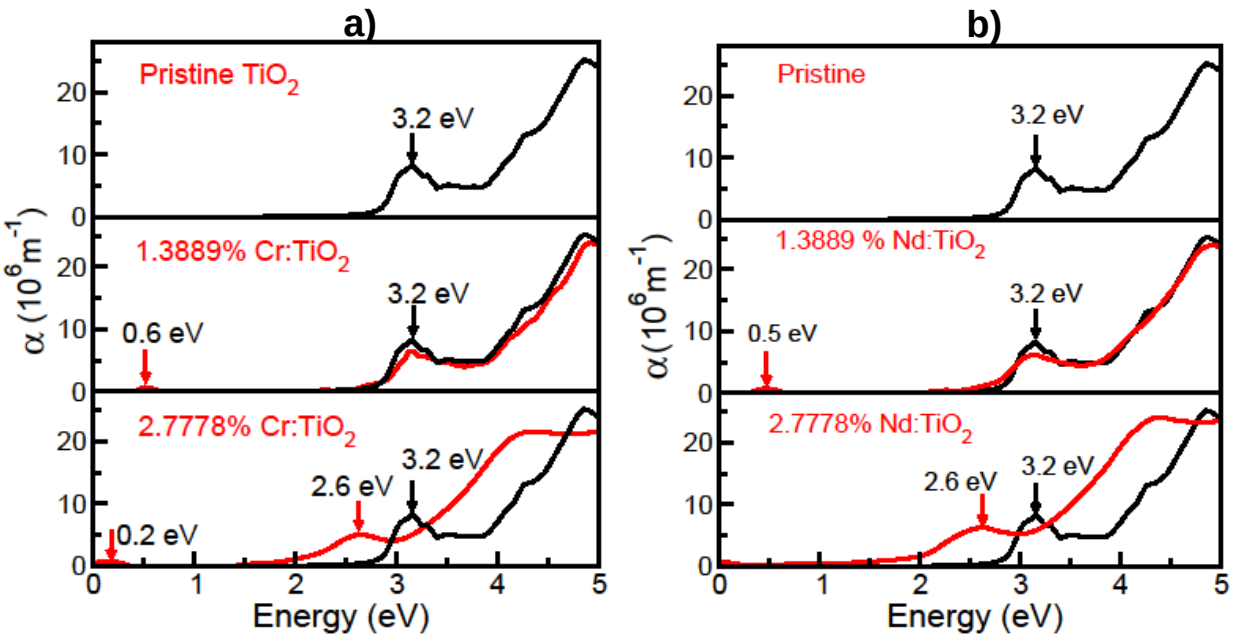

Figure 8.4 Calculated optical absorption spectra of Nd:TiO_2 and Cr:TiO_2 at different doping percentage concentrations.

As evident in Figure 8.4, the absorption spectrum of Nd:TiO_2 and Cr:TiO_2 at ~1.4% doping concentration had two peaks at 0.5 eV and 3.2 eV and 0.6 eV and 3.2 eV respectively which corresponds to emissions in the infrared and UV regions respectively. At ~2.8% there were absorption peaks at 2.6 eV in both cases which is in the visible region. These absorption peaks were due to the fact that, on doping, new states introduced within the band gap formed new unoccupied molecular orbitals, resulting to absorption edge transition to be from occupied O_2p states to the new states instead of transition from O_2p to Ti_3d in pure TiO_2. This shows that on doping, the absorption edge is at a higher wavelength than before, representing a red shift from the UV to visible spectra. From this, ~2.8% dopant concentration was found to be the optimal doping concentration of Nd and Cr in anatase TiO_2 as it is the percentage that led to absorption in the visible region since the goal of this study was to extend the absorption of TiO_2 to the visible regime. Having established the right doping percentage, the absorption for the rest of the dopants, at this doping percentage, were then obtained and compared to that of pristine TiO_2 (see Figure 8.6).

The absorption spectrum of pristine TiO_2 had peaks only UV region. This shows that doping TiO_2 with optically active elements extends the absorption spectrum of TiO_2 to the visible regime. All the different dopants show red shift in the band energy of TiO_2 when compared to the pristine sample. The photocatalytic effect is considered to be best at ~480nm (2.6 eV) [39]. Therefore, Nb, Cr, Tm and Nd can be said to improve the photocatalytic properties of TiO2 since their absorption at 2.7 eV (459 nm) and 2.9 eV (427 nm) are close to the recommended photocatalytic wavelength or energy.

The projected density of states (PDOS) of doped TiO_2 at the same dopant concentration is shown in figure 8.5. From the figure, it was evident that the presence of dopants within the matrix of the host introduces new energy states (levels) within the host band gap. In the case of lanthanides, Nd and Tm, the new states resulted mainly from the 4*f* states. As seen from figure 8.5, the band gap shifted from 3.2 eV (387 nm) to 2.7 eV (459 nm) after the incorporation of Nb ions in the TiO_2 matrix which confirms the introduction of lattice disorder from Nb doping. A similar shift from 3.0 eV (412 nm) to 2.48 eV (2.48 nm) in 5% Nb doped TiO_2 was realized by [40]. From figure 8.5, the introduction of new states in the conduction band minimum modifies the conduction band because of hybridization of Nb_4d and Ti_3d states [41]. This shows that absorption in Nb doped TiO_2 is due to transition between O_2p in the valence band and mid-gap states below the conduction band edge originating from Nb doping that is, Ti^{4+} to Ti^{3+} for each Nb^{5+} introduced or one Ti vacancy for every four Nb^{5+} introduced [42]. In the case of Cr doping, the absorption edge of TiO_2 shifted towards longer wavelengths (red shift) from 3.2 eV (412 nm) for pristine TiO_2 to 2.9 eV (427 nm) for Cr:TiO_2. This red shift on doping TiO_2 with Cr was also realized experimentally by [43]. This absorption in the visible region can be ascribed to the newly formed energy levels of Cr_3d close to the conduction band. In the case of pristine TiO_2, the valence band (VB) is mainly composed of the hybridization of oxygen 2*p* and titanium 3*d* states while the conduction band (CB) mainly consists of titanium 3*d* states an observation consistent with other studies [20,34].

The 4f states of Tm are situated in the valence band and extend into the band gap just above the valence band edge. For the Nd doped TiO_2, two impurity states of the dopant are situated in the band gap region of the host at 1.7 eV and 2.5 eV, besides the 4f states which are within the

valence band. These two states of Nd are also found in the absorption spectrum as shown in figure 8.6. Cr_3d donor states were found 0.3 eV below the CBM which corresponds to the 2.9 eV peak in figure 8.6. Figure 8.5 shows the different dopant states position in different configurations.

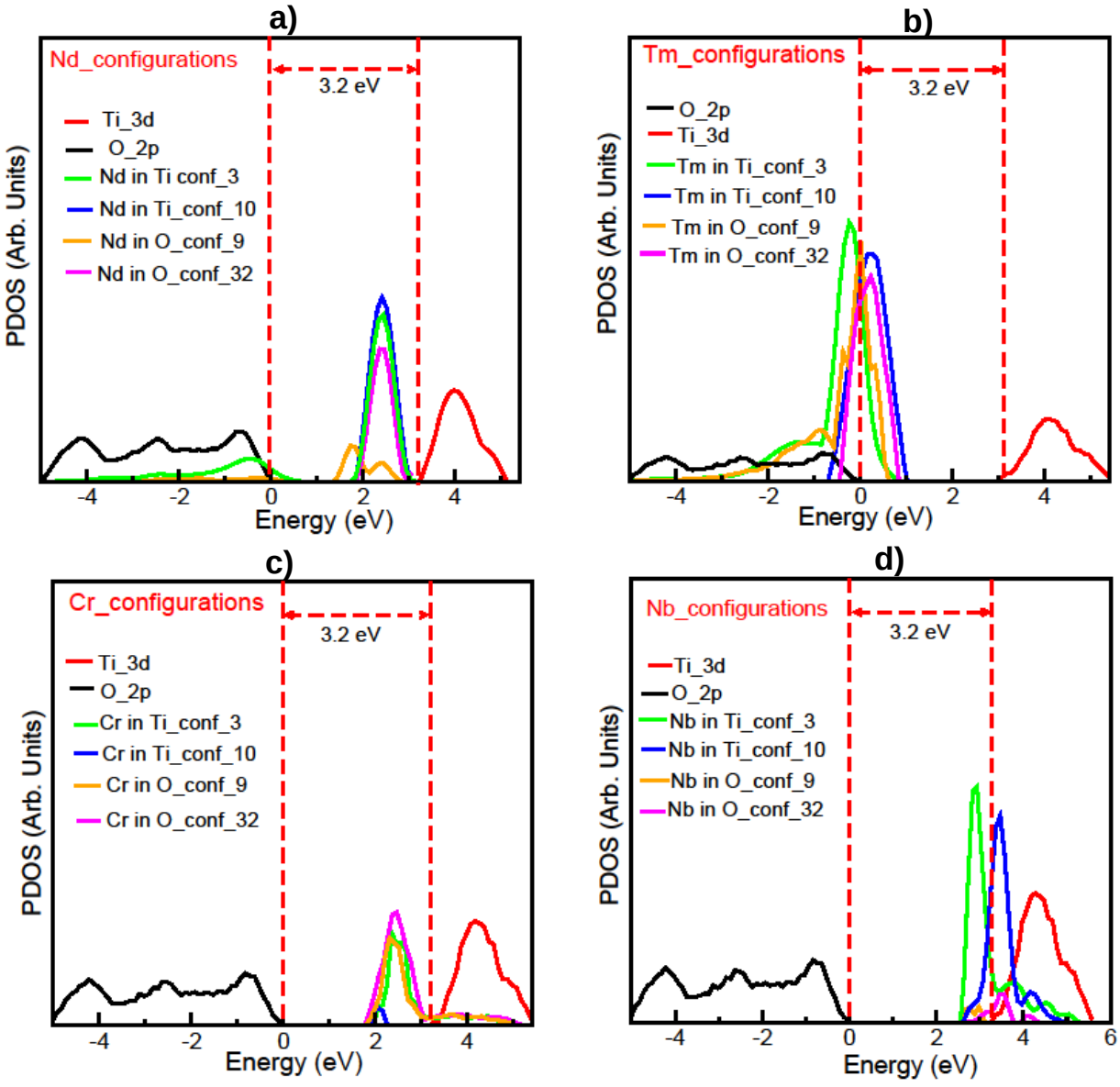

Figure 8.5 Computationally calculated density of states pristine and Nd,Tm,Cr and Nb:TiO_2.

From figure 8.5, it is evident that different configurations have their dopant states located at different positions although in the same region for each dopant. Consequently, the absorption coefficient peaks will be found to red shift to correspond to this dopant states. This was analyzed in figure 8.6.

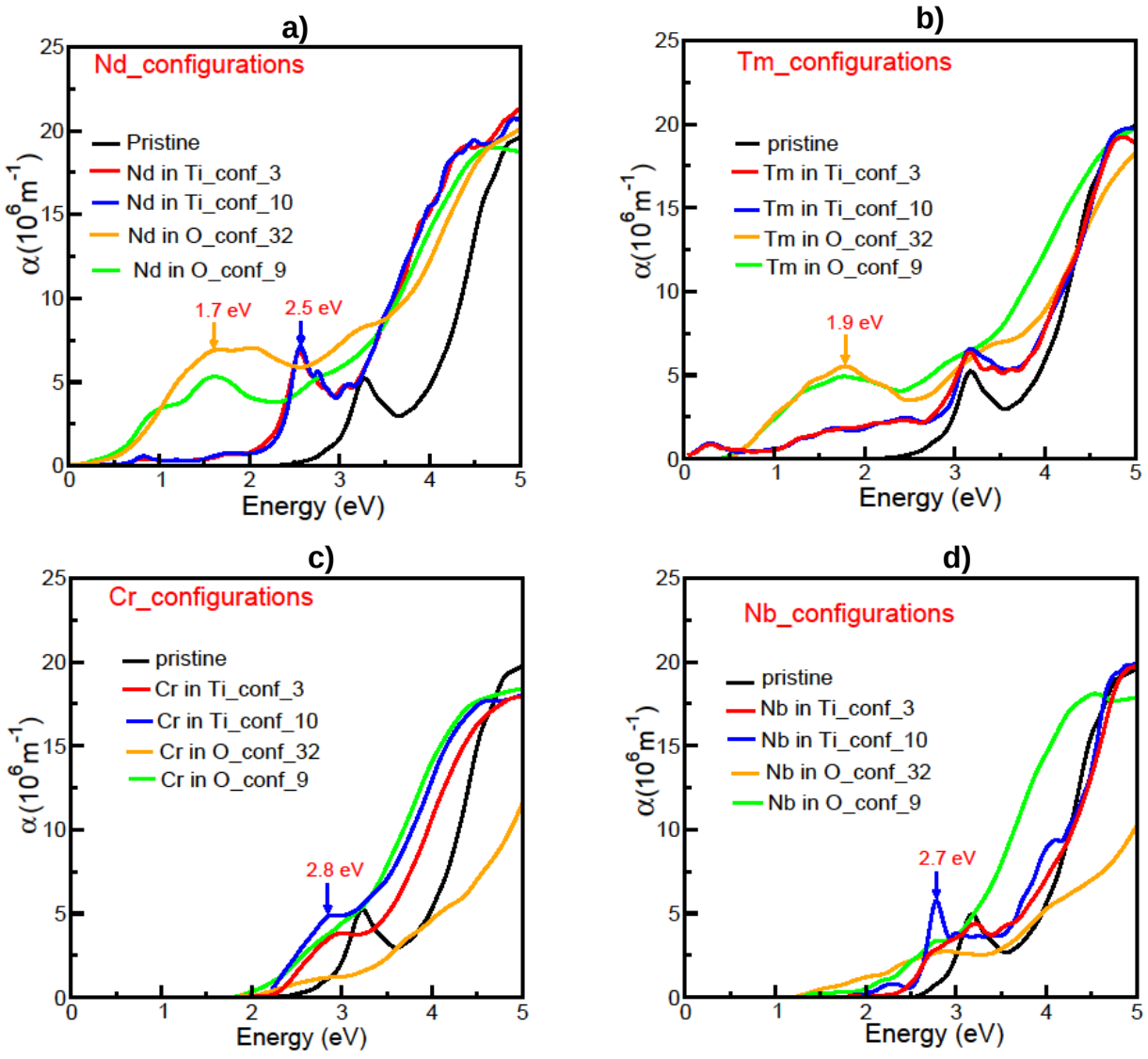

Figure 8.6 Absorption spectra of Tm:TiO_2 and Ln:TiO_2

From figure 8.6, the absorption peaks were analyzed with respect to dopant states position in figure 8.5. Nd configuration was found to have two peaks at 1.7 eV and 2.5 eV, corresponding to

the dopant states at 1.7 eV and 2.5 eV in figure 8.5. Absorption peak at 1.9 eV for Tm, was in agreement with dopant state at 1.5 eV in figure 8.5, while the Cr absorption peak at 2.8 eV corresponds to 2.8 eV dopant state in the same figure. Nb absorption peak at 2.7 eV relates to the dopant state at 2.8 eV in figure 8.5. This shows that the position of the absorption peaks which is dictated by the type of configuration is determined by the position of the dopant peak. Table 8.4 shows the analysis.

Table 8.4: Absorption coefficients of Tm:TiO_2 and Ln:TiO_2

Dopant		**configuration**	**Absorption peak**	**Absorption peak**	
			(eV)	(nm)	
Nd	Ti	Configuration3	2.7	459	visible
		Configuration10	2.7	459	visible
	O	Configuration9	1.7	729	visible
		Configuration32	1.7	729	visible
Tm	Ti	Configuration3	3.2	387	UV
		Configuration10	3.2	387	UV
	O	Configuration9	1.9	652	visible
		Configuration10	1.9	652	visible
Cr	Ti	Configuration3	2.8	442	visible
		Configuration10	2.8	442	visible
	O	Configuration9	2.8	459	visible
		Configuration32	2.8	459	visible
Nb	Ti	Configuration3	2.7	459	visible
		Configuration10	2.7	459	visible
	O	Configuration9	2.7	459	visible
		Configuration32	2.7	459	visible

8.5 Conclusion

The electronic and optical properties of Cr, Nb, Nd and Tm doped anatase TiO_2 at different doping concentrations were calculated using the first principles LDA+*U* method, with the corresponding properties of the pristine anatase TiO_2 as a reference. Cr, Nb, Nd and Tm doping at Ti sites was found to introduce dopants states within the band gap hence reducing the host's band gap and thus changing the optoelectronic activity of TiO_2. For all the dopants, ~2.8% dopant concentration was found as the optimal doping concentration since good absorption spectra were obtained at this percentage concentration. Among the dopants, Cr, Nd and Nb doping were found to greatly improve the optical properties of TiO_2. This is because, they had their absorption peaks positioned at 2.5 eV, 2.8 eV and 2.7 eV respectively, which is within the range of photocatalytic effect.

References

[1] T. Morikawa, R. Asahi, T. Ohwaki, K. Aoki, Y. Taga, *J. Appl. Phys.* **40** (2001) L561.

[2] X. Chen, C. Burda, *J. Am. Chem. Soc.* **130** (2008) 5018.

[3] C. Burda, Y. Lou, X. Chen, A. C. S. Samia, J. Stout, J. L. Gole, *Nano Lett.* **3** (2003) 1049.

[4] J. Zhang, P. Zhou, J. Liu, J. Yu, *Phys. Chem. Chem. Phys.* **16** (2014) 20382.

[5] H. Tang, H. Berger, P. E. Schmid, F. Levy, G. Burri, *Solid State Commun.* **87** (1993) 847.

[6] H. Tang, F. Levy, H. Berger, P. E. Schmid, *Phys. Rev. B* **52** (1995) 7771.

[7] H. Tang, H. Berger, P. E. Schmid, F. Levy, *Solid State Commun.* **92** (1994) 267.

[8] H. Tang, K. Prasad, R. Sanjines, P. E. Schmid, F. Levy, *J. Appl. Phys.* **75** (1994) 2042.

[9] A. Fujishima, T.N. Rao, D.A. Tryk, *J. Photochem. Photobiol. C Photochem. Rev.* **1** (2000) 1.

[10] Y. Gai, J. Li, S. S. Li, J. B. Xia, S. H. We, *Phys. Rev. Lett.* **102** (2009) 36402.

[11] C. Di Valentin, G. Pacchioni, A. Selloni, S. Livraghi, E. Giamello, *J. Phys. Chem. B* **109** (2005) 11414.

[12] S. Livraghi, M.C. Paganini, E. Giamello, A. Selloni, C. Di Valentin, G. Pacchioni, *J. Am. Chem. Soc.* **128** (2006) 15666.

[13] C. Di Valentin, E. Finazzi, G. Pacchioni, A. Selloni, S. Livraghi, M.C. Paganini, *Chem. Phys.* **339** (2007) 44.

[14] J. Wang, D.N. Tafen, J.P. Lewis, Z. Hong, A. Manivannan, M. Zhi, *J. Am. Chem. Soc.* **131** (2009) 12290.

[15] M. Khan, W. Cao, M. Ullah, *Phys. Status Solidi. B* **250** (2013) 364.

[26] C. Di Valentin, G. Pacchioni, A. Selloni, *Phys. Rev. B* **70** (2004) 85116.

[17] R. S. Zhang, Y. Liu, Q. Gao, F. Teng, C. L. Song, W. Wang, *J. Alloys Compd.* **509** (2011) 9178.

[18] A. Ali, I. Ruzybayev, E. Yassitepe, S.I. Shah, A.S. Bhatti, *J. Phys. Chem. C* **117** (2013) 19517.

[19] A. Ali, E. Yassitepe, I. Ruzybayev, S.I. Shah, A.S. Bhatti, *J. Appl. Phys.* **112** (2012) 113505.

[20] H. Kato, A. Kudo, *J. Phys. Chem. B* **106** (2002) 5029.

[21] U. Takeuchi, A. Chikamatsu, T. Hitosugi, H. Kumigashira, M. Oshima, Y. Hirose, *J. Appl. Phys.* **107** (2010) 23705.

[22] W. Li, A.I. Frenkel, J.C. Woicik, C. Ni, S.I. Shah, *Phys. Rev. B* **72** (2005) 155315.

[22] Z. Lin, A. Orlov, R.M. Lambert, M.C. Payne, *J. Phys. Chem. B* **109** (2005) 20948.

[24] K. Yang, Y. Dai, B. Huang, M. H. Whangbo, *Chem. Mater.* **20** (2008) 6528.

[25] H. Irie, Y. Watanabe, K. Hashimoto, *J. Phys, Chem. B* **107** (2003) 5483.

[26] A. Ghicov, B. Schmidt, J. Kunze, P. Schmuki, *Chem. Phys. Lett.* **433** (2007) 323.

[27] L.G. Devi, N. Kottam, B.N. Murthy, S.G. Kumar, *J. Mol. Catal. A Chem.* **328** (2010) 44.

[28] M. Khan, J. Xu, N. Chen, W. Cao, *J. Alloys Compd.* **513** (2012) 539.

[29] C. N. M. Ouma, W. E. Meyer, *Phys. B Condens. Matter.* **439** (2014) 141.

[30] P. Giannozzi, S. Baroni, N. Bonini, M. Calandra, R. Car, C. Cavazzoni, *J. Phys. Condens. Matter.* **21** (2009) 395502.

[31] A.G. Petukhov, I.I. Mazin, L. Chioncel, A.I. Lichtenstein, *Phys. Rev. B* **67** (2003) 153106.

[32] G. Mattioli, F. Filippone, P. Alippi, A. Amore Bonapasta, *Phys. Rev. B* **78** (2008) 241201.

[33] K. Yang, Y. Dai, B. Huang, *J. Phys. Chem. C* **111** (2007) 12086.

[34] J. Sun, H.-T. Wang, J. He, Y. Tian, *Phys. Rev. B* **71** (2005) 125132.

[35] P. Nath, S. Chowdhury, D. Sanyal, D. Jana, *Carbon.* **73** (2014) 275.

[36] E.H. Hwang, S. Das Sarma, *Phys. Rev. B* **75** (2007) 205418.

[37] M.E. Arroyo-de Dompablo, A. Morales-García, M. Taravillo, *J. Chem. Phys.* **135** (2011) 54503.

[38] Winfred M. Mulwa, Cecil N.M. Ouma, Martin O. Onani, Francis B. Dejene, *J. Solid State Chem.* **237** (2016) 129.

[39] S. Rengaraj, S. Venkataraj, J. W. Yeon, Y. Kim, X.Z. Li, G.K.H. Pang, *Appl. Catal. B Environ.* **77** (2007) 157.

[40] Jikai Yang, Xintong Zhang, Changhua Wang, Panpan Sun, Lingling Wang, Bin Xia, Yichun Liu, *Solid State Sci.* **14** (2012) 139.

[41] B. Mei, M.D. Sanchez, T. Reinecke, S. Kauza, W. Xia, M. Muhler, *J. Mater. Chem.* **21** (2009) 11781.

[42] A. M. Ruiz, G. Dezanneau, J. Arbiol, A. Cornet, J. R. Morante. *Chem. Mater.* **16** (2004) 862.

[43] Yan-Hua Peng, Gui-Fang Huang, Wei-Qing Huang, *Adv. Powder Technol.* **23** (2012) 8.

Chapter 9

9.1 Conclusions

In this study, *ab initio* density function theory with the Hubbard U term (DFT+U) has been used to investigate structural, magnetic, electronic and optical properties of transition metal and lanthanide doped semiconductor metal oxides ($ZnAl_2O_4$, Al_2O_3 and TiO_2). The Hubbard U term is known to overcome the failure of standard DFT in predicting the electronic properties in metal oxides. Experimentally, doped and undoped metal oxides ($ZnAl_2O_4$ and Al_2O_3) were synthesized by use of the sol-gel technique and the effect of lanthanides and transition metal doping on the materials properties is discussed. Characterization was done by use of different techniques. There was no experimental analysis done on TiO_2 studies but the computational findings agreed well with already available experimental results.

Experiment and DFT work on transition metal doped systems

$ZnAl_2O_4$ doped with a transition metal (Cu^{2+}) was investigated both computationally and experimentally. Local density approximation with the Hubbard U correction (LDA+U) for the exchange correlation (XC) potential was used to investigate structural, electronic and optical properties of $ZnAl_2O_4$ and $ZnAl_2O_4$:Cu^{2+}. The said properties were also investigated experimentally on two compounds then experimental and computational results compared. The XRD results showed a cubic crystal structure with diffraction peak at (220), (311), (400), (331), (422), (511), (440), (620) and (533), which was confirmed by XCrySDen programme. The slight shift of the diffraction peaks with increase in doping concentration compared to the host ($ZnAl_2O_4$) diffraction peak was confirmed computationally by the slight change in bond length between $ZnAl_2O_4$ and $ZnAl_2O_4$:Cu^{2+}. Band structure calculation reduced band gap which was confirmed by the UV-vis spectroscopy results showing optical absorption edge showed a shifting

to higher wavelengths. Calculated formation energies were very low suggesting that Cu^{2+} is easily incorporated in $ZnAl_2O_4$ crystal lattice. The calculated PL emission peak was in the blue region of the visible spectrum (435 nm). Experimentally, $ZnAl_2O_4$:Cu^{2+} showed maximum intensity of emission peaks at 283 nm excitation. These emission peaks were found at 425 nm and 480 nm in the blue region, suggesting good comparison between computational and experimental findings.

Experiment and DFT work on lanthanide doped systems

In γ-Al_2O_3, introduction of Ce^{3+} in the crystal lattice was done both experimentally and computationally. The Perdew-Wang parameterized local density approximation was utilized for exchange correlation approximation, while the sol-gel technique was used in synthesis and different characterization techniques were utilized. XRD results showed a cubic crystal structure with diffraction peak at (220), (311), (222), (400), (511), (440). This cubic structure was also witnessed by XCrySDen programme. There was a significant shift of the diffraction peaks to the lower angles which was confirmed by a significant change in computational bond lengths, suggesting crystal distortion with increase in dopant concentration. Due to its low formation energy, Ce^{3+} was easily introduced in the γ-Al_2O_3 crystal lattice computationally leading to a computational PL emission in the bluish-green region (502 nm) of the visible spectrum. Experimentally, the PL investigation in γ-Al_2O:Ce^{3+} showed maximum intensity of emission peaks at 240 nm excitation. These emission peaks were at 445 nm and 475 nm which is in the blue region also, suggesting a good agreement between computational and experimental results.

DFT work on lanthanide and transition metal doped systems

In TiO_2, lanthanides were introduced computationally by employing projector augmented plane wave (PAW). DFT calculations showed that on doping anatase TiO_2 with lanthanides, Ce^{3+} and Gd^{3+} dopants had the lowest substitutional energy in all the tested charge states showing that these two lanthanides are the best dopants among all the other lanthanides. A slight distortion of the crystal lattice was realized on introduction of lanthanides which also resulted in reduction of the band gap. Upon doping, the reduction in band gap caused a shift of absorption edge from ultra violet (UV) to visible region of the electromagnetic spectrum. A transition metal (Cr) was introduced in the crystal lattice of two phases of TiO_2 (rutile and anatase) and their magnetic properties investigated. At the same doping concentration, that is 6% of Cr dopant, rutile had a higher magnetic moment of 2.59 μB compared to 2.49 μB observed in anatase.

9.2. Recommendations for Future Work

The work presented in this thesis has not exhausted all the properties of semiconductor metal oxides and suggests future research is still necessary in order to gain more fundamental understanding of these oxides. For example:

- Another type of spinel for example $ZnGa_2O_4$ should be doped with the transition metal (Cu^{2+}) both computationally and experimentally in order to see whether one can obtain similar results as the ones obtained in this study.
- All the other lanthanides should be used to dope γ-Al_2O_3, both computationally and experimentally, the properties investigated before and after doping and a better conclusion draw on the effects of lanthanide doping in γ-Al_2O_3.
- Experimentally, we have several PL mission peaks which may be due to introduction of the dopant or they may be due to oxygen vacancies in the investigated metal oxides.

Computationally, we have one emission peak which is due to the dopant. Advanced computational analysis is crucial in order to find out whether we can get the exact emission peaks due to the oxygen vacancies.

Appendix A: Publications and conferences

a) Publications

1. Winfred M. Mulwa, Cecil N.M. Ouma, Martin O. Onani, Francis B. Dejene, *Energetic, electronic and optical properties of lanthanide doped TiO_2: An ab initio study*, Journal of Solid State Chemistry **237** (2016) 129-137.

2. W.M. Mulwa, B.F. Dejene, M.O. Onani, C.N.M. Ouma, *Effects of Cu^{2+} doping on the structural, electronic and optical properties of $ZnAl_2O_4$: A combined experimental and DFT+U study*. Journal of Luminescence **184** (2017) 7-16.

3. Winfred M. Mulwa, Cecil N.M. Ouma, Martin O. Onani, Francis B. Dejene, *Electronic and magnetic structure of Cr doped rutile and anatase TiO_2; an ab initio DFT+U study*. Conference proceedings, South African Institute of Physics 2015. *ISBN: 978-0-620-70714-5*.

4. W.M. Mulwa, B.F. Dejene, M.O. Onani, C.N.M. Ouma, *Structural, electronic and optical properties of Ce^{3+} doped gamma-alumina*. Under review, the Journal of Materials Research Bulletin.

5. W.M. Mulwa, B.F. Dejene, M.O. Onani, C.N.M. Ouma, *Tuning the electronic and optical properties of TiO_2: an ab initio LDA+U study*. Under review, the Journal of semiconductor science and technology.

6. W.M. Mulwa, B.F. Dejene, M.O. Onani, C.N.M. Ouma, *Electronic structure and bandgap of γ Al_2O_3:Eu^{3+} from first principles calculations*. Under review South African Institute of Physics 2016.

(b) Presentations in conferences

1. Winfred M. Mulwa, Cecil N.M. Ouma, Martin O. Onani, Francis B. Dejene, *Electronic and optical properties of Nb and Cr doped TiO_2: an ab initio DFT+U study.* 6^{th} South African Conference on Photonic Materials, 5-7 May 2015, Mabula Game Lodge, Limpopo, South Africa.

2. W. M. Mulwa, B.F. Dejene, M.O. Onani, C.N.M. Ouma, *Electronic and magnetic structure of Cr doped Rutile and Anatase TiO_2: an ab initio DFT+U study,* 60^{th} Annual Conference of the South African Institute of Physics, 29 June- 3 July 2015, Port Elizabeth, South Africa.

3. W. M. Mulwa, B.F. Dejene, M.O. Onani, C.N.M. Ouma, Electronic structure and bandgap of γ-Al_2O_3:Eu^{3+} *from first principles calculations, 60^{th} Annual Conference of the South African Institute of Physics,* 4^{th}-8^{th} July 2016, University of Cape Town, South Africa.

4. W. M. Mulwa, B.F. Dejene, M.O. Onani, C.N.M. Ouma, DFT+U and experimental studies of γ-Al_2O_3:$Ce^{3+}Cu^{2+}$ *7^{th} South African Conference on Photonic Materials,* 27^{th}-31^{st} March 2017, Amanzi Game Reserve, Brandfort, South Africa.

Journal of Luminescence 184 (2017) 7–16

Contents lists available at ScienceDirect

Journal of Luminescence

journal homepage: www.elsevier.com/locate/jlumin

Effect of Cu^{2+} doping on the structural, electronic and optical properties of $ZnAl_2O_4$: A combined experimental and DFT+U study

W.M. Mulwa [a], B.F. Dejene [a], M.O. Onani [b], C.N.M. Ouma [c,*]

[a] Department of Physics, University of the Free State (Qwa Qwa Campus), Private Bag X 13, Phuthaditjhaba 9866, South Africa
[b] Department of Chemistry, University of the Western Cape, Private Bag X17, Bellville, Cape Town, South Africa
[c] Natural Resources and Environment, Council for Scientific and Industrial Research, P.O. Box 395, Pretoria 0001, South Africa

ARTICLE INFO

Article history:
Received 1 August 2016
Received in revised form
21 November 2016
Accepted 8 December 2016
Available online 9 December 2016

Keywords:
Spinel
DFT+U
doping
$ZnAl_2O_4$
Luminescence

ABSTRACT

Using the sol-gel technique, undoped and Cu^{2+} doped $ZnAl_2O_4$ samples were prepared at $0 \leq x \leq 1.24$ Cu^{2+} percentages. X-ray diffraction (XRD) analysis confirmed that the prepared samples were cubic and that there was no phase segregation. Energy dispersive X-rays (EDS) was then used to investigate and confirm the purity of Zn, Al, O and Cu samples with no other characteristic peaks. From the XRD spectra of Cu^{2+} at different concentrations, Cu^{2+} doping was found not to lead to significant lattice distortion an observation that was corroborated with density functional theory (DFT) calculations. As the Cu^{2+} concentration was increased a slight shift to higher angles was recorded in XRD analysis, suggesting a larger ionic radius atom substituted by a smaller ionic radius atom. At 283 nm excitation, the doped samples were found to emit in the blue region (at 425 nm and 480 nm) of the color spectrum. Theoretically using DFT with the Hubbard correction term U, the doped system was found to emit at 435 nm which is within the emission range observed experimentally. From the calculated substitutional energies, O_{vac} was found to have negative formation energies indicating ease of formation form in $ZnAl_2O_4$. The binding energy for Cu_{Zn}+O_{vac} was negative indicating that these two point defects don't exist as pair inside $ZnAl_2O_4$.

1. Introduction

$ZnAl_2O_4$ belongs to the spinel class of semiconductors with a wide band gap ~3.8 eV [1]. Depending on the synthesis method, the material's crystal structure is either inverse or normal cubic spinel [2]. Spinel semiconductors are associated with a group of metal oxides whose common chemical compound is AB_2O_4 where A and B are cations with A atoms having a valence of 2 and B atoms having a valence of 3. These A and B are cations occupy 12.5% of the 64 tetrahedral interstitials and 50% of the 32 octahedral interstitials respectively [3]. Spinel structures, have many advantages such as low annealing temperatures and high quantum yields [4], high mechanical resistance [5], high photoluminescence efficiency, high chemical and thermal stability, high photocatalytic activity, low surface acidity and hydrophobic behavior [6]. All these advantages make spinel semiconductors suitable for many applications such as, catalysts, electroluminescence displays, stress imaging devices, highly efficient phosphors, photo-electronic devices and optical coating [7]. Due to these vast applications lots of research has been directed towards understanding the fundamental properties of theses spinel semiconductors as well as how these properties can be enhanced. In addition, based on the above mentioned applications, several morphologies of spinel $ZnAl_2O_4$ have been investigated namely; nanotubes, nanorods and porous structures among others [8].

This material has been studied both theoretically [9,10] and experimentally [11–13]. Theoretically, using first principles calculations, the high-pressure phase transformation of $ZnAl_2O_4$ and $ZnGa_2O_4$ has also been investigated where it was observed that there is a first-order phase transition in $ZnGa_2O_4$ and $ZnAl_2O_4$[9]. Density functional theory (DFT) combined with inelastic neutron-scattering experiments have also been used to investigate the phonon spectrum of this material in the spinel structure[10]. Experimentally, there was no phase transition on pressure increase up to 43 GPa [11].

Despite $ZnAl_2O_4$ attracting both theoretical and experimental investigations, the effect of doping on the optical properties $ZnAl_2O_4$ is still an open book. Optical properties of spinel materials are known to strongly dependent mainly on the synthesis methods [14] and their anatomy [15]. Particle size is also known to have significant influence on the optical characteristics of spinel semiconductors [16] Studies have shown that, as the size of particles approach the nano regime, differences in morphology and size

* Corresponding author.
E-mail address: moronaphtaly84@gmail.com (C.N.M. Ouma).

http://dx.doi.org/10.1016/j.jlumin.2016.12.008
0022-2313/

distribution results in differences in the chemical and physical properties [17]. This in turn implies that the size of particle has direct influences on the surface characteristics and is also likely to affect the defect levels as well as photoluminescence characteristics of the material [16].

Doping of semiconductors with transition metal elements has been shown both experimentally [18] and theoretically [19] to have an effect on the host's mechanical, electronic and physical properties. The introduction of a dopant within the host lattice usually results in defect/dopant levels being observed within the host's band gap as well as either an improvement or a decline in optical emissions of the host [20]. The effect of a dopant on the optical properties of the host is largely dependent on the type and nature of the dopant, the dopant concentration and the presence of other defects interacting with the dopant within the host's lattice [21].

Cu^{2+} forms deep trap energy levels between valence band and conduction band (t_2 energy level of Cu^{2+}). When used as a dopant, these energy levels acts as recombination centers (luminescence centers) for the excited electron-hole pair, resulting in strong luminescence [22]. This has been observed experimentally in the case of ZnO [23–26] as well as ZnS [22]. In the case of ZnS, Cu^{2+} was found to lead to blue and green emissions at 420 and 520 nm respectively [27]. This observed green emission peaks have been attributed to the recombination between the shallow donor level (sulphur vacancy) and the t_2 level of Cu^{2+}[22]. Although there are extensive investigations on the Cu^{2+} doped semiconductors, the effect that Cu^{2+} has on the optical properties of spinel semiconductors still warrants an investigation.

In this study we endeavor to investigate both experimentally and theoretically within the DFT formalism with Hubbard correction, the effect of doping on the structural, electronic and optical properties of $ZnAl_2O_4$ as function of doping concentration.

2. Methodology

2.1. Experimental details

The metal composite precursor was synthesized by sol-gel technique [28] with the use of citric acid as a chelating agent as realized from earlier findings [29]. This method is advantageous in that it can speedily produce fine and homogeneous samples after the pyrolysis of the gel [30]. Stoichiometric quantities of the metal nitrates (Zn:Al = 1:2) were dissolved in deionized water to achieve metal nitrate compound. The citric acid solution was acquired independently by introduction of citric acid into deionized water, such that the molar quotient of citric acid to the metal ions is 2:1. The citric acid solution was then added to the nitrate solution accompanied by constant mixing to guarantee homogeneous solution. After absolute mixing, the solution was then heated up at 70 °C and constantly stirred using a magnetic stirrer to evaporate the water for 3hrs. A yellowish gel was obtained. The gel was then placed in an oven at 110 °C in order to dry. The $ZnAl_2O_4$ citrate precursor was realized in a fluffy powder form. This precursor was grinded and calcined at 600 °C for 2hrs to obtain the $ZnAl_2O_4$ powder samples. The synthesis of $ZnAl_2O_4$ nanostructures with Cu^{2+} cations as dopants was performed by adding different amounts of $Cu(NO_3)_2.4H_2O$ to the $Zn(NO_3)_2.6H_2O$,$Al(NO_3)_3.9H_2O$ precursor, to obtain concentrations of 0.31, 0.62, 0.93, 1.24 mol% Cu^{2+}.

2.1.1. Characterization techniques

The crystal structures of the powders were investigated using the Bruker AXS Discover diffractometer with Cu Kα(1.5418 Å) radiation. High-resolution transmission electron microscope (HR-TEM) was done using the Shimadzu Superscan SSX-550 system. Scanning electron microscope (SEM) and selected area electron diffraction (SAED) micrographs were used to determine the morphology of synthesised nanoparticles. The optical properties were obtained via the use of the Agilent HP1100 diode-array UV-visible spectrophotometer while photoluminescence spectroscopy (PL) was done using the Hitachi F-7000 fluorescence spectrometer.

2.2. Computational details

Ab initio calculations were done within the DFT formalism with the ad hoc Hubbard correction U (DFT+U) as implemented in the DFT code quantum ESPRESSO code [31]. Self-consistent calculations were used to solve the Kohn-Sham equations employing local density approximation (LDA) with the Hubbard U correction (LDA+U) [32] for the exchange-correlation (XC) potential. By converging the value of U with respect to the experimental band gap of ZnO and CuO, the values of U for Zn and Cu were found to be 5.0 eV and U=4.0 eV respectively. Within this approach, the Hubbard U introduced is evaluated just as an empirical parameter needed to rectify the band gap [33–36]. Equilibrium properties were then obtained using; A 60 Rydberg (Ry) cut-off energy for the plane waves and a 2×2×2 Monkhorst-Pack [37] mesh was used for the Brillouin-zone integration. The self-consistent calculations were converged to 10^{-6} Ry. The calculated equilibrium lattice constant and band gap of $ZnAl_2O_4$ were 7.09 Å and 4.0 eV compared to experimental values of 8.04 Å and 4.38 eV and theoretical values of 7.99 Å [10] for lattice constant and band gap of 3.8 eV [9].

Supercells of 112 atoms were then constructed from the optimized unit cell coordinates. Doping was done via the substitution of Zn atoms with copper, until the desired concentration was reached, and the supercell was relaxed by allowing only the ions to move keeping the volume fixed. From this, substitutional energies, thermodynamic transition levels as well as optical transitions were obtained using the methodology of [33]. Using the methodology of [38,39], we included the finite size and image charge corrections in calculating the substitutional energies at different charge states. A uniformly distributed 38 k-points dense mesh was then used to obtain the optical properties according to the formalism presented in [40,41]. Thermodynamic charge transition level can also be obtained from the plot of substitutional energies at different charge states as a function of the Fermi level position where the Fermi level is allowed to shift from the top of the valence band to the bottom of the conduction band. The transition level in this case is the point at which any two lines intersect (a schematic of this is shown in results section). In order to avoid avoiding severe dopant-dopant interactions within the crystal lattice on dopant concentration increase, we have only the next-nearest Zn^{2+} location with respect to the initial substitution in this work. Fig. 1(a) and (b) shows the pristine and Cu^{2+}:$ZnAl_2O_4$ supercells.

3. Results and discussion

To investigate the structure, crystal orientation, particle size and phase determination, the sample XRD analysis were conducted on $ZnAl_2O_4$ and Cu^{2+}:$ZnAl_2O_4$ samples. The observed diffraction peaks recorded in the obtained XRD patterns agrees well with those of the standard patterns of cubic $ZnAl_2O_4$ spinel, JCPDS card No.82-1534. The diffraction peaks can be classified as (220), (311), (400), (331), (422), (511), (440), (620) and (533) diffraction lines. Energy dispersive X-rays (EDS) investigation revealed the occurance of Zn and Al in the 1:2 M ratio ascertaining the formation of single-phase $ZnAl_2O_4$ nanoparticles. The ratio of the peak intensity of prepared samples to the standard peak intensity

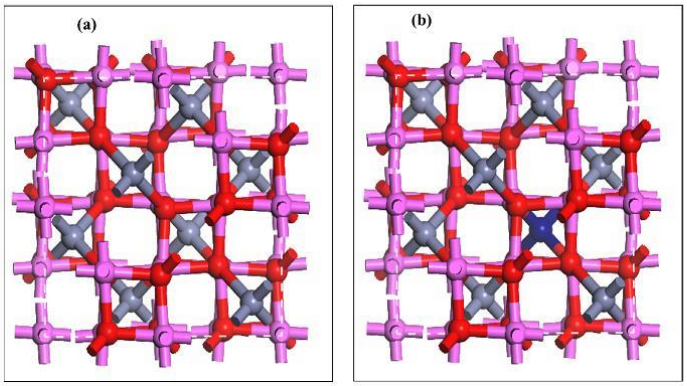

Fig. 1. (a) Undoped $ZnAl_2O_4$ and (b) $ZnAl_2O_4$:Cu^{2+}. Grey balls represent Zn atoms, red balls represent O atoms, magenta balls represent Al atoms and blue ball represent Cu^{2+} atom. (For interpretation of the references to color in this figure legend, the reader is referred to the web version of this article.)

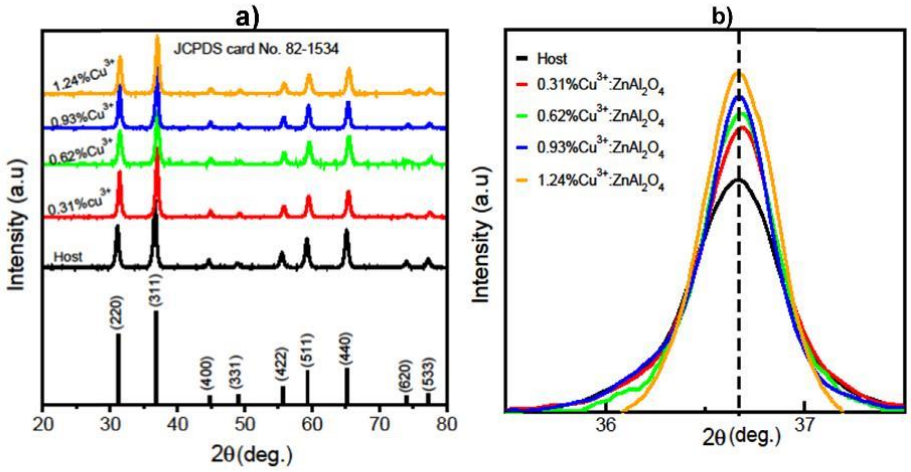

Fig. 2. (a) XRD patterns of the $ZnAl_2O_4$:Cu^{2+} ($0 - 1.24\%$) and (b) Gaussian fits of (311) diffraction peak.

Table 1
Calculated averaged Mulliken bond lengths of the $ZnAl_2O_4$:x% Cu^{2+} ($0 < x \leq 1.24\%$).

	0%	0.31%	0.62%	0.93%	1.24%
Zn-O	1.95	1.95	1.95	1.95	1.95
Al-O	1.91	1.91	1.91	1.91	1.91
Cu^{2+}-O	–	1.94	1.94	1.94	1.94

is constant. There was no peak pattern due to aluminum or zinc oxides or other phases realized in the XRD report indicating that Cu^{2+} ions were incorporated in $ZnAl_2O_4$ lattice. The XRD peaks pattern realized agreed well with the spinel structure findings of [42]. From Fig. 2(b), the Gaussian fits of the diffraction peak with highest intensity (311) positions shifted slightly towards the higher angles on Cu^{2+} percentage concentration increase. This slight shift was attributed to the small lattice strain caused when Cu^{2+} is substitutes in Zn^{2+} at a lattice site, given that there is significant difference between the ionic radii of Cu^{2+} (0.73 Å) and Zn^{2+} (0.74 Å). From the ionic radii, it is clear that substituting Zn^{2+} with Cu^{2+} will not cause significant lattice distortion. This was consistent with the calculated *ab initio* results shown in Table 1.

The mean crystallite size of the compound is evaluated based on the line broadening of the peak (311) using Debye-Scherrer equation:

$$D_{(hkl)} = \frac{0.9\lambda}{\beta_{\frac{1}{2}} \cos\theta} \quad (1)$$

where D=mean particle size of the crystal, λ=wavelength of incident X-ray, θ=corresponding Bragg angle, $\beta_{\frac{1}{2}}$=full width at the half maximum height (FWHM) of the peak. Table 2 presents calculations obtained from XRD pattern. The lattice constant was calculated using the equation;

$$a = d_{hkl}\sqrt{h^2 + k^2 + l^2} \quad (2)$$

where a=lattice constant, d=inter-planar distance and hkl are the miller indices of the planes. From the SAED pattern, we realized that $ZnAl_2O_4$ nanoparticles have inter-planar spacing of 2.823 Å, 2.416 Å, 2.020 Å, 1.632 Å, 1.553 Å and 1.420 Å corresponding to the planes (220), (311), (400), (422), (511) and (440), respectively.

Table 2
Analyzed XRD pattern corresponding to 2θ at 36.834.

Concentration	Lattice constant a_0 (Å)	2θ	FWHM(β)	Size (nm)
Host	8.039	36.834	0.6271	14.0
0.31% Cu^{2+}	8.033	36.835	0.6272	13.9
0.62% Cu^{2+}	8.026	36.837	0.6272	13.9
0.93% Cu^{2+}	8.019	36.839	0.6272	13.9
1.24% Cu^{2+}	8.013	36.841	0.6271	14.0

Further analysis on the highest intensity peak (311) revealed that the inter-planar spacing was 2.424 Å, 2.422 Å, 2.420 Å, 2.418 Å and 2.416 Å for the 0% Cu^{2+}, 0.31% Cu^{2+}, 0.62% Cu^{2+}, 0.93% Cu^{2+} and 1.24% Cu^{2+} respectively. This caused a reduction in lattice constant as the defect percentage is increased as shown in Table 2.

From Table 2, it can be seen that from the (311) diffraction peaks, the broadening of the peaks is very small, meaning that the crystallite sizes almost remained constant.

3.1. Morphological studies

Fig. 3 shows the SEM micrographs of the $ZnAl_2O_4$ and $ZnAl_2O_4$:Cu^{2+} phosphor calcined at 600 °C for 2 h. From Fig. 3, it is clear that phosphor synthesized by the sol-gel technique reveals uniform, distributive and spherical morphology. Phosphor nanoparticles with uniform size are therefore important in production of highly efficient and uniform luminescence [43]. This is because as mentioned earlier, size and size rationing has a direct influence on the luminescent characteristics of a phosphor. Smaller nanoparticles have a tendency to possess extra surface luminous states occurring from their magnified surface/bulk volume quotient. This shows that finer nanoparticles have conflicting luminescent characteristics compared to the sizable particles [44,45].

Fig. 3(c) shows existence of angular particles composed of very small crystals. The average particle size is about 40.00 nm. Apart from angular crystals, the powders show porous structures. The identified portion in Fig. 3a) is magnified to obtain the identified part in Fig. 3(b). This shows that the samples are highly porous.

Fig. 4, exhibits the HR-TEM micrograph of the sol-gel synthesized samples. The Figure indicates that these particles of nano size are comparably spherical. HR-TEM (Fig. 4) showed that the crystallite sizes (in nm-scale) and particle agglomeration is influenced by the Cu^{2+} concentration percentage. The average estimated crystallite size from Fig. 4 in both host and doped HR-TEM images is around 14.05 nm. This is consistent to what was observed in the XRD line broadening calculations. The host particles are slightly dispersed from each other while in the doped system, sticking of particles to one another is witnessed in Fig. 4(b) which is due to the slight distortion on substituting Cu^{2+} (ionic radius 0.73 Å) in Zn^{2+} (ionic radius 0.74 Å) site. As can be seen in Fig. 4, the particle distribution of undoped $ZnAl_2O_4$ is non agglomerated while that of Cu^{2+}:$ZnAl_2O_4$ is agglomerated.

Fig. 5a) shows the interplanar distance of pristine $ZnAl_2O_4$ to be 2.42 Å while Fig. 5b) shows the reduction of the interplanar distance to 2.41 Å of introduction of Cu^{2+} in the $ZnAl_2O_4$ crystal lattice. This reduction in interplanar distance means a reduction in the lattice constant as presented in Table 2.

Fig. 6a) shows the (hkl) miller indices of $ZnAl_2O_4$. The diameter of the diffraction rings which was arrived at by use of imageJ program was found to directly proportional to $\sqrt{h^2 + k^2 + l^2}$. It is

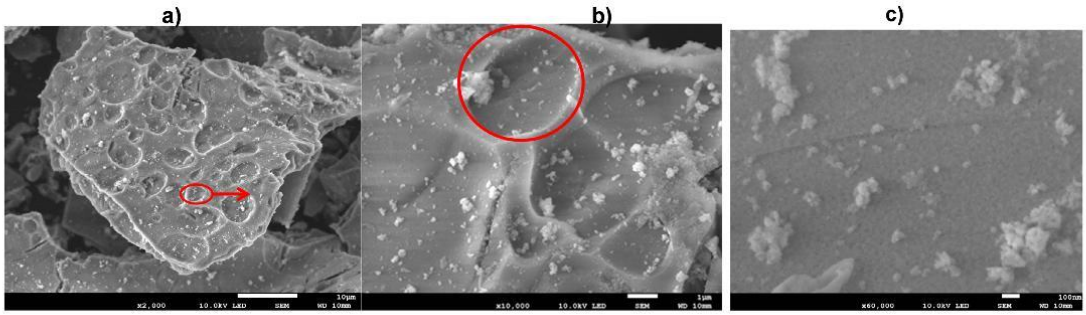

Fig. 3. SEM micrographs of $ZnAl_2O_4$:Cu^{2+} a) ×2000 b) ×10000 c) ×60000 magnifications.

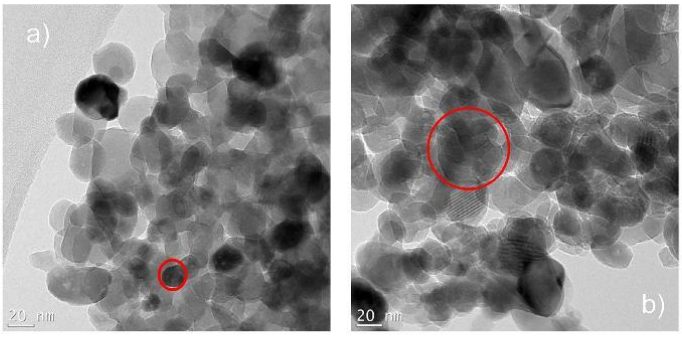

Fig. 4. TEM micrographs of a) $ZnAl_2O_4$ and b)$ZnAl_2O_4$:Cu^{2+}.

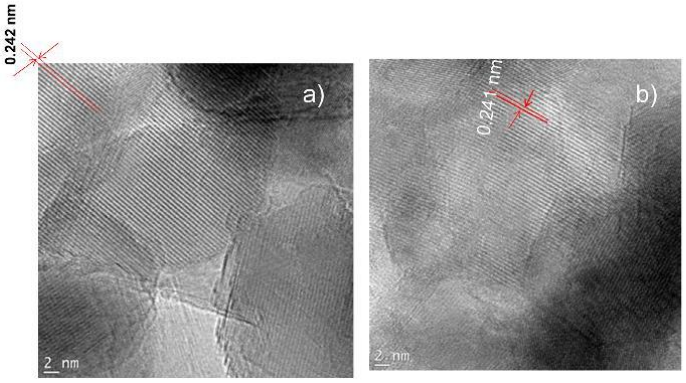

Fig. 5. The lattice fringes of a) $ZnAl_2O_4$ b) $ZnAl_2O_4$:Cu^{2+}.

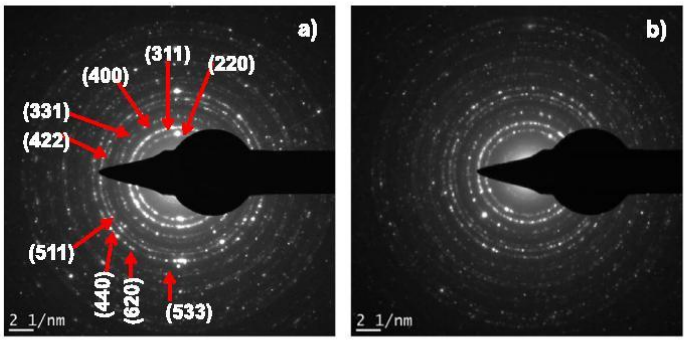

Fig. 6. Selected area electron diffraction of a) $ZnAl_2O_4$ b) ZnAl2O4:Cu^{2+}.

from this relationship that we were able to label the diffraction rings as shown in Fig. 6a). Fig. 6b) shows diffuse diffraction spots compared to Fig. 6a). These diffraction spots mean that there was lattice strain on introduction of a dopant. They also show that there was reduction in the interplanar distance as explained before (Fig. 5b)).

Fig. 7: shows the peaks corresponding to Zn, Al, O in pristine $ZnAl_2O_4$ and peaks corresponding to Zn, Al, O, Cu^{2+} in $ZnAl_2O_4$:Cu^{2+}. The observed percentage of Cu, Zn, Al and O corresponds well with the quantities of Cu, Zn, Al and O used in respective precursors without any other characteristic peaks. The analysis proved that the sol-gel technique is very successful as no depletion of elements arose during the synthesis. An O characteristic peak appeared at 0.25, 0.5 and 0.75 KeV while that of Zn appeared at 8.3, 8.5 and 9.5 KeV, and Al at 1.0, 1.5, 7.5 and 8.7 KeV. The Cu^{2+} peak was observed at 8.3 and 8.9 KeV for the doped system.

Theoretically, upon optimizing the unit cell of $ZnAl_2O_4$ and using the Murnaghan's equation of state (EOS)[46], the equilibrium lattice constant was found to be 7.09 Å which corresponds to the experimental lattice constant 8.039 Å reported in Table 2. This value is in accordance with the (311) lattice spacing of the $ZnAl_2O_4$[47]. Suppose a semiconductor with a direct band gap, at the band edge, the absorption coefficient is arrived at by use of Eq. 3;

$$\alpha = \frac{A}{h\nu}(h\nu - E_g)^{\frac{1}{2}} \tag{3}$$

Where α = absorption coefficient, $h\nu$ = photon energy, E_g = energy gap and A = a constant determined by the type of transition. For any energy, Eq. 3 can be rearranged to

$$(\alpha h\nu)^2 = A^2(h\nu - E_g)^{\frac{1}{2}} \tag{4}$$

From Eq. 4, when the value of $h\nu$ is 0, and the value of E_g is same as $h\nu$, The band gap can be obtained by plotting $(\alpha h\nu)^2$ as a function of $h\nu$ and determining the intercept on the $h\nu$ axis by extrapolating the linear part of the plot to $(\alpha h\nu)^2 = 0$ as shown in Fig. 12 (c). Fig. 12 (c) agrees well with the transition in Fig. 8 which is a direct band gap model at Γ giving an effective band gap of 2.2 eV. According to the electronic configurations, of the elements involved, Cu_4p as well as Cu_4s orbitals are found in the conduction band while Cu_3d orbitals makes a filled valence band. The expected transition is therefore from Cu_3d to Cu_4p or from Cu_3d to Cu_4s.

3.2. Substitutional energies and thermodynamic charge transitions

In order to determine how easy it is to incorporate the dopant into the host lattice, we calculated *ab initio*, the defect substitutional energies at different charge states were calculated. The computed substitutional energies at different defect states are

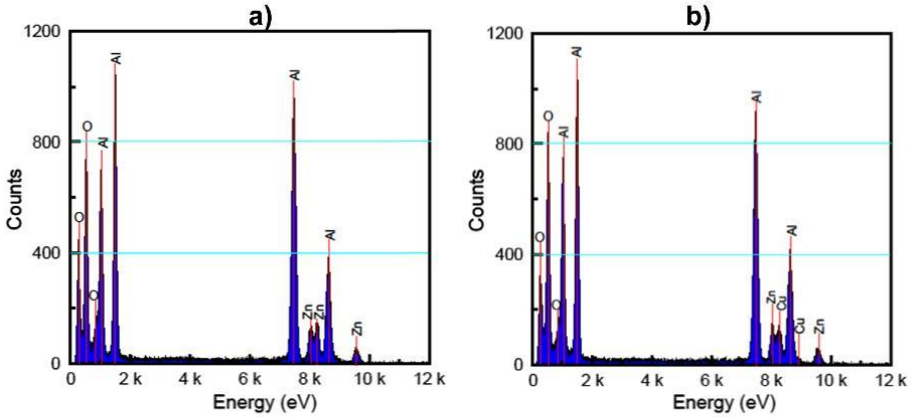

Fig. 7. EDS spectra of a) $ZnAl_2O_4$ b) $ZnAl_2O_4$:Cu^{2+}.

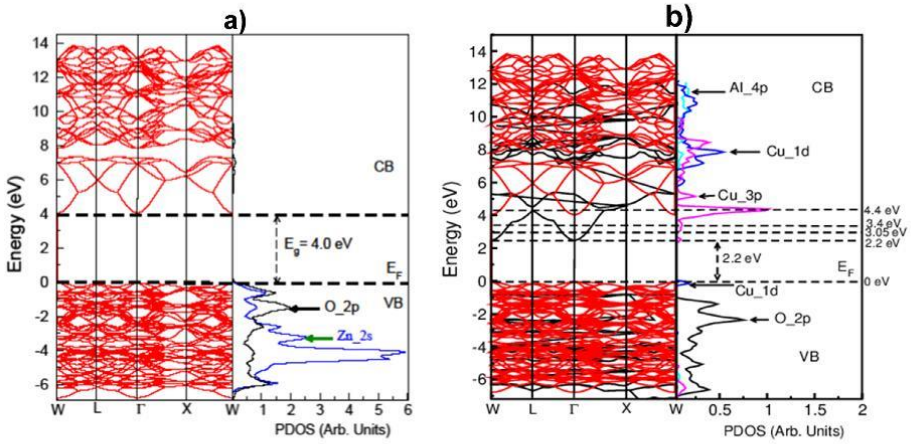

Fig. 8. Band structure and PDOS of a) pristine $ZnAl_2O_4$, (b $ZnAl_2O_4$:1.24%Cu^{2+}.

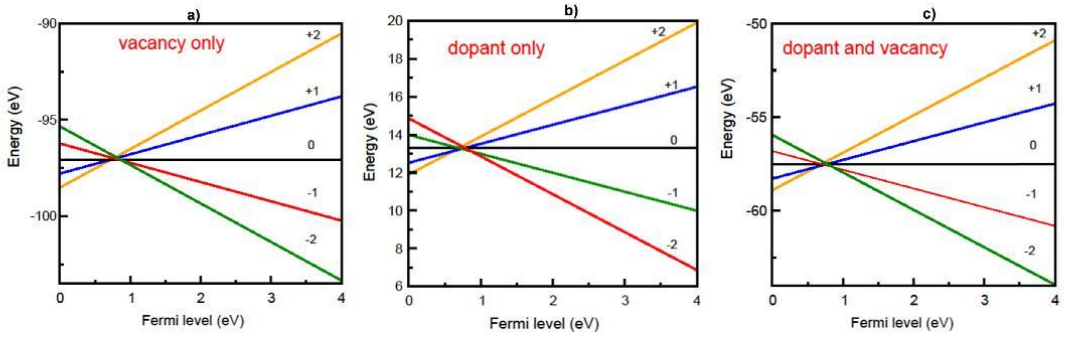

Fig. 9. Calculated thermodynamic transition levels for $ZnAl_2O_4$:Cu^{2+} at different dopant concentrations.

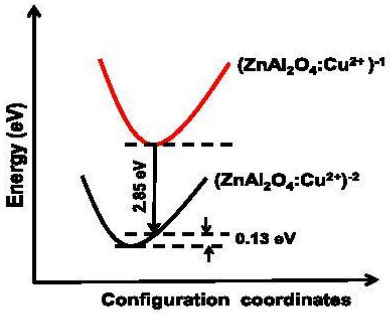

Fig. 10. Calculated configuration coordinate diagram for Cu^{2+} doped $ZnAl_2O_4$ showing the PL emission energy for exchanging an electron with the conduction band for one atom substitution.

shown in Table 3. From the calculated substitutional energies it can be seen that it's possible to easily dope $ZnAl_2O_4$ with Cu^{2+} as there substitutional/formation energies are sufficiently low especially for one (1) and two (2) atom substitutions. (Table 3).

From Table 3 it can be seen that both oxygen vacancy O_{vac} as well as Cu_{Zn}+O_{vac} defect complex (pair) spontaneously forms in $ZnAl_2O_4$ because they had negative formation energies. Only Cu_{Zn} had positive formation energy although this was also very low. We then calculated the binding energy of the defect complex. The binding energy can be obtained as $E_B = E^f{}_{O_{vac}} + E^f{}_{Cu_{Zn}} - E^f{}_{Cu_{Zn}-O_{vac}}$ where, E_B is the binding energy, $E^f{}_{O_{vac}}$, $E^f{}_{Cu_{Zn}}$ *and* $E^f{}_{Cu_{Zn}-O_{vac}}$ are the calculated substitutional/formation energies of defects. The calculated binding energies were negative indicating that the Cu_{Zn}+O_{vac} defect complex cannot form with $ZnAl_2O_4$ and that these two point defects exist individually within the lattice. This implies that it is possible to experimentally observe distinctive emission peaks associated with O_{vac} and Cu_{Zn} alone with no peaks

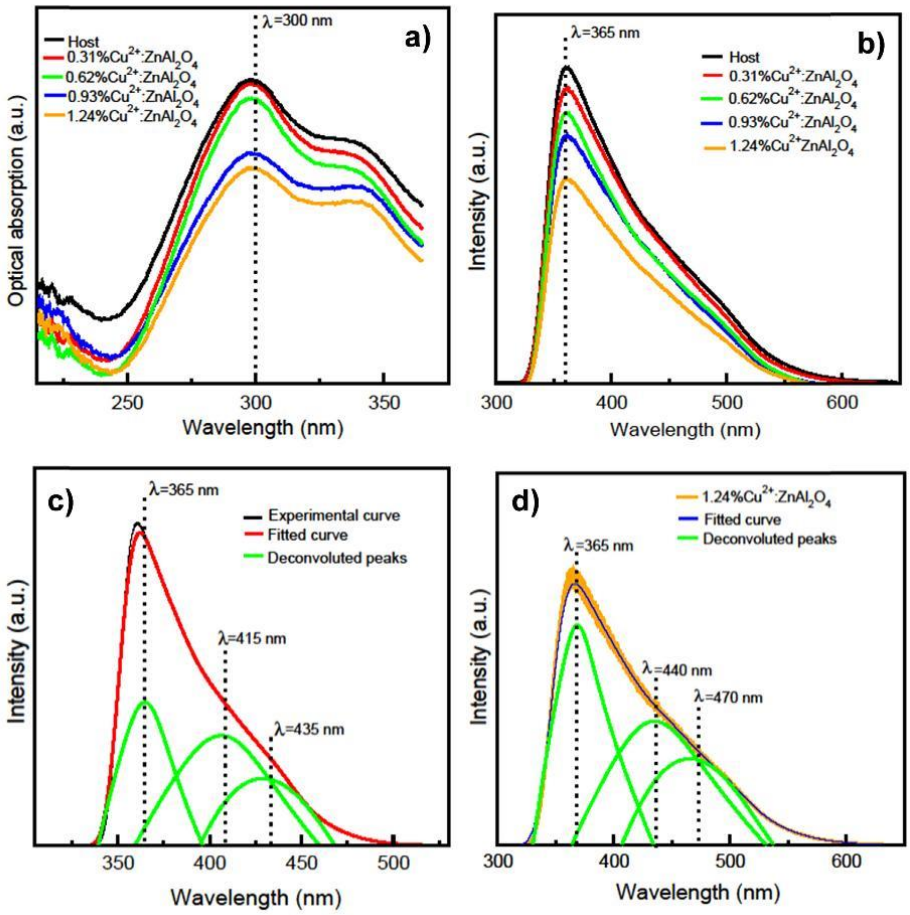

Fig. 11. PL (a) optical absorption spectra of the undoped and different % of $ZnAl_2O_4$:Cu^{2+} (b) emission spectra for $ZnAl_2O_4$ and $ZnAl_2O_4$:Cu^{2+} (0 – 1.24%) phosphor (c) Deconvoluted experimental curve (pristine) (d) Deconvoluted 1.24%Cu^{2+}:$ZnAl_2O_4$ spectrum. (For interpretation of the references to color in this figure legend, the reader is referred to the web version of this article.)

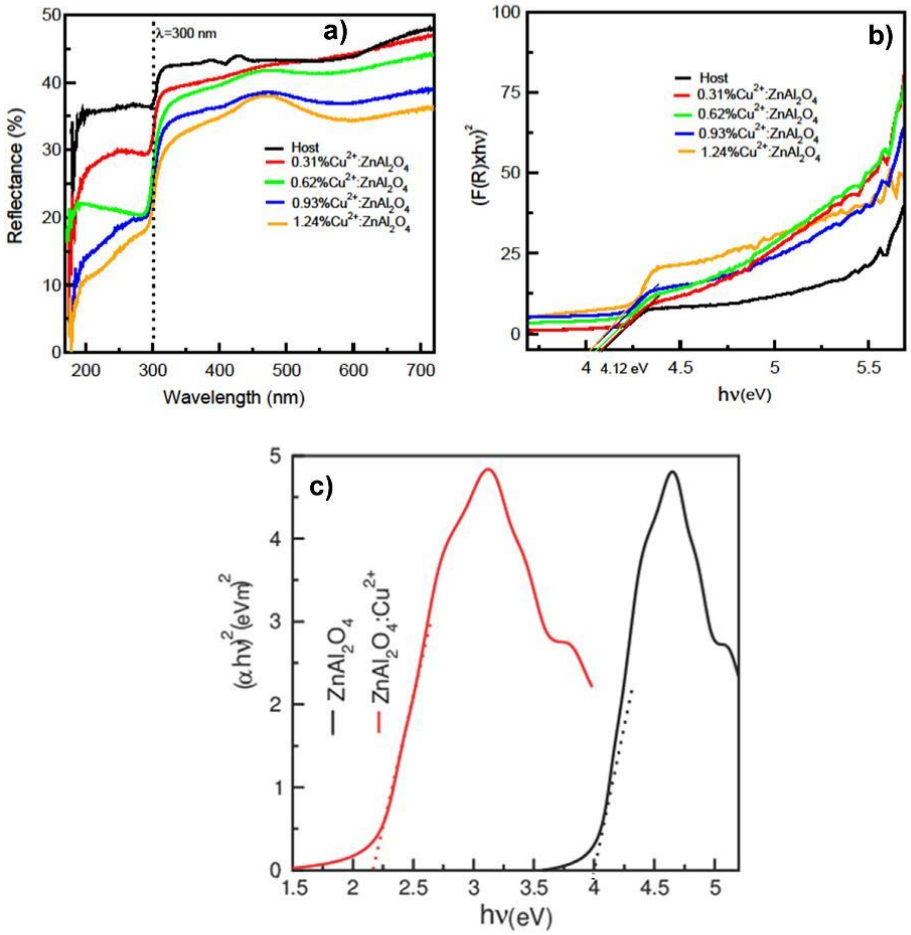

Fig. 12. a) Reflectance spectrum of host $ZnAl_2O_4$: b)Kubelka-Munk plot and band gap energy estimation for host $ZnAl_2O_4$. (c) DFT Tauc determination of band gap. (For interpretation of the references to color in this figure legend, the reader is referred to the web version of this article.)

Table 3
Calculated substitutional energies (eV) of doped $ZnAl_2O_4$ at different defect states in different charge states. ϵ^{therm} is the thermodynamic transition level, E_{PL} is the calculated PL energy, λ_{PL} is the emission wavelength and E_{rel} is the Frank-Condon shift.

					Charge state	ϵ^{therm}	E_{PL}(eV)	λ_{PL}(nm)	E_{rel}
	−2	−1	0	+1	+2	(-2/-1)	(−2/−1)	(−2/−1)	
O_{vac}	−7.01	−7.07	−7.14	−7.19	−7.24	0.91	2.96	418.92	0.13
Cu_{zn}	1.09	1.03	0.98	0.92	0.86	0.95	2.94	421.77	0.11
$Cu_{zn}+O_{vac}$	−4.11	−4.18	−4.23	−4.29	−4.33	1.02	2.85	435.09	0.13
Binding energy	−1.81	−1.86	−1.93	−1.98	−2.05				

associated to $Cu_{Zn}+O_{vac}$. This is confirmed from the emission spectra in Fig. 11a) and b) where some peaks were deduced as occurring as results of either O_{vac} or Cu_{Zn}.

On plotting the substitutional energy as function of the Fermi level position (i.e. Fermi level position shifts from the VBM to CBM), it is evident, from Fig. 9, the −1/−2 transition level was the one that was found to be the closest to conduction band. A thermodynamic transition level is the position within the band gap of a host where a defect in two different charge states has the same substitutional energy. The values of this level for all the defects are also presented in Table 3. These thermodynamic transition levels can be compared to experimentally observed defect levels obtained via the use of Deep-level transient spectroscopy [48,49]. Each of thermodynamic transition levels usually has an associated optical transition. We then calculated the associated optical transition using

$$E_{PL} = E_g - \varepsilon^{therm}(-2/-1) - E_{rel} \quad (6)$$

where, E_{PL} is the optical transition, E_g is the band gap energy, $\varepsilon^{therm}(-2/-1)$ is thermodynamic transition level (-1 and -2 charge sates have just been used to illustrate how the calculation is done). E_{rel} is the lattice relaxation energy (the Frank-Condon shift). The obtained PL energies and wavelengths are presented in Table 3. From the calculated PL energies and wavelengths, we found that Cu^{2+} doping led to blue luminescence in $ZnAl_2O_4$ implying that Cu^{2+} doped $ZnAl_2O_4$ can be used as a blue pigment ceramic. A schematic representation of the optical transition is presented in Fig. 10. The Cu^{2+} doped $ZnAl_2O_4$ production of blue emission at 435 nm (see Fig. 10) agrees well with the findings of [50]. The blue emission is ascribed to the spin-orbit splitting of the Cu^{2+} d^9 state into $^2D_{5/2}$ and $^2D_{3/2}$ states.

Photoluminescence spectroscopy is a useful tool for the investigation of the excited electron-hole pairs recombination phenomena in semiconductors. It is used in determining transitions related to defects in a semiconductor [51]. Defects densities depend on formation procedures, morphology and size of the crystallites. From Fig. 12 (b), the $ZnAl_2O_4$ band gap (absorption energy) was determined along with the relative energetic positions of inter-band gap defect states. This absorption energy, 4.38 eV (283 nm) was used to get the emission spectra in Fig. 11 (b). Monitoring the excitation spectra at 388 nm, it was observed that there was a highest intensity peak at 283 nm as shown in Fig. 11 (a). This peak can be attributed to the elementary band-to-band electron transition within filled O_2p orbitals and empty Al_3 s orbitals, with possibility of few Al_3p wave functions incorporated as has been previously proposed for pure $ZnAl_2O_4$[2].

This phenomenon has also been confirmed computationally in Fig. 8(a), where the valence band was completely occupied O_2p orbitals while the conduction band had empty orbitals. In Fig. 11 (a), a shoulder at 325 nm is also observed in the excitation spectra of pristine sample. The shoulder is related to electronic excitation between occupied O_2p and unoccupied Zn_4 s orbitals and is known to depend heavily on the spinel's intrinsic characteristics (mostly spinel defects). For transition metal doped oxides, the optical response is usually explained by the charge transfer shift or transition within multiplet stages of 3d electrons [52]. The absorption bands appearing at higher wavelength (330 nm) are attribute to d-d transitions within copper atoms filling tetrahedral (e-t_2) sites of the spinel.

In principle, a reverse mechanism can take place (de-excitation transition), where an electron is transferred from a metal ion to a ligand [53]. The emission spectra of undoped $ZnAl_2O_4$ as well as $ZnAl_2O_4$:Cu^{2+} samples are wide and were thus deconvoluted (see Fig. 11 (c) and (d)). In Fig. 11 c), there are Gaussian peaks at 388 nm (3.19 eV), 425 nm (2.91 eV) and 480 nm (2.58 eV) in the case of undoped $ZnAl_2O_4$. Since the band gap of $ZnAl_2O_4$ is 4.38 eV, these peaks can be ascribed to intra-band gap defects for example oxygen vacancies which give donor levels near the oxide's conduction band edge [54]. In the undoped system, electron transition took place from valence band maximum (VBM) into the oxygen vacancy energy level (intra-band gap defects) before transiting from this level to the conduction band (CB). Due to vibrational relaxation, this electron losses energy and drops back to the intra-band gap defects and consequently dropping back to the VBM. It then goes through radiative recombination with a hole in the VBM at the same time emitting blue light. Fig. 11 d) shows the deconvoluted spectra of Cu^{2+}:$ZnAl_2O_4$ where peaks at 388 nm, 425 nm and 480 nm and 586 nm were observed. The additional peak at 586 nm is associated with Cu^{2+} as a luminescent centre. This type of emission from Cu^{2+} was also realized by Tongtong Xuan et al. [55] where doping CdS with Cu^{2+} caused a red shift from 563 nm to 586 nm (undoped and doped CdS respectively). The peak at 586 nm (2.1 eV) corresponds to the Cu_4p states at 2.2 eV in the band gap of $ZnAl_2O_4$ as seen in Fig. 8 b).

Fig. 12(a) shows the UV–vis diffuse reflectance spectra of $ZnAl_2O_4$ samples at 283 nm. The information which can be extracted from the UV-visible spectra is the band gap energy, which is arrived at by extrapolating the linear portion of Fig. 12b), and the point of intersection with the X-axis gives us the value of the band gap. In pristine $ZnAl_2O_4$, the electronic transition takes place directly from valence band maximum to conduction band minimum. Upon doping, the electrons were not excited directly to the conduction band minimum since oxygen vacancies as well as empty Cu^{2+} s and p states capture the electrons. This shows that oxygen defects as well as sub-band states of Cu^{2+} are accountable for the slight decrease of effective band gap of $ZnAl_2O_4$ as confirmed in Figure 8. The red shift realized in $ZnAl_2O_4$ band gap upon Cu^{2+} introduction and shifting of absorption edge are commanded by the nanoparticle's surface, lattice strain and oxygen vacancies[5]. Given that $ZnAl_2O_4$ is regarded as a semiconductor with a direct band gap, the band gap size of the powders were approximated from plots of $(\alpha h\nu)^2$as a function of $h\nu$, that is the kubelka-Munk relation [56]. This was presented in Fig. 12(b) where h=planks constant, α=Kubelka-Munk (K-M) absorption coefficient, and ν=frequency. The straight potions realized from the plots are extrapolated up to the $h\nu$axis in order to acquire the size of band gap at different doping concentrations, giving the host band gap at 4.38 eV (283 nm). It was noted that, there was very small changed in the band gap, owing to the fact that the crystallite size of the samples did not change much as was shown in Table 2. This is in agreement with [57] where a band gap of 4.11 eV was obtained. It is worth noting that the excitation peak observed at 283 (UV region) was as a result of the elementary band-to-band electron excitations and it corresponds to the band gap of the analyzed powders.

4. Conclusions

Experimental characterization and theoretical calculations were used to study the properties of $ZnAl_2O_4$:Cu^{2+}. Structural characterization shows a cubic spinel structure without phase segregation. Both experiment and ab *initio* calculation show small lattice distortion for the doped structure which is attributed to the similarity of ionic radii of Cu^{2+} and Zn^{2+} ions. The introduction of Cu^{2+} in the host did not affect its structure. Theoretical calculation show that the doped spinel emits blue light (435 nm), while experimental result indicate that it emits in the blue region (at 425 and 480 nm). DFT+U results were consistent with the experimental findings on both the structural and optical properties of $ZnAl_2O_4$:Cu^{2+} with the Tauc's transition energy relating very well with that in the electronic structure calculations. HR-TEM confirmed the cubic structure of $ZnAl_2O_4$ and the crystallite size of our samples. Non-radiative relaxations which were due to the new defect sites in the host gave rise to concentration quenching.

Acknowledgement

This work is based on the research supported in part by the National Research Foundation of South Africa. The Grant holder acknowledges that opinions, findings and conclusions or recommendations expressed in any publication generated by the NRF supported research are that of the author(s) and that the NRF accepts no liability whatsoever in this regard.

References

[1] R.F. Martins, O.A. Serra, J. Braz. Chem. Soc. 21 (2010) 1395–1398.
[2] S.K. Sampath, J.F. Cordaro, J. Am. Ceram. Soc. 81 (1998) 649–654.
[3] J. Popović, B. Gržeta, B. Rakvin, E. Tkalčec, M. Vrankić, S. Kurajica, J. Alloy. Compd. 509 (2011) 8487–8492.
[4] Y. Yang, X.W. Sun, B.K. Tay, J.X. Wang, Z.L. Dong, H.M. Fan, Adv. Mater. 19 (2007) 1839–1844.
[5] S. Mathur, M. Veith, M. Haas, H. Shen, N. Lecerf, V. Huch, S. Hüfner, R. Haberkorn, H.P. Beck, M. Jilavi, J. Am. Ceram. Soc. 84 (2001) 1921–1928.
[6] J. Wrzyszcz, M. Zawadzki, J. Trawczyński, H. Grabowska, W. Miśta, Appl. Catal. A Gen. 210 (2001) 263–269.
[7] K. Kumar, K. Ramamoorthy, P.M. Koinkar, R. Chandramohan, K. Sankaranarayanan, J. Nanopart. Res 9 (2007) 331–335.
[8] X. Li, Z. Zhu, Q. Zhao, L. Wang, J. Hazard. Mater. 186 (2011) 2089–2096.
[9] S. López, A.H. Romero, P. Rodriguez-Hernandez, A. Munoz, Phys. Rev. B: Condens. Matter Mater. Phys. 79 (2009) 214103.
[10] C.M. Fang, C.-K. Loong, G.A. de Wijs (others), Phys. Rev. B 66 (2002) 144301.
[11] D. Levy, A. Pavese, A. Sani, V. Pischedda, Phys. Chem. Miner. 28 (2001) 612–618.
[12] H.J. Reichmann, S.D. Jacobsen, Am. Mineral. 91 (2006) 1049–1054.
[13] P.T. Lanh, N.N. Long, T.T. Loan (others, in), J. Phys. Conf. Ser. (2009) 12053.
[14] J.L. Wilson, P. Poddar, N.A. Frey, H. Srikanth, K. Mohomed, J.P. Harmon, S. Kotha, J. Wachsmuth, J. Appl. Phys. 95 (2004) 1439.
[15] *,† M.Fernández-García, † A. Martínez-Arias, ‡ and J. C. Hanson, ‡ J. A. Rodriguez*, 2004.
[16] Z.Q. Yu, C. Li, N. Zhang, J. Lumin. 99 (2002) 29–34.
[17] L. Wischmeier, T. Voss, I. Rückmann, J. Gutowski, A.C. Mofor, A. Bakin, A. Waag, Phys. Rev. B 74 (2006) 195333.
[18] L.D. DeLoach, R.H. Page, G.D. Wilke, S.A. Payne, W.F. Krupke, IEEE J. Quantum Electron. 32 (1996) 885–895.
[19] M.D. Segall, J. Phys. Condens. Matter 14 (2002) 2717–2744.
[20] H.M. Yadav, S.V. Otari, V.B. Koli, S.S. Mali, C.K. Hong, S.H. Pawar, S.D. Delekar, J. Photochem. Photobiol. A: Chem. 280 (2014) 32–38.
[21] W. Chen, J.Z. Zhang, A.G. Joly, J. Nanosci. Nanotechnol. 4 (2004) 919–947.
[22] A.A. Khosravi, M. Kundu, L. Jatwa, S.K. Deshpande, U.A. Bhagwat, M. Sastry, S. K. Kulkarni, Appl. Phys. Lett. 67 (1995) 2702–2704.
[23] R. Elilarassi, G. Chandrasekaran, J. Mater. Sci. Mater. Electron. 21 (2010) 1168–1173.
[24] L. Ma, S. Ma, H. Chen, X. Ai, X. Huang, Appl. Surf. Sci. 257 (2011) 10036–10041.
[25] Y. Chen, X.L. Xu, G.H. Zhang, H. Xue, S.Y. Ma, Phys, B. Condens, Matter 404 (2009) 3645–3649.
[26] M. Caglar, F. Yakuphanoglu, Appl. Surf. Sci. 258 (2012) 3039–3044.
[27] S.Lee, D.Song, D.Kim, J.Lee, S.Kim, I.Y.Park, Y.D.Choi, Effects of Synthesis Temperature on Particle Size/shape and Photoluminescence Characteristics of ZnS: Cu Nanocrystals, 2004.
[28] N. Bayal, P. Jeevanandam, J. Alloy. Compd. 516 (2012) 27–32.
[29] H. Liu, Z. Zhang, Z. Gong, Y. Yang, Solid State Ion. 166 (2004) 317–325.
[30] X.L. Duan, D.R. Yuan, L.H. Wang, F.P. Yu, X.F. Cheng, Z.Q. Liu, S.S. Yan, J. Cryst. Growth 296 (2006) 234–238.
[31] P.Giannozzi, S.Baroni, N.Bonini, M.Calandra, R.Car, C.Cavazzoni, D.Ceresoli, G.L. Chiarotti, M.Cococcioni, I.Dabo, others, J. Phys. Condens. Matter 21 (n.d.), 395502.
[32] A.G. Petukhov, I.I. Mazin, L. Chioncel, A.I. Lichtenstein, Phys. Rev. B 67 (2003) 153106.
[33] W.M. Mulwa, C.N.M. Ouma, M.O. Onani, F.B. Dejene, J. Solid State Chem. 237 (2016) 129–137.
[34] A. Janotti, D. Segev, C. Van de Walle, Phys. Rev. B 74 (2006) 045202.
[35] A. Calzolari, A. Ruini, A. Catellani, J. Am. Chem. Soc. 133 (2011) 5893–5899.
[36] A. Calzolari, M.B. Nardelli, Sci. Rep. 3 (2013).
[37] H.J. Monkhorst, J.D. Pack, Phys. Rev. B 13 (1976) 5188–5192.
[38] C. Freysoldt, J. Neugebauer, C.G. Van de Walle, Phys. Status Solidi 248 (2011) 1067–1076.
[39] C. Freysoldt, J. Neugebauer, C. Van de Walle, Phys. Rev. Lett. 102 (2009) 016402.
[40] J. Sun, H.-T. Wang, J. He, Y. Tian, Phys. Rev. B 71 (2005) 125132.
[41] P. Nath, S. Chowdhury, D. Sanyal, D. Jana, Carbon N.Y. 73 (2014) 275–282.
[42] M. Zawadzki, W. Staszak, F.E. López-Suárez, M.J. Illán-Gómez, A. Bueno-López, Appl. Catal. A Gen. 371 (2009) 92–98.
[43] J.-G. Li, X. Li, X. Sun, T. Ishigaki, J. Phys. Chem. C 112 (2008) 11707–11716.
[44] I. Yu, Mater. Res. Bull. 41 (2006) 1403–1406.
[45] S.H. Shin, J.H. Kang, D.Y. Jeon, D.S. Zang, J. Solid State Chem. 178 (2005) 2205–2210.
[46] F.D. Murnaghan, Proc. Natl. Acad. Sci. USA 30 (1944) 244.
[47] M. Zawadzki, Solid State Sci. 8 (2006) 14–18.
[48] C.G. Van de Walle, J. Appl. Phys. 95 (2004) 3851.
[49] D.V. Lang, J. Appl. Phys. 45 (1974) 3023.
[50] R. Viswanatha, S. Chakraborty, S. Basu, D.D. Sarma, J. Phys. Chem. B 110 (2006) 22310–22312.
[51] T. Schmidt, K. Lischka, W. Zulehner, Phys. Rev. B 45 (1992) 8989.
[52] K. Izumi, S. Miyazaki, S. Yoshida, T. Mizokawa, E. Hanamura, Phys. Rev. B 76 (2007) 75111.
[53] L. Prodi, F. Bolletta, M. Montalti, N. Zaccheroni, Coord. Chem. Rev. 205 (2000) 59–83.
[54] S. Clement, S. Mohammed Aly, D. Fortin, L. Guyard, M. Knorr, A.S. Abd-El-Aziz, P.D. Harvey, Inorg. Chem. 47 (2008) 10816–10824.
[55] C. Ragupathi, L.J. Kennedy, J.J. Vijaya, Adv. Powder Technol. 25 (2014) 267–273.
[56] C. Ragupathi, J.J. Vijaya, A. Manikandan, L.J. Kennedy, J. Nanosci. Nanotechnol. 13 (2013) 8298–8306.
[57] G. Buvaneswari, V. Aswathy, R. Rajakumari, Dye Pigment. 123 (2015) 413–419.

Journal of Solid State Chemistry 237 (2016) 129–137

Contents lists available at ScienceDirect

Journal of Solid State Chemistry

journal homepage: www.elsevier.com/locate/jssc

Energetic, electronic and optical properties of lanthanide doped TiO_2: An *ab initio* LDA+*U* study

Winfred M. Mulwa [a], Cecil N.M. Ouma [b,*], Martin O. Onani [c], Francis B. Dejene [a]

[a] Department of physics, University of the Free State-Qwaqwa Campus, Private Bag X13, Phuthaditjhaba 9866, South Africa
[b] Natural Resources and Environment, Council for Scientific and Industrial Research, P.O. Box 395, Pretoria 0001, South Africa
[c] Chemistry Department, University of the Western Cape, Private Bag X17, Bellville, Cape Town, South Africa

ARTICLE INFO

Article history:
Received 13 November 2015
Received in revised form
6 January 2016
Accepted 1 February 2016
Available online 3 February 2016

Keywords:
Doped-TiO_2
Anatase
Rutile
Dopant levels
DFT+*U*
Optical properties

ABSTRACT

Substitutional energies, thermodynamic charge transition levels and optical properties of lanthanide doped anatase TiO_2 has been investigated using local density approximation with the Hubbard *U* correction (LDA+*U*) within the density functional theory formalism. All the lanthanides apart from La introduced impurity states in the host band gap on doping. The calculated substitutional energies indicate that it is possible to dope TiO_2 with lanthanide ions. The optimal doping percentage was predicted to be ~3% and dopant levels resulting from Ce, Nd, Sm, Gd and Tm doping were found to possess negative U characteristics. In addition the calculated thermodynamic transition levels predicted Lu as not having any possible charge transitions within the host band gap. The calculated optical absorption coefficients indicate that lanthanide doping led to optical absorption in the visible regime.

1. Introduction

Titanium dioxide (TiO_2) has vast applications in electronics, energy and photonics among other applications [1]. One of the key applications is photocatalysis where solar energy is converted into hydrogen energy via the splitting of water, decomposing toxic organic and inorganic pollutants to purify water and air, and providing super-hydrophilicity to solid surfaces [2]. TiO_2, a wide band gap compound semiconductor, is known to be active only in the ultraviolet (UV) region of the photoemission spectrum. However, in order for TiO_2 to fully utilize the major part of the solar spectrum, besides UV which is just 5% of the solar spectrum, several studies aimed at improving the properties of TiO_2 via doping and co-doping TiO_2 with various elements have been carried out with varied measures of success [3]. TiO_2 has rutile, anatase and brookite polymorphs. Rutile and brookite are direct band gap semiconductors. The higher photocatalytic activity of the anatase TiO_2 over the rutile and brookite polymorphs can be attributed to the indirect band gap of the anatase which leads to a slow decay lifetime of photoexcited charge carriers [1].

Good photocatalysts are known to have conduction band edges that are more negative than the reduction (redox) potential of water. However, visible-light photocatalysts have been found to be either unstable under light illumination (CdSe) [4] or have low activity (Fe_2O_3) [5]. Attempts have been made in trying to use transition metal (TM) oxides such as Cr_2O_3 as photocatalysts since they have good visible light absorption [6]. Experimentally, Cr_2O_3 has a band gap of 3.4 eV [7] which is larger than the experimental band gap of rutile. This explains why Cr_2O_3 conduction band edges were found to be more negative compared to the redox potential of water [8]. Therefore, incorporating a dopant into TiO_2, in such a way that the conduction band levels are made more negative than the redox potential of water can facilitate the visible light absorption of the host oxide under visible irradiation.

The most widely used semiconductor photo-catalyst is titanium dioxide (TiO_2), because it is relatively easy and inexpensive to synthesize, it is highly stable under irradiation conditions, non-toxic, and can completely degrade several classes of pollutants in aqueous and gas phases [2,3]. However, its success as a semiconductor photo-catalyst is limited by its wide band-gap (3.2 eV) and the recombination of the photogenerated electron–hole pairs [4]. A 3.2 eV (387 nm) band gap necessitates the use of UV light in the photo-production of electrons and holes.

Conflicting reports exist in the literature regarding the photocatalytic activities on semiconductors doped with transition metal ions [5]. The disparities are due to a number of reasons including; variability in the synthetic procedures employed for the preparation of catalysts which lead to the formation of photo catalysts with varying physio-chemical characteristics, varying experimental conditions used

* Corresponding author.
E-mail addresses: moronaphtaly84@gmail.com, COuma@csir.co.za (C.N.M. Ouma).

http://dx.doi.org/10.1016/j.jssc.2016.02.003
0022-4596/

in the photocatalytic reactions and the different quantitative methods used for analysis of reactant or product concentrations [6]. In recent times, Herrmann et al., [7] made a compelling argument that both *n*- and *p*-doping by transition metal ions leads to an increase in the recombination rate of the photogenerated electron–hole pairs. In recent years, anion doping has gained popularity and the prime motivation in this direction has been in extending the visible light response of large band-gap semiconductors [8,9].

It has been reported that TiO_2 co-doped with La^{3+} and Eu^{3+} exhibits better photocatalytic properties compared to that of pristine TiO_2[10]. The improved photocatalytic properties resulted from transitions of 4f electrons in the dopants. A similar observation was made when TiO_2 was doped with lanthanides [11,12]. Doping TiO_2 with lanthanides has been the subject of intense investigation both experimentally [11–14] and theoretically [15–17]. This is because lanthanide doping could remarkably improve the photocatalytic activity of TiO_2 as it registers visible light response as well as strong redox potential at the same time. Lanthanides are among the rare-earth elements with great luminescent properties. They are characterized by the 4f orbitals which in some cases are shielded by filled $5p^6 6s^2$ sub orbitals leading to very important spectroscopic properties [18] however, lanthanides ions are not excited efficiently without a host [19]. Their properties are known to greatly depend on their electronic configuration and ionic radius, which decreases steadily along the lanthanide series with respect to the fillings of the 4f orbitals [20].

Density functional theory (DFT) has been the basis for most of the electronic structure calculations, however it has limitations when it comes to describing properties such as band gaps (see ref [21–24]). Another key shortcoming of standard DFT is that it cannot accurately describe systems with strong correlation effects. This is because within DFT, the electron–electron interaction is expressed as the sum of the Hartree and exchange–correlation (XC) terms however, the XC term is usually approximated. Due to this approximation, the XC term cannot accurately account for electronic interactions in strongly correlated systems, hence the need for DFT+*U* technique where a Hubbard correction *U* is added to the standard DFT formalism [25,26].

In this study we investigate lanthanide doped anatase TiO_2 using density functional theory with Hubbard *U* correction (DFT+*U*) because lanthanides are known to have 4f orbitals which cannot be accurately described using standard DFT. The electronic and optical properties of anatase doped TiO_2 with each of the eleven (11) different lanthanides namely: La, Ce, Pr, Nd, Pm, Sm, Eu, Gd, Tm, Yb and Lu has been investigated. In addition we have also calculated the dopant substitutional energies, thermodynamic charge transitions energies as well as their optical absorption spectra.

2. Computational details

Projector augmented plane wave (PAW) method [27] as implemented in the Quantum ESPRESSO code [28], has been used to study the properties of interest within the DFT+*U* formalism. PAW potentials were used for Ti, O and all the lanthanides investigated in this study. PAW is an improvement to the pseudopotential approximation as it combines the pseudopotential approximation with linearized augmented-plane-wave (LAPW) method [29,30], making PAW more accurate compared to the pseudopotential approximation. The Brillouin zone of the unit cell of anatase TiO_2 was sampled using a converged Monkhorst–Pack [31] k-point mesh of $6\times6\times3$ and kinetic energy cut-off of 80 Ry. Standard DFT is known to severely underestimate the band gap in semiconductors, in the case of TiO2, the band gap of anatase TiO_2 obtained using spin polarized local density approximation (LDA) was found to be 1.89 eV compared to the experimental value of 3.2 eV [32]. This underestimation stems from the wrong energy position of the 3d orbitals of Ti within the pseudopotential description which intern courses (spurious) interaction with the O *sp* bands. To correct for the band gap underestimation in standard LDA, we have adopted the methodology of [33–35] where an *ad hoc* Hubbard *U* potential is included in the DFT+*U* scheme. Within this formalism, the Hubbard *U* values used should be considered as empirical parameters introduced to correct the gap and not the physical on-site electron–electron screened potentials, in the sense of the many-body Hubbard Hamiltonian. The unphysical Ti_{3d}–O_{2sp} is overcome by including a Hubbard potential $U=10$ eV on 3d orbital of Ti and 5 eV on the 2p orbital of O was found to produce the experimental of gap of TiO_2. A similar approach was used to obtain *U* values for the lanthanide ions whereby we used lanthanide sesquioxides varied the Hubbard term until a band gap close to experimental value is arrived at. The experimental data used was obtained from [36–38]. The obtained values of *U* for the case of lanthanides were found to be consistent with other studies [36].

The calculated equilibrium parameters were; $a=3.792$ Å c/a=2.502, which were in good agreement with experimental values, $a=3.785$ Å and c/a=2.513 [39], as well as another theoretical LDA+*U* results, $a=3.819$ Å and c/a=2.502 [40]. After obtaining the equilibrium structure, 72 atom supercells were constructed from the equilibrium structure. The choice of the 72 atom supercell was made by calculating the dopant substitutional energy as function of supercell size up to 288 atoms, the substitutional energy difference between the 72 atom unit cell and the 288 atom unit cell was found to be ~1 eV thus due to computational efficiency, the 72 atom unit was preferred. Doping was then done by substituting Ti atoms with lanthanide atoms. In order to avoid significant dopant–dopant interaction within the lattice, lanthanide atoms were introduced at the next-nearest Ti atom sites from the site of the first substitution until the desired dopant concentration was achieved. The atomic positions of the supercells containing the dopants were then relaxed keeping the volume constant. Fig. 1 shows a supercell containing a dopant within its lattice.

2.1. Optical properties

The response function for the optical properties of a solid, describing the absorption or emission of electrons or photons is the dielectric function. From the imaginary part of the dielectric function, it is possible to obtain some of the optical properties of a solid. In this study, the optical properties have been obtained through the frequency-dependent dielectric function, $\varepsilon(\omega)=\varepsilon_1(\omega)+i\varepsilon_2(\omega)$ using the formalism of Ehrenreich and Cohen [41]. Within this formalism, the imaginary part of the dielectric function is given as:

$$\varepsilon_2(\omega)=\frac{4\pi^2e^2\hbar}{m^2\omega^2}\sum_{vc}\frac{2}{(2\pi)^2}\int_{BZ}\delta[\omega_{cv}(k)-\omega]\left|M_{cv}(k)\right|^2d^3k \tag{1.0}$$

where the integral is over the first Brillouin zone, $M_{cv}(k)=\left\langle u_{ck}\middle|\hat{e}.\nabla\middle|u_{ck}\right\rangle$ are the dipole matrix elements for the direct transitions between valence and conduction bands states. $\hbar\omega_{cv}(k)=E_{ck}-E_{vk}$ is the excited energy, $\hat{e}$ is the polarization vector of the electric field, and $u_{ck}(r)$ is the periodic part of the Bloch wave function for a conduction band state with wave vector *k*. Although DFT is known to underestimate the band gap of semiconductors, our results show that optical properties obtained using DFT outputs are surprisingly in good agreement with experiment. This is attributed to the ability of the local density approximation to yield accurate matrix elements between occupied and empty states.

In this study our first goal was to determine the doping percentage that would yield visible light absorption in TiO_2 since high concentrations may lead to low photocatalytic activity. Large impurity states in the band gap that act as recombination centres for photo-excited electron–hole pairs. To achieve this, some of the optically

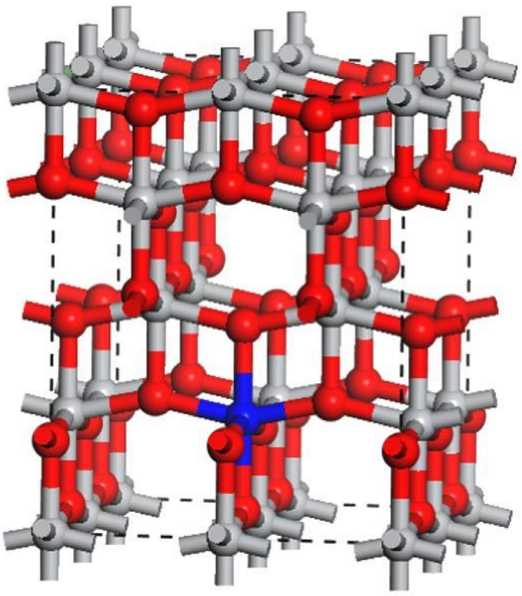

Fig. 1. A supercell of doped anatase TiO_2 (red, grey and blue balls represents O, Ti and dopant atoms respectively). (For interpretation of the references to colour in this figure legend, the reader is referred to the web version of this article.)

active lanthanide elements namely; Gd, Eu and Sm were used to determine this optimal doping percentage. This was done by plotting the optical absorption of spectrum of TiO_2 doped with each of the chosen lanthanide ions individually at different concentrations as seen in Fig. 2. From the figure, it can be seen that the doping percentage that led to absorption on the visible regime is 2.7778% (~3.0%) which is within the experimental doping percentage range [35].

After obtaining the doping percentage that lead to absorption in the visible regime, substitutional energies, electronic properties and optical properties for all the dopants were obtained at this dopant percentage (~3.0%).

2.2. Dopant substitutional energies

According to the Zhang–Northrup [42] formalism, the dopant substitutional energy at any given charge state q can be obtained as

$$E^q_{\text{dopant}} = E_{\text{undoped}} - E_{\text{doped}} + n\mu_{\text{Ti}} - n\mu_{\text{dopant}} + q(E_{\text{VBM}} + E_{\text{Fermi}}) + E^q_{\text{corr}} \quad (2.0)$$

where E_{undoped} is the total energy of pristine TiO_2, E_{doped} is the total energy of the lanthanide doped TiO_2, μ_{Ti} and μ_{dopant} are the chemical potentials of Ti and dopant respectively,n is the number of atoms substituted or added to the supercell, E_{VBM} and E_{Fermi} are the energy of the valence band maximum and fermi energy respectively and E^q_{corr} is the correction made to calculated substitutional energies due to finite size errors and image charge corrections obtained using the charge model of Freysoldt et al.[43,44]. $E_{\text{corr}} = E_{\text{iso}} - E_{\text{per}} - q\Delta V_{q/b}$, E_{iso} is the self-energy of the isolated charge distribution, E_{per} the electrostatic energy of the system subject to periodic boundary conditions and $q\Delta V_{q/b}$ is the potential alignment term. The calculated substitutional energies at different charge sates are presented in Table 2.

2.3. Thermodynamic transition levels

Using the calculated substitutional energies, it is possible to obtain the thermodynamic charge transition level $\varepsilon^{q/q'}$ which is defined as the Fermi energy position where a dopant in two different charge states has the same dopant substitutional (formation) energy [45]. This can be obtained for say 0 and +1 charge states as follows.

$$\varepsilon^{0/+1} = \frac{\left(E^{+1}_{\text{dopant}} - E^{0}_{\text{dopant}}\right)}{((0) - (+1))} \quad (3.0)$$

where E^{+1}_{dopant} and E^{0}_{dopant} are the dopant substitutional energies for +1 and 0 charge states obtained using equation (2). Additionally the same thermodynamic charge transition levels can be obtained by making plots of dopant substitutional energies as functions of the Fermi level position as presented in Fig. 3. In the figure, the gradient of each line is the defect charge state, and the intersection of two lines is the thermodynamic charge transition level of the defect. The thermodynamic charge transition levels can be associated to defect levels observed from deep level transient spectroscopy (DLTS) or temperature dependent Hall measurements [45].

3. Results and discussions

3.1. Substitutional energies

Dopant substitutional energies were calculated using equation (2.0). In order to bench mark our calculation with previous studies [46,47]. We have calculated the dopant substitutional energies at ~1.4% doping (one (1) atom lanthanide substitution) in the neutral charge state so as to compare our methodology to previous

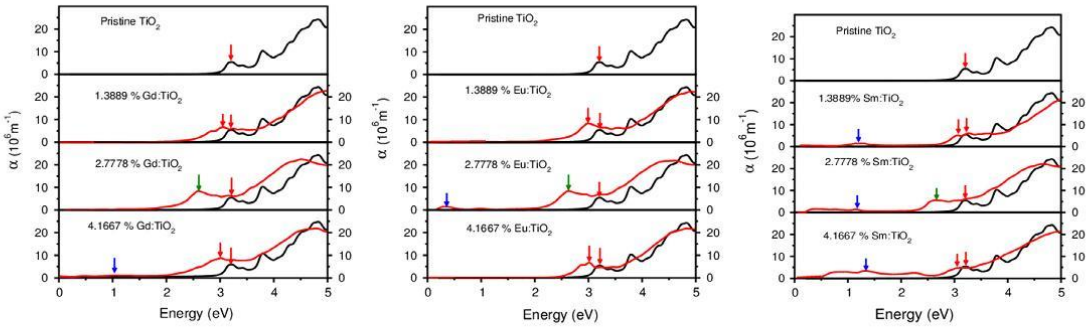

Fig. 2. Calculated absorption spectra of TiO_2 doped with different lanthanide elements at different percentage concentrations. (red, green and blue arrows represent UV, visible and IR absorption peaks respectively). (For interpretation of the references to color in this figure legend, the reader is referred to the web version of this article.)

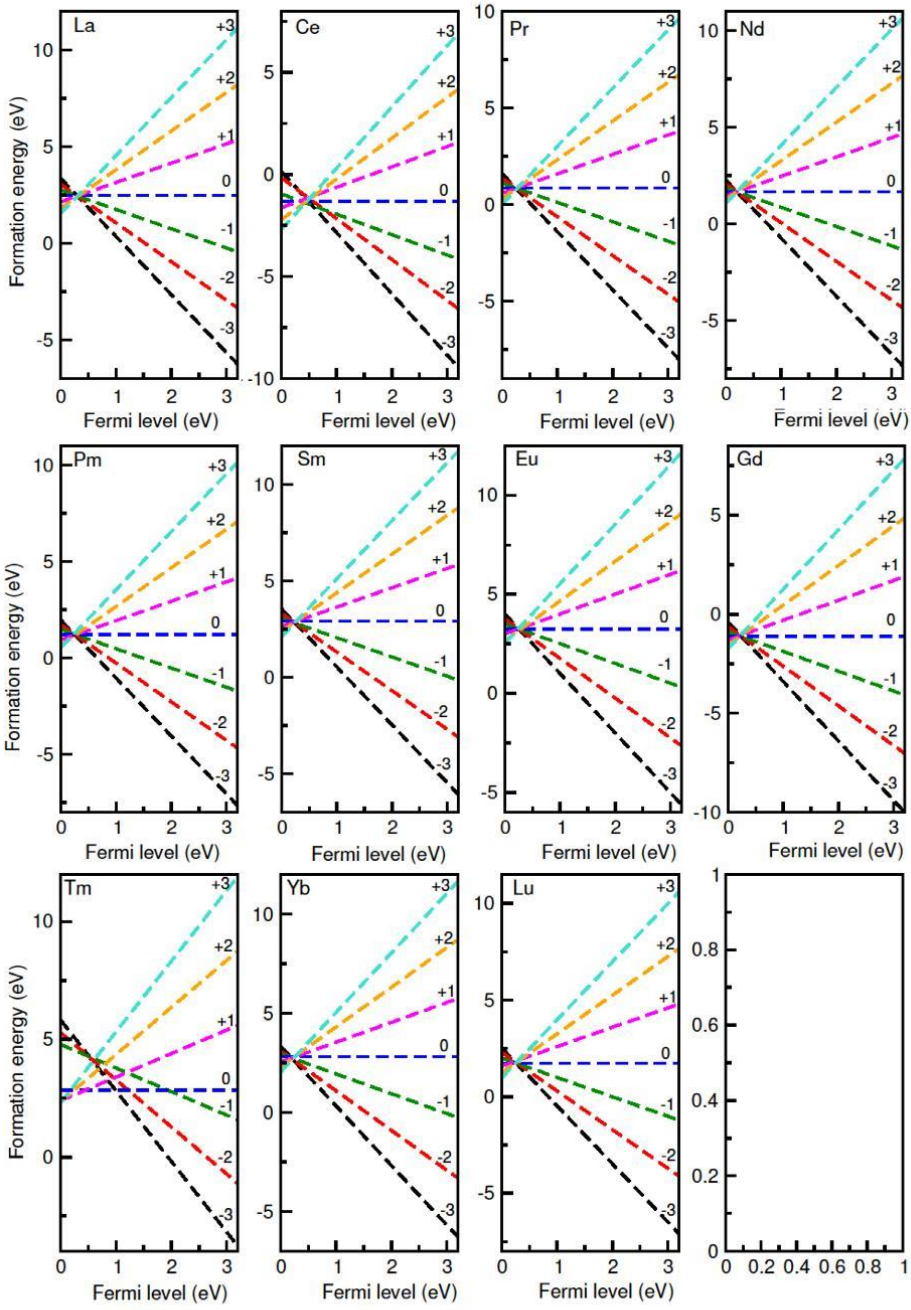

Fig. 3. Calculated substitutional energies of doped TiO_2 as a function of the Fermi level.

studies (see Table 1). From the table it can be seen that our results are consistent previous studies when it comes to the order of which atom easily dopes anatase TiO2 i.e. Ce < Gd < Pr < Eu. There is difference in the substitutional energies compared to previous studies, this can be attributed to [47] not using the Hubbard term in the study and [46] using different values of *U* on the lanthanides compared to the ones used in this study. The different values of *U* resulted from using different experimental results used to bench

mark/callibrate the Hubbard term.

We then proceeded using equation (2.0), to calculate the dopant substitutional energies at ~3.0 dopant concentration percentage (two (2) atom lanthanide substitution) (see Table 2. From the table it can be seen that the substitutional energies varies depending on the charge state. It can also be seen from the table that it is easy to dope TiO_2 with a majority lanthanide elements since the dopant substitutional energies are relatively low ($\lesssim 3$ eV) hence the reason why lanthanide doped TiO_2 have attracted lots of experimental scrutiny. Ce and Gd had the lowest substitutional energies compared to the rest of the lanthanides. Their formation energies were also negative indication the ease of doping anatase TiO_2 with Ce and Gd. This consistent with [46,47] as well as an experimental study that reported Ce as having the highest photo-catalytic activity in TiO_2 [48]. The order of the dopant substitutional energies in ascending order are as follows; Ce < Gd < Pr < Pm < Nd < Lu < La < Yb < Tm < Eu. This order is also consistent with ab initio results of [47].

We then calculated the dopant substitutional energies a function of the Fermi level also using equation (2.0) and the results are presented in Fig. 3. As earlier mentioned, the intersection of any two lines in each of the figures, that is, the Fermi level position at which the dopant substitutional energies of the dopant in two different charge states are equal. This was also confirmed using equation (3.0). From Fig. 3 it is evident that thermodynamic transitions resulting from the doped systems occur very close to the valence band maximum (VBM), about 1.5 eV above the VBM, Equation 3.0 was then used to identify the possible transitions associated with the doped systems (see Table 3) than may be observed experimentally through DLTS measurements.

As can be seen from the Table, Pr, Sm, Gd, Yb had no possible thermodynamic charge transition levels. A survey of present available literature indicate that no DLTS measurements have been done of the lanthanide doped TiO_2 however, the absence of thermodynamic charge transition levels can in part be attributed to the inadequacies of standard DFT/DFT+U when it comes to defect studies [49] hence the need for techniques beyond the one used in this present study. Ce, Nd, Sm, Gd and Tm had levels that exhibited negative U characteristic. A defect has negative-U properties if it can trap two electrons (or holes) with the second being bound more strongly than the first [50]. How these negative U defects affect the photocatalytic properties of doped TiO_2 is still an open question.

3.2. Electronic properties

In order to understand the electronic properties of doped TiO_2, we calculated and obtained the projected density of states using LDA+U. As can be seen in Fig. 4, the band gap of pristine TiO_2 is 3.2 eV and it is characterized by Ti 3d and O 2p orbitals in valence and conduction band respectively. On doping TiO_2, there is hybridization of Ti 3d and O 2p with the dopant states, there was no hybridization between the O 2p states or Ti 3d states with 4f states when TiO_2 is doped with La (see Fig. 4a)). Fig. 4 also shows four sets of results as a consequence of the location of the impurity levels within the host band gap.

It can be seen from Fig. 4 that, as the atomic number increases from La to Lu, the energy level of the impurity states shifts from conduction band (La,Ce,Pr,Nd,Pm) through the middle of the band gap (Sm,Eu,Gd) to the valence band (Tm,Yb,Lu). It can also be seen in the case of Sm, Eu and Gd (see Fig. 3b)) that the dopant impurity levels are inside the band gap of TiO_2. It therefore implies in these three cases that, if photon energy is absorbed, the electrons in the valence band will first be excited to the new states (impurity states) and finally excited to the conduction band. From the PDOS of La, Pr and Nd it can be seen in Fig. 3a) and b) that they do not introduce any impurity states within the band gap TiO_2. Although Pr and Nd have dopant the states deep in the conduction band, La was found not to be having the 4f states an observation also made by [51]. Lu, Yb and Tm introduced acceptor states while Ce and Pm introduced donor states within the band gap of TiO_2 as seen in Fig. 3a), b) and c) which are likely the source of absorption peaks that lead to visible light absorption in doped TiO_2.

Similar to previous studies [47], it was observed in this study that doping anatse TiO_2 with lanthanide ions resulted in delocalized 4f states and that it is these delocalized 4f states that produce impurity energy levels within the band gap. The 4f states were found not to hybridize with either the O 2p states or Ti 3d states unlike the case of transition metal doped TiO_2 [17]. The impurity energy levels due to the delocalized 4f states are broader than peaks of transition metal-doped TiO_2 this is consistent with what was observed by [47] and the reason for this broadening was explained as resulting from 4f states possessing seven orbits for electrons to occupy. Another consistency with [47] was observed in the comparison doped and undoped anatase TiO_2 where PDOS of doped TiO_2 were broader in comparison to the undoped. This was attributed to the reduction of crystal symmetry which results in electronic nonlocality [52].

3.3. Optical properties

The optical properties of a semiconductor are mainly determined by its electronic structure, because of this, we investigated the relationship between electronic structure and optical properties

Table 2
Substitutional energies and averaged bond lengths of ~1.4% Ln-doped TiO_2.

At. no.	Atom	U (eV)	Substitutional energy (eV)		Bond lengths	
			This work	Other works	Ti–O (Å)	Ln–O (Å)
58	Ce	3	−1.73	−2.2[46], 1.58[47]	1.912	1.981
59	Pr	2	0.62	1.4[46], 2.83[47]	1.916	1.991
63	Eu	3	3.08	10.5[46], 5.52[47]	1.911	1.971
64	Gd	2	−1.44	0.2[46], 1.76[47]	1.922	1.982
	TiO_2				1.901	

Table 1
Extracted absorption coefficient of doped anatase TiO_2.

Ln:TiO_2	Dopant	U (eV)	Absorption peaks (ev)		Absorption peaks (nm)			
0%			3.2		387.5		UV	
1.3889%	Gd	2	3.1		400		UV	
	Eu	3	3.1		400		UV	
	Sm	2	1.1	3.1	1127	400	IR	UV
2.7778%	Gd	2	2.6		476		Visible	
	Eu	3	0.4	2.6	3100	476	IR	Visible
	Sm	2	1.1	2.6	1127	476	IR	Visible
4.1667%	Gd	2	1.1	3.1	1127	400	IR	UV
	Eu	3	3.1		400		UV	
	Sm	2	1.3	3.1	953	400	IR	UV

Table 3
Substitutional energies of ~3.0% Ln-doped TiO_2 at different charge states under Ti-rich conditions.

Atm. no	Dopant	*U* (eV)	−3	−2	−1	0	1	2	3
57	La	2	3.35	3.05	2.75	2.48	2.14	1.80	1.53
58	Ce	3	0.15	−0.17	−0.95	−1.31	−1.63	−2.22	−2.69
59	Pr	2	1.59	1.36	1.11	0.86	0.59	0.32	0.02
60	Nd	3	2.26	2.06	1.86	1.66	1.46	1.26	1.06
61	Pm	1.5	1.96	1.73	1.48	1.21	0.94	0.67	0.54
62	Sm	2	3.53	3.30	3.05	2.91	2.64	2.39	2.12
63	Eu	3	4.00	3.76	3.51	3.26	3.01	2.67	2.54
64	Gd	2	−0.40	−0.63	−0.88	−1.13	−.30	−1.54	−1.74
69	Tm	2	5.82	5.28	4.78	2.84	2.39	2.35	2.31
70	Yb	2	3.32	3.09	2.94	2.81	2.54	2.31	2.04
71	Lu	3.5	2.52	2.29	1.99	1.72	1.59	1.25	0.98

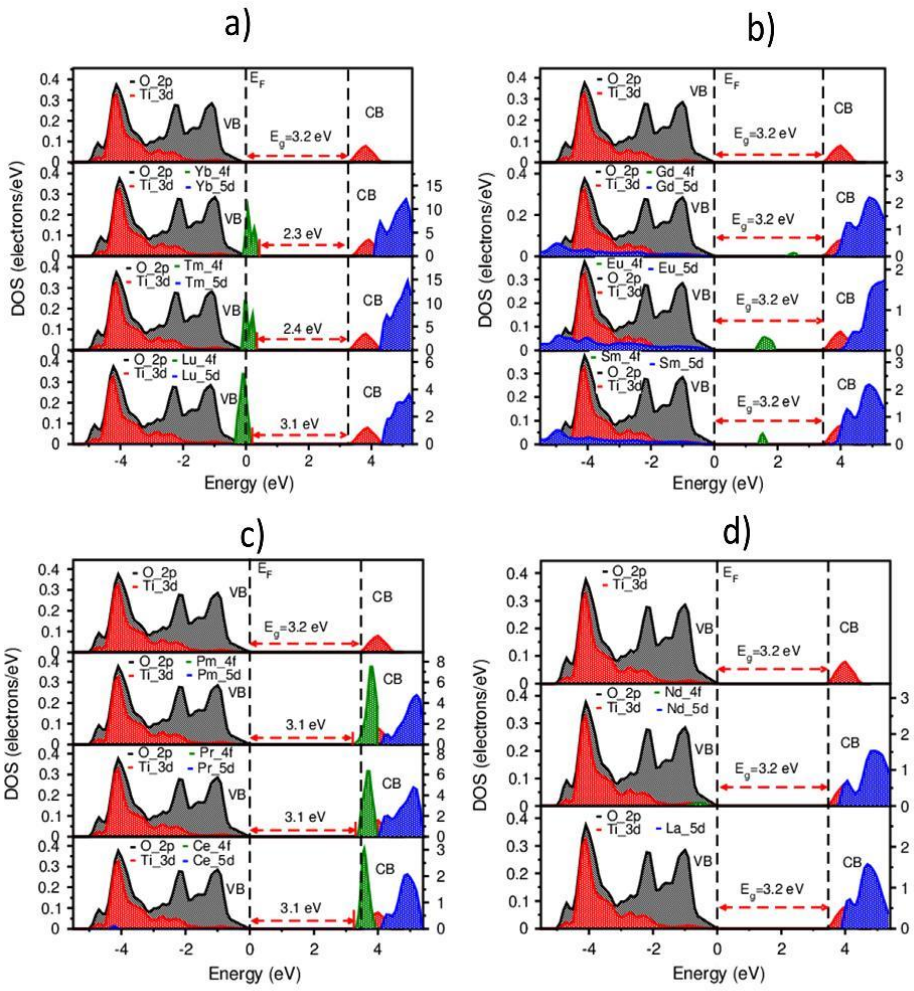

Fig. 4. Calculated projected density of states of doped TiO_2.

of lanthanide-doped TiO_2 systems.

As seen in Fig. 4 from the PDOS of Pristine TiO_2, the band gap of anatase TiO_2 was found to be 3.2 eV, which is consistent with the optical absorption coefficient presented in Fig. 5 and Table 4. Pristine TiO_2 had an optical absorption peak at 3.2 eV (388 nm) which is in the UV region in conformity with experimental results

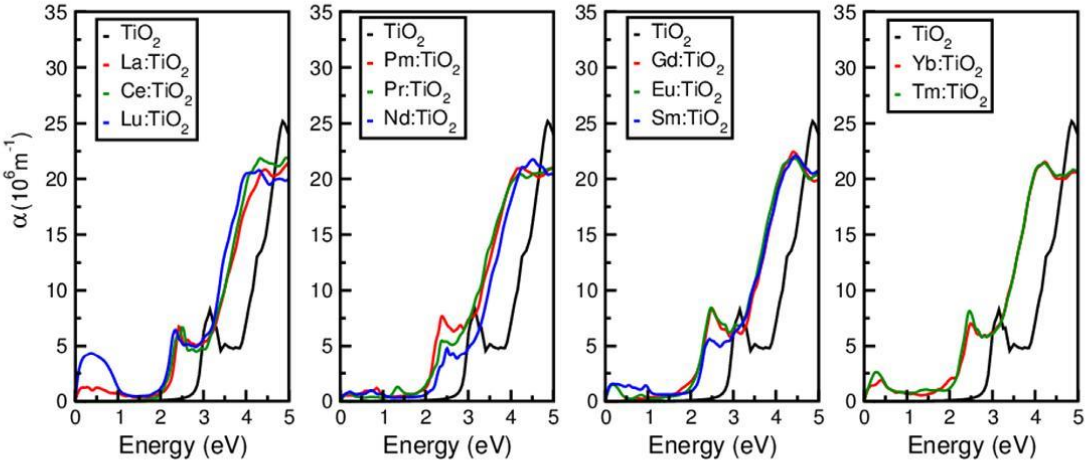

Fig. 5. Optical absorption spectra of Ln:TiO_2.

Table 4
Calculated thermodynamic charge transition levels in eV of ~3.0% Ln-doped TiO_2 referenced to the valence band maximum (VBM).

At. no.		(+3/+2)	(+1/0)	(0/−1)	(−2/−3)	(0/−2)	(−1/−3)
57	La	–	–	–	0.30	0.28	–
58	Ce	0.47	–	–	–	–	–
59	Pr	–	–	–	–	–	–
60	Nd	–	–	0.20	–	–	0.20
61	Pm	–	–	–	–	0.26	0.24
62	Sm	–	–	–	–	–	–
63	Eu	0.13	0.25	–	0.23	0.25	–
64	Gd	–	–	–	–	–	–
69	Tm	–	–	0.45	–	–	–
70	Yb	–	–	–	–	–	–
71	Lu	–	–	–	0.23	0.29	–

[53]. This peak at 388 nm was used as benchmark to locate the other peaks resulting from lanthanide-doped TiO_2. For an orderly discussion on absorption coefficients, of lanthanide doped TiO_2, using the impurity state position we have come up four categories (Table 5).

Category I: Impurity states located at or around the valence band maximum (VBM) (Yb, Tm and Lu). The 4f impurity states of the lanthanides are at the top of the VB and new absorption peaks were observed to occur at 2.5 eV (496 nm) for Yb and Tm and 2.4 eV (516.7 nm) for Lu owing to the narrowing of the band gap as shown in Fig. 5. This was consistent with experimental results [54,55] where absorption peaks were of Yb, Tm and Lu were observed at 2.6 eV (476 nm), 2.75 eV (450 nm) and 2.8 eV (442 nm) respectively where all dopant led to peaks in the visible regime. The difference in energies might be attributes the exchange–correlation functional which is an approximated term within the DFT formalism.

Category II: Impurity states within the band gap region of the host (Gd, Eu and Sm). When the lanthanides are in the octahedral discrete point charges field, the crystal field theory necessitates the intraband transition of lanthanide 4f electronic states [56]. Due to the position of the impurity states around the mid gap region of the host band gap, and the intraband transitions, the absorption coefficient peaks of Sm, Eu and Gd were found to shift absorption peak of the host from 3.2 eV (388 nm) which is in UV region to the visible light region at 2.6 eV (476.9 nm) as also shown in Fig. 5 in agreement with [57–59] where the absorption peaks of Gd, Eu and Sm were observed at 2.0 eV (620 nm).

Category III: Impurity states at/around conduction band minimum (CBM) (Pm, Pr and Ce). The impurity states of Pm Pr and Ce were found to adequately cover the CBM resulting in the narrowing the bandgap to 3.1 eV which facilitates the shifting of absorption peaks from 3.2 eV (388 nm) in the pristine TiO_2 to 2.4 eV (516.7 nm) after both Pm and Pr doping and to 2.5 eV (496 nm) on Ce doping as seen in Fig. 5. These results are in good agreement with experimental results [60,61] in which the absorption peaks on Pm, Pr and Ce absorption were observed at 2.8 eV (442 nm) for Pm and Pr while for Ce the peak was at 2.9 eV (422 nm).

Category IV: Clean band gap (Nd and La) the 4f states of Nd are found right inside the VB resulting in reduction in electronic occupation O 2p. The crystal field effect thus facilitates the shifting of absorption coefficient of the undoped host into the visible region at around 2.4 eV (516.7 nm). This was also in agreement with experimental results [62] where the absorption peak resulting from Nd doping was observed at 2.57 eV (482 nm). In the case of La doping, no impurity states from the 4f states were observed either within the band gap or at/around VBM or CBM however on ploting the absorption spectrum of the La-doped system, an optical absorption peak in the visible region at 2.5 eV (496 nm) was observed. There is no explanation in literature on why La behaves in this manner it has only be report that it has an “exceptional phenomena [51]”.

4. Conclusions

We have investigated the electronic and optical properties of pristine anatase TiO_2 as well as lanthanides doped TiO_2 in addition substitutional energies of one atom and two atom substitution were investigated using DFT calculations applying LDA+U method. Ce and Gd had the least substitution energy in all charge states. The calculated thermodynamic transition levels exhibited negative U behaviour in the case of Ce, Nd, Sm, Gd and Tm. An optimal doping concentration was realized at 2.78% (~3.00%) which was within the experimental doping range. Doping TiO_2 with lanthanide ions was fund to results in shifying the absorption peaks of the of the pristine for the UV into the the visible regime. Lanthanide doping in TiO_2 was also found to lead to narrowing of the

Table 5
Extracted absorption coefficients of Ln:TiO_2.

Ln:TiO_2	*U* (eV)	Absorption peaks (eV)		Absorption peaks (nm)			
0%		3.2		387.5		UV	
La	2	0.6	2.5	2066.7	496	IR	Visible
Ce	3	2.5		496		Visible	
Pr	2	1.4	2.4	885.7	516.7	IR	Visible
Nd	3	0.7	2.4	1771.4	516.7	IR	Visible
Pm	1.5	0.8	2.4	1550	516.7	IR	Visible
Sm	2	1.0	2.6	1240	476.9	IR	Visible
Eu	3	1.0	2.6	1240	476.9	IR	Visible
Gd	2	2.6		476.9		Visible	
Tm	2	0.4	2.5	3100	496	IR	Visible
Yb	2	0.4	2.5	3100	496	IR	Visible
Lu	3.5	0.4	2.4	3100	516.7	IR	Visible

band gap (i.e. red shift). From our study there was consistency between calculated electronic and optical properties of both the pristine and lanthanide doped TiO_2 to both the observed experimental results as well as other theoretical investigations.

Acknowledgement

This work is based on the research supported in part by the National Research Foundation of South Africa. The Grant holder acknowledges that opinions, findings and conclusions or recommendations expressed in any publication generated by the NRF (NTF13091944109) supported research are that of the author (s) and that the NRF accepts no liability whatsoever in this regard.

Appendix A. Supplementary material

Supplementary data associated with this article can be found in the online version at http://dx.doi.org/10.1016/j.jssc.2016.02.003.

References

[1] J. Zhang, P. Zhou, J. Liu, J. Yu, New understanding of the difference of photocatalytic activity among anatase, rutile and brookite TiO_2, Phys. Chem. Chem. Phys. 16 (2014) 20382–20386.
[2] I.K. Konstantinou, T.A. Albanis, Photocatalytic transformation of pesticides in aqueous titanium dioxide suspensions using artificial and solar light: intermediates and degradation pathways, Appl. Catal. B Environ. 42 (2003) 319–335.
[3] Y. Zhang, Z.-R. Tang, X. Fu, Y.-J. Xu, TiO_2-graphene nanocomposites for gas-phase photocatalytic degradation of volatile aromatic pollutant: is TiO_2-graphene truly different from other TiO_2-carbon composite materials? ACS Nano 4 (2010) 7303–7314.
[4] M. Ni, M.K.H. Leung, D.Y.C. Leung, K. Sumathy, A review and recent developments in photocatalytic water-splitting using TiO_2 for hydrogen production, Renew. Sustain. Energy Rev. 11 (2007) 401–425.
[5] M.D. Hernández-Alonso, F. Fresno, S. Suárez, J.M. Coronado, Development of alternative photocatalysts to TiO_2: challenges and opportunities, Energy Environ. Sci. 2 (2009) 1231–1257.
[6] M. Yan, F. Chen, J. Zhang, M. Anpo, Preparation of controllable crystalline titania and study on the photocatalytic properties, J. Phys. Chem. B 109 (2005) 8673–8678.
[7] J.-M. Herrmann, Fundamentals and misconceptions in photocatalysis, J. Photochem. Photobiol. A Chem. 216 (2010) 85–93.
[8] Z. Zhang, X. Wang, J. Long, Q. Gu, Z. Ding, X. Fu, Nitrogen-doped titanium dioxide visible light photocatalyst: spectroscopic identification of photoactive centers, J. Catal. 276 (2010) 201–214.
[9] R. Long, N.J. English, Tailoring the electronic structure of TiO_2 by cation co-doping from hybrid density functional theory calculations, Phys. Rev. B 83 (2011) 155209.
[10] A.B. Yusov, V.P. Shilov, Photochemistry of f-element ions, Russ. Chem. Bull. 49 (2000) 1925–1953.
[11] D.M. Tobaldi, A.S. Škapin, R.C. Pullar, M.P. Seabra, J.A. Labrincha, Titanium dioxide modified with transition metals and rare earth elements: phase composition, optical properties, and photocatalytic activity, Ceram. Int. 39 (2013) 2619–2629.
[12] S.H.I. Huixian, T. Zhang, W. Hongliang, Preparation and photocatalytic activity of La 3+ and Eu 3+ co-doped TiO_2 nanoparticles: photo-assisted degradation of methylene blue, J. Rare Earths 29 (2011) 746–752.
[13] K.T. Ranjit, I. Willner, S.H. Bossmann, A.M. Braun, Lanthanide oxide doped titanium dioxide photocatalysts: effective photocatalysts for the enhanced degradation of salicylic acid and t-cinnamic acid, J. Catal. 204 (2001) 305–313.
[14] K.T. Ranjit, I. Willner, S.H. Bossmann, A.M. Braun, Lanthanide oxide-doped titanium dioxide photocatalysts: novel photocatalysts for the enhanced degradation of p-chlorophenoxyacetic acid, Environ. Sci. Technol. 35 (2001) 1544–1549.
[15] S. Matsuo, N. Sakaguchi, K. Yamada, T. Matsuo, H. Wakita, Role in photocatalysis and coordination structure of metal ions adsorbed on titanium dioxide particles: a comparison between lanthanide and iron ions, Appl. Surf. Sci. 228 (2004) 233–244.
[16] D. Li, N. Ohashi, S. Hishita, T. Kolodiazhnyi, H. Haneda, Origin of visible-light-driven photocatalysis: a comparative study on N/F-doped and N–F-codoped TiO_2 powders by means of experimental characterizations and theoretical calculations, J. Solid State Chem. 178 (2005) 3293–3302.
[17] T. Umebayashi, T. Yamaki, H. Itoh, K. Asai, Analysis of electronic structures of 3d transition metal-doped TiO_2 based on band calculations, J. Phys. Chem. Solids 63 (2002) 1909–1920.
[18] J.-C.G. Bünzli, C. Piguet, Taking advantage of luminescent lanthanide ions, Chem. Soc. Rev. 34 (2005) 1048–1077.
[19] B.M. Tissue, Synthesis and luminescence of lanthanide ions in nanoscale insulating hosts, Chem. Mater. 10 (1998) 2837–2845.
[20] W. Liu, W. Küchle, M. Dolg, Ab initio pseudopotential and density-functional all-electron study of ionization and excitation energies of actinide atoms, Phys. Rev. A 58 (1998) 1103.
[21] J. Paier, M. Marsman, K. Hummer, G. Kresse, I.C. Gerber, J.G. Angyán, Screened hybrid density functionals applied to solids, J. Chem. Phys. 124 (2006) 154709, http://dx.doi.org/10.1063/1.2187006.
[22] J. Heyd, G.E. Scuseria, M. Ernzerhof, Hybrid functionals based on a screened Coulomb potential, J. Chem. Phys. 118 (2003) 8207, http://dx.doi.org/10.1063/1.1564060.
[23] X. Ren, Beyond LDA and GGA - Tackling exact exchange , hybrid functional , MP2 , and RPA with numeric atom-centered orbitals. The Fritz-Haber-Institute ab initio molecular simulations package, 2009.
[24] C.N.M. Ouma, M.Z. Mapelu, N.W. Makau, G.O. Amolo, R. Maezono, Quantum Monte Carlo study of pressure-induced B3-B1 phase transition in GaAs, Phys. Rev. B 86 (2012) 104115, http://dx.doi.org/10.1103/PhysRevB.86.104115.
[25] B. Himmetoglu, A. Floris, S. de Gironcoli, M. Cococcioni, Hubbard-corrected DFT energy functionals: the LDA+U description of correlated systems, Int. J. Quantum Chem. 114 (2014) 14–49, http://dx.doi.org/10.1002/qua.24521.
[26] M. Cococcioni, S. De Gironcoli, Linear response approach to the calculation of the effective interaction parameters in the LDA+*U* method, Phys. Rev. B 71 (2005) 35105.
[27] G. Kresse, D. Joubert, From ultrasoft pseudopotentials to the projector augmented-wave method, Phys. Rev. B 59 (1999) 1758–1775, http://dx.doi.org/10.1103/PhysRevB.59.1758.
[28] P. Giannozzi, S. Baroni, N. Bonini, M. Calandra, R. Car, C. Cavazzoni, et al., Quantum espresso: a modular and open-source software project for quantum simulations of materials, J. Phys. Condens. Matter. 21 (n.d.) 395502.
[29] O.K. Andersen, Linear methods in band theory, Phys. Rev. B 12 (1975) 3060–3083, http://dx.doi.org/10.1103/PhysRevB.12.3060.
[30] D.D. Koelling, G.O. Arbman, Use of energy derivative of the radial solution in an augmented plane wave method: application to copper, J. Phys. F: Met. Phys. 5 (1975) 2041–2054, http://dx.doi.org/10.1088/0305-4608/5/11/016.
[31] H.J. Monkhorst, J.D. Pack, Special points for Brillouin-zone integrations, Phys. Rev. B 13 (12) (1976) 5188–5192.
[32] H. Tang, H. Berger, P.E. Schmid, F. Levy, G. Burri, Photoluminescence in TiO_2 anatase single crystals, Solid State Commun. 87 (1993) 847–850.
[33] A. Janotti, D. Segev, C. Van de Walle, Effects of cation d states on the structural and electronic properties of III-nitride and II-oxide wide-band-gap semiconductors, Phys. Rev. B 74 (2006) 045202, http://dx.doi.org/10.1103/

PhysRevB.74.045202.
[34] A. Calzolari, M.B. Nardelli, Dielectric properties and Raman spectra of ZnO from a first principles finite-differences/finite-fields approach, Sci. Rep. 3 (2013).
[35] A. Calzolari, A. Ruini, A. Catellani, Anchor group versus conjugation: toward the gap-state engineering of functionalized ZnO ($10\bar{1}0$) surface for optoelectronic applications, J. Am. Chem. Soc. 133 (2011) 5893–5899.
[36] R. Gillen, S.J. Clark, J. Robertson, Nature of the electronic band gap in lanthanide oxides, Phys. Rev. B 87 (2013) 125116.
[37] A.V. Prokofiev, A.I. Shelykh, B.T. Melekh, Periodicity in the band gap variation of Ln_2X_3 (X=O, S, Se) in the lanthanide series, J. Alloy. Compd. 242 (1996) 41–44.
[38] S. Kimura, F. Arai, M. Ikezawa, Optical study on electronic structure of rare-earth sesquioxides, J. Phys. Soc. Jpn. 69 (2000) 3451–3457.
[39] T. Arlt, M. Bermejo, M.A. Blanco, L. Gerward, J.Z. Jiang, J.S. Olsen, et al., High-pressure polymorphs of anatase TiO_2, Phys. Rev. B 61 (2000) 14414.
[40] M.E. Arroyo-de Dompablo, A. Morales-García, M. Taravillo, DFT+*U* calculations of crystal lattice, electronic structure, and phase stability under pressure of TiO_2 polymorphs, J. Chem. Phys. 135 (2011) 54503.
[41] H. Ehrenreich, M.H. Cohen, Self-consistent field approach to the many-electron problem, Phys. Rev. 115 (1959) 786.
[42] S. Zhang, J. Northrup, Chemical potential dependence of defect formation energies in GaAs: application to Ga self-diffusion, Phys. Rev. Lett. 67 (1991) 2339–2342, http://dx.doi.org/10.1103/PhysRevLett.67.2339.
[43] C. Freysoldt, J. Neugebauer, C.G. Van de Walle, Electrostatic interactions between charged defects in supercells, Phys. Status Solidi 248 (2011) 1067–1076, http://dx.doi.org/10.1002/pssb.201046289.
[44] C. Freysoldt, J. Neugebauer, C. Van de Walle, Fully ab initio finite-size corrections for charged-defect supercell calculations, Phys. Rev. Lett. 102 (2009) 016402, http://dx.doi.org/10.1103/PhysRevLett.102.016402.
[45] C.G. Van de Walle, First-principles calculations for defects and impurities: applications to III-nitrides, J. Appl. Phys. 95 (2004) 3851, http://dx.doi.org/10.1063/1.1682673.
[46] W. Chen, P. Yuan, S. Zhang, Q. Sun, E. Liang, Y. Jia, Electronic properties of anatase TiO_2 doped by lanthanides: a DFT+*U* study, Phys. B: Condens. Matter 407 (2012) 1038–1043.
[47] Z. Zhao, Q. Liu, Effects of lanthanide doping on electronic structures and optical properties of anatase TiO_2 from density functional theory calculations, J. Phys. D: Appl. Phys. 41 (2008) 85417.
[48] Y. Du, M. Du, Y. Qiao, J. Dai, J. Xu, P. Yang, Ce (4+) doped TiO_2 thin films: characterization and photocatalysis, Colloid J. 69 (2007) 695–699.
[49] A. Janotti, C.G. Van de Walle, LDA +*U* and hybrid functional calculations for defects in ZnO, SnO_2, and TiO_2, Phys. Status Solidi 248 (2011) 799–804, http://dx.doi.org/10.1002/pssb.201046384.
[50] G.D. Watkins, Negative-*U* properties for defects in solids, Adv. Solid State Phys. 24 (1984) 163–189, Springer.
[51] W. Guan, F. Ji, Z. Xie, R. Li, N. Mei, Preparation and photocatalytic performance of nano-TiO_2 codoped with Iron III and Lanthanum III, J. Nanomater. (2015).
[52] G. Shao, Electronic structures of manganese-doped rutile TiO_2 from first principles, J. Phys. Chem. C. 112 (2008) 18677–18685.
[53] G.K. Boschloo, A. Goossens, J. Schoonman, Photoelectrochemical study of thin anatase TiO_2 films prepared by metallorganic chemical vapor deposition, J. Electrochem. Soc. 144 (1997) 1311–1317.
[54] M. Pal, U. Pal, R. Silva Gonzalez, E. Sanchez Mora, P. Santiago, Synthesis and photocatalytic activity of Yb doped TiO_2 nanoparticles under visible light, J. Nano Res. (2009) 193–200.
[55] K. Binnemans, Lanthanide-based luminescent hybrid materials, Chem. Rev. 109 (2009) 4283–4374.
[56] B. Henderson, G.F. Imbusch, Optical Spectroscopy of Inorganic Solids, Oxford University Press, Oxford, 1989.
[57] M.A. Farrukh, M. Shahid, I. Muneer, S. Javaid, M. Khaleeq-ur-Rahman, Influence of gadolinium precursor on the enhanced red shift of Gd/SnO_2–TiO_2 nanoparticles and catalytic activity, J. Mater. Sci. Mater. Electron., (n.d.), pp. 1–9.
[58] A. Podhorodecki, G. Zatryb, P. Sitarek, J. Misiewicz, D. Kaczmarek, J. Domaradzki, et al., Excitation mechanism of europium ions embedded into TiO_2 nanocrystalline matrix, Thin Solid Films 517 (2009) 6331–6333.
[59] Q. Xiao, Z. Si, Z. Yu, G. Qiu, Sol–gel auto-combustion synthesis of samarium-doped TiO_2 nanoparticles and their photocatalytic activity under visible light irradiation, Mater. Sci. Eng. B 137 (2007) 189–194.
[60] J. Reszczynska, D.A. Esteban, M. Gazda, A. Zaleska, Pr-doped TiO_2. The effect of metal content on photocatalytic activity, Physicochem. Probl. Miner. Process. 50 (2014) 515–524.
[61] A. Malik, S. Hameed, M.J. Siddiqui, M.M. Haque, M. Muneer, Influence of Ce doping on the electrical and optical properties of TiO_2 and its photocatalytic activity for the degradation of remazol brilliant blue R, Int. J. Photoenergy 2013 (2013).
[62] D. Nassoko, Y.-F. Li, J.-L. Li, X. Li, Y. Yu, Neodymium-doped with anatase and brookite two phases: mechanism for photocatalytic activity enhancement under visible light and the role of electron, Int. J. Photoenergy 2012 (2012).